

π -magnetism and quantum transport in graphene-based nanostructures

Departamento de Polímeros y Materiales Avanzados:
Física, Química y Tecnología

Sofia Sanz Wuhl

Supervised by
Professor Thomas Frederiksen

Donostia-San Sebastián, Spain
August 20, 2022

A mis padres,
Judith y Fernando

Preface

Creo que la gente que más nos influye suele pasar más desapercibida. Cuando era adolescente no me daba cuenta de la gran importancia que han tenido ciertas personas en mi vida y que casi diré que de no ser por ellos y ellas quizás no estaría donde estoy. Cada día que pasa me doy más cuenta de la importancia de los profesores y profesoras en la etapa del instituto, en mi caso el Ramiro de Maeztu, donde se empieza a forjar la personalidad y tomamos (algunas) de las decisiones más importantes que nos hacen ser quien somos. Para mí esas personas son Carmen Rábade, Patricio Gómez y Amparo Medina-Bocos. Habéis sido una grandísima inspiración para mí. A día de hoy me sigo acordando de vosotros y vosotras.

Tras mi paso por la Universidad Autónoma de Madrid, llegué a uno de los que considero los mejores y más punteros centros de investigación de física de la materia condensada: Donostia International Physics Center (DIPC). Quiero agradecer al DIPC (Ricardo Díez Muiño y Pedro Etxenike) por haberme proporcionado un espacio de trabajo en un entorno del conocimiento tan bueno y por haberme ayudado con la financiación durante mi primer año de tesis y también del máster junto al Centro de Física de Materiales (CFM). Qué pena que no existan más centros como este que *no permitan* que los y las estudiantes de doctorado trabajen gratis.

I have a lot of people to be grateful to for their help, assistance and teaching during this thesis. First of all and foremost I would like to start with my thesis supervisor, Prof. Thomas Frederiksen, for all his patience and careful guidance. His enthusiasm provided me with great motivation throughout all the interesting projects that we developed together. I have learnt a lot during these past years, and still am! Thank you for all the good advises and for treating me always with respect in every aspect. I really felt the team spirit.

From the DIPC, CFM, Nanogune and CiQUS I would like to give special thanks to (with no special order) Géza Giedke, Pedro Brandimarte, Daniel Sánchez-Portal, Aran García-Lekue, Nacho Pascual, Dimas de Oteyza, Jingcheng Li, Niklas Friedrich, Martina Corso, Deung-Jang Choi, Néstor Merino Díez and Diego Peña, for those really nice projects together and those interesting discussions about physics! I have learnt the most with all of you!

Outside Spain, I would like to thank Mads Brandbyge from the Denmark Technical University (DTU) for his deep knowledge on the non-equilibrium Green's function methodology and his help to implement this formalism in the HUBBARD PYTHON package. In fact, the following collaborations resulted in one of the most important parts of this present thesis. Thank you for kindly receiving me with open arms all the times that I went to visit to the DTU, I had an exceptional time there and the projects that came out were incredibly interesting! I would also like to thank Nick Papior, a great programmer and better physicist, for his assistance and large contribution to the development of the HUBBARD module, I have learnt a lot from you! In the same line, I would like to take this opportunity to thank Aleksander Bach Lorentzen for his implementation of the block tridiagonalization, which can make this code much more efficient.

Ya más a nivel personal quería empezar por agradecer a mis amigos y amigas del DIPIC y CFM: Mireia, Irene, Raulillo, Jon Lasa, Edurne, Mikel Iraola, Martín, Carmen, Marina, Miguel Ángel, Fer, Diego, Xabier D. de C., Maru, María Blanco, Mikel O., Mole y Txiki, muchísimas gracias por ser tan maravillosos y maravillosas, qué alegría haberos conocido! Al equipo de informáticos, que son tan listos y trabajadores como majos, Dani F. y Jose C. Gracias por estar tan dispuestos siempre a resolver cualquier duda por muy tonta que sea. Especial y eterno agradecimiento a Jorge por los cafés y las risas que nos hemos echado. Me han dado y me siguen dando la vida. Te mereces lo mejor allá donde vayas como persona y científico top que eres. Yo también te llevo dentro. Cris, no sé ni por donde empezar contigo. Estos cuatro años han sido maravillosos y en gran parte gracias a ti, a tu presencia y actitud. Creo que una de las partes más positivas de haber ido a Donosti es haberte conocido. Me río muchísimo contigo y también lloro. Lo tienes todo. Me emociono al pensar que los dos estaréis ahí para siempre :) Me aportáis en todos los aspectos.

Por supuesto agradecer a mis padres Judith y Fernando, que me han apoyado tanto financiera como con todo su corazón durante toda mi vida; no estaría aquí (ni en ningún otro sitio) si no fuera por vosotrxs. Nunca habrá suficientes tesis para agradecerlos tanto. El amor que os tengo es incalculable. A mi hermano Tati, que a pesar de tener seis años menos que yo nunca dejo de aprender de él, nunca dejas de sorprenderme! Al resto de mis familiares, por parte de la familia Sanz, mi abuela Ana, mis primos y primas Félix y Valentín, Dolores, Paula y Luciana y mis tíos y tías Daniel, Eduardo y Nilda. Por parte de mi familia Wuhl, a mi abuela Baba, a mis primos y primas Félix, Renata y Lisa. A mi prima Luli (y Nadine), que me acompañó durante la más dulce infancia que podría haber tenido. A mis tíos y tías Daniel, Silvina, María y Tío Li, quien también me apoyó siempre y me valora por lo que soy. A todos deciros que aunque la distancia nos separe, la vida nos une.

A mis mejores amigos y amigas, los de (y para) toda la vida, quiero agradecerlos todo el apoyo que me habéis brindado siempre y todas esas chapas que me habéis aguantado desde los inicios de nuestra amistad ;) que sepáis que era mi *yo pre-científica* intentando salir. A Casado mi amigo del alma, de montaña y de todo. No sé qué haría sin ti honestamente. La vida es mejor a tu lado. Paloma y Dafne, mis robochis de corazón de oro, sois la energía femenina que necesito en mi vida, me brindáis amor, sabiduría y emoción. Nunca dejo de aprender con vosotras. Hacéis del mundo un lugar mejor. Chopillo, tu brillantez en prácticamente todos los aspectos de la vida no deja de asombrarme, me siento muy orgullosa de estar tan cerca de tí. Edu G. eres una de las personas más especiales que conozco, me haces sentir y flotar. Al resto de mis amigos, pero no menos importantes, Alejo, Chupi, Vic, Nikalva, Manubrio, Beto, Ana Moñino, Diego y Miki, me siento especial a vuestro lado. Vuestra amistad es mi verdadero tesoro.

A mis mejores amigos de la universidad, agradecerlos lo muchísimo que he crecido con vosotros, Gonzalo Troncoso, Eduardo Zubizarreta y Carlos de la Vera. No me imagino estar donde estoy de no haber aprendido tanto a vuestro lado, y no me refiero solo a aspectos científicos (que también), sino a todo lo que he crecido como persona gracias a vuestra amistad. Sois increíbles. A mis otros compañeros y compañeras de clase, Julia, Lucas, Manu y lxs demás deciros que cada vez que os veo es como si no hubiera pasado el tiempo. Me siento en familia. Por último añadido también a mis nuevos amigos y amigas de la uni que han estado ahí siempre pero los he conocido recientemente: Sergio, Guille, Javi, Raquel, Pablo, Álvaro, Darío y Mario. Bienvenidos y bienvenidas a mi vida :)

Por último quería dedicarte el final de estos agradecimientos a tí, Ion M., que aunque nuestros destinos ya no tengan por qué ser los mismos, nuestros caminos pasean en paralelo. Eso me reconforta infinitamente. Gracias por todos esos buenos (y también malos) momentos. El sentimiento de agradecimiento contigo va mucho más allá de la tesis, pero este espacio me parece igual de bueno como cualquier otro para compartirlo.

ESKERRIK ASKO

This thesis was funded partially by the DIPC (first year) and by the Departamento de Educación del Gobierno Vasco (Eusko Jaurlaritza) through the grants PRE_2018_1_0153, PRE_2019_2_0218, PRE_2020_2_0049 and PRE_2021_2_0190 (remaining years). Additionally I would like to acknowledge the funding of the different projects such as the project Spanish Ministerio de Economía y Competitividad (MINECO) through the Grants no. FIS2017-83780-P (Graphene Nanostructures “GRANAS”), Spanish AEI through project no. PID2020-115406GB-I00 “GEQCO”, the European Union (EU) through Horizon 2020 (FET-Open project “SPRING” Grant No. 863098), that have helped to develop the publications included in this thesis.

Resumen

En las últimas décadas hemos podido presenciar avances drásticos en el campo de la electrónica, que han ocasionado un fuerte impacto en aplicaciones que afectan prácticamente todos los aspectos de nuestra vida. Estos progresos surgen, en gran medida, por la continua miniaturización de los dispositivos electrónicos, en particular de los transistores basados en silíceo, que han dado lugar a circuitos más eficientes y menos costosos. Obviamente dicho escalamiento no puede continuar indefinidamente. Por ejemplo, a la escala nanométrica los efectos de la mecánica cuántica comienzan a ganar importancia, así como otras limitaciones de naturaleza científica y tecnológica, que ponen límites al tamaño mínimo y funcionamiento de los dispositivos basados en silíceo.

Desde que se consiguió aislar el grafeno, una capa de grosor monoatómica de átomos de carbono dispuestos en forma de panel de abeja, ha habido un gran esfuerzo generalizado a la hora de explorar las infinitas posibilidades que este material ofrece para el diseño de dispositivos que podrían suponer la próxima generación de la electrónica actual basada en transistores de silíceo. Sin embargo, el grafeno posee una estructura de bandas que no presenta un gap (carácter metálico), lo que imposibilita su uso como material *canal* en la arquitectura del transistor de efecto campo. Esto se puede solventar utilizando grafeno nanoestructurado en su lugar, ya que dichos sistemas pueden heredar algunas de las propiedades excepcionales del grafeno a la par que permiten moldear las propiedades electrónicas y magnéticas como se desee. De la misma manera, los materiales magnéticos son esenciales para la tecnología moderna, ya que juegan un papel importantísimo en el almacenamiento de datos, así como en dispositivos espintrónicos (en los que se aprovecha el grado de libertad del espín del electrón además de su carga). Mientras que el grafeno no es en principio un material magnético, derivados del grafeno y el grafeno nanoestructurado pueden mostrar magnetismo ya que una red de carbonos conjugados puede disponer de electrones desapareados que dan lugar a espines localizados (π -magnetism).

A la hora de construir dispositivos electrónicos y espintrónicos, se requiere un control a nivel molecular de las partes que componen dicho dispositivo a través de fuertes enlaces covalentes entre moléculas que permita un transporte de electrones eficiente entre ellas y que provea de alta estabilidad. En el caso de los métodos ‘top-down’, como la fotolitografía, la calidad de los bordes en las estructuras—que juegan un papel crucial en las propiedades del material—es difícil de controlar a escala atómica, mientras que en el caso de técnicas tipo ‘bottom-up’, como la síntesis sobre superficies de moléculas orgánicas en ultra-alto vacío, pueden dar muestras de precisión atomística, lo que la convierte en uno

de los métodos más poderosos para una construcción controlada de nanoarquitecturas funcionales.

En la primera parte de esta tesis analizamos, desde un punto de vista teórico, el origen del magnetismo en muchas nanoestructuras de grafeno que han sido sintetizadas experimentalmente y que muestran señales de magnetismo. Para ello hemos desarrollado un software en PYTHON (llamada librería HUBBARD) que, basado en el modelo de Hubbard en aproximación de campo medio, nos ha permitido estudiar la estructura electrónica en función del espín, teniendo en cuenta la repulsión electrónica, en las moléculas que dan lugar a la presencia de magnetismo.

En el artículo I ([Nat. Commun. 10, 200 \(2019\)](#)) estudiamos un sistema compuesto por una unión de dos nanocintas quirales que, aun teniendo la *misma geometría molecular*, muestran diferentes escenarios: en algunos casos esta molécula muestra una resonancia al nivel de Fermi, asociada al efecto Kondo, que implica un electrón localizado (estos casos fueron nombrados como tipo-1 y tipo-2), mientras que en otros casos (tipo-3) estas moléculas muestran una curva de transición singlete-triplete. Para entender la existencia de esta diferencia encontrada en los espectros de la corriente frente al voltaje recogidos con el microscopio de efecto túnel, simulamos dicha estructura con nuestro paquete HUBBARD en combinación con teoría del funcional de la densidad (Density Functional Theory, DFT). Así pudimos comprobar que, dado que las funciones de onda de los orbitales moleculares eran extremadamente localizadas, la presencia de la repulsión electrónica lleva a los electrones a reorganizarse en la molécula para desaparecer y ocupar orbitales moleculares diferentes con el fin de reducir dicha interacción (estos electrones desaparecidos componen los llamados radicales). Teniendo este escenario en mente, para entender que en algunos casos solo hubiera un único radical (tipo-1 y tipo-2) lo que hicimos fue pasivar cada uno de los radicales con un átomo extra de hidrógeno. De esta manera se elimina el radical correspondiente y permanece el otro. En el caso en el que hay dos radicales presentes, estos se acoplan formando un singlete, lo que da lugar al espectro encontrado tipo-3. Cabe remarcar que tanto las funciones de onda encontradas como las polarizaciones de espín se corresponden con un gran parecido tanto cualitativo como cuantitativo a los resultados experimentales.

En el artículo II ([Phys. Rev. Lett. 124, 177201 \(2020\)](#)) estudiamos el caso de una molécula tipo trianguleno. Dicha molécula acomoda un imbalance entre las subredes de la red bipartita, lo que origina un espín total distinto de cero (en este caso, el estado de más baja energía es aquél con $S = 1$, ya que tiene 19 átomos de carbono en una subred mientras que 17 en la otra). De nuevo, simulamos el sistema con nuestro paquete HUBBARD y con DFT. Dichas simulaciones muestran una excelente similitud con el experimento, y demuestran que efectivamente el estado de más baja energía es aquél

con $S = 1$. Experimentalmente dicho resultado se observó al medir el espectro de la corriente frente al voltaje en el microscopio de efecto túnel, en el que se ve una resonancia tipo Kondo infra-apantallado (underscreened Kondo), asociado al efecto Kondo de un estado tipo triplete. En este artículo no solo estudiamos el caso del monómero sino también del dímero (unión de dos monómeros). Al tener un conjunto de dos sistemas con dos radicales cada uno, se esperaría que el conjunto de ellos tuviera cuatro radicales presentes, sin embargo, en el proceso de la síntesis sobre la superficie, la geometría molecular resultante presenta un pentágono que cambia la naturaleza de cuatro radicales a solo dos (demostrado tanto teórica como experimentalmente). En este artículo también estudiamos el efecto de la pasivación de los radicales con átomos extra de hidrógeno, que además constituye una forma de demostrar el número de radicales presentes en las moléculas.

En los artículos mencionados anteriormente estudiamos los casos particulares de geometrías tipo sp^2 basadas únicamente en carbono. En el artículo III ([Nano Lett. 22, 164–171 \(2022\)](#)) estudiamos también el efecto de la presencia de heteroátomos en la geometría molecular, manteniendo el carácter sp^2 , que como demostramos en este artículo pueden jugar un papel fundamental en las propiedades magnéticas. Por ejemplo, al reemplazar un grupo CH en el borde de una nanocinta quiral pristina por un grupo C=O (grupo carbonilo), se añade un electrón a la red π del sistema. Como consecuencia, el número impar de electrones causa la presencia de radicales tipo π . Lo mismo ocurre en el caso contrario, en el que empezamos con una nanocinta quiral completamente funcionalizada con ketonas, en la que se reemplaza un grupo C=O por un grupo CH. En este estudio demostramos cómo el acoplo entre los presentes electrones desapareados depende de su posición relativa, que incluye una gran dependencia en la quiralidad, así como de la naturaleza química que la rodea (es decir, con o sin estar funcionalizados con ketonas). Dado que el grupo carbonilo también pertenece a una hibridización tipo sp^2 , éste contribuye con un electrón p_z , y puede como primera aproximación considerarse como un sitio p_z en su correspondiente subred. En un intento de construir un modelo sencillo para estudiar estos sistemas con nuestro paquete HUBBARD, comenzamos utilizando los mismos parámetros para los átomos de carbono que para los de oxígeno, a este modelo lo llamamos MFH-TB(1). Sin embargo, la existencia de discrepancias de este modelo con otros más exactos (DFT) nos llevaron a considerar otro modelo en el que cambiamos los elementos de matriz del Hamiltoniano entre primeros vecinos a $t = 3.8$ eV y los potenciales a $\epsilon_i = -1.5$ eV para los átomos de oxígeno enlazados a átomos de carbono (manteniendo $t = 2.7$ eV y los potenciales a $\epsilon_i = 0$ para el resto de los átomos). Este modelo mejoró drásticamente tanto resultados cuantitativos como cualitativos en comparación con lo obtenido con DFT. Cualitativamente estos parámetros se pueden

relacionar directamente con el hecho de que el enlace C=O es más corto que el enlace C–C, mientras que el potencial ‘más negativo’ del oxígeno se relaciona con su más alta electronegatividad con respecto a los átomos de carbono.

En la segunda parte de esta tesis, nos centramos en el transporte cuántico de electrones en estructuras de grafeno. Inspirado por las muchas similitudes entre fotones propagando en guías de onda y electrones viajando de forma balística en estructuras de grafeno, nace el campo de la ‘óptica electrónica en estructuras de grafeno’, donde los electrones se comportan como fotones en dichos medios. Teniendo las ideas de los experimentos del campo de la óptica en mente, podemos pensar en estudiar interferometría electrónica, para lo cual se necesitan ciertos bloques fundamentales para la construcción de los interferómetros, como por ejemplo espejos electrónicos, divisores del haz, filtros, etc. Aquí demostramos que las nanocintas de grafeno pueden ser unos buenos candidatos para desarrollar este tipo de experimentos, ya que además de presentar buenas propiedades para este fin, hay perspectiva de posible realización experimental gracias al desarrollo de la síntesis sobre superficies.

En el artículo IV ([Phys. Rev. B **102**, 035436 \(2020\)](#)) estudiamos de forma general dispositivos formados por nanocintas de grafeno cruzadas con un ángulo relativo de 60° y dispuestas una encima de la otra a una distancia típica de van der Waals en grafito (unos 3.34 \AA aproximadamente). Debido a la simetría de la red hexagonal del grafeno, cuando el ángulo de cruce entre las cintas es de 60° , se produce una maximización en la transferencia de electrones entre las cintas. En este artículo demostramos que este fenómeno da lugar a que los electrones puedan transmitirse por este dispositivo de cuatro terminales sin reflexión y con un ratio de transmisión dentro y entre nanocintas que depende de la anchura de las nanocintas y de la energía del electrón transmitido. En este contexto podemos encontrar que en función de estos parámetros estos dispositivos pueden comportarse como espejos electrónicos direccionales (donde el electrón es completamente transmitido a la otra cinta), como un divisor del haz (en el que el electrón es igualmente transmitido en las dos posibles direcciones sin reflexión), como un filtro de longitud de onda, etc. Estos datos fueron recogidos en una figura de mérito en la se muestra los distintos regímenes de transporte de estos dispositivos, con intención de que sirva como guía para el diseño y optimización de los interferómetros basados en nanocintas de grafeno para el estudio de la óptica electrónica. El estudio realizado cubre distintas nanocintas (con distintos bordes, como por ejemplo tipo ‘armchair’ y ‘zigzag’) y distintos alineamientos entre las cintas (AA y AB, existentes con un ángulo de 60°). Además, dado que utilizamos un modelo de ‘tight-binding’ general basado en la parametrización Slater-Koster, donde los elementos de matrix dependen exponencialmente de las distancias entre los pares atómicos, estudiamos el efecto de posibles distorsiones en los cruces,

como diferentes ángulos de cruce, posibles traslaciones de una cinta con respecto a la otra, diferentes distancias de separación entre las cintas, diferentes potenciales entre las cintas, etc. Con esto, en este estudio, contribuimos con una caracterización completa del funcionamiento de dichos dispositivos a la par que estudiamos el efecto de posibles adversidades a las que se podría enfrentar el resultante dispositivo construido experimentalmente.

En el artículo anterior estudiamos las propiedades de transporte de electrones en dispositivos formados por nanocintas de grafeno en ausencia de interacción electrónica. Sin embargo, se conoce que las cintas de grafeno con bordes tipo ‘zigzag’ presentan estados localizados cerca del nivel de Fermi (bandas planas) que dan lugar a inestabilidades magnéticas que originan estados polarizados de espín localizados en los bordes, y la apertura de un gap de correlación alrededor del nivel de Fermi. Teniendo este fenómeno en mente, en el artículo V ([Phys. Rev. Lett. 129, 037701 \(2022\)](#)) estudiamos las propiedades de transporte de dichos dispositivos incluyendo el término de repulsión electrónica en el Hamiltoniano. Para describir la física de espín en estos sistemas utilizamos el modelo de Hubbard en aproximación de campo medio, implementado en nuestra librería HUBBARD. Dado que las cintas son infinitas, pero el sistema carece de periodicidad, utilizamos el formalismo de funciones de Green fuera del equilibrio para resolver la ecuación de Schrödinger. En este artículo queda demostrado que estos dispositivos son aún más interesantes, ya que no sólo mantienen sus propiedades de transporte al incluir la repulsión electrónica (transmisión únicamente en dos de los cuatro brazos del dispositivo sin reflexión) sino que además pueden funcionar como divisores del haz que polarizan en espín la corriente saliente, ya que las probabilidades de transmisión en cada una de las posibles direcciones de salida son muy diferentes dependiendo del índice de espín.

Abstract

The drastic advances in the field of electronics in the past few decades have arisen, to a large extent, from the continuous miniaturization of silicon-based transistors, which have already reached the nanoscale. Nevertheless, this ‘down-scaling’ cannot continue indefinitely, as some limitations of fundamental scientific and technological nature start to appear. Since the isolation of graphene there has been a huge effort to explore the infinite possibilities that this material offers for device designing, that could be the next generation of electronics. However, while the gapless bandstructure of graphene prevents its usage as the channel material in field-effect transistor architectures, nanostructured graphene systems are gaining interest since they can inherit some of the exceptional properties from graphene while having a tunable electronic structure. Moreover, magnetic materials are essential for modern technology since they play the main role in data storage and are also of particular interest for spintronics and quantum computing applications. While graphene is not magnetic itself, many of its derivatives have shown magnetic features, opening the doors for carbon-based magnetism. Now, custom-crafted graphene nanostructures can be synthesized through chemical reactions of rationally designed precursor molecules assisted by metal surfaces (on-surface synthesis). Following this line, in the first part of this thesis we provide with fundamental insights and understanding of the origins of the source of magnetism in several nanographenes of diradical character with crafted shapes that show interesting magnetic features. The magnetic exchange coupling can be in fact quite tunable and versatile, as it highly depends on the relative position between the radicals (unpaired electrons), the occupying underlying sublattices and their chemical environment.

Another interesting property from graphene comes from the similarities between electrons circulating ballistically in graphene constrictions and photon propagation in wave guides, which have opened the doors for studying optics-like experiments in graphene nanostructures, where electrons play the role of photons. One of the most elementary building blocks necessary to perform electron quantum optics is the electron beam splitter, which is the electronic analog of a beam splitter for light. Remarkably, it has been shown that there is an enhancement in the electron transfer process between two crossed graphene nanoribbons (GNR) with an intersecting angle close to 60° as a consequence of the symmetry of the honeycomb lattice, since this crossing angle yields a perfect matching of the bottom and top GNR atomic structures. In this thesis we show that by tuning the electronic energy of valence and conduction band electrons, and the width of the ribbons these devices can behave as fundamental blocks for electron quantum optics experiments, such as, *e.g.*, mirrors, beam splitters (half-transparent mirrors) and

wavelength filters. Furthermore, GNRs with zigzag edge topology host localized magnetic edge states, that give rise to additional interesting features for the charge and spin transport. In this thesis we also show that such devices can create a spin-polarizing scattering potential which enables them to operate as a *spin-polarizing beam splitter*.

We employ the tight-binding (TB) methodology that allowed us to explore a large number of systems of considerable sizes in a fast and transparent way, where the accuracy of the description depends on the chosen parametrization. To describe the spin physics we make use of the Hubbard model within the mean-field approximation backed up with density functional theory (DFT) calculations. To perform spin and electron quantum transport calculations we make use of the non-equilibrium Green's function (NEGF) formalism to solve the Schrödinger equation for the open quantum systems.

The results presented in this thesis intend to reflect the potential of graphene nanostructures as ideal systems for carbon-based electronics, spintronics, and electron quantum optics with potential applications in next-generation quantum computation.

Contents

Preface	iii
Resumen	vi
Abstract	xi
Abbreviations	xv
List of publications	xvi
1 Introduction	1
1.1 General objectives	8
1.2 Organization of this thesis	9
2 Models and theoretical methods	10
2.1 Non-equilibrium Green's function formalism and partitioning scheme	10
2.1.1 Wide-band limit approximation	12
2.2 Scattering matrix from Green's function	13
2.3 Electronic structure of graphene systems: general considerations	17
2.4 Tight-binding	20
2.4.1 Bloch's theorem: periodic band structure	21
2.5 Magnetism in graphene: the mean-field Hubbard Hamiltonian	27
2.5.1 Measure of error: Spin contamination	30
2.5.2 Calculation of spin densities and total energy	30
2.5.3 The HUBBARD package	33
2.6 Density functional theory: The SIESTA method	37
3 Magnetism in nanographenes	40
3.1 Spin localization and manipulation in GNR junctions	40

3.2	Triangulene-like nanostructures	42
3.3	Exchange interaction between radical pairs in heteroatomic structures . .	44
4	Electron quantum optics in GNR-based architectures	46
4.1	Inter-GNR coupling description	46
4.2	Symmetry aspects of crossed GNRs	46
4.3	GNR networks for electron interferometry	47
4.4	Spin-polarizing electron beam-splitting effect in crossed ZGNRs	48
5	Conclusions and outlook	50
I	Single spin localization and manipulation in graphene open-shell nanostructures, Nat. Commun. 10, 200 (2019)	54
II	Uncovering the triplet ground state of triangular graphene nanoflakes engineered with atomic precision on a metal surface, Phys. Rev. Lett. 124, 177201 (2020)	62
III	Magnetic interactions between radical pairs in chiral graphene nanoribbons, Nano Lett. 22, 164–171 (2022)	69
IV	Crossed graphene nanoribbons as beam splitters and mirrors for electron quantum optics, Phys. Rev. B 102, 035436 (2020)	78
V	Spin-polarizing beam splitter realized with crossed zigzag graphene nanoribbons, Phys. Rev. Lett. 129, 037701 (2022)	93
	Bibliography	138

Acronyms/Abbreviations

Abbreviation	Definition
1NN, 2NN, 3NN	First, second and third nearest-neighbors
1D, 2D	One dimension, two dimensions
AGNR	Armchair graphene nanoribbon
BZ	Brillouin zone
chGNR	Chiral graphene nanoribbon
DFT	Density functional theory
DOS	Density of states
DZP	Double- ζ polarized
GGA	Generalized gradient approximation
GNR	Graphene nanoribbon
HOMO	Highest occupied molecular orbital
KS	Kohn-Sham
LDA	Local density approximation
LDOS	Local density of states
LUMO	Lowest unoccupied molecular orbital
MFH	Mean-field Hubbard
NEGF	Non-equilibrium Green's function
NFE	Nearly-free electrons
OBC	Open boundary conditions
OSS	On-surface synthesis
PBC	Periodic boundary conditions
PDOS	Projected density of states
SCF	Self-consistent field
SOMO	Singly occupied molecular orbital
STM	Scanning tunneling microscope
SK	Slater-Koster
TB	Tight-binding
WBL	Wide-band limit
WF	Wave function
XC	Exchange and correlation
ZGNR	Zigzag graphene nanoribbon

List of publications

π -magnetism in graphene nanostructures:

- I. “*Single spin localization and manipulation in graphene open-shell nanostructures*”, Jingcheng Li, **Sofia Sanz**, Martina Corso, Deung Jang Choi, Diego Peña, Thomas Frederiksen, Jose Ignacio Pascual, [Nat. Commun. **10**, 200 \(2019\)](#)
- II. “*Uncovering the triplet ground state of triangular graphene nanoflakes engineered with atomic precision on a metal surface*”, Jingcheng Li, **Sofia Sanz**, Jesus Castro-Esteban, Manuel Vilas-Varela, Niklas Friedrich, Thomas Frederiksen, Diego Peña, and Jose Ignacio Pascual, [Phys. Rev. Lett. **124**, 177201 \(2020\)](#)
- III. “*Magnetic interactions between radical pairs in chiral graphene nanoribbons*”, Tao Wang, **Sofia Sanz**, Jesús Castro-Esteban, James Lawrence, Alejandro Berdonces-Layunta, Mohammed S. G. Mohammed, Manuel Vilas-Varela, Martina Corso, Diego Peña, Thomas Frederiksen, Dimas G. de Oteyza, [Nano Lett. **22**, 164–171 \(2022\)](#)

Quantum transport in graphene nanoribbon junctions:

- IV. “*Crossed graphene nanoribbons as beam splitters and mirrors for electron quantum optics*”, **Sofia Sanz**, Pedro Brandimarte, Géza Giedke, Daniel Sánchez-Portal, and Thomas Frederiksen, [Phys. Rev. B **102**, 035436 \(2020\)](#)
- V. “*Spin-polarizing beam splitters with crossed zigzag graphene nanoribbons*”, **Sofia Sanz**, Nick Papior, Géza Giedke, Daniel Sánchez-Portal, Mads Brandbyge, Thomas Frederiksen, [Phys. Rev. Lett. **129**, 037701 \(2022\)](#)

Not included in this thesis

- VI. “*Topological phase transition in chiral graphene nanoribbons: from edge bands to end states*”, Jingcheng Li, **Sofia Sanz**, Nestor Merino-Díez, Manuel Vilas-Varela, Aran Garcia-Lekue, Martina Corso, Dimas G. de Oteyza, Thomas Frederiksen, Diego Peña, Jose Ignacio Pascual, [Nat. Commun. 12, 5538 \(2021\)](#)
- VII. “*On-surface synthesis and collective spin excitations of a triangulene-based nanostar*”, Jeremy Hieulle, Silvia Castro, Niklas Friedrich, Alessio Vegliante, Francisco Romero Lara, **Sofia Sanz**, Dulce Rey, Martina Corso, Thomas Frederiksen, Jose Ignacio Pascual, Diego Peña, [Angew. Chem. Int. Ed. 60, 25224-25229 \(2021\)](#)

In the past few decades we have witnessed drastic advances in the field of electronics that have had tremendous impact in applications that affect about every aspect of our lives. These progresses have arisen, to a large extent, from the continuous ‘down-scaling’ of electronic devices, more specifically of silicon-based transistors, that has led to more generally efficient and less expensive circuitry [1–4]. Obviously, this device scaling cannot continue indefinitely. For instance, at the nanometer scale quantum mechanical effects start to gain importance, as well as other limitations of fundamental scientific and technological nature, which place limits on the minimum size and performance of silicon devices. Hence, the approaching end point has inspired a worldwide effort to develop alternative setups to substitute current silicon-based technologies.

Since the isolation of graphene [5–7], a material that has shown superior electrical and mechanical properties, graphene-based transistors have developed rapidly and are now considered as an option for the next-generation post-silicon electronics [8]. One of the taken approaches in this direction is to replace the conducting channel—a key component of the device—with carbon nanomaterials while maintaining the operating principles of the currently used devices, primarily that of the field-effect transistor (FET). However, the absence of a sizeable and well-defined band gap and the resulting lack of a pronounced drain-current saturation limits prohibit two-dimensional (2D) graphene as the channel material in FETs architectures for logic applications [9]. To overcome this issue, other architectures have been recently proposed: a graphene base transistor [10], a hot electron transistor with a base contact made of graphene [11], etc. Even bilayer graphene is still gapless, however if an electric field is applied perpendicular to the bilayer, a band gap opens and the bands near the K point take on the so-called Mexican-hat shape [12–15]. Other approaches involve moving away from traditional electron transport-based electronics, that have no analogue in silicon-based applications: for example, the development of spin-based devices (spintronics), or even the possibility to manipulate the valley (energy extrema in the electronic band structure) degree of

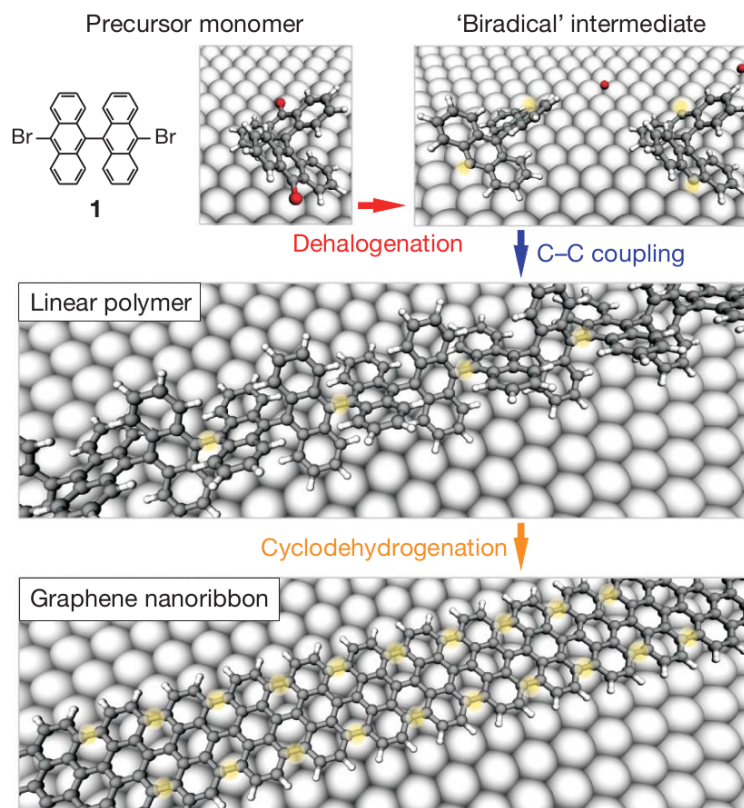


Figure 1.1: On-surface synthesis (OSS) route for the bottom-up fabrication of atomically precise GNRs. Illustration of the basic steps for surface-supported GNR synthesis exemplified with 10,10'-dibromo-9,9'-bianthryl monomers of 7-AGNR. Reproduced from [18].

freedom, which defines the field of valleytronics, the valley analogue of spintronics [16,17].

Fortunately, a solution to the gapless condition of 2D graphene is to use nanostructured graphene systems, that, while inheriting some of the exceptional properties of graphene, offer a tunable electronic structure as a consequence of electron confinement. When it comes to molecular electronics and spintronics, the construction of such devices requires a controlled arrangement of the molecular counterparts by strong covalent intermolecular connections, enabling efficient electron transport between the molecules and providing high stability. Since in the case of top-down methods, such as photolithography, the quality of edge structures—which play a crucial role in the properties of the synthesized materials—are difficult to control at the atomic scale, there has been a large effort in developing new strategies to obtain cleaner structures experimentally. This

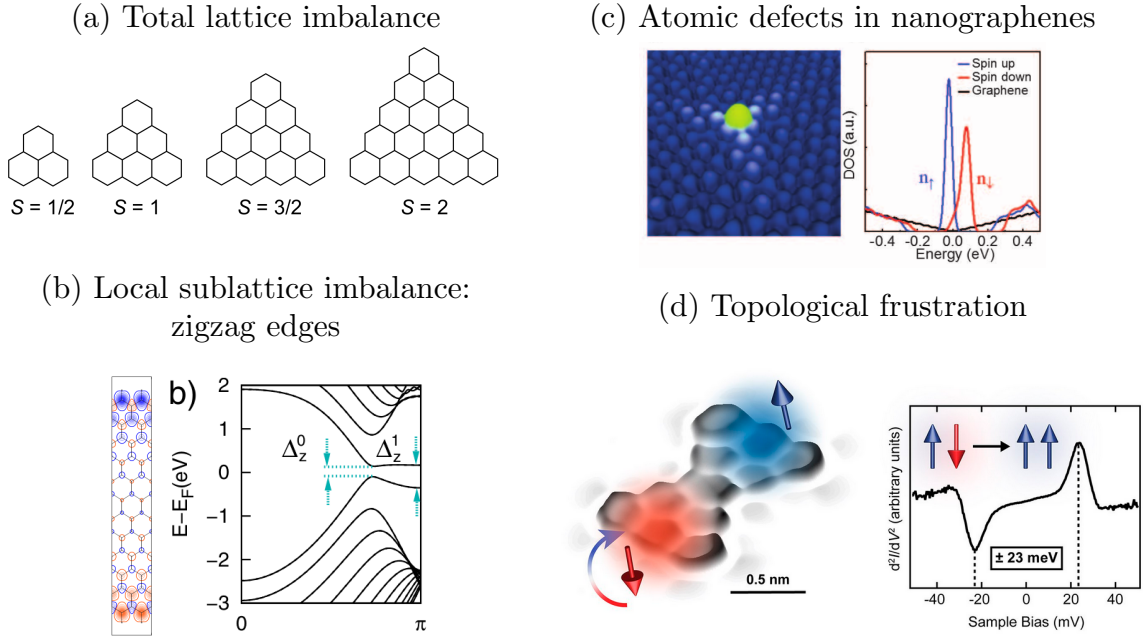


Figure 1.2: Possible routes towards magnetism in graphene. (a) Evolution of the sublattice imbalance and therefore the total spin S of triangular graphene fragments with the molecular size, as stated by the Lieb's theorem (extracted from [21]). (b) Appearance of localized magnetic moments at the zigzag edges and correlation gap opening in its bandstructure due to the local sublattice imbalance. Figures taken from Ref. [22]. (c) Atomic defects in nanographene. Image taken from Ref. [23]. (d) Topological frustration in the Clar's goblet structure. Panel taken from Ref. [24, 25].

is the case of bottom-up OSS [18–20] of self-assembled organic molecules in ultra-high vacuum (see Fig. 1.1). This technique, which is in a sense an extension of heterogeneous catalysis whereby the chemical reactants (precursors), the intermediate states, and the reaction products remain in an adsorbed state, can give clean samples of atomistic precision, leading to one of the most powerful strategies towards a controllable construction of functional nanoarchitectures.

Origins of magnetism in sp^2 carbon compounds and emergence of π -magnetism. Magnetic materials are essential for modern technology, they play the main role in data storage and are also of particular interest for spintronics and quantum computing applications. The most typical used magnetic atoms involve the elements belonging to either the d - or the f -block of the periodic table. In fact, among the atomic elements only the late transition metals, Fe, Co and Ni, are ferromagnets at room temperature. However, while ideal graphene is non-magnetic itself, many of its derivative

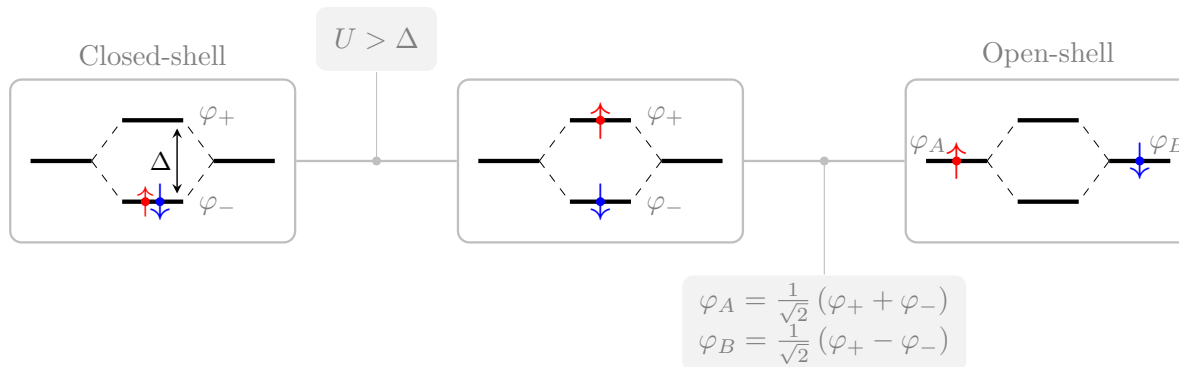


Figure 1.3: Orbital recombination of the highest occupied molecular orbital (HOMO) and lowest unoccupied molecular orbital (LUMO) ψ_{\pm} to form singly occupied molecular orbital (MO) $\psi_{A,B}$ that reduce the Coulomb repulsion between electrons and leads to the open-shell character.

materials and nanostructures show various scenarios of magnetism since an arrangement of sp^2 carbons in a cross-conjugated manner affords a branched π -system that exhibits magnetism due to the intrinsic appearance of unpaired electrons. For instance, a number of reports have pointed out that even untreated graphite exhibits ferromagnetism [26,27]. In fact, graphene π -paramagnetism is more delocalized, mobile, and isotropic than conventional magnetism arising from d or f states [28]. For these reasons (among many others) the field of light-element magnetism and, in particular, of carbon-based magnetism is currently gaining increasing importance [29,30]. Furthermore, it was predicted that the magnetic moments and their correlations in nanographenes can be precisely engineered through their sizes, edge topology, or chemical doping [31–34]. However, until recently the magnetic properties of such nanosystems were not possible to reproduce as they rely on the presence of unpaired π -electrons, whose high chemical reactivity either hindered their synthesis in solution or impeded their characterization [35]. With the advent of OSS, one can now design custom-crafted nanostructures that can be both synthesized and characterized as they are produced under ultra-high vacuum conditions and can be measured with scanning probe techniques [25,36–43].

To understand the magnetic ordering in a nanographene one can make use of a set of rules that predicts the magnetic nature of the ground state. Generally, in polycyclic aromatic hydrocarbons (PAH) the spin of the ground state can be anticipated using Ovchinnikov’s rule [44], which states that its spin S is given by $S = \frac{1}{2}|N_A - N_B|$, where N_A , N_B are the number of C atoms in each of the interpenetrating triangular sublattices that form the honeycomb lattice. This rule was later upgraded into a theorem by E. H. Lieb [45], who generalized the exact interacting ground state of the Hubbard model

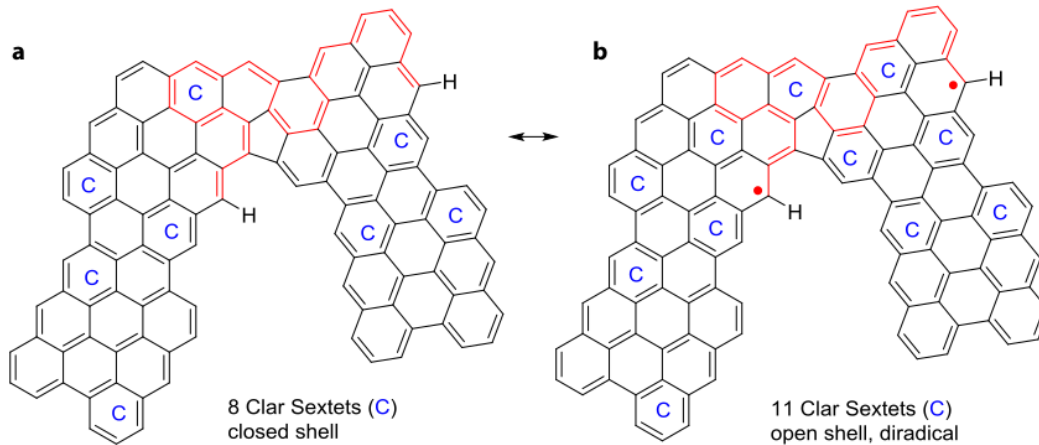


Figure 1.4: Open-shell character: Understanding the appearance of radicals in the nanostructures from Clar’s theory. The Clar’s sextets are indicated by C in the molecular geometry. Panels (a) and (b) show the closed-shell and the open-shell scenarios, respectively. Figure taken from the supplemental information of Ref. [36].

for *any* bipartite system, where N_A , N_B now are the number of atoms corresponding to the existing sublattices. This picture was further completed by R. Ortiz *et al.* by providing a set of rules that determine the multiplicity and the open-/closed-shell nature of the lowest energy many-body states for (the previously not-very-well addressed) nanographenes of diradical character [46]. For instance, this gives a way in which planar π -conjugated hydrocarbons can be turned magnetic, *e.g.*, by designing a nanographene with a sublattice imbalance [33], as seen in Fig. 1.2a-b.

Another source of magnetism in graphene is the presence of atomic defects, *e.g.*, chemisorpted hydrogen or vacancy defects [21, 23, 47, 48], as shown in Fig. 1.2c, or even chemical functionalization. For instance, chiral GNRs (chGNRs) oxidize when exposed to oxygen [49], where the resulting replacement of CH at the edge by a C=O (carbonyl) group leads to one additional π -electron in the system. However, there is another mechanism in which carbon compounds can become magnetic even for systems with low total spin ($S = 0$), *e.g.*, topologically frustrated systems [25] as shown in Fig. 1.2d, and systems where the Lieb’s theorem does not apply [36]. This mechanism is based on the simple fact that electrons occupying the same MO will suffer from a strong Coulomb repulsion for highly localized MO. In those cases, if this interaction energy is stronger than the energy difference between the valence electrons and the first unoccupied states, then the electron will be promoted to an unoccupied state, as sketched in Fig. 1.3. The resulting radicals (unpaired electrons) can interact and be magnetically coupled forming a magnetic singlet or triplet depending on the preferred orientation. An alternative

chemical schematic picture behind the emergence of singly occupied radical states can be drawn bearing in mind Clar's aromatic π -sextet rule [50] in which the emergence of two unpaired electrons is compensated by the energy gain of the creation of more aromatic rings (Clar's sextets), see Fig. 1.4.

GNRs as a platform for electron quantum optics and spintronics. The similarities between the wave nature of electrons propagating coherently in ballistic conductors with photon propagation in optical waveguides has sparked the field of electron quantum optics [52, 53]. For instance, the electron wave nature can manifest itself in a variety of interference, diffraction, and refraction effects, for example, when transmitted across a boundary separating regions of different electron density [51, 54, 55], *e.g.*, as shown in Fig. 1.5. This resemblance makes it possible to manipulate electrons like photons by using components inspired by geometrical optics, such as mirrors, lenses, prisms, and beam splitters. A platform with remarkable prospects for electron quantum optics are graphene-based systems, in which several pioneering experiments on electron beam splitters and related devices have been performed [51, 56]. Recently, semicon-

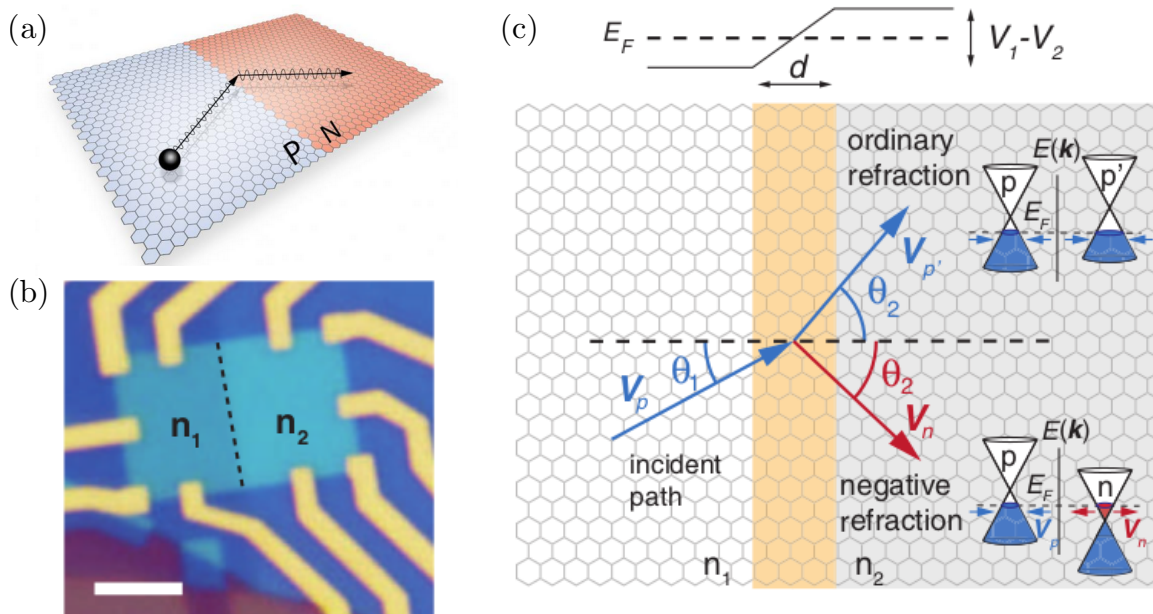


Figure 1.5: First hints of electron quantum optics in graphene nanoconstrictions. (a) Sketch of the p - n junction. (b) Real image of the split gate device. (c) Sketch of the Snell's law that electrons' velocity suffers when entering different regions of the p - n junction with different dopings, leading to different refractive indices. Images taken from [51].

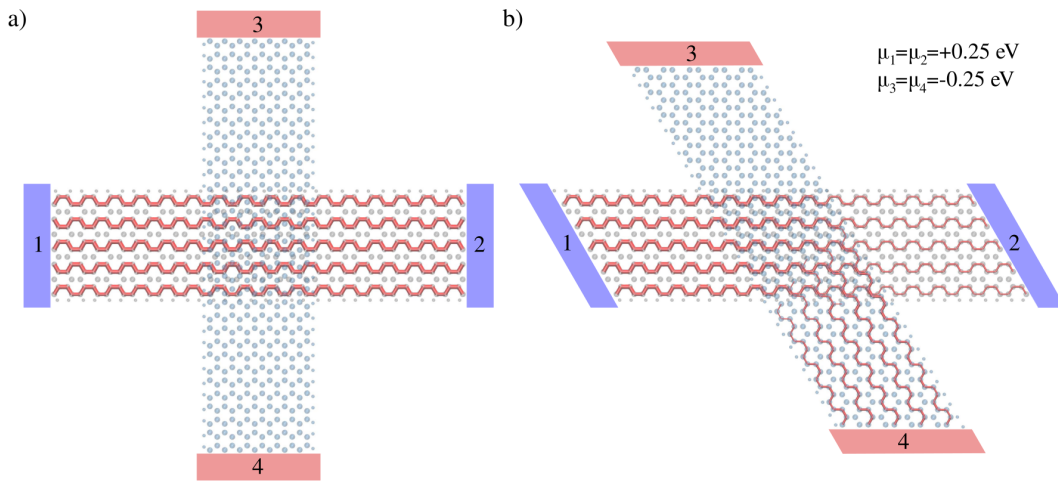


Figure 1.6: Electron beam splitting effect in multiterminal junctions formed of crossed GNRs. Images taken from [77].

ducting one-dimensional (1D) carbon nanotubes and GNRs have emerged as attractive candidates for the construction of molecular-scale electronic devices [9, 57, 58] since they inherit some of the exceptional properties from graphene while having tunable direct band gaps [22, 59–64]. Furthermore, it has been established experimentally that electrons can propagate without scattering over large distances of the order of ~ 100 nm in GNRs [65–67]. For instance, ballistic transport in ZGNRs can be rather insensitive to edge defects because of the dominating Dirac-like physics, that make the current flow maximally through the center of the ribbon [68]. Moreover, with the advent of bottom-up fabrication techniques via OSS, long defect-free samples can be chemically synthesized with both armchair (AGNR) [18] and zigzag (ZGNR) [69] edge topologies. Manipulation of GNRs with scanning tunneling probes has been also demonstrated [70, 71], opening the possibility to build two-dimensional multiterminal graphene-based electronic circuits [72–75]. For instance, it has been recently proposed that the transfer process between two crossed GNRs is strongly enhanced with negligible reflection when intersecting with an angle of 60° , as a consequence of the honeycomb lattice symmetry. In fact, such four-terminal devices were found to divide the electron beam into two out of the four arms with an almost equal transmission probability of 50% [76, 77] as shown in Fig. 1.6.

Among their many possibilities, graphene derivatives have also shown to be an interesting platform for spintronics [78] due to the light mass and the near absence of nuclear magnetic moments in carbon, which give small spin-orbit interaction and hyper-

fine couplings—the major sources of spin relaxation and decoherence [28, 31, 78–81]. In general, materials that enjoy *sp*-bonding are expected to have high magnitudes of spin-wave stiffness [82] and long spin coherence lengths [82, 83] even at room temperature [84]. Furthermore, ZGNRs develop spin-polarized edge states as theoretically [85] and experimentally [86, 87] demonstrated that can lead to interesting spin transport effects. For instance, it has been shown that 4-terminal devices with zigzag edges can generate a spin-polarizing scattering potential [88], and moreover that one rough zigzag edge can be used to boost spin injection [89].

1.1 General objectives

The objectives of this thesis are the following:

Development of open-source software to describe spin physics in graphene-based extended structures. In first place, the large systems that are currently being synthesized brought the need for a software that allows to treat large-sized Hamiltonians to assist in understanding experimental results. Motivated by this we developed the HUBBARD package [90] which is a python-based module that allows one to find the magnetic ground state of a system within the mean-field Hubbard (MFH) approximation. The HUBBARD package aims to provide with an open-source tool easy to manipulate that quickly obtains the self-consistent solution for many different systems, that, inspired by the capabilities from SIESTA/TRANSIESTA [91, 92] can solve isolated, periodic and open boundary conditions. The advantages of it relying on SISL [93, 94]—an efficient tight-binding (TB) and density functional theory (DFT) interface library—permits to combine MFH- and DFT-based calculations easily.

Characterization of magnetic exchange interaction in diradical systems. In second place, by combining and comparing multiple calculations using both the HUBBARD package and SIESTA we were able to characterize many different systems showing magnetic fingerprints where the source of magnetism is of different natures. For instance, we were able to understand and characterize the exchange interaction in diradical systems in terms of (i) the origin of the spin localization and the role of Hydrogen passivation in chGNR junctions showing both a Kondo resonance and a singlet-triplet transition curve [36] (Paper I), (ii) the magnetic nature of triangulene-like nanographenes that showed underscreened Kondo effect [38] (Paper II), as well as (iii) the chemical environment and the relative position of the radicals in chGNRs with ketone functionalization [95] (Paper III).

Classification, characterization and proposition of devices for electron and spin quantum optics in GNR-based architectures. In third place, although pre-

vious studies revealed the presence of beam splitting effect in crossed GNRs junctions, there was a lack of generalization and systematic classification of these junctions in terms of their transport properties. In publication [96] (Paper IV) we provide a complete analysis of the regions in the parameters space where the junctions can act as fundamental components for electron interferometry, such as mirrors (where the electrons are fully transferred into the other ribbon), beam splitters (half-transparent mirrors, where the electrons are transmitted with a 50:50 ratio in two outgoing terminals), and wavelength filters, in a figure of merit that outline the transport properties of these devices. Furthermore, in the case of ZGNR devices, its performance as a beam splitter had been only studied for the *unpolarized case*, while it is known that ZGNRs tend to polarize due to the magnetic instabilities of the localized edge states when the Coulomb repulsion term is included in the recipe. In publication [97] (Paper V) we provide an analysis of the spin transport properties for these devices, and in particular their performance as *spin-polarizing electron beam splitters*.

1.2 Organization of this thesis

This thesis is organized as follows: In Chapter 2 the theoretical framework and methods are explained in detail. Both the methodology for transport calculations (Green's function and scattering matrix formalism), and electronic Hamiltonian to describe the electronic and magnetic properties of graphene-based nanostructures are introduced. In Chapter 3 the results for magnetism in nanographenes are summarized, and in Chapter 4 the results for electron quantum transport in graphene based nanostructures. Finally, in Chapter 5 the conclusions and prospects for the future are described.

This chapter is organized as follows: firstly, the non-equilibrium Green's function (NEGF) formalism and the definition of the concept of self-energies are explained in Sec. 2.1. Secondly the scattering matrix formalism and how it can be computed from the Green's function is detailed in Sec. 2.2. Then the electronic structure of carbon compounds is generally introduced in Sec. 2.3, followed by the different frameworks to calculate it, *i.e.*, the TB method in Sec. 2.4, the MFH model in Sec. 2.5, and DFT in Sec. 2.6.

2.1 Non-equilibrium Green's function formalism and partitioning scheme

To introduce the NEGF formalism we follow the approach of Ref. [98]. Green's functions [98–100] give the response at any point (inside or outside the system) due to an excitation (source) $|v\rangle$ at any other. The Green operator can then be defined to express the response of the system to such perturbation as,

$$\begin{aligned} \mathbf{H} |\psi\rangle &= E |\psi\rangle + |v\rangle \Rightarrow \\ (\mathbf{H} - E) |\psi\rangle &= |v\rangle \Rightarrow \\ |\psi\rangle &= \mathbf{G}(E) |v\rangle. \end{aligned} \tag{2.1}$$

Where $|\psi\rangle$, \mathbf{H} and E , are the wave function (WF), the Hamiltonian and the energy of the system, respectively. In these terms, the quantum mechanical problem can be expressed in terms of this differential operator $\mathbf{G} = (\mathbf{H} - E)^{-1}$. If the excitation is a point-like pulse, *i.e.*, a Dirac delta-like function, then the Green's function itself will reveal the WF (response) of the system. The inverse of a *differential* operator (integral form) is not uniquely defined unless the boundary conditions are properly specified. Eq. (2.1) has two solutions, called the retarded \mathbf{G} and advanced \mathbf{G}^\dagger Green's functions. The former

represents incoming waves, while the latter outgoing waves with respect to the placement of the source. In practice these two solutions are usually obtained by adding in Eq. (2.1) an infinitesimal imaginary part (η) to the energy. The limit ($\eta \rightarrow 0^+$) gives the retarded solution, while ($\eta \rightarrow 0^-$) gives the advanced (usually η is a parameter justified to ensure the convergence of a Fourier transform) [99, 101].

For the matrix representation of the Hamiltonian (and thus the Green's function), the equation that gives the Green's function is given in Eq. (2.2), where \mathbb{I} is the identity matrix of the given dimension.

$$\mathbf{G} = [(E + i\eta)\mathbb{I} - \mathbf{H}]^{-1}, \quad (\eta \rightarrow 0^+). \quad (2.2)$$

For the discrete Schrödinger equation, we can start by dividing the Hamiltonian and WFs into the contacts ($\mathbf{H}_{1,2}$, $|\psi_{1,2}\rangle$) and device subspaces (\mathbf{H}_d , $|\psi_d\rangle$). In the following example we consider a simple case where the device connected to only two contacts 1, 2, which are coupled to the device via the coupling matrices $\boldsymbol{\tau}_{1,2}$:

$$\begin{pmatrix} \mathbf{H}_1 & \boldsymbol{\tau}_1 & 0 \\ \boldsymbol{\tau}_1^\dagger & \mathbf{H}_d & \boldsymbol{\tau}_2^\dagger \\ 0 & \boldsymbol{\tau}_2 & \mathbf{H}_2 \end{pmatrix} \begin{pmatrix} |\psi_1\rangle \\ |\psi_d\rangle \\ |\psi_2\rangle \end{pmatrix} = E \begin{pmatrix} |\psi_1\rangle \\ |\psi_d\rangle \\ |\psi_2\rangle \end{pmatrix}. \quad (2.3)$$

The real interest in calculating the Green's function is that is easier than solving the eigenvalue problem and most (all for one-particle systems) properties can be calculated from it. On the other hand, the Green's function of the device, \mathbf{G}_d , can be calculated without calculating the whole Green's function.

$$\begin{pmatrix} E\mathbb{I} - \mathbf{H}_1 & -\boldsymbol{\tau}_1 & 0 \\ -\boldsymbol{\tau}_1^\dagger & E\mathbb{I} - \mathbf{H}_d & -\boldsymbol{\tau}_2^\dagger \\ 0 & -\boldsymbol{\tau}_2 & E\mathbb{I} - \mathbf{H}_2 \end{pmatrix} \begin{pmatrix} \mathbf{G}_1 & \mathbf{G}_{1d} & \mathbf{G}_{12} \\ \mathbf{G}_{d1} & \mathbf{G}_d & \mathbf{G}_{d2} \\ \mathbf{G}_{21} & \mathbf{G}_{2d} & \mathbf{G}_2 \end{pmatrix} = E \begin{pmatrix} \mathbb{I} & 0 & 0 \\ 0 & \mathbb{I} & 0 \\ 0 & 0 & \mathbb{I} \end{pmatrix}. \quad (2.4)$$

Selecting the three equations in the second column, we obtain the following system of equations

$$(E\mathbb{I} - \mathbf{H}_1)\mathbf{G}_{1d} - \boldsymbol{\tau}_1\mathbf{G}_d = 0 \quad (2.5)$$

$$-\boldsymbol{\tau}_1^\dagger\mathbf{G}_{1d} + (E\mathbb{I} - \mathbf{H}_d)\mathbf{G}_d - \boldsymbol{\tau}_2^\dagger\mathbf{G}_{2d} = \mathbb{I} \quad (2.6)$$

$$(E\mathbb{I} - \mathbf{H}_2)\mathbf{G}_{2d} - \boldsymbol{\tau}_2\mathbf{G}_d = 0. \quad (2.7)$$

From Eq. (2.5) and Eq. (2.7) we obtain $\mathbf{G}_{1d,2d} = g_{1,2}\boldsymbol{\tau}_{1,2}\mathbf{G}_d$, where $g_{1,2}$ is the *surface Green's function* of the isolated contacts, which are usually calculated recursively using

the Lopez-Sancho method [102, 103]. With this we can build the definition of the Green's function of the device,

$$\mathbf{G}_d = (E - \mathbf{H}_d - \sum_{\alpha} \Sigma_{\alpha})^{-1}, \quad (2.8)$$

where $\Sigma_{\alpha} = \tau_{\alpha}^{\dagger} g_{\alpha} \tau_{\alpha}$ is the *self-energy* for the α -th electrode, which encode the effect of the contacts on the device. The idea behind this mathematical approach is sketched in Fig. 2.1.

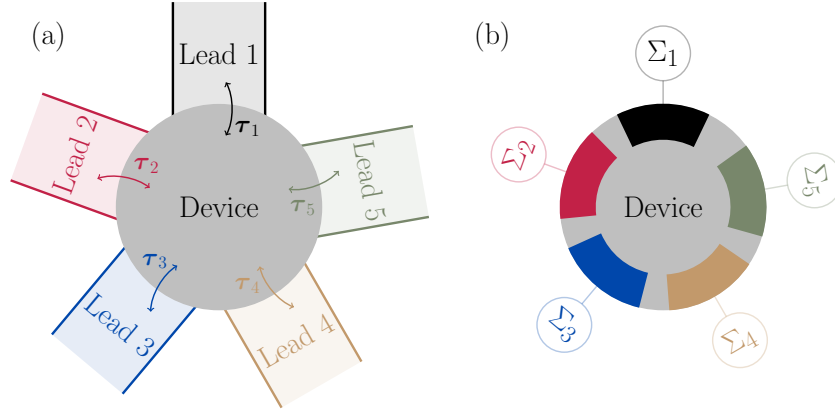


Figure 2.1: (a) Device connected to 5 semi-infinite leads through the coupling matrices, $\tau_i, i \in \{1, \dots, 5\}$, that can be conceptually replaced by the self-energy terms as sketched in (b).

2.1.1 Wide-band limit approximation

When the bandwidth is large compared to the applied bias, the density of states (DOS) in the electrodes can be considered fairly constant near the Fermi energy, or, in other words, the detailed structure of the DOS in the leads is not important for the description of transport in the device. In this limit, the effective wide-band limit (WBL) approximation can be employed to treat the self-energies of the leads in the nanoscale, which substantially simplifies computations. For instance, since the eigenspectrum of the Green's function does not depend on energy under this approximation, it can be diagonalized before evaluating the transport properties, dramatically reducing the computational cost [104–107]. Firstly, let's express the α th electrode's self-energy by splitting it into the Hermitian and anti-Hermitian parts,

$$\Sigma_{\alpha} = \Lambda_{\alpha}(E) - \frac{i}{2}\Gamma_{\alpha}(E), \quad (2.9)$$

where both $\mathbf{\Lambda}_\alpha$ and $\mathbf{\Gamma}_\alpha$ are real matrices. Effectively, the former introduces a shift of the orbital resonances, *i.e.*, affecting the poles of the Green's function, while the latter introduces a level broadening. To a first approximation, we can consider $\mathbf{\Gamma}$ to be independent of energy E and neglect the level-shift $\mathbf{\Lambda}$, which leads to the WBL approximation. This yields a self-energy of the form:

$$\Sigma_\alpha^{\text{WBL}} = -\frac{i}{2}\mathbf{\Gamma}_\alpha. \quad (2.10)$$

An example of the applicability of this approximation are systems with bulk-metal electrodes, as, *e.g.*, shown in Refs. [104, 106, 107]. In fact, this method was applied to successfully describe a GNR on a surface lifted by a scanning tunneling microscope (STM) tip [108, 109]. In these experiments, the STM tip would act as one of the bulk-metal electrodes and the substrate on which the GNR is standing would be the other electrode.

This approximation can be quite useful, for example, to understand what is the role of the surface in the localized spins in a molecule. For this reason, we have implemented this feature in the HUBBARD package so one can perform this type of calculations.

2.2 Scattering matrix from Green's function

In order to see how the scattering region affects the electron transport through a device, it can be convenient to make use of the scattering matrix (S-matrix), \mathbf{S} . By using this formalism one is able to obtain the outgoing states Ψ_{out} from a general input wave Ψ_{in} as

$$\Psi_{\text{out}} = \mathbf{S}\Psi_{\text{in}}. \quad (2.11)$$

This matrix can be easily computed from the retarded Green's function of the device for a given energy E by means of the generalized Fisher-Lee relations [110]:

$$\mathbf{S}_{\alpha\beta} = -\delta_{\alpha\beta}\mathbb{I} + i\tilde{\mathbf{\Gamma}}_\beta^T \mathbf{G} \tilde{\mathbf{\Gamma}}_\alpha. \quad (2.12)$$

Where α, β represent incoming and outgoing electrodes, respectively, $\delta_{\alpha\beta}$ is the Kronecker delta and $\tilde{\mathbf{\Gamma}}_\alpha = \text{diag}\{\sqrt{\gamma_\alpha}\}\mathbf{U}_\alpha$ is related to the level broadening matrix resulting from the coupling between lead α to the device region by

$$\mathbf{\Gamma}_\alpha = i(\Sigma_\alpha - \Sigma_\alpha^\dagger) = \mathbf{U}_\alpha^T \text{diag}\{\gamma_\alpha\}\mathbf{U}_\alpha. \quad (2.13)$$

It is convenient to express the broadening matrices in terms of their eigenvectors \mathbf{U}_α , which physically map into the transverse modes of the electrodes that are coupled to the device by the eigenvalues $\{\gamma_\alpha\}$, since now we can use only the modes that are actually coupled to the device (by neglecting those vectors of \mathbf{U}_α associated to $\gamma_\alpha \simeq 0$). We note that it is common to see the S-matrix expressed as $\mathbf{S}_{\alpha\beta} = -\delta_{\alpha\beta}\mathbb{I} + i\mathbf{\Gamma}_\alpha^{\frac{1}{2}}\mathbf{G}\mathbf{\Gamma}_\beta^{\frac{1}{2}}$. However, this identification is somehow misleading, because this expression acts on the Hilbert space of the device, which is subject to the chosen partitioning scheme (arbitrary size), as observed in Ref. [111], while Eq. (2.12) acts on the transverse part of the leads.

It is easy to see from Eq. (2.12) that the off-diagonal elements of $\mathbf{S}_{\alpha\beta}$ correspond to the transmission amplitude matrices between leads $\alpha \neq \beta$, while the diagonal elements $\mathbf{S}_{\alpha\alpha}$ correspond to the reflection amplitude matrices. Note that the dimension of $\mathbf{S}_{\alpha\beta}$ is $n_\alpha \times n_\beta$, where $n_{\alpha,\beta}$ is the number of modes (open channels) in the α -th and β -th electrodes at a particular energy.

The transmission probabilities can be computed from the S-matrix, recovering the Landauer-Büttiker transmission formula [112, 113] for (ideal) mesoscopic conductors:

$$T_{\alpha\beta} = \text{Tr} \left[\mathbf{S}_{\alpha\beta}^\dagger \mathbf{S}_{\alpha\beta} \right] = \text{Tr} \left[\mathbf{G}\mathbf{\Gamma}_\alpha \mathbf{G}^\dagger \mathbf{\Gamma}_\beta \right] = \sum_n T_n, \quad (2.14)$$

where T_n is the transmission probability of the n th eigenchannel (particular scattering state with a well-defined transmission probability) [114–117]. In addition to being useful for analyzing theoretical calculations, the eigenchannel transmissions may be obtained experimentally (i) with superconducting electrodes connecting the atomic-scale conductor [118] or (ii) from shot noise measurements, where information about the individual channel contributions can be obtained from the Fano factor [119].

The reflection probability can be conveniently written as a difference between the total number of open channels/modes (n_α) available at that energy and the scattered transmission into all the $\beta \neq \alpha$ electrodes, *i.e.*,

$$R_\alpha = M_\alpha - \sum_{\beta \neq \alpha} T_{\alpha\beta}. \quad (2.15)$$

The net current into lead α can be also obtained from the Landauer-Büttiker formula [112, 113, 120]:

$$I_\alpha = G_0 \int_0^\infty dE \sum_{\beta \neq \alpha} [f(E, \mu_\alpha) - f(E, \mu_\beta)] T_{\alpha\beta} \quad (2.16)$$

where $f(E, \mu_{\alpha,\beta})$ are the Fermi functions with $\mu_{\alpha,\beta}$ the chemical potential of leads α, β , and $G_0 = \frac{2e^2}{h}$ is the conductance quantum.

Combining S-matrices

In practice it is difficult to handle large conductors because of the size of the matrix that needs to be inverted. One solution to this problem is to divide the conductor into a few sections as shown in Fig. 2.2, compute the individual S-matrices and then coherently combine them to obtain the overall full S-matrix of the composite system [99, 121], *i.e.*, $\mathbf{S} = \mathbf{S}^1 \otimes \mathbf{S}^2 \otimes \mathbf{S}^3 \dots$. We will now describe the rules for combining S-matrices; that is, the meaning of the symbol \otimes . The full individual S-matrices applying to the corresponding

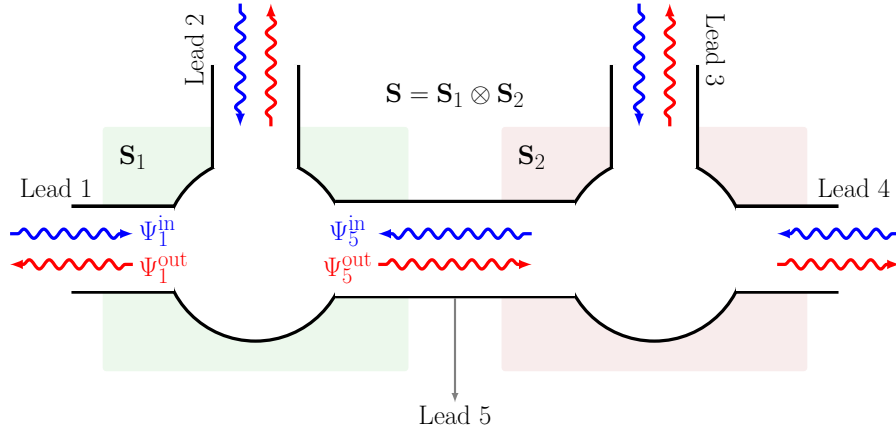


Figure 2.2: Two obstacles with separated scattering matrices $\mathbf{S}_1, \mathbf{S}_2$ are placed in series, as represented inside the rectangles with colors light green and light red. Ports 1-4 are indicated. Lead 5 correspond to the connection between the two scattering areas. Blue and red wiggly arrows indicate incoming and outgoing waves, respectively.

incoming Ψ^{in} with the resulting outgoing waves Ψ^{out} in each port follows,

$$\begin{pmatrix} \Psi_1^{\text{out}} \\ \Psi_2^{\text{out}} \\ \Psi_5^{\text{out}} \end{pmatrix} = \begin{pmatrix} \mathbf{r}^{(1)} & \mathbf{t}'^{(1)} \\ \mathbf{t}^{(1)} & \mathbf{r}'^{(1)} \end{pmatrix} \begin{pmatrix} \Psi_1^{\text{in}} \\ \Psi_2^{\text{in}} \\ \Psi_5^{\text{in}} \end{pmatrix} \quad \text{and} \quad \begin{pmatrix} \Psi_5^{\text{in}} \\ \Psi_3^{\text{out}} \\ \Psi_4^{\text{out}} \end{pmatrix} = \begin{pmatrix} \mathbf{r}^{(2)} & \mathbf{t}'^{(2)} \\ \mathbf{t}^{(2)} & \mathbf{r}'^{(2)} \end{pmatrix} \begin{pmatrix} \Psi_5^{\text{out}} \\ \Psi_3^{\text{in}} \\ \Psi_4^{\text{in}} \end{pmatrix} \quad (2.17)$$

Note that Ψ_5^{in} (Ψ_5^{out}) is the incoming (outgoing) wave for the first scattering center whilst the outgoing (incoming) wave for the second scattering center. To ease the development of this part we reduce the 3×3 S-matrices by considering the colored submatrice sepa-

rations in Eq. (2.17), leading to the following reduced equations:

$$\begin{pmatrix} \Psi_{1,2}^{\text{out}} \\ \Psi_5^{\text{out}} \end{pmatrix} = \begin{pmatrix} \mathbf{r}^{(1)} & \mathbf{t}'^{(1)} \\ \mathbf{t}^{(1)} & \mathbf{r}'^{(1)} \end{pmatrix} \begin{pmatrix} \Psi_{1,2}^{\text{in}} \\ \Psi_5^{\text{in}} \end{pmatrix} \quad \text{and} \quad \begin{pmatrix} \Psi_5^{\text{in}} \\ \Psi_{3,4}^{\text{out}} \end{pmatrix} = \begin{pmatrix} \mathbf{r}^{(2)} & \mathbf{t}'^{(2)} \\ \mathbf{t}^{(2)} & \mathbf{r}'^{(2)} \end{pmatrix} \begin{pmatrix} \Psi_5^{\text{out}} \\ \Psi_{3,4}^{\text{in}} \end{pmatrix}. \quad (2.18)$$

Where $\Psi_{1,2}^{\text{in}}$ ($\Psi_{1,2}^{\text{out}}$) vector represents the incoming (outgoing) wave amplitudes in all the various modes in terminals 1 and 2 and similarly for $\Psi_{3,4}^{\text{in}}$ and $\Psi_{3,4}^{\text{out}}$ with terminals 3 and 4. From the above system of equations we can straightforwardly eliminate Ψ_5^{in} and Ψ_5^{out} to get

$$\begin{pmatrix} \Psi_{1,2}^{\text{in}} \\ \Psi_{3,4}^{\text{in}} \end{pmatrix} = \begin{pmatrix} \mathbf{r} & \mathbf{t}' \\ \mathbf{t} & \mathbf{r}' \end{pmatrix} \begin{pmatrix} \Psi_{1,2}^{\text{out}} \\ \Psi_{3,4}^{\text{out}} \end{pmatrix}, \quad (2.19)$$

where

$$\begin{aligned} \mathbf{t} &= \mathbf{t}^{(2)} [\mathbb{I} - \mathbf{r}'^{(1)} \mathbf{r}^{(2)}]^{-1} \mathbf{t}^{(1)}, & \mathbf{r} &= \mathbf{r}^{(1)} + \mathbf{t}'^{(1)} \mathbf{r}^{(2)} [\mathbb{I} - \mathbf{r}'^{(1)} \mathbf{r}^{(2)}]^{-1} \mathbf{t}^{(1)} \\ \mathbf{t}' &= \mathbf{t}'^{(1)} [\mathbb{I} - \mathbf{r}^{(2)} \mathbf{r}'^{(1)}]^{-1} \mathbf{t}'^{(2)}, & \mathbf{r}' &= \mathbf{r}'^{(2)} + \mathbf{t}^{(2)} [\mathbb{I} - \mathbf{r}'^{(1)} \mathbf{r}^{(2)}]^{-1} \mathbf{r}'^{(1)} \mathbf{t}'^{(2)}. \end{aligned} \quad (2.20)$$

We can get further insight by expanding the above product into a resulting geometrical series which lead to the famous Feynman paths [99],

$$\begin{aligned} \mathbf{t} &= \mathbf{t}^{(2)} [\mathbb{I} - \mathbf{r}'^{(1)} \mathbf{r}^{(2)}]^{-1} \mathbf{t}^{(1)} \\ &= \mathbf{t}^{(2)} \mathbf{t}^{(1)} + \mathbf{t}^{(2)} [\mathbf{r}'^{(1)} \mathbf{r}^{(2)}] \mathbf{t}^{(1)} + \mathbf{t}^{(2)} [\mathbf{r}'^{(1)} \mathbf{r}^{(2)}] [\mathbf{r}'^{(1)} \mathbf{r}^{(2)}] \mathbf{t}^{(1)} + \dots \end{aligned} \quad (2.21)$$

where the successive terms have a simple physical interpretation. The first term is the amplitude for transmission through the obstacles without any reflection, the second term for transmission with two reflections, the third term for transmission with four reflections and so on. From Eq. (2.21), it can be seen that if the reflection amplitude is zero, then the overall transmission amplitude is calculated as $\mathbf{t} = \prod_i \mathbf{t}^{(i)}$.

Unitarity of S-matrix

The S-matrix has to be unitary in order to satisfy the current conservation law, which means that it must fulfill $\mathbf{S}^\dagger \mathbf{S} = \mathbb{I}$. For N terminal case the full S-matrix, \mathbf{S} , will be a $N \times N$ matrix of submatrices $S_{\alpha\beta}$. In terms of the N submatrices, they must fulfill: $\sum_{\nu=1}^N \mathbf{S}_{\alpha\nu}^\dagger \mathbf{S}_{\beta\nu} = \mathbb{I}_\alpha \delta_{\alpha\beta}$. To prove that the S-matrix proposed in Eq. (2.12) indeed is unitary, we will separate in the diagonal and the off-diagonal terms of the dot product $\mathbf{S}^\dagger \mathbf{S}$.

(i) Diagonal terms:

$$\begin{aligned}
(\mathbf{S}^\dagger \mathbf{S})_{\alpha\alpha} &= \sum_{\beta}^N \mathbf{S}_{\alpha\beta}^\dagger \mathbf{S}_{\alpha\beta} = \mathbf{S}_{\alpha\alpha}^\dagger \mathbf{S}_{\alpha\alpha} + \sum_{\beta \neq \alpha} \mathbf{S}_{\alpha\beta}^\dagger \mathbf{S}_{\alpha\beta} \\
&= \mathbb{I} + \tilde{\mathbf{\Gamma}}_\alpha^T \left[i(\mathbf{G}^\dagger - \mathbf{G}) + \mathbf{G} \left(\sum_{\beta}^N \mathbf{\Gamma}_\beta \right) \mathbf{G}^\dagger \right] \tilde{\mathbf{\Gamma}}_\alpha
\end{aligned} \tag{2.22}$$

(ii) Off-diagonal terms ($\alpha \neq \beta$):

$$\begin{aligned}
(\mathbf{S}^\dagger \mathbf{S})_{\alpha\beta} &= \sum_{\nu} \mathbf{S}_{\alpha\nu}^\dagger \mathbf{S}_{\beta\nu} = \mathbf{S}_{\alpha\alpha}^\dagger \mathbf{S}_{\beta\alpha} + \mathbf{S}_{\alpha\beta}^\dagger \mathbf{S}_{\beta\beta} + \sum_{\nu \neq \alpha, \beta} \mathbf{S}_{\alpha\nu}^\dagger \mathbf{S}_{\beta\nu} \\
&= \tilde{\mathbf{\Gamma}}_\alpha^T \left[i(\mathbf{G}^\dagger - \mathbf{G}) + \mathbf{G} \left(\sum_{\nu}^N \mathbf{\Gamma}_\nu \right) \mathbf{G}^\dagger \right] \tilde{\mathbf{\Gamma}}_\beta
\end{aligned} \tag{2.23}$$

Using the definition of the (total) spectral function,

$$\mathbf{A} = \mathbf{G} \mathbf{\Gamma} \mathbf{G}^\dagger = -i(\mathbf{G}^\dagger - \mathbf{G}), \tag{2.24}$$

where $\mathbf{\Gamma} = \sum_{\nu} \mathbf{\Gamma}_\nu$ is the total broadening matrix due to the coupling of the device to all the leads, it is easy to see that what is inside the squared brackets in Eq. (2.22) and Eq. (2.23) vanishes. Therefore it leaves us with the result $(\mathbf{S}^\dagger \mathbf{S})_{\alpha\alpha} = \mathbb{I}$ and $(\mathbf{S}^\dagger \mathbf{S})_{\alpha\beta} = 0$. Provided the results found in (i) and (ii), it has been proved that the S-matrix defined in Eq. (2.12) is unitary.

Additionally, under time reversal symmetry the condition is further simplified since the matrix is symmetric, *i.e.*, $\mathbf{S}^T = \mathbf{S}$, then the conjugate transpose (\dagger) becomes only conjugate ($*$) and the unitarity is fulfilled by $\mathbf{S}^* \mathbf{S} = \mathbb{I}$. In absence of time reversal symmetry, *e.g.*, in presence of a magnetic field \mathbf{B} , the S-matrix is said to be reciprocal, *i.e.*, $\mathbf{S}^T(-\mathbf{B}) = \mathbf{S}(\mathbf{B})$.

2.3 Electronic structure of graphene systems: general considerations

The electronic configuration of isolated atomic carbon is $1s^2 2s^2 2p^4$. In a solid-state environment the $|1s\rangle$ electrons typically remain inert, but the $|2s\rangle$ and $|2p\rangle$ orbitals hybridize into new orbitals to form covalent bonding [122], as sketched in Fig. 2.3. The

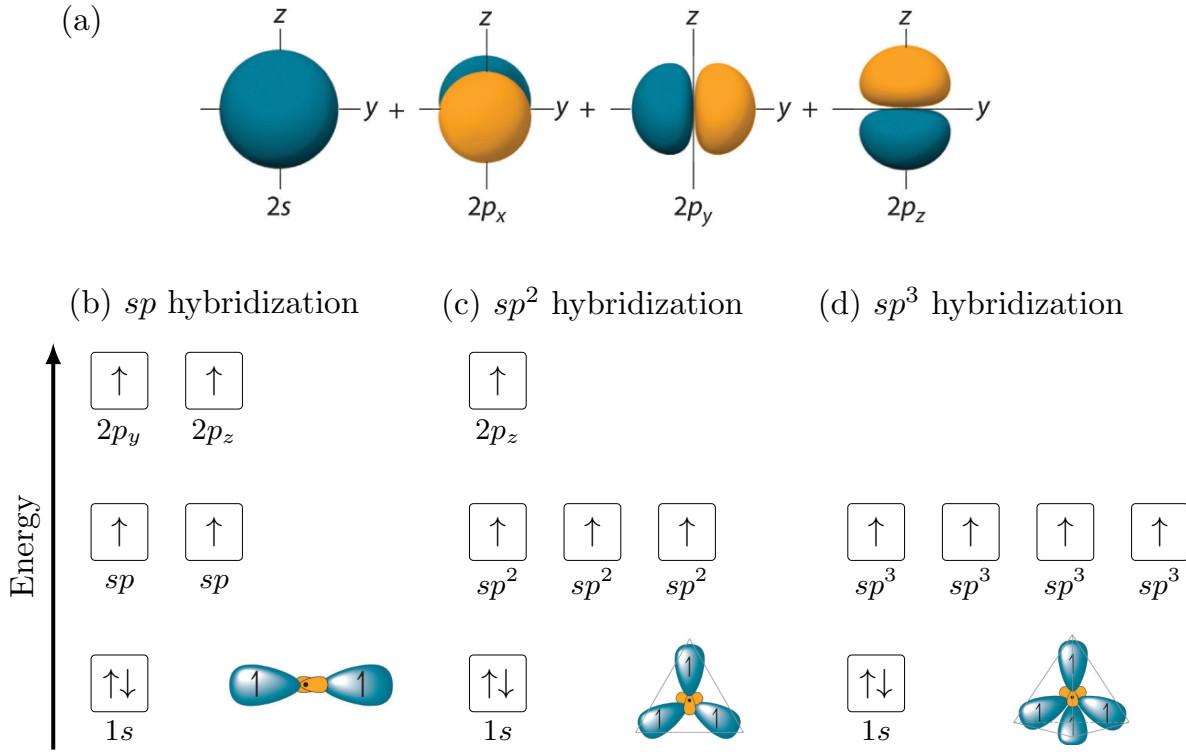


Figure 2.3: Possible covalent bond hybridization of s, p_x, p_y, p_z orbitals (a). (b) The sp hybridization leads to a planar molecular geometry (angle between atoms is 180°). An example of this molecular structure is acetylene (C_2H_2). (c) The sp^2 hybridization leads to a 120° planar structure (e.g., benzene C_6H_6). (d) The sp^3 hybridization that leads to a tetrahedral molecular structure (e.g., diamond). The angle between atoms in this geometry is of 109° .

energy cost of promoting an electron from the $|2s\rangle$ to the $|2p\rangle$ atomic level (roughly 4 eV) is compensated by the energy gain in subsequently forming chemical bonds. The superposition of $|2s\rangle$ with n $|2p\rangle$ orbitals denotes sp^n hybridization. As a representative case, in benzene-like structures (such as graphene), carbon atoms hybridize in a sp^2 configuration (Fig. 2.3b) to form bonds. The sp^2 hybridization leads to a strong planar bonding in the xy plane (localization of shell electrons) and delocalized electrons that jump between the p_z (atomic) orbitals (π -network).

In a solid, the full electronic Hamiltonian for N electrons is expressed as [123, 124]

$$H = \sum_{m=1}^N \left[-\frac{\hbar^2 \nabla_m^2}{2m_e} + V_{e-n}(\mathbf{r}_m) + \frac{1}{2} \sum_{m \neq m'} V(\mathbf{r}_m - \mathbf{r}_{m'}) \right], \quad (2.25)$$

where m_e and \hbar are the electron mass and the Planck constant, respectively, \mathbf{r}_m the position vector and $\nabla_m^2 = \left(\frac{\partial^2}{\partial x^2} + \frac{\partial^2}{\partial y^2} + \frac{\partial^2}{\partial z^2} \right)$ the Laplace operator for the m -th electron. Here it has been already taken into account the Born-Oppenheimer approximation, in which the nuclei behave as stationary particles, since their masses are much larger than the electron mass. This approximation allows one to decouple the nuclear and electronic Hamiltonians and deal only with the electronic part of the full Hamiltonian by considering the effective potential produced by the nuclei (ionic potential), $V_{e-n}(\mathbf{r}_m) = \sum_i V_{e-n}(\mathbf{r}_m - \mathbf{R}_i)$, which expresses the interaction between the m th-electron and all the nuclei located at \mathbf{R}_i . The term $V(\mathbf{r}_m - \mathbf{r}_{m'})$ corresponds to the electron-electron interaction.

The electronic Hamiltonian of Eq. (2.25) is exact provided we have a complete (and therefore infinite) basis, but practical calculations require the use of finite basis sets. For the particular case of carbon-based compounds, it is often sufficient to choose a basis of localized atomic orbitals of carbon's valence electrons $|\phi_i\rangle = \{|2s\rangle, |2p_x\rangle, |2p_y\rangle, |2p_z\rangle\}$ [125–127] (called single- ζ in chemical literature).

On the other hand, the difficulty of finding the solution to the many-body Hamiltonian Eq. (2.25) arises from the last term $V(\mathbf{r}_m - \mathbf{r}_{m'})$, since it makes the motion of particles correlated and couples the corresponding differential equations. Therefore, it is of great importance to develop approximate methods which provide a simplified form of the electron-electron interaction and reduces the number of equations needed to be solved. Among the most accurate methods we find the full configuration interaction (FCI) [123] in which all Slater determinants obtained by exciting all possible electrons to all possible virtual orbitals (unoccupied orbitals) in the electronic ground state configuration are considered in the variational problem. However this method is extremely computational demanding. In fact, because the number of determinants required in the FCI expansion grows in a factorial fashion with the number of electrons and orbitals, FCI is only possible for very small molecules. One first step can be to reduce the active space, as in the complete active space multiconfiguration [128]. Here a certain number of electrons are allowed to populate the active orbitals in appropriate combinations, developing a finite-size space of determinants. If the active space is extended to all MOs then the FCI treatment is recovered. However, this method is still largely resource and time consuming, so we need to go beyond and take more approximations.

A natural next step would be to treat the Hamiltonian within the Hartree–Fock method [123], which assumes that the exact N -body WF of the system can be approximated by a single Slater-determinant. Within this framework we find methods such as DFT and MFH models, where the N coupled equations are solved iteratively within a self-consistent field (SCF). These two methods are differentiated by the Hamiltonian

to be solved. A step beyond is to take the independent electrons approximation in which the electron-electron interactions are fully neglected, as, *e.g.*, in the TB picture or the nearly-free electrons approximation (NFE). These methods allow to deal with large scale simulations needed, for instance, to understand many of the systems studied in this thesis.

2.4 Tight-binding

The TB model [129–134]—also known as linear combination of atomic orbitals (LCAO) or the Hückel MO theory [135–137] in the context of molecular systems (especially π -delocalized molecules)—is an effective tool to describe the motion of electrons in a solid (crystal). In opposition to the NFE approximation, in this model the potential is so strong that the electron lives mostly bound to the ionic core with a small probability to jump to a nearby atom. In these terms, we start by replacing the Coulomb interaction among electrons themselves and between electron and nuclei by an effective one-electron potential $U(\mathbf{r})$

$$H_m = \overbrace{-\frac{\hbar^2 \nabla_m^2}{2m_e}}^{H_{at}} + U(\mathbf{r}_m) + \sum_{\mathbf{R}_j \neq 0} U(\mathbf{r}_m - \mathbf{R}_j) \equiv H_{at} + \Delta U, \quad (2.26)$$

where ΔU ($\Delta U \rightarrow 0$ at the center of each atom in the crystal) contains all the corrections to the atomic potential needed to produce the full potential landscape of the system and may be treated perturbatively. This TB matrix can be expressed in second quantization as

$$H_0 = \sum_i \epsilon_i c_i^\dagger c_i + \sum_{i \neq j} t_{ij} c_i^\dagger c_j, \quad (2.27)$$

where t_{ij} is the *hopping integral*, *i.e.*, overlap between neighboring orbitals i and j ,

$$t_{ij} = \int d\mathbf{r} \phi_i^*(\mathbf{r} - \mathbf{R}_i) \Delta U \phi_j(\mathbf{r} - \mathbf{R}_j), \quad (2.28)$$

and $\epsilon_i = t_{ii}$ is the on-site potential.

The wave WF can then be described as linear combinations of the atomic orbitals (solutions of the isolated atomic Hamiltonian, H_{at}) $\{|\phi_i\rangle\}$:

$$|\Psi_n\rangle = \sum_i b_{n,i} |\phi_i\rangle, \quad H_{at} |\phi_i\rangle = \epsilon_i |\phi_i\rangle, \quad (2.29)$$

where $b_{n,i} = \langle \phi_i | \Psi_n \rangle$ is the projection of state n into the atomic orbital localized at site i .

The most important feature of the TB approximation is that it is a single-particle Hamiltonian of non-interacting electrons and the resulting MOs are therefore not dependent on the occupation of other orbitals. The parameters of this Hamiltonian (t_{ij} and ϵ_i) are found empirically, typically by adjusting to other more accurate theoretical frames, or to match the experiment. Although this methodology might seem too simplistic, the power of this procedure relies on various advantages: (i) on one hand this model can be actually very descriptive, as the desired level of accuracy is determined by the number of parameters present in the Hamiltonian. For instance, one can choose an orthogonal or non-orthogonal basis to describe the atomic orbitals, where the latter includes the overlap between these WFs, which will provide a better description of the system, while the former is less costly to compute. (ii) On the other side, it allows for a deep understanding on the important physics as a first approximation, especially for π -conjugated systems [64, 125].

2.4.1 Bloch's theorem: periodic band structure

For periodic systems (crystals), the ionic potential follows $U(\mathbf{r}) = U(\mathbf{r} + \mathbf{R})$ for a lattice vector \mathbf{R} . The electron WF then must respect the discrete translation symmetry of the lattice (Bloch's theorem [138]), *i.e.*, the Bloch Hamiltonian must commute with the translation symmetry operator $T_{\mathbf{R}}$. In quantum mechanics this discrete symmetry operator is defined as $T_{\mathbf{R}} = \exp(-i\mathbf{k} \cdot \mathbf{R}) \rightarrow T_{\mathbf{R}}\psi(\mathbf{r}) = \psi(\mathbf{r} + \mathbf{R})$, where \mathbf{k} is the electron wave vector. This implies that the WF $\Psi_{n\mathbf{k}}$ with band index n can be expressed as a linear combination of Bloch waves $\Phi_{\mathbf{k}}(\mathbf{r})$,

$$\Psi_{n\mathbf{k}} = \sum_{j,o \in j} b_{n,o\mathbf{k}} \Phi_{o\mathbf{k}}(\mathbf{r}) = \sum_{j,o \in j} b_{n,o\mathbf{k}} \sum_{\mathbf{R}} e^{i\mathbf{k} \cdot \mathbf{R}} \phi_o(\mathbf{r} - \mathbf{R} - \mathbf{r}_j), \quad (2.30)$$

where the first summation goes over the existing N_o atomic orbitals $|\phi_o\rangle$ localized at each lattice (atomic) site \mathbf{r}_j . Therefore the total dimension of the Hamiltonian will be $N_b \times N_b$, where $N_b = N_a \times N_o$ (number of atoms in the cell times the number of orbitals per atom).

The graphene lattice is formed of two inequivalent interpenetrating triangular sublattices, here labeled A and B , forming the graphene unit cell [c.f. Fig. 2.4]. The honeycomb lattice is said to be bipartite since each site in the lattice is surrounded only by atoms

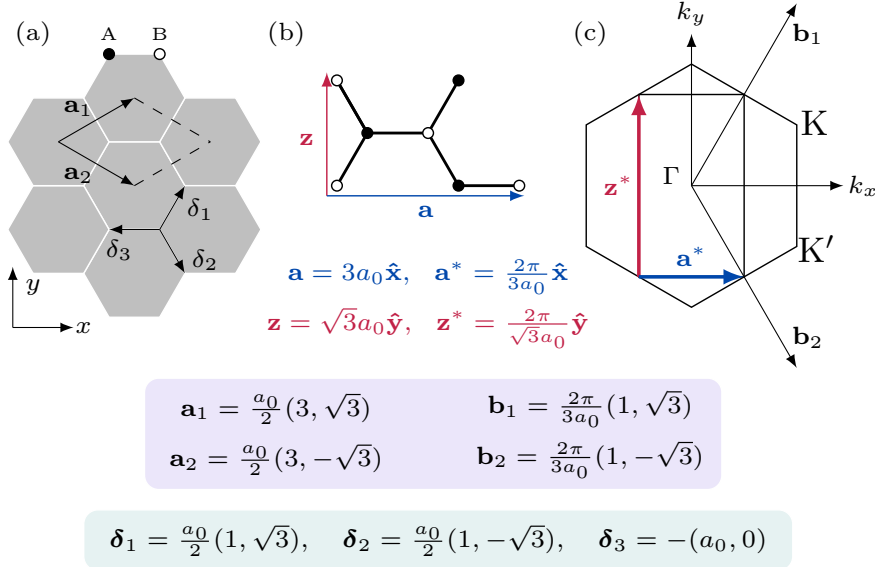


Figure 2.4: (a) Graphene atomic lattice. $\mathbf{a}_{1,2}$ are the lattice vectors and $\boldsymbol{\delta}_{1,2,3}$ the vectors defining the nearest neighbors relative positions. The filled (open) circle denotes the A (B) sublattice. (b) Definition of AGNR (vector \mathbf{a}) and ZGNR (vector \mathbf{z}) periodic directions. (c) Graphene 1BZ (hexagon) with $\mathbf{b}_{1,2}$ the reciprocal lattice vectors. The high-symmetry points of the BZ K, K' and Γ are indicated. The 1BZ of graphene is folded into the embedded rectangular 1BZ of GNRs, defined by the \mathbf{a}^* and \mathbf{z}^* directions. This rectangular BZ corresponds in the reciprocal space to the unit cell constructed using the \mathbf{a} and \mathbf{z} vectors in real space as illustrated in (b). Vectors inside the purple and green rectangles are defined following the (\mathbf{x}, \mathbf{y}) notation.

belonging to the other existing sublattice. The WF can be expressed then as

$$\Psi_{n\mathbf{k}}(\mathbf{r}) = \sum_{o \in A} b_{n,o\mathbf{k}} \sum_{\mathbf{R}} e^{i\mathbf{k}\mathbf{R}} \phi_o(\mathbf{r} - \mathbf{R} - \mathbf{r}_A) + \sum_{o \in B} b_{n,o\mathbf{k}} \sum_{\mathbf{R}} e^{i\mathbf{k}\mathbf{R}} \phi_o(\mathbf{r} - \mathbf{R} - \mathbf{r}_B). \quad (2.31)$$

The Bloch WF diagonalizes the Bloch Hamiltonian, *i.e.*, $\mathbf{H}_{\mathbf{k}}\Psi_{n\mathbf{k}} = \epsilon_{n\mathbf{k}}\Psi_{n\mathbf{k}}$ whose matrix elements $H_{ij,\mathbf{k}}$ are found by projecting Eq. (2.26) onto the Bloch waves $H_{ij,\mathbf{k}} = \langle \Phi_{i\mathbf{k}}(\mathbf{r} + \mathbf{R}) | H | \Phi_{j\mathbf{k}}(\mathbf{r}) \rangle$ (ij being orbital indices). Explicitly, the matrix element $H_{ij,\mathbf{k}}$ corresponding to an orbital ϕ_i situated at \mathbf{r}_A with an orbital ϕ_j situated at \mathbf{r}_B is calculated as following:

$$H_{ij,\mathbf{k}} = \sum_{\mathbf{R}} e^{i\mathbf{k}\mathbf{R}} \underbrace{\int \phi_i(\mathbf{r} - \mathbf{r}_A) H \phi_j(\mathbf{r} - \mathbf{R} - \mathbf{r}_B) d\mathbf{r}}_{t_{ij}(\mathbf{R})}. \quad (2.32)$$

The TB parameters t_{ij} [c.f. Eq. (2.27)] can be computed from the Slater-Koster (SK) bond integrals for graphene $V_{pp\pi}, V_{pp\sigma}, V_{ss\sigma}, V_{sp\sigma}$ [139].

Note that the choice of the coefficients $b_{n\mathbf{k}}$ is not unique, but they are fixed up to an overall $U(1)$ phase (gauge symmetry) [140]. Thus, there exists a freedom of choosing the phases of coefficients connected by nontrivial diagonal unitary transformations that leads to two forms of the Hamiltonian. In this thesis the used gauge for the k -point is called the *lattice gauge*, however, another possible gauge is to use the site distance between atoms in the unit cell, *i.e.*, $\mathbf{d}_{ij} = (\mathbf{r}_i - \mathbf{r}_j)$, also called the *atomic gauge*, where $\mathbf{r}_{i,j}$ are the positions of the atomic sites *in the unit cell*. In this second choice one simply would have to use the phase factor $\exp i\mathbf{k}(\mathbf{R} + \mathbf{r}_j)$ in Eq. (2.30) instead of $\exp(i\mathbf{k}\mathbf{R})$. The gauge transformation that connects these two possible choices then is performed by multiplying the above defined Hamiltonian matrix elements $H_{ij\mathbf{k}}$ with the following phase factor $\tilde{H}_{ij,\mathbf{k}} \rightarrow H_{ij,\mathbf{k}} \exp(i\mathbf{G} \cdot \mathbf{d}_{ij})$, with \mathbf{G} the reciprocal lattice vector. See for instance the implementation in SISL [93]. The chosen gauge can be of importance when considering topological characterizations, although the physics should be invariant under these choices, the two gauges define two different Berry curvatures [140]. The same happens for 1D systems when calculating the Zak phase [141]. The gauge arbitrariness, however, is present only for systems with more than one atom per unit cell.

In this section we will first revise the electronic structure for periodic 2D graphene from which we will later derive the electronic properties of 1D graphene nanoribbons. In the basis of atomic orbitals, the intracell ($\mathbf{R} = 0$) graphene TB Hamiltonian H_{ij} reads

$$\begin{array}{cccccccc}
 & p_z^A & p_z^B & s^A & s^B & p_x^A & p_x^B & p_y^A & p_y^B \\
 p_z^A & \epsilon_{p_z} & t & & & & & & \\
 p_z^B & t^* & \epsilon_{p_z} & & & & & & \\
 s^A & & & \epsilon_s & t_{ss} & 0 & t_{sp_x} & 0 & t_{sp_y} \\
 s^B & & & t_{ss}^* & \epsilon_s & t_{sp_x} & 0 & t_{sp_y} & 0 \\
 p_x^A & & & 0 & t_{sp_x}^* & \epsilon_{p_x} & t_{p_x p_x} & 0 & 0 \\
 p_x^B & & & t_{sp_x}^* & 0 & t_{p_x p_x}^* & \epsilon_{p_x} & 0 & 0 \\
 p_y^A & & & 0 & t_{sp_y}^* & 0 & 0 & \epsilon_{p_y} & t_{p_y p_y} \\
 p_y^B & & & t_{sp_y}^* & 0 & 0 & 0 & t_{p_y p_y}^* & \epsilon_{p_y}
 \end{array} \tag{2.33}$$

where $t = V_{pp\pi}$ is the hopping element between p_z orbitals located at A and B sites.

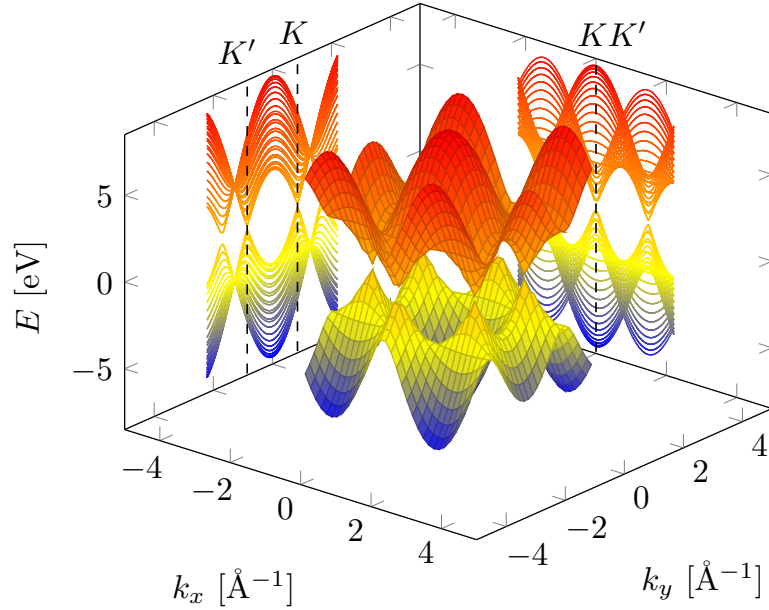


Figure 2.5: Calculated bandstructure for the 1NN TB Hamiltonian. The projected bands at the xz and yz planes correspond to the projection of the graphene BZ onto the periodic directions along the AGNR (vector \mathbf{a} in Fig. 2.4) and ZGNR (vector \mathbf{z} in Fig. 2.4) directions.

The letters in gray on the left and top sides of the matrix indicate the atomic orbital to which the Hamiltonian matrix element correspond to. Note that the basis here is defined such as the p_x , p_y and p_z orbitals are aligned with the x , y and z axes. For practical purposes, in the following development of this section we will only consider one orbital per atom, $|\phi_o\rangle = \{|2p_z\rangle\}$ (*i.e.*, the first 2×2 block of matrix of Eq. (2.33) shown in light blue) since the low-energy electronic properties of nanographenes, to a large extent, are governed by the π -electrons of the unhybridized $|2p_z\rangle$ orbitals, whereas the σ -electrons of the sp^2 orbitals form molecular states that lie far in energy with respect to the Fermi energy [61, 64, 85, 142] as demonstrated experimentally [143]. Nevertheless, there are some important situations in which the remaining atomic orbitals are necessary to be taken into account explicitly, for instance, to describe cases in which the π and σ bands are *not* decoupled, *e.g.*, if spin-orbit coupling (SOC) is considered [144–146] or in the case of curved graphene-like lattices [144, 147, 148].

The dispersion relation for the simplest graphene TB Hamiltonian with first-nearest

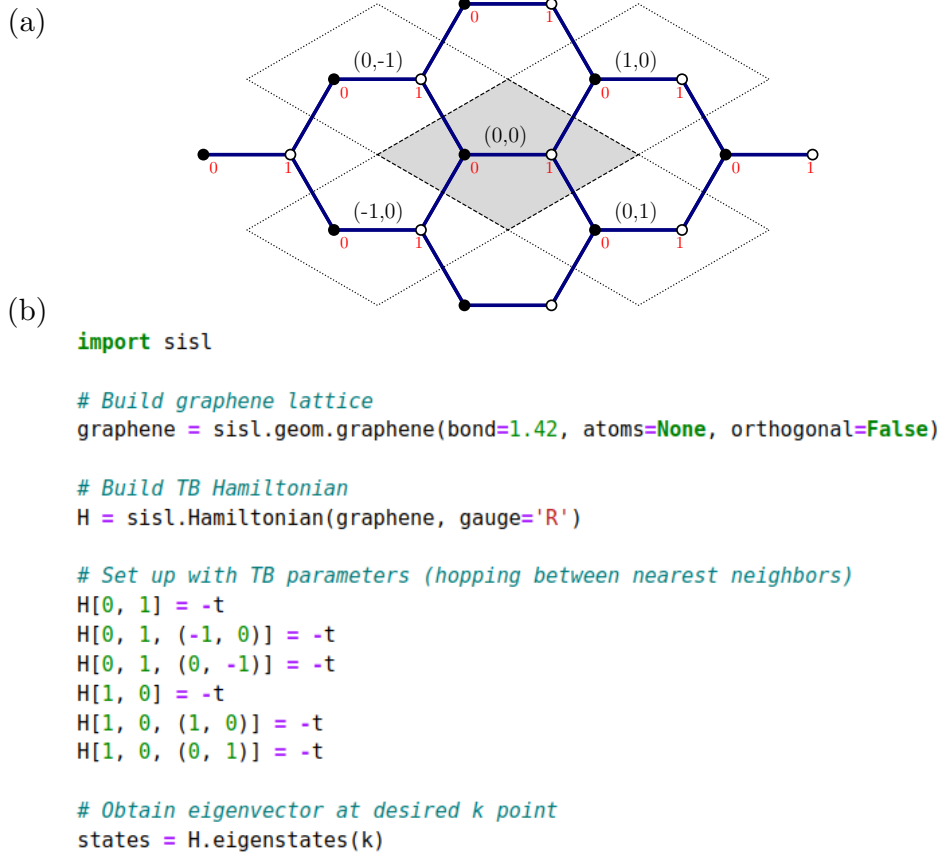


Figure 2.6: (a) The unit cell connected via de lattice vectors ($\mathbf{a}_1, \mathbf{a}_2$). The numbers inside the parenthesis indicate the corresponding position of the adjacent cells with respect to the $(0,0)$ unit cell. The two atoms inside the graphene unit cell are numbered by red numbers 0 and 1, which correspond respectively to the sublattices A and B. (b) The piece of code below exemplifies how the graphene TB Hamiltonian is built using SISL considering only 1NN connections with t .

neighbors (1NN) hopping, can be written

$$E_{\pm}(\mathbf{k}) = \pm t \sqrt{3 + f(\mathbf{k})},$$

$$f(\mathbf{k}) = 2 \cos\left(\sqrt{3}k_y a\right) + \cos\left(\frac{\sqrt{3}}{2}k_y a\right) \cos\left(\frac{3}{2}k_x a\right). \quad (2.34)$$

Typically $|t| \approx 2.7$ eV for graphene [64, 142, 149]. Other more descriptive parametrizations include also hopping parameters between next nearest neighbors, which improve

the comparison between the TB calculated electronic bands and the ones obtained with DFT [64, 142, 149]. For instance, if we include also interactions between second nearest-neighbors (2NN) through the hopping parameter t' , the dispersion relation from above is $E_{\pm}(\mathbf{k}) = \pm t\sqrt{3 + f(\mathbf{k})} - t'f(\mathbf{k})$. We observe that one of the main effects introduced by the 2NN parameter t' is the particle-hole symmetry breaking between the valence (VB) and conduction (CB) bands. In the case of graphene nanostructures other more accurate parametrizations may also include the edge effect consequence of quantum confinement, *e.g.*, as in the case of graphene nanoribbons [22, 142] that has been observed experimentally [150, 151].

Analogously, the existence of two sublattices in real space lead to two nonequivalent “valleys” at the hexagon vertices of the Brillouin zone (BZ), with positions in the reciprocal space

$$K = \left(\frac{2\pi}{3a_0}, \frac{2\pi}{3\sqrt{3}a_0} \right), \quad K' = \left(\frac{2\pi}{3a_0}, -\frac{2\pi}{3\sqrt{3}a_0} \right), \quad (2.35)$$

at which $E(\mathbf{k} = K) = E(\mathbf{k} = K') = 0$, as shown in Fig. 2.5. Close to these k -points electrons behave as Dirac fermions since the reciprocal lattice hold linear dispersion relation. This can be understood by expanding the TB Hamiltonian of graphene around the K point, using the relative momentum $\mathbf{q} \equiv \mathbf{k} - K$. In the vicinity of this symmetry point, the dispersion relation becomes Dirac-like (linear) $E_{\pm}(\mathbf{q}) \approx \pm v_F \mathbf{q} + O[(q/K)^2]$ [6, 7, 125, 152], where the electron Fermi velocity can reach values of $v_F \sim 10^6$ m/s.

Computationally, the electronic structure of TB Hamiltonians can be obtained using the open-source code SISL [93], as exemplified in Fig. 2.6.

GNRs are found by applying hard-wall boundary conditions on both edges of the confined direction, and periodic boundary conditions along the non-confined direction [64, 153, 154]. As a consequence, the energy projections are discretized, giving rise to a set of subbands along the confined direction of the \mathbf{k} -vector, *i.e.*, the quantized $k_{n,\perp}$, where n is the band index. The number of existing subbands will depend on the width of the GNR, W (quantum box size).

First of all, let us express the two terms in Eq. (2.31) as $\Psi_{n\mathbf{k}} = \psi_{n\mathbf{k}}^A + \psi_{n\mathbf{k}}^B$. For the armchair shaped GNR the edges are conformed by both A- and B-type atoms, thus the WF of Eq. (2.31) will have to satisfy $\psi_{n\mathbf{k}}^A(y = 0) = \psi_{n\mathbf{k}}^B(y = 0) = \psi_{n\mathbf{k}}^A(y = W) = \psi_{n\mathbf{k}}^B(y = W) = 0$. While in the zigzag shaped GNR, as each edge of the ribbon has either A- or B-type atoms exclusively, the WF must satisfy $\psi_{n\mathbf{k}}^A(x = 0) = 0$ and $\psi_{n\mathbf{k}}^B(x = W) = 0$ separately. The reciprocal lattice of graphene nanostructures can be seen as the projection of the 2D graphene dispersion surface along the appropriate direction as plotted in Fig. 2.4 and explicitly calculated in Fig. 2.5. With this picture it

becomes clear that the existence of edge states in ZGNRs are actually a consequence of the quantum confinement and the boundary conditions, as these appear by solving the following transcendental equation [153, 154],

$$k_y = \frac{k_n}{\tan(k_n W)}. \quad (2.36)$$

Interestingly, for values of k_y larger than a certain critical value k_y^c , Eq. (2.36) does not support nodeless solutions, indicating the existence of surface states in this region of the reciprocal space. On the other hand, in the case for AGNRs, the allowed k_n are found by the following expression

$$k_n = \frac{n\pi}{W} - \frac{4\pi}{3a_0}, \quad (2.37)$$

which leads to the existence of three families with different electronic characteristics, given by confinement conditions, depending on the number of carbon atoms along the confined direction that defines the width of the AGNR, $N_a = \{3p, 3p + 1, 3p + 2\}$ with $p \in \mathbb{Z}$ [22, 60, 64]. At the 1NN theory level the $(3p + 2)$ -AGNRs are metallic at the Fermi level. However, at a more sophisticated theory level (such as, *e.g.*, DFT and third-nearest neighbor (3NN) TB model), even the $(3p + 2)$ -AGNRs develop a small band gap, whose origin relies on a geometrical edge effect where the carbon bonds are not equivalent under the conditions at the edges (no upper carbon to bind) than inside the GNR (where it preserves the original graphene nature) [22, 142, 155]. This causes the bonds at the edges (saturated by hydrogen atoms) to be slightly stronger than those inside the GNR. In the case of ZGNRs the band gap opening comes from magnetic instabilities of the localized states at the edges [59, 85, 142].

More generally, for chiral GNRs (chGNRs) of arbitrary edge-terminations [156–161], where the growth (chiral) direction is defined as $\mathbf{C}_h = l\mathbf{a}_1 + m\mathbf{a}_2$, with l, m two integer numbers, the WF will have to satisfy the particular implied boundary conditions, and the 1BZ will be found by projecting the hexagonal graphene BZ along a periodic direction of certain inclination (defined by the chiral angle θ_{ch}).

2.5 Magnetism in graphene: the mean-field Hubbard Hamiltonian

In the previous sections we have ignored both the spin degree of freedom and electron-electron Coulomb repulsion interactions. One of the simplest models to include electron

interactions in the description is the Hubbard Hamiltonian [162, 163],

$$H = H_0 + \overbrace{\sum_i U_i n_{i\uparrow} n_{i\downarrow}}^{H_U}. \quad (2.38)$$

where $n_{i\sigma} = c_{i\sigma}^\dagger c_{i\sigma}$ is the number operator at site i for spin index σ and H_0 corresponds to the TB Hamiltonian of Eq. (2.27). The Coulomb parameter (U_i), which accounts for the repulsion between two electrons occupying site i , is typically found empirically by fitting to *ab-initio* calculations or extracted from experimental data, in a similar way as the TB parameters.

This Hamiltonian can be seen as an extension of the TB Hamiltonian, where a short-range interaction term is added. In contrast to the non-interacting TB model, the added term (H_U) captures the physics well enough to offer an insight into how the interactions between electrons give rise to insulating, magnetic, and even novel superconducting effects in a solid [162–165].

Despite its apparent simplicity, however, the Hubbard Hamiltonian cannot be solved for most of the cases, since the dimension of the Hilbert space scales as $\sum_{N=0}^{2L} \binom{2L}{N} = 4^L$, where N represents the number of electrons that can be distributed in $2L$ number of sites [166]. Hence, one way to approach the solution is by approximating the two-particle operator $n_{i\uparrow} n_{i\downarrow}$ by the motion of single electrons in the average SCF generated by all the other electrons in the system,

$$\begin{aligned} n_{i\uparrow} n_{i\downarrow} &= (\delta_{i\uparrow} + \langle n_{i\uparrow} \rangle) (\delta_{i\downarrow} + \langle n_{i\downarrow} \rangle) = \\ &= \delta_{i\uparrow} \delta_{i\downarrow} + \langle n_{i\uparrow} \rangle \delta_{i\downarrow} + \delta_{i\uparrow} \langle n_{i\downarrow} \rangle + \langle n_{i\uparrow} \rangle \langle n_{i\downarrow} \rangle \approx \\ &\approx \langle n_{i\uparrow} \rangle n_{i\downarrow} + \langle n_{i\downarrow} \rangle n_{i\uparrow} - \langle n_{i\uparrow} \rangle \langle n_{i\downarrow} \rangle \Rightarrow \\ \Rightarrow H_U &\approx \sum_{i\sigma} U_i \langle n_{i\sigma} \rangle n_{i\bar{\sigma}} + E_U. \end{aligned} \quad (2.39)$$

In this approximation it is assumed that the electronic density operator is very close to its expected value, that is $n_{i\sigma} \approx \langle n_{i\sigma} \rangle$. This means that the density fluctuations (defined as $\delta_{i\sigma} = n_{i\sigma} - \langle n_{i\sigma} \rangle$) can be considered small compared to its mean value $\langle n_{i\sigma} \rangle$. With this in mind we can neglect the quadratic terms $\delta_{i\uparrow} \delta_{i\downarrow} \approx 0$. The constant term that comes out from the mean-field approximation reads

$$E_U = - \sum_i U_i \langle n_{i\uparrow} \rangle \langle n_{i\downarrow} \rangle. \quad (2.40)$$

It can be readily seen that the mean-field approximation reduces the Hubbard Hamil-

tonian to a one-particle problem of two matrices of $N \times N$ with $2N$ mean-field parameters (N local densities $\langle n_{i\uparrow} \rangle$ and N local densities $\langle n_{i\downarrow} \rangle$), which is an enormous advantage. In fact this method allows to deal with very large systems of thousands of atoms, where the Hamiltonian can be solved iteratively until the SCF solution for a given magnetic configuration is achieved. Note also that the WF in this semi-empirical model is just a simple direct product of two single-particle WFs (one for the spin-up electrons and another for the spin-down electrons), *i.e.*, $|\Psi\rangle = |\psi_{\uparrow}\rangle \otimes |\psi_{\downarrow}\rangle$, constituting a single Slater determinant. This is the basic idea of the Hartree-Fock (HF) approximation, where the main difference with the Hartree-Fock Hamiltonian is that the exchange interaction is not taken into account in the Hubbard Hamiltonian.

It is worth mentioning that the expression Eq. (2.38) can be generalized to the *extended Hubbard model* which also includes Coulomb repulsion interactions between particles that are occupying different sites $i \neq j$ as we actually have implemented in our HUBBARD library [90], although in the most typical scenario $U_{i \neq j} = 0$. In graphene, for instance, the presence of the non-local interactions can give rise to a rich phase diagram [167].

The MFH can give good results especially in the case of weakly interacting systems. It is a powerful method to study large system sizes, compute real-space quantities and consider systems with complex geometries. In fact, this model has proven to be particularly suitable especially for π -electron carbon structures [31, 33, 142, 158, 168], as compared to other more sophisticated theoretical models such as Monte Carlo simulations [169], and DFT [36, 38, 95] and experimental results [36, 38, 95, 161, 170] (more insight on this will be shown in Chap. 3). However, we should keep in mind, that the mean-field approximation overestimates the magnetic order [171].

Spin-degenerate calculations

To calculate the closed-shell (CS) solutions when considering Coulomb repulsion, we can use the MFH model for the spin-degenerate case. This is, the spin densities are equal for both spin components, *i.e.*, with the constriction $\langle n_{i\uparrow} \rangle = \langle n_{i\downarrow} \rangle = \frac{1}{2}\langle n_i \rangle$. In this case, instead of dealing with two Hamiltonians and two spin densities we use one single Hamiltonian. We force in this sense equal occupations of the eigenstates for the two spin components (*i.e.*, CS solution). Eq. (2.38) becomes then

$$H_{\text{CS}} = \sum_i U_i \langle n_i \rangle + E_U, \quad (2.41)$$

with the constant term in this case

$$E_U = -\frac{1}{4} \sum_i U_i \langle n_i \rangle^2. \quad (2.42)$$

Note that in Eq. (2.39) there is a summation over spin indices (which implies a factor 2 when the electron densities are equal for both spin channels).

2.5.1 Measure of error: Spin contamination

The unrestricted form of the MFH Hamiltonian allows the spatial parts of the eigenstates associated to different spin indices to differ. The consequence is that the eigenstates of the Hamiltonian no longer diagonalize the spin-squared operator, \hat{S}^2 , and the WF is usually contaminated to some extent by higher-order spin eigenstates. To compute the expectation value of \hat{S}^2 in the MFH context we can use the following expression [172],

$$\langle \hat{S}^2 \rangle_{\text{MFH}} = \langle S^2 \rangle_{\text{exact}} + N_\beta - \sum_{nn'}^{\text{occ}} |\langle \psi_n^\alpha | \psi_{n'}^\beta \rangle|^2, \quad (2.43)$$

where the exact spin-squared expectation value is obtained as

$$\langle \hat{S}^2 \rangle_{\text{exact}} = \left(\frac{N_\alpha - N_\beta}{2} \right) \left(\frac{N_\alpha - N_\beta}{2} + 1 \right). \quad (2.44)$$

In this context α refers to the spin index $\sigma = \{\uparrow, \downarrow\}$ that corresponds to $N_\alpha \geq N_\beta$. By computing the difference between $\langle \hat{S}^2 \rangle_{\text{MFH}} - \langle \hat{S}^2 \rangle_{\text{exact}}$ one is able to obtain the spin contamination.

With this (available in the HUBBARD module) we were able to calculate this error for the molecules that we studied in this thesis. For example, calculated expectation value for the SCF ground state for the GNR junction (paper I) is $\langle \hat{S}^2 \rangle_{\text{MFH}} = 0.963$ for $U = 3.5$ eV. This means that the MFH state is a mixture of $S = 1$ (for which $\langle \hat{S}^2 \rangle_{\text{exact}} = S(S + 1) = 2$) and $S = 0$ ($\langle \hat{S}^2 \rangle_{\text{exact}} = 0$). In the case of the triangulene-like molecule of paper I, the calculated expectation value for the SCF ground state (which is the one with ferromagnetic alignment) is $\langle \hat{S}^2 \rangle_{\text{MFH}} = 2.0429$ with $U = 3$ eV, leading to a spin contamination of 0.0429.

2.5.2 Calculation of spin densities and total energy

As mentioned above, depending on the system and the boundary conditions, *e.g.*, if the system is isolated, periodic or an open quantum system, both the spin densities $\langle n_{i\sigma} \rangle$

and the total electronic energy E_{tot} will be computed differently. In this section the expressions are explicitly defined for these three cases.

Periodic Boundary Conditions (PBC) and isolated systems

The occupations $\langle n_{i\sigma} \rangle$ are found as the charge with spin σ associated with site i of the lattice explicitly. For periodic systems they are computed by diagonalizing the Bloch Hamiltonian in the reciprocal space [c.f. Sec. 2.4.1]. For generality, we consider here the generalized Bloch Hamiltonian $\Psi_{n\mathbf{k}}\mathbf{H}_{\mathbf{k}} = \varepsilon_{n\mathbf{k}}\mathbf{S}_{\mathbf{k}}\Psi_{\mathbf{k}}$ with the overlap between Bloch waves $S_{ij\mathbf{k}} = \langle \Phi_{i\mathbf{k}} | \Phi_{j\mathbf{k}} \rangle$. Typically we use an orthogonal basis LCAO set, *i.e.*, $S_{ij\mathbf{k}} = \delta_{ij}$. Once the Hamiltonian has been diagonalized per \mathbf{k} -point, the spin densities can be computed as:

$$\langle n_{i\sigma} \rangle = \sum_{\mathbf{k}} \omega_{\mathbf{k}} \sum_n f_{n\mathbf{k}\sigma} \sum_j b_{n,i\mathbf{k}}^{\sigma} b_{n,j\mathbf{k}}^{\sigma*} S_{ij\mathbf{k}}, \quad (2.45)$$

where $f_{n\mathbf{k}\sigma}$ is the occupation number obtained from the Fermi-Dirac distribution function for electrons in band n at each \mathbf{k} point for spin σ and $\omega_{\mathbf{k}}$ the weight to perform the discretized integration along the band. $b_{n,i\mathbf{k}\sigma}$ are the coefficients of the Bloch WFs [cf. Eq. (2.30)]. A similar derivation is found for instance in Ref. [173], to obtain the orbital charge (Mulliken populations [174]) in the DFT context.

As a practical note, when the orbitals vary smoothly with \mathbf{k} , one can sample the BZ using a finite number of points. Generally, we choose a rectangular grid of dimensions $M_x \times M_y \times M_z$ in fractional coordinates, spaced evenly throughout the BZ (Monkhorst-Pack grid) [175].

The total electronic energy, on its side can be calculated as

$$E_{\text{tot}} = \sum_{\mathbf{k}} \omega_{\mathbf{k}} \sum_{n\sigma} f_{n\mathbf{k}\sigma} \varepsilon_{n\mathbf{k}\sigma} + E_U, \quad (2.46)$$

where now the summation goes over the occupied bands and the interaction term E_U is calculated as in Eq. (2.40).

For an isolated structure, *e.g.*, a molecule in the gas phase (in absence of a substrate) there simply is no variation with \mathbf{k} (and therefore $\omega_{\mathbf{k}} = 1$), and $f_{n\sigma}$ are either zero or one (per spin).

Open Boundary Conditions (OBC)

For infinite but non-periodic systems the calculation is slightly more complicated since Bloch's theorem is no longer applicable to these systems and the diagonalization of an infinite matrix is undoable. To properly account for the effect of the semi-infinite

leads in the device Hamiltonian, the spin densities in equilibrium are computed by an integration of the Green's function [c.f. Sec. 2.1]. Numerically, the self-energy matrices of the electrodes are computed by means of the López-Sancho–López-Sancho recursive method [102, 103] as implemented in SISL [93, 94].

The equilibrium density matrix can be calculated by an integration of the spectral function

$$\langle n_{i\sigma} \rangle = \frac{1}{\pi} \text{Im} \left[\int_{-\infty}^{\infty} d\varepsilon \mathbf{A}_{\sigma}(\varepsilon) n_F(\varepsilon - \mu) \right]_{ii}, \quad (2.47)$$

where \mathbf{A}_{σ} is the spectral DOS for $\sigma = \uparrow, \downarrow$ as defined in Eq. (2.24).

By the residue theorem the integral of Eq. (2.47) can be performed in the complex plane, since all the poles of the retarded Green's function lie on the real axis, while the function is analytic elsewhere. The additional term arising from the residues of the poles of the Fermi function are included within the contour. Numerically, the integral is performed by Gaussian quadrature, where n_F is used as the weight function [176]. The used energy contour has the shape plotted in Fig. 2.7 for a given finite temperature, as extracted from TRANSIESTA [92, 94]. The black dots represent the points at which the Green's function is evaluated to compute the integral.

On the other hand, for equilibrium calculations, the electronic part of the total energy can be calculated as

$$E_{\text{tot}} = \sum_{\sigma=\uparrow,\downarrow} \frac{1}{2\pi} \int \text{Tr} [\mathbf{A}_{\sigma}(\varepsilon)] n_F(\varepsilon - \mu) \varepsilon d\varepsilon + E_U. \quad (2.48)$$

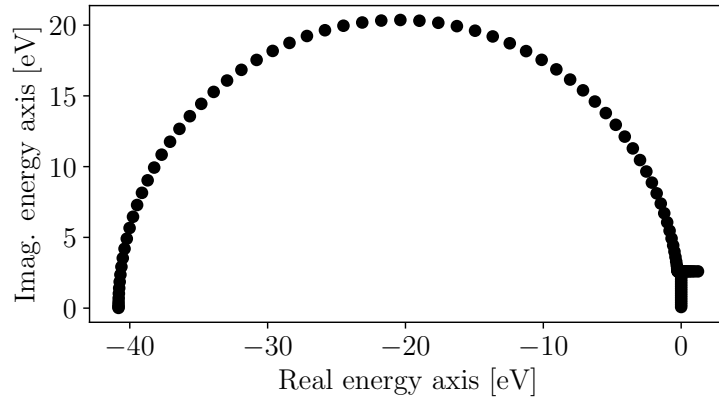


Figure 2.7: Example of the energy contour in the complex plane for the integration of the retarded Green's function in equilibrium extracted from TRANSIESTA [92, 94] at room temperature ($k_B T = 0.025$ eV with k_B the Boltzmann constant).

2.5.3 The hubbard package

In this section the structure of our numerical implementation of the MFH model is detailed. This development is collected in an open-source PYTHON package called `HUBBARD` [90]. Our implementation relies on `SISL` [93, 94], an open source PYTHON code that we use to build the geometry and the TB Hamiltonian of the systems of interest. The idea of this tool is to provide a library of functionalities that allows to perform a SCF calculation onto a TB Hamiltonian with a fixed U_i for the interaction part (chosen by the user). As explained in Sec. 2.5, the MFH Hamiltonian is solved iteratively until the convergence criterion is achieved. The main iterative procedure of the SCF goes as follows:

1. Set up the TB Hamiltonian and initialize the spin-densities
2. Obtain new spin densities $\langle n_\sigma \rangle$ and total electronic energy E_{tot}
3. Pass convergence criterion by evaluating $\max(\langle n_{i\sigma}^j \rangle - \langle n_{i\sigma}^{j-1} \rangle) < \text{tol}$ (for the j -th iteration)?
4. If not, update the Hamiltonian with new spin-densities and go to step 2 again until step 3 is achieved

While steps 1, 3 and 4 are common steps of the iterative cycle for all systems, item 2. will need different implementations depending on the system and the boundary conditions, as explained in Sec. 2.5.2. In a more pictorial way, this is shown in Fig. 2.8 where item 2. is substituted with methods A, B and C as corresponding to Sec. 2.5.2.

It is important to remark that a SCF solution is not necessarily the ground state. The ground state will be the SCF solution that minimizes the energy of the system. Given the possible existing energy barriers, the choice of the initial conditions can be determinant in the SCF and push one particular solution. Apart from the different spin spatial distribution that may change with the initial conditions one can also obtain different magnetic solutions in which there may be an imbalance between the spin components, *i.e.*, $N_\uparrow \neq N_\downarrow$ (different S_z eigenstates).

As a side note, a usual problem of convergence is the oscillation between two states, $\langle n_{i\sigma} \rangle_n \rightarrow \langle n_{i\sigma} \rangle_{n+1}$ and $\langle n_{i\sigma} \rangle_{n+1} \rightarrow \langle n_{i\sigma} \rangle_n$. One way to help the code avoid this issue is to introduce a form of damping by mixing the solution of iteration n with the solution of the previous iterations $\{\dots, n-2, n-1\}$. In our case, the mixing scheme can be linear or Pulay (DIIS) mixing [177, 178], as implemented in `SISL`.

Fig. 2.9 and Fig. 2.10 are pseudo-code representations of how to use the `HUBBARD` package. The former aims to exemplify how to find the SCF solution for a periodic

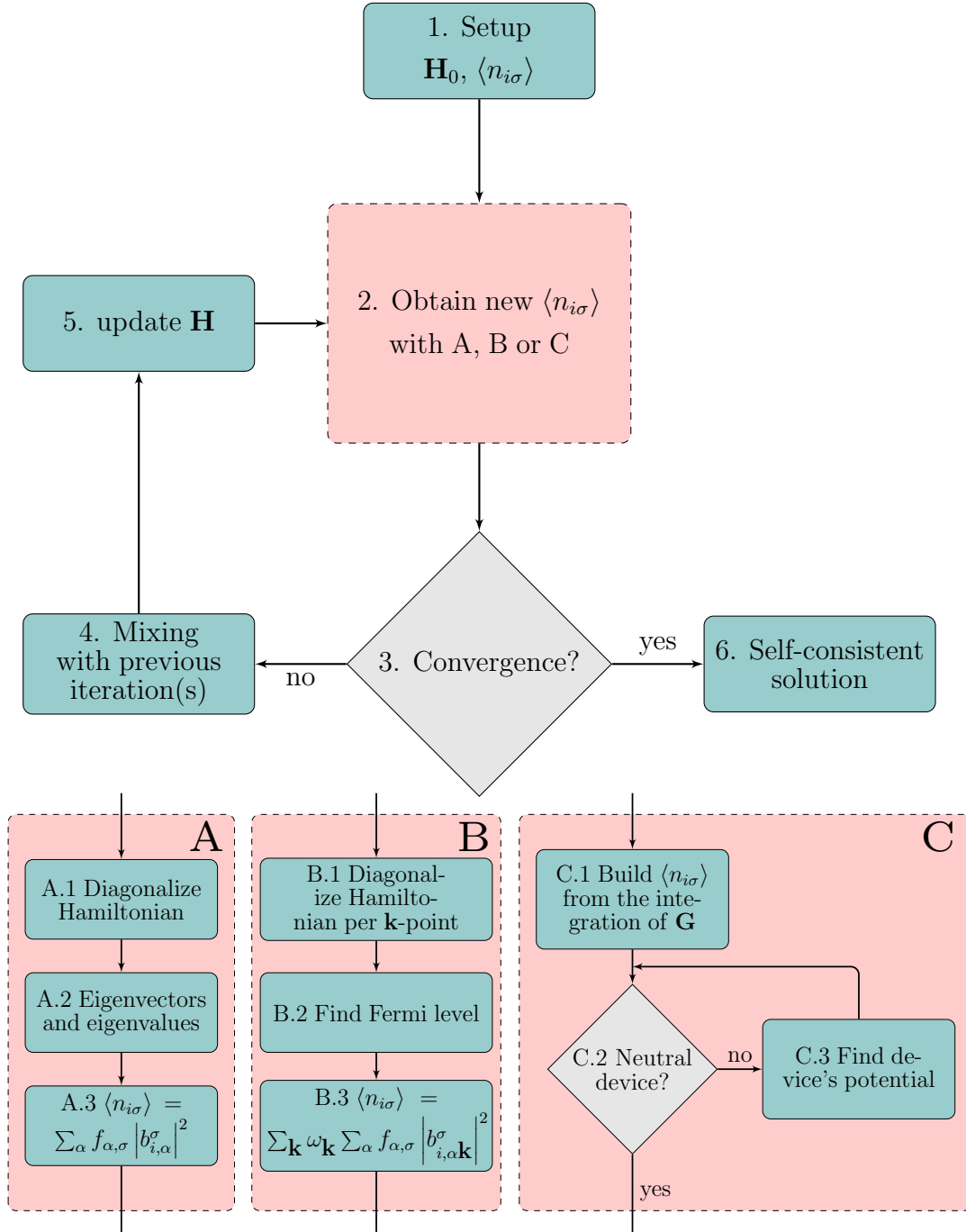


Figure 2.8: Algorithm of the SCF to solve the MFH Hamiltonian depending on the different systems and boundary conditions, namely (A) isolated systems, (B) periodic structures and (C) open quantum systems.

system, while the latter is for an open quantum system. More detailed code examples can be found in the [online documentation](#).

As it can be seen from the examples shown here, to build the `HubbardHamiltonian` object one only has to pass the TB Hamiltonian of the geometry, the desired U (which can be an array parametrizing different Coulomb repulsion terms at each site) and the system temperature kT (with k the Boltzmann constant). In the particular case of periodic systems one should also pass the number of \mathbf{k} -points in which the BZ is going to be sampled along each direction, `nkpt=[nkx,nky,nkz]`. The larger `nkx,nky,nkz` are, the finer the discretization of the BZ but the slower the iteration process will be.

After building the `HubbardHamiltonian` object, the user should initialize the calculation with an initial spin-polarization. One way to do this is by using the implemented function `set_polarization(sites_up, sites_dn)` which maximizes the spin \uparrow (\downarrow) occupations at `sites_up` (`sites_dn`). Then the convergence process can start by using the method `converge`, to which the specific callable to calculate the spin densities has to be passed, up to a desired tolerance (`tol`).

On the other hand, whether the calculation corresponds to a spin-polarized one or to an unpolarized Hamiltonian, is determined by creating the corresponding `sisl.Hamiltonian`. Then the `HubbardHamiltonian` class internally determines

```
import sisl
from hubbard import HubbardHamiltonian, sp2, density, plot

# Build tight-binding sisl Hamiltonian enabling the polarized option
H0 = sisl.Hamiltonian(geometry, spin='polarized')

# Build the HubbardHamiltonian with onsite Coulomb repulsion U,
# at temperature kT
# pass the number of k-points to sample HH along each direction
HH = HubbardHamiltonian(H0, U=U, kT=kT, nkpt=[nkx, nky, nkz])

# Initialize spin densities e.g. by placing up electrons
# at sites up_sites and down electrons on sites dn_sites
HH.set_polarization(up_sites, dn_sites)

# Converge up to a certain tolerance
# using density.calc_n method to obtain spin densities
HH.converge(density.calc_n, tol=1e-6, print_info=True)

# Plot interesting physical quantities, e.g.:
p = plot.SpinPolarization(HH)
```

Figure 2.9: Pseudo-code representing how to use the HUBBARD package to converge a system with PBC.

```

import sisl
from hubbard import HubbardHamiltonian, sp2, density, NEGF

# Build tight-binding sisl Hamiltonian enabling the polarized option
# for the device
H0 = sisl.Hamiltonian(geometry, spin='polarized')

# Build the HubbardHamiltonian of the scattering region
# same kT and U as the electrodes!
MFH_HC = HubbardHamiltonian(H0, U=U, kT=kT)

# Start initial spin-densities
MFH_HC.set_polarization(up_sites, dn_sites)

# Map electrodes in the device region,
# i.e. extract the atomic indices that correspond
# to the electrodes inside the device
elec_indx = [sites_elec1, sites_elec2]

# First we create the NEGF object
# where we pass the converged MFH electrodes (MFH_elec1, ...)
# along with their semi infinite directions (SI_dir1, ...) and
# the device (scattering region) HubbardHamiltonian object
negf = NEGF(MFH_HC, [(MFH_elec1, SI_dir1), (MFH_elec2, SI_dir2)], elec_indx)

# Converge up to a certain tolerance
# using dnegf.calc_n_open method to obtain the spin densities
dn = HH.converge(negf.calc_n_open, tol=1e-6, print_info=True)

```

Figure 2.10: Pseudo-code representing how to use the HUBBARD package to converge a system with OBC.

which type of calculation corresponds to. A priori, following the SISL documentation one can build a TB Hamiltonian with several possibilities: `spin = {'unpolarized', 'polarized', 'collinear', 'spinorbit'}`. However, currently the `HubbardHamiltonian` class is programmed only to accept a polarized or unpolarized Hamiltonian.

In the case of OBC calculations, the first step is to converge the electrodes (once). Then the MFH converged electrode Hamiltonians are used to obtain the lead self-energies. As seen in Fig. 2.10 the user has to pass the MFH objects of the electrodes (`MFH_elec1` and `MFH_elec2`) to the `NEGF` class along with their corresponding semi-infinite directions `SI_dir1` and `SI_dir2`, which, following SISL notation they can be `'+/-A'`, `'+/-B'` and `'+/-C'`. The imported libraries needed to run these codes are listed at the top. Additionally, we have developed a plotting library, based on `MATPLOTLIB`, of functions that allows to post-process calculations with HUBBARD and graphicate the different interesting physical quantities that come out from a MFH calculation, such as the spin polarization, the WFs for the different spin channels, the accumulated charge per atom,

the PDOS and the LDOS, etc.

2.6 Density functional theory: The SIESTA method

DFT constitutes one of the most commonly used theoretical methods for solving the correlation problem that arises from the Hartree-Fock Hamiltonian. DFT calculations can be considered the workhorse of all *ab initio* methods, as they can provide accurate predictions of structural, electronic, vibrational and magnetic properties for a wide range of systems. The theoretical framework of DFT is based on the Hohenberg-Kohn theorems [179], which state that the ground state electron density $\rho(\mathbf{r})$ uniquely defines the potential of a system and the ground state energy (and therefore all other related ground-state properties), as these quantities can be written as the minimum of a functional of ρ . By means of the Hohenberg-Kohn theorems, Kohn and Sham developed the Kohn-Sham (KS) equations (or KS DFT) with which the intractable many-body problem is reduced to a tractable problem of noninteracting electrons moving in an effective potential [180]. The energy functional of the KS Hamiltonian [180] is obtained and then minimized until self-consistency is reached for the ground state charge densities.

There are several available DFT implementations that have been developed over many years, each of them offers different capabilities, such as the used basis (plane waves, Gaussian orbitals or LCAO), the possibility or not to use semi-empirical quantum chemistry methods, etc. In this thesis the SIESTA [91] and TRANSIESTA [92,94] methods for the DFT were employed. Based on a flexible LCAO basis set, it allows for extremely fast calculations using small basis sets, and very accurate calculations for larger basis sets depending on the required precision. The strictly confined basis orbitals go to zero beyond a certain cutoff radius from their center [181]. The orbitals are of the atomic type, being the product of a numerical radial function times a spherical harmonic. The angular momentum of the basis orbitals can be arbitrarily large, and for each atom there can be one or several orbitals with the same angular shape but different radial shape (multiple- ζ and polarized bases). As opposed to the case of plane wave approaches, being based on localized orbitals, SIESTA is well suited to describe systems with arbitrary dimensionality (from small clusters or molecules to three-dimensional crystals), since the presence of vacuum does not involve an extra cost. On the other hand, another important motivation for using the SIESTA/TRANSIESTA methods comes from the ability to solve the electronic structure for open systems which allows also to perform transport calculations at the atomic (quantum) level, an important part of this present thesis.

With regard to the taken approximations, apart from the Born-Oppenheimer approximation, the most basic approximations concern the treatment of exchange and

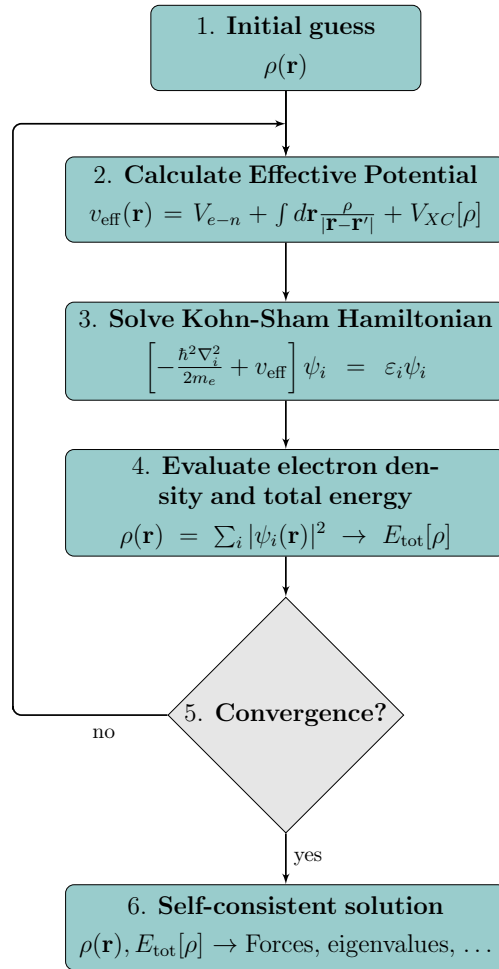


Figure 2.11: SCF convergence procedure for DFT. It starts with an initial guess for the electron density, since it is required for the calculation of $v_{\text{eff}}(\mathbf{r})$. Then it follows the diagonalization of the KS Hamiltonian, and the subsequent evaluation of ρ along with E_{tot} . The numerical procedure is continued with the last calculated ρ until the convergence criterion is achieved.

correlation (XC), and the use of pseudopotentials. From the nuclei system forces can be obtained which are then used to obtain the relaxed geometry by minimizing the forces. The many-body electronic problem is overcome using the KS ansatz [180], in which the fully-interacting system is replaced by a non-interacting one solved by a mean-field approach, where the WF is decomposed into a product of single-electron orbitals $\psi_i(\mathbf{r})$. This is done by applying the variational principle to the KS Hamiltonian that includes an effective potential $v_{\text{eff}}(\mathbf{r})$, which is produced by the Coulomb forces of all other electrons and nuclei and incorporates the exchange and correlation interactions. Then, the

electronic total energy functional can be written as

$$E_{\text{tot}}[\rho] = T[\rho] + V_{e-n}[\rho] + V_{e-e}[\rho] + E_{XC}[\rho] \quad (2.49)$$

where $T[\rho]$ is the electron kinetic energies, $V_{e-n}[\rho]$ the Coulomb interactions between the electrons and the nuclei and $V_{e-e}[\rho]$ those between pairs of electrons. The sum of these three terms constitutes what we call the “known” part. E_{XC} is defined to include all the quantum mechanical effects that are not included in this “known” part. A schematic representation of the SCF loop in this numerical method is depicted in Fig. 2.11.

Exchange and correlation are treated within KS DFT [180], where both the local (spin) density approximation (LDA/LSDA) [182] and the generalized gradient approximation (GGA) [183] are implemented in SIESTA, as well as the recently implemented [184] non-local functional that includes van der Waals interactions (vdW) [185, 186]. To deal with the core region, standard norm-conserving pseudopotentials [187, 188] treated in the fully non-local form [189] are used, as well as the included scalar-relativistic effects and the nonlinear partial-core correction to treat XC in this region [190].

Magnetism in nanographenes

3.1 Spin localization and manipulation in GNR junctions

The nanostructure under study in this section (paper I) is created by coupling two adjacent (3,1)-chGNRs into a V-shaped junction. For these systems, in the experiment, we observed two types of clear magnetic fingerprints by measuring the dI/dV spectra for different samples with the *same molecular geometry*: (i) some of them displayed a Kondo-resonance placed at the Fermi level, (ii) while some displayed a singlet-triplet transition energy. The molecules of the first kind (i) were called **type-1** and **type-2**, while those of the second kind (ii) were called **type-3**.

This system displays a pentagon resulting from the fusing process of the two chGNRs. The presence of the pentagon in the molecular geometry removes the bipartite character of the system, which prevents us from using the Lieb's theorem [45] to predict the origin of its magnetic properties using this simple rule. One way to understand the origin of the magnetic fingerprints in this nanographene is by looking at the WFs. The highly localized character of the HOMO reveals that electrons will likely suffer from a large Coulomb repulsion when occupying this MO, which can be reduced by adopting the open-shell configuration, where now the two separated electrons lie in singly occupied MOs (SOMO). These two unpaired electrons will couple magnetically via the exchange interaction, which explains the dI/dV spectra observed for **type-3**. The singlet-triplet transition curve can indicate the singlet character of the ground state (otherwise it would likely be observed as an underscreened Kondo resonance [38]). The presence of two unpaired electrons at the mentioned molecular regions was further confirmed by the addition/removal of hydrogen atoms. The pairing of an extra hydrogen atom to one of the two radicals (H-passivation) leaves only one localized $S = 1/2$ spin in the molecule which was observed as a Kondo resonance (peak at the Fermi level) in the experimental

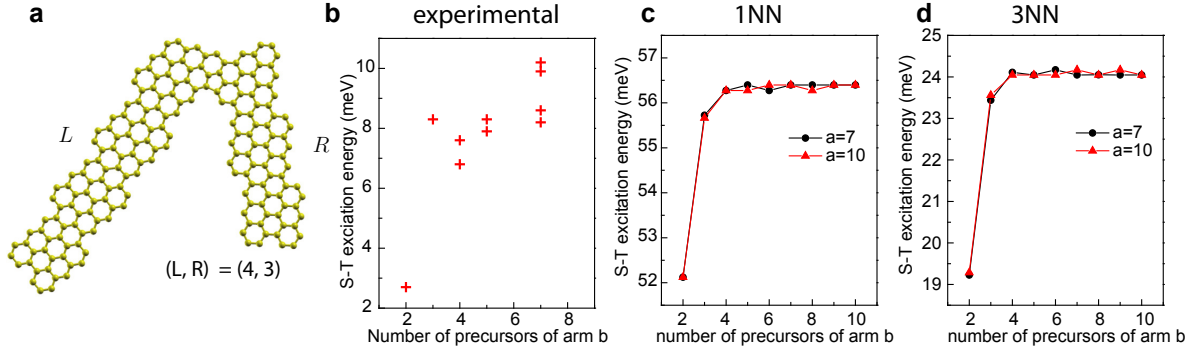


Figure 3.1: Singlet-triplet excitations as a function of the length of the molecular arms. (a) Molecular geometry with the definition of the size of the junction measured in terms of the number of precursor units in the left (L) and right (R) arms. (b) Experimentally obtained singlet-triplet excitations plotted as a function of the length of arm R extracted from a fit of dI/dV spectra. All junctions had arm $L > 7$. (c) Calculated excitation energies as a function of the length of arm R within MFH using $U = 3.5$ eV and the 1NN model for the TB part. Here the length of arm a are fixed as 7 and 10, respectively. (d) Same as (c) but for the 3NN model. Taken from the [supplemental material](#) of paper [I](#).

dI/dV spectra, explaining the case of **type-1** and **type-2**.

Another interesting result from this project is that the singlet-triplet excitation energy grows with the molecular size as a consequence of the orbital localization (see Fig. 3.1), which *a priori* can be an unintuitive behavior since one would expect that the gap decreased with the size of the quantum box. Bearing in mind that the exchange interaction results from an interplay between the Coulomb repulsion and the overlap between the SOMOs, one can understand this behavior since the SOMOs slightly delocalize when the L arm (cf. Fig. 3.1a) goes from 2 to 4 precursor units (PU), resulting in a larger overlap and lower Coulomb repulsion, and consequently a larger exchange coupling observed in Fig. 3.1b-d. For more than 4 PU, the localization of these states remains practically constant.

In this work we computed the spin densities within both DFT and MFH theoretical frameworks. To analyze the effect of the empirical TB parameters, we compared simulations performed with 1NN and 3NN models. The inclusion of next-nearest neighbor couplings goes towards a better description of the system as compared to DFT and the experiment, as can for instance be inferred in Fig. 3.1, where the energies obtained with the 3NN (Fig. 3.1c) are closer to the experiment (Fig. 3.1a) than the ones obtained with 1NN (Fig. 3.1b). On the other hand, the Coulomb parameter U —that should be in the

range $U \sim t$ in the limit of weak correlations—was taken to reproduce better the DFT results, and therefore, the experimental results. By comparing several calculations of the spin density distribution, as well as the (3,1)-chGNR band structure, obtained with the MFH for different U values with DFT and the experiment, we concluded that the most suitable value for this parameter was $U \sim 3.5$ eV. This value also leads to a reasonable agreement of the approximate singlet-triplet excitation energy with (albeit larger than) the experimentally observed peak splitting.

3.2 Triangulene-like nanostructures

As already explained, certain shapes of graphene structures may accommodate a spin imbalance in the π electron cloud, resulting in graphene nanosystems with a net magnetic moment, however, the fabrication of such GNFs has been hindered due to their high reactivity [191]. In paper II, we report the OSS fabrication of a triangulene-like geometry, called extended-triangulene (ETRI). This nanographene has 19 carbon atoms on one sublattice and 17 carbon atoms on the other, leading to an expected total spin for this molecule of $S = 1$. In this work we also explore the magnetic properties of ETRI dimers.

We simulate the system with the MFH model using $U \sim 3.0$ eV for the interaction term, and the 3NN model to address the kinetic part of the Hamiltonian, as these parameters successfully described other sp^2 carbon systems (as seen in paper I). For comparison, we also ran calculations with DFT, which showed excellent agreement with our MFH results. For instance, in Fig. 3.2 we show the SCF solution of different magnetic states obtained with SIESTA [91] for three different systems: the ETRI and two possible geometries for the ETRI dimer (with and without a pentagonal ring). Here we observe that, according to the Lieb’s theorem [45], the ETRI and the dimer shown in panels Fig. 3.2a-e (both bipartite lattices) present $S = 1$ and $S = 2$ ground states corresponding to their respective lattice imbalances. In reality, during the cyclodehydrogenation step in the OSS, an extra pentagonal ring is created between them, reducing the number of radicals of the dimer from four (without pentagon) to only two. This is also confirmed by our simulations, where we obtained that the magnetic ground state is the one with $S = 1$ for this geometry. Experimentally, the presence of the FM coupled spins system is observed as a peak at the Fermi energy in the dI/dV spectra, corresponding to the underscreened Kondo effect [38, 192–194]. Further experiments with an applied magnetic field proved that the ground state indeed reacts as an underscreened spin triplet, shown in the [Supplemental Material](#) of the mentioned paper.

As in the previous section, the $S = 1$ ground state for the ETRI can be turned into an uncoupled $S = 1/2$ state by additional hydrogen atoms attached to one of the radical

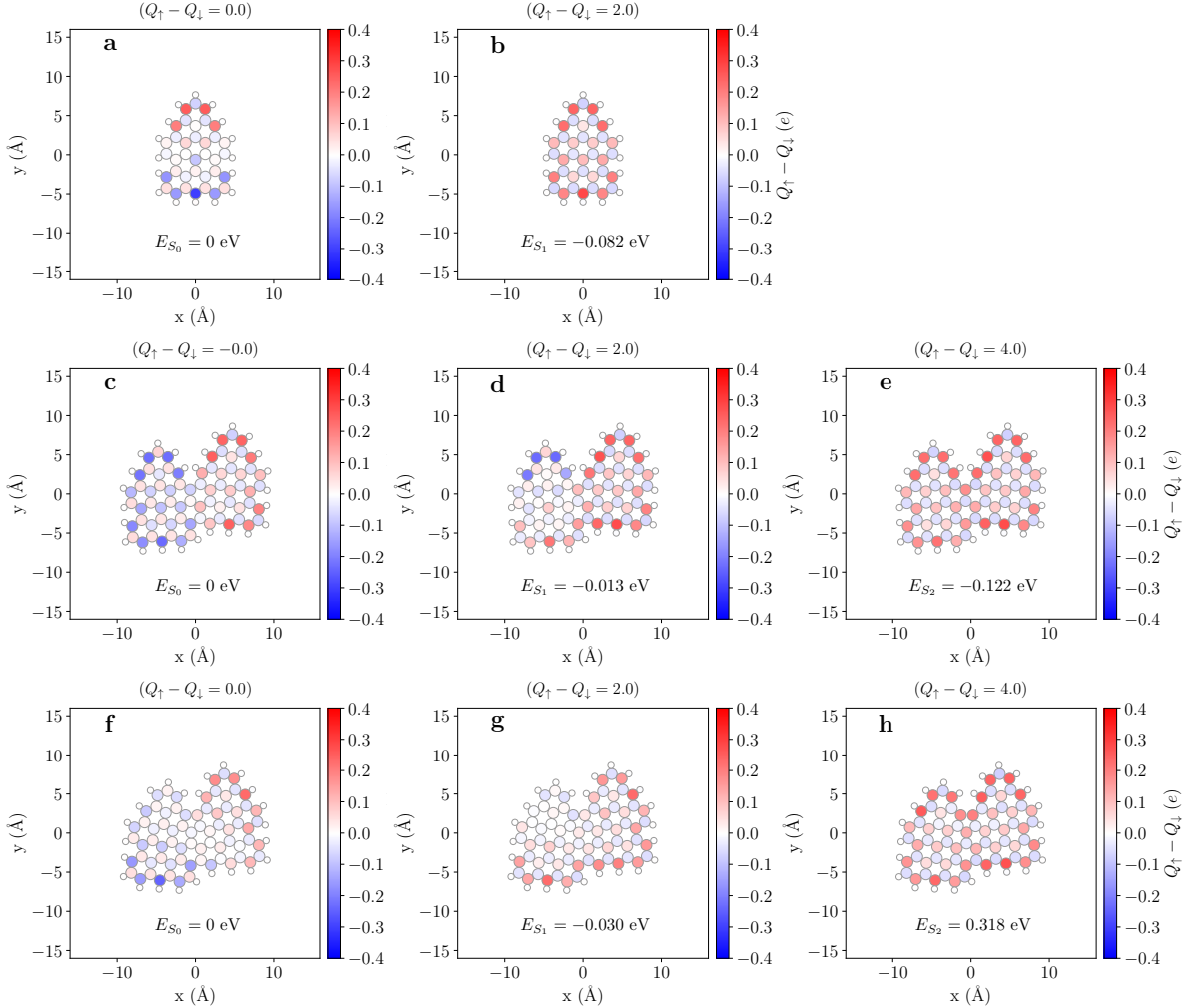


Figure 3.2: (a,b) Spin polarization from SIESTA of the ETRI monomer with $S = 0$ ($Q_{\uparrow} - Q_{\downarrow} = 0$) and $S = 1$ ($Q_{\uparrow} - Q_{\downarrow} = 2e$) respectively. (c,d,e) Spin polarization of the dimer with fixed $S = 0$, $S = 1$, and $S = 2$, respectively. (f,g,h) Spin polarization of a ETRI dimer with pentagon, imposing $S = 0$, $S = 1$ and $S = 2$, respectively. The energy of every state relative to the $S=0$ state is annotated in each panel. We used the generalized gradient approximation (GGA) [182] for exchange and correlation, a 400 Ry cut off energy for the real-space grid integrations, and a double-zeta plus polarization (DZP) basis. The force tolerance was set to $2 \text{ meV}/\text{\AA}$ and the density was converged to a criterion of 10^5 . The geometries were first relaxed in the spin degenerate calculations and then frozen to a specific spin value for the spin-polarized calculations.

sites. Theoretically, we analyzed the magnetic nature of these passivated systems by removing the corresponding p_z orbital (the one bonded to the extra hydrogen atom) and

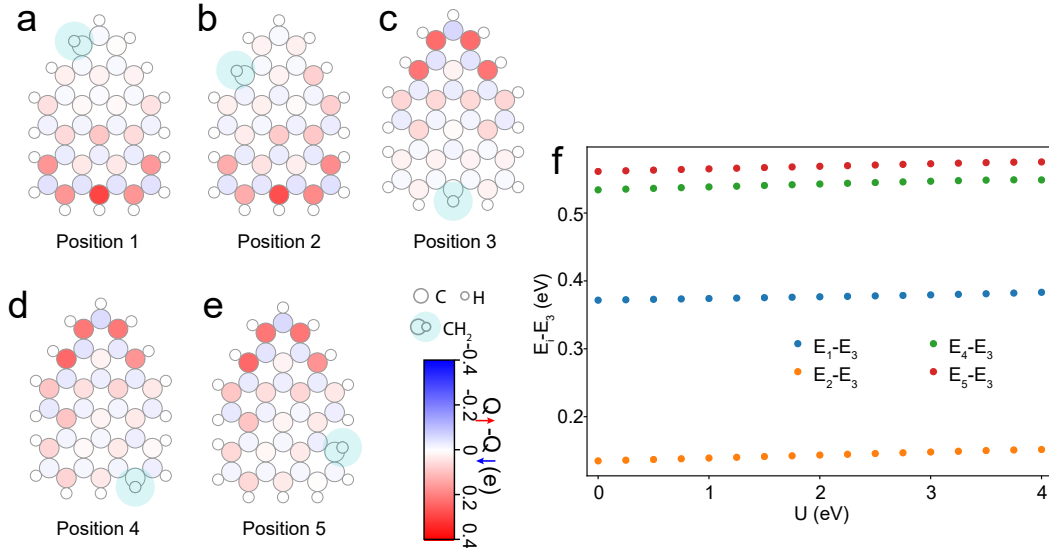


Figure 3.3: (a-e) Spin polarization of the extended-triangulene molecule with H-passivated C-atom sites in five different positions from MFH simulations with $U = 3.0$ eV. (f) Comparison of total energy differences between the five different configurations for different U values with the most stable configuration (position 3) as reference. Figure extracted from the supplemental material from paper II

computing the spin densities.

We also tested different possible positions of the extra hydrogen at the edge sites of the molecule observing that the most stable one (lowest in energy) is position 3 in Fig. 3.3, which agrees with the observed experimental statistics of H-passivation for this molecule. Hereby, it is confirmed that the H-passivation eliminates one of the present radicals and changes the biradical character of the molecule to a single radical present. On the other hand, experimentally, the fact that the remaining radical behaves as a $S = 1/2$ Kondo resonance further confirms the existence of two radicals in the ETRI molecule.

3.3 Exchange interaction between radical pairs in heteroatomic structures

In previous sections we have seen the coupling of spin states in strict sp^2 carbon structures. However, the presence of heteroatoms can play a major role in the exchange coupling of such unpaired spins [195]. For instance, replacing a CH at the

pristine chGNR edge by a C=O (carbonyl group) adds one π -electron to the system. As a result, the odd number of total electrons causes the appearance of a π -radical. The same is applicable for regularly ketone-functionalized chGNRs, the other way around. Therefore, in chGNRs, the coupling between two radical states will depend on their relative position, which includes a remarkable dependence on the chirality, as well as on the nature of the surrounding ribbon, *i.e.*, with or without ketone functionalization, as explained in paper III. Since the ketone group is also sp^2 hybridized (see sketch in Fig. 3.4), it contributes with one p_z electron to the system and can—to a first approximation—be considered as an additional p_z site on its corresponding sublattice.

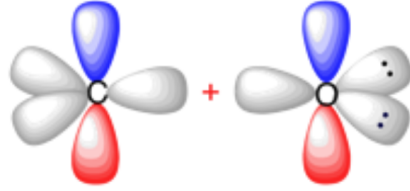


Figure 3.4: Sketch of the resulting sp^2 hybridization of the carbonyl group (C=O).

A radical pair located at the same/opposite side is expected to be ferromagnetically (FM)/antiferromagnetically (AFM) aligned since atoms at same edges of the chGNRs belong to the same sublattice, whereas the atoms at the opposite edge belong to the other sublattice. The nomenclature of the geometry label is K-/P- for ketone/pristine chGNRs, S/O for radicals in same/opposite and n for the number of precursor units between the radicals. All radical pairs match this prediction, except K-S1 which is AFM as confirmed by DFT calculations with SIESTA [91] and the experimental dI/dV measured spectra.

In an attempt to make the simple MFH calculations also applicable to these heteroatomic chGNRs, we included modified TB parameters for the oxygen heteroatoms in what we call the MFH-TB(2) model. By comparing the calculated band structures obtained from DFT for fully ketone-functionalized chGNRs to those obtained with our MFH-TB models, we observed an improvement of the TB model with MFH-TB(2) changing the 1NN hopping and on-site energy values to $|t| = 3.8$ and $\epsilon_i = -1.5$ eV for oxygen atoms bonded to carbon (maintaining $|t| = 2.7$ and $\epsilon_i = 0$ eV for C–C atoms). Qualitatively, the increased hopping amplitude on the C=O bonds can be directly related to its shorter length and the nonzero on-site energy to the increased electronegativity of oxygen.

Electron quantum optics in GNR-based architectures

In this chapter we analyze the electron and spin transport properties of four-terminal devices formed of two crossed GNRs placed one on top of the other with a relative crossing angle of 60° , while the distance between them is the typical vdW distance of graphene layers in graphite, *i.e.*, $d = 3.34 \text{ \AA}$. This chapter is based on papers [IV](#) and [V](#) [[96,97](#)].

4.1 Inter-GNR coupling description

To properly account for the coupling between p_z orbitals in and out of the plane, we describe the matrix element t_{ij} between orbitals i and j with Slater–Koster type two-centre π and σ bond integrals between two p_z atomic orbitals [[139,196](#)]

$$t_{ij} = V_{pp\pi}(1 - l^2) + V_{pp\sigma}l^2, \quad (4.1)$$

where l is the cosine of the angle formed between the distance vector \hat{r}_{ij} for the ij atom pair and the unit vector that defines the z -direction, *i.e.*, $l = \hat{r}_{ij} \cdot \hat{e}_z / |r_{ij}|$. The two-centre integrals $V_{pp\pi}$ and $V_{pp\sigma}$ are expressed in terms of exponential decay functions of the distance $|r_{ij}|$. The parameters used to describe these integrals were obtained by fitting to the low-energy band structure of AB-stacked bilayer graphene simulated with SIESTA [[91](#)] as explained in paper [IV](#).

4.2 Symmetry aspects of crossed GNRs

Because of the symmetry of the honeycomb lattice, when the crossing angle between the GNRs is 60° there is a perfect matching between the bottom and top ribbon lattices,

which yields an enhancement of the transfer process of electrons between them [76, 77]. At this crossing angle, there are two possible high symmetry configurations which are the AB- and AA-stackings. Apart from the time-reversal symmetry ($T_{\alpha\beta} = T_{\beta\alpha}$) in absence of a magnetic field, there are two geometrical symmetry axes: $y_1 = \sin(-60^\circ)x$ and $y_2 = \sin(30^\circ)x$. AB and AA-stacked GNRs can possess either zero, one or the two of them. As a consequence of the presence of these symmetries, there will exist some equivalent symmetric electrode combinations leading to some constraints in the transmission probabilities. Therefore, the 4×4 matrix of transmission probabilities will not have 16 independent elements but less (10, 6 or 4 depending on the degree of symmetry that a given device displays).

4.3 GNR networks for electron interferometry

To analyze the transport properties for general crossed GNRs, in paper IV we give a complete classification and characterization of the transport properties of these type of junctions by varying the edge topology of the GNRs (zigzag or armchair), stacking sequence (AA or AB), width of the ribbons, and energy for the propagating electrons. While for the crossed ZGNRs we only found one AA- and AB-stackings (ZGNR-AA and ZGNR-AB), interestingly, for the crossed AGNRs we found two possible geometries for each of them, which we called: AGNR-AA-1, AGNR-AA-2, AGNR-AB-1 and AGNR-AB-2. Each of them shows different behavior in terms of the electron quantum transport. For this reason, we first classify and collect the transport properties of these six systems by calculating and analyzing the transmission probability matrix varying the different parameters that determine the problem: the edge topology of the GNRs (armchair or zigzag), the precise stacking, width of the ribbons, and energy for the propagating electrons. Interestingly, we discovered that AGNR-AA-1 and AA-2, that show little geometrical difference, behave very differently from each other in terms of the electron transport for low-energy electrons. For instance, in the case of AA-1 geometries electrons are only allowed to turn 60° , while in the AA-2 case electrons only turn 120° .

Secondly, focusing on the features that these devices can offer more specifically for electron quantum optics experiments, we built a figure of merit to find the regions in which crossed GNRs can perform as fundamental components for electron interferometry and their quality as such. In these terms, we looked in the parameters space where these devices would work as *mirrors* (where electrons are fully transferred into the other ribbon), *beam splitters* (where electrons are equally transmitted with a 50:50 ratio in two outgoing ribbons), and *wavelength filters*. One important result is that, while AA-stacked AGNRs could be good candidates for electron quantum optics experiments, AB-stacked

devices do not show good electron quantum optical features due to the comparatively larger losses and low inter-GNR transmission. Unfortunately, AA-stacked configurations are probably harder to realize in practice (not the most stable energetically) compared to the AB-stacked one [197]. Combined with a generally larger variability of the AGNR transport behavior, these facts indicate that ZGNRs are more interesting objects for the considered device applications than AGNRs.

Finally, with the general TB model that we use for the interlayer coupling (Sec. 4.1) we were able to describe a plethora of crossed GNRs geometries of arbitrary relative positions. Being aware of that precise control of the device geometry is likely a significant experimental challenge, we analyzed the transport properties of such devices against possible deviations from the “ideal” 60° that was presented. We observed that, although the intra- and inter-transmission probabilities may suffer from quantitative variations, these distortions do not affect the needed conditions for the beam splitting effect which are the zero back-scattering and zero transmission into port 4 in crossed ZGNR devices.

4.4 Spin-polarizing electron beam-splitting effect in crossed ZGNRs

As ZGNRs tend to polarize, the natural next step is to study the *spin* transport in crossed ZGNRs when the Coulomb repulsion between electrons is included in the device Hamiltonian, as explained in paper V. Since there are four terminals in the device and there are two possible solutions of equal energy for each electrode, there are in principle 16 spin configurations, although only 8 of them are inequivalent. Some of these 8 spin configurations involve a grain boundary, in particular those that the spin density distribution of the electrodes belonging to the same ribbon are inverted. The presence of such boundary increases 200 meV to the total electronic energy. On the other hand, the AA stacking are less energetically favorable than the AB stacking, as has been also obtained with DFT [197]. For these reasons, in the main text of paper V we only consider the two states of lowest energy (labeled $\boxed{\uparrow\downarrow}$ and $\boxed{\uparrow\uparrow}$).

The state of lowest energy is found to be the spin configuration with AFM interlayer coupling, *i.e.*, the atoms that sit on top in the crossing area have opposite spin indices, which is also inline with results shown in Ref. [198].

To understand the electron and spin quantum transport, it can be very useful to analyze the symmetries behind these junctions. For instance, apart from the mirror symmetry axis hosted by the AB-stacked ZGNRs, the spin density distribution adds an extra spatial component to be taken into account, which will be responsible of the spin

transport properties of these devices. Depending on the spatial spin distribution, the symmetry axes can either invert ($\boxed{\uparrow\downarrow}$) or conserve ($\boxed{\uparrow\uparrow}$) the spin index of each atom. In the former case, the symmetry protects $T_{\alpha\beta}^{\sigma} = T_{\gamma\delta}^{\sigma}$ for the electrode combinations connected by the symmetry axis, while in the latter we have $T_{\alpha\beta}^{\sigma} = T_{\gamma\delta}^{\sigma}$. In other words, in $\boxed{\uparrow\downarrow}$ we expect to have a symmetric spin transport behavior, while in $\boxed{\uparrow\uparrow}$ we expect non-symmetrical transport behaviors for the existing spin channels.

On the other hand, the non-polarizing case ($\boxed{\uparrow\downarrow}$) is specific for high-symmetry configurations, as this class of electronic devices are generally predicted to create a spin-dependent scattering potential. To show that, we calculated the spin polarization in the transmission probabilities for non-symmetrical geometries by applying a translation of the on-top ribbon with respect to the bottom one along the directions defined by the graphene lattice vectors. From this result, it can clearly be observed that regardless of the spin density distribution of this device it can behave as a spin polarizing beam splitter. Furthermore, the spin polarizing effect can be enhanced by placing several consecutive crossings, that can lead to outgoing electrons with almost $\sim 100\%$ polarization.

For a more realistic simulation of the device, we also calculated the averaged spin polarization from a distribution of 10^7 arrays where the crossing angle, the stacking registry and the spin configurations were chosen randomly. Fortunately, we observed that in fact it is not necessary to have an atomistic control over the crossings since the averaged spin polarization still monotonically grows with the number of present junctions even in the worst scenario.

Conclusions and outlook

Magnetism in graphene nanostructures. We presented a complete electronic and magnetic characterization of several open-shell graphene nanoflakes. We have fundamentally understood the source of magnetism in these structures, supported by our calculations, and seen that it can be (among others) triggered by the Coulomb repulsion between electrons, the sublattice imbalance, and due to the presence of heteroatoms. For the biradical systems that we have studied, the two unpaired electrons can be magnetically coupled in a singlet ($S = 0$) or a triplet ($S = 1$) state, which will be observed experimentally as a singlet-triplet transition curve or as an underscreened Kondo resonance in the dI/dV spectra, respectively. On the other hand, we observed that the magnetic interaction between two unpaired radicals is highly dependent not only on their relative position (where the chirality and distance between them play a major role) but it also depends on their chemical environment.

We have also seen that there are ways to manipulate the magnetic state in the system. For instance, by adding extra H-atoms to the radical sites one can modify the biradical character of the molecule from two to a single radical present, which actually is a reversible process. The creation of pentagon rings may change the nature of the spin ground state as well. Moreover, the fact that the remaining radical behaves as a $S = 1/2$ Kondo resonance further confirms the existence of two radicals in the molecule, as shown both experimentally and theoretically. In a similar way, the magnetic properties of graphene-systems can be tuned by chemical functionalization. For instance, an extra C=O group adds an unpaired π electron to the network, which acts as a radical state. Furthermore, the electronegativity of the oxygen and the stronger bond created by the carbonyl can even change the expected FM coupling between two radicals to a preferred AFM alignment. Strikingly, the encountered magnetic features in graphene nanoribbons standing on gold surfaces confirm the survival of the spin states even on metallic surfaces in spite of the ubiquitous charge screening by the underlying substrate. The rich structure-dependency relationship in nanographenes allows one to tune the above mag-

netic properties through a rational design of the shape, size, edge structure and chemical environment of nanographenes, which makes these systems potentially useful in organic quantum spintronic devices [199–201], as *e.g.* spin-logic operations [202].

In terms of implementation, we observed excellent agreement between MFH and DFT calculations under the correct parametrization for sp^2 carbon structures, as generally seen in many different contexts. The description provided by this model has shown a very good qualitative representation of the experiment, as confirmed by the works presented in papers V, II, III and Refs. [43, 161]. We have seen that the presence of heteroatoms in the structure can be well described with the MFH model and even H-passivated systems. However, although finding a suitable U parameter for the MFH model is of great importance, we have seen the cruciality of the TB parametrization in order to capture a good qualitative picture of the system.

Electron quantum optics in graphene. We presented a full classification and characterization of the different functionalities that can be found in junctions formed of crossed GNRs by varying their edge topology (zigzag or armchair), stacking sequence (AA or AB), width of the ribbons, and energy for the propagating electrons in the valence or conduction bands. We identified the regions in the parameters space where the junctions can act as fundamental components for electron interferometry, such as mirrors (where the electrons are fully transferred into the other ribbon), beam splitters (half-transparent mirrors, where the electrons are transmitted with a 50:50 ratio in two outgoing terminals), and wavelength filters, in a figure of merit that outline the transport properties of these devices. This figure is intended to serve as a guide for the design optimization for GNR-based electron quantum optical setups.

One very important result is that, while the performance depending on the GNR edge topology is different, the beam splitting effect (transmission into two outgoing ports without reflection) is general for crossed AGNRs and ZGNRs devices. Furthermore, transport properties of crossed ZGNRs are quite robust as it is rather insensitive to geometrical distortions such as rotations, translations and even strain deformations.

The inclusion of Coulomb repulsion and the spin degree of freedom also does not change the main important features such as the zero reflection probability and zero transmission into the undesired port in crossed ZGNRs. However, the spin transport in these nanodevices is quite interesting as it gives polarized transmission probability, which can be even further enhanced by placing more consecutive crossing potentially leading to highly polarized transmitted electrons where one of the two spin components is filtered away. Importantly, these devices can overcome one of the major challenges of semiconductor spintronics, which is the fabrication of a controllable source of a spin-polarized current that operates in the absence of a magnetic field. Among their potential

applications in this field, these devices could be used to determine the entanglement of injected pairs of spins.

Prospects for the future

A possible useful extension of the HUBBARD package could be to implement an exact treatment of the many-body problem defined by the Hubbard Hamiltonian, so all the options are collected in a PYTHON package. For instance, instead of treating the system with a mean-field approach, one can use the CAS method, which in this context consists of splitting the single-particle spectrum into “frozen” low- and high-energy sectors and an active window which is solved by exact diagonalization to capture the low-energy states accurately [46, 203]. This method was used, for instance, to understand the magnetic exchange interaction in nanographenes with diradical character [46], triangulene dimers [40] and trimers [41]. By having this implementation in the HUBBARD module, one would be able to easily compare the obtained solutions with the available frameworks.

Additionally, while the HUBBARD package is able to solve self-consistently systems with open boundary conditions, for now it only computes correctly the spin densities for systems in equilibrium. However, it could be very advantageous to have also the option to solve the non-equilibrium situation, where the electrodes can have different temperatures and/or chemical potentials. The implementation to find the self-consistent solution for an open quantum system out of equilibrium could follow a similar procedure as the one implemented in TRANSIESTA [92, 94] for DFT. This tool can be very useful, for example, to explore the effect of an applied bias on the magnetic exchange coupling between two localized spins. Furthermore, while in this thesis we have neglected the time dependency of the Hamiltonian, it could be very interesting to compute electron spin decoherence and relaxation times due to spin-spin and spin-orbit interactions, which are limiting factors for quantum operations [28, 31, 78–81]. The time dependent Hamiltonian could also open the possibility to study how to manipulate electron spins by external means (current pulses, time-varying fields, etc), as for example shown in Ref. [204].

With respect to the evolution of electron quantum optics in graphene, with the fundamental building blocks that we have presented for electron interferometry one would now be able to build larger electronic GNR networks. For instance, at this stage one can now construct the electronic analog of the Mach-Zehnder interferometer, consisting of two beam splitters and two oriented mirrors at the intersection of pairwise parallel ribbons (as displayed in Fig. 5.1), which has proven to work as a quantum logic processor [205]. Other two paths setups have demonstrated to act as a manipulable flying qubit architecture [206] using the Aharonov-Bohm effect [207]. When it comes to electron in-

terference, it requires clean systems and long phase coherence lengths, for which ZGNRs provide an outstanding platform for studying electron interference. In the GNR-based interferometer of Fig. 5.1, we can induce the Aharonov-Bohm effect, for instance, by applying an external magnetic field parallel to the axis perpendicular to the geometry. In this scenario the electron transport will have a cosine dependency with the magnetic flux enclosed by the GNRs, due to the interference term between the two possible paths. If we consider the spin degree of freedom, these device could also act as a spin-polarizing interferometer, which can have potential applications in the field of graphene spintronics (S. Sanz *et al.*, in preparation).

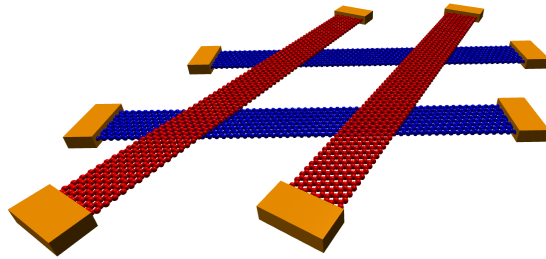


Figure 5.1: Geometry of the 8-terminal Mach-Zehnder interferometer realized with four crossed GNRs with a relative rotation angle of 60° . GNRs displayed in red (blue) lie on top (bottom).

I Single spin localization and manipulation in graphene open-shell nanostructures, *Nat. Commun.* 10, 200 (2019)

ARTICLE

<https://doi.org/10.1038/s41467-018-08060-6>

OPEN

Single spin localization and manipulation in graphene open-shell nanostructures

Jingcheng Li¹, Sofia Sanz², Martina Corso^{2,3}, Deung Jang Choi^{2,3,4}, Diego Peña⁵, Thomas Frederiksen^{2,4} & Jose Ignacio Pascual^{1,4}

Turning graphene magnetic is a promising challenge to make it an active material for spintronics. Predictions state that graphene structures with specific shapes can spontaneously develop magnetism driven by Coulomb repulsion of π -electrons, but its experimental verification is demanding. Here, we report on the observation and manipulation of individual magnetic moments in graphene open-shell nanostructures on a gold surface. Using scanning tunneling spectroscopy, we detect the presence of single electron spins localized around certain zigzag sites of the carbon backbone via the Kondo effect. We find near-by spins coupled into a singlet ground state and quantify their exchange interaction via singlet-triplet inelastic electron excitations. Theoretical simulations picture how electron correlations result in spin-polarized radical states with the experimentally observed spatial distributions. Extra hydrogen atoms bound to radical sites quench their magnetic moment and switch the spin of the nanostructure in half-integer amounts. Our work demonstrates the intrinsic π -paramagnetism of graphene nanostructures.

¹CIC nanoGUNE, 20018 Donostia-San Sebastián, Spain. ²Donostia International Physics Center (DIPC), 20018 Donostia-San Sebastián, Spain. ³Centro de Física de Materiales CFM/MPC (CSIC-UPV/EHU), 20018 Donostia-San Sebastián, Spain. ⁴Ikerbasque, Basque Foundation for Science, 48013 Bilbao, Spain. ⁵Centro Singular de Investigación en Química Biolóxica e Materiais Moleculares (CiQUS), and Departamento de Química Orgánica, Universidade de Santiago de Compostela, Santiago de Compostela 15782, Spain. Correspondence and requests for materials should be addressed to J.I.P. (email: ji.pascual@nanogune.eu)

Among the many applications predicted for graphene, its use as a source of magnetism is the most unexpected one, and an attractive challenge for its active role in spintronic devices¹. Generally, magnetism is associated to a large degree of electron localization and strong spin-orbit interaction. Both premises are absent in graphene, a strongly diamagnetic material. The simplest method to induce magnetism in graphene is to create an imbalance in the number of carbon atoms in each of the two sublattices, what, according to the Lieb's theorem for bipartite lattices², causes a spin imbalance in the system. This can be done by either inserting defects that remove a single p_z orbital³⁻⁶ or by shaping graphene with zigzag (ZZ) edges^{7,8}. However, magnetism can also emerge in graphene nanostructures where Lieb's theorem does not apply^{9,10}. For example, in π -conjugated systems with small band gaps, Coulomb repulsion between valence electrons forces the electronic system to reorganize into open-shell configurations¹¹ with unpaired electrons (radicals) localized at different atomic sites. Although the net magnetization of the nanostructures may be zero, each radical state hosts a magnetic moment of size μ_B , the Bohr magneton, turning the graphene nanostructure paramagnetic. This basic principle predicts, for example, the emergence of edge magnetization originating from zero-energy modes in sufficiently wide ZZ¹²⁻¹⁴ and chiral^{15,16} graphene nanoribbons (chGNRs).

The experimental observation of spontaneous magnetization driven by electron correlations is still challenging, because, for example, atomic defects and metal impurities in the graphene structures¹⁷⁻¹⁹ hide the weak paramagnetism of radical sites²⁰. Scanning probe microscopies can spatially localize the source states of magnetism^{6,19}, but they require both atomic-scale resolution and spin-sensitive measurements. Here we achieve these conditions to demonstrate that atomically defined graphene nanostructures can host localized spins at specific sites and give

rise to the Kondo effect^{21,22}, a many-body phenomenon caused by the interaction between a localized spin and free conduction electrons in its proximity. Using a low-temperature scanning tunneling microscope (STM) we use this signal to map the spin localization within the nanostructure and to detect spin-spin interactions.

Results

Formation of GNR nanostructures. The graphene nanostructures studied here are directly created on a Au(111) surface by cross-dehydrogenative coupling of adjacent chiral GNRs (chGNRs)²³. We deposited the organic molecular precursors 2,2'-dibromo-9,9'-bianthracene (Fig. 1a) on a clean Au(111) surface, and annealed stepwisely to 250 °C (step 1 in Fig. 1a) to produce narrow (3,1)chGNRs, i.e. ribbons that alternate three zig-zag sites with one armchair along the edge²⁴. They are semiconductors with a band-gap of 0.7 eV and show two enantiomeric forms on the surface²⁵. By further annealing the substrate to 350 °C (step 2 in Fig. 1a), chGNRs fuse together into junctions, as shown in Fig. 1b. The chGNR junctions highlighted by dashed rectangles are the most frequently found in our experiments. They consist of two chGNRs with the same chirality linked together by their termination (Fig. 1c). The creation of this stable nanostructure implies the reorganization of the carbon atoms around the initial contact point²⁶ into the final structure shown in Fig. 1d, as described in Supplementary Note 1.

In Fig. 1b, certain regions of the junctions appear brighter when recorded at low sample bias, reflecting enhancements of the local density of states (LDOS) close to the Fermi level. Interestingly, the precise location of the bright regions is not unique, but can be localized over the pentagonal cove (PC) site (Type 1, Fig. 1e), over the terminal ZZ site of the junction (Type

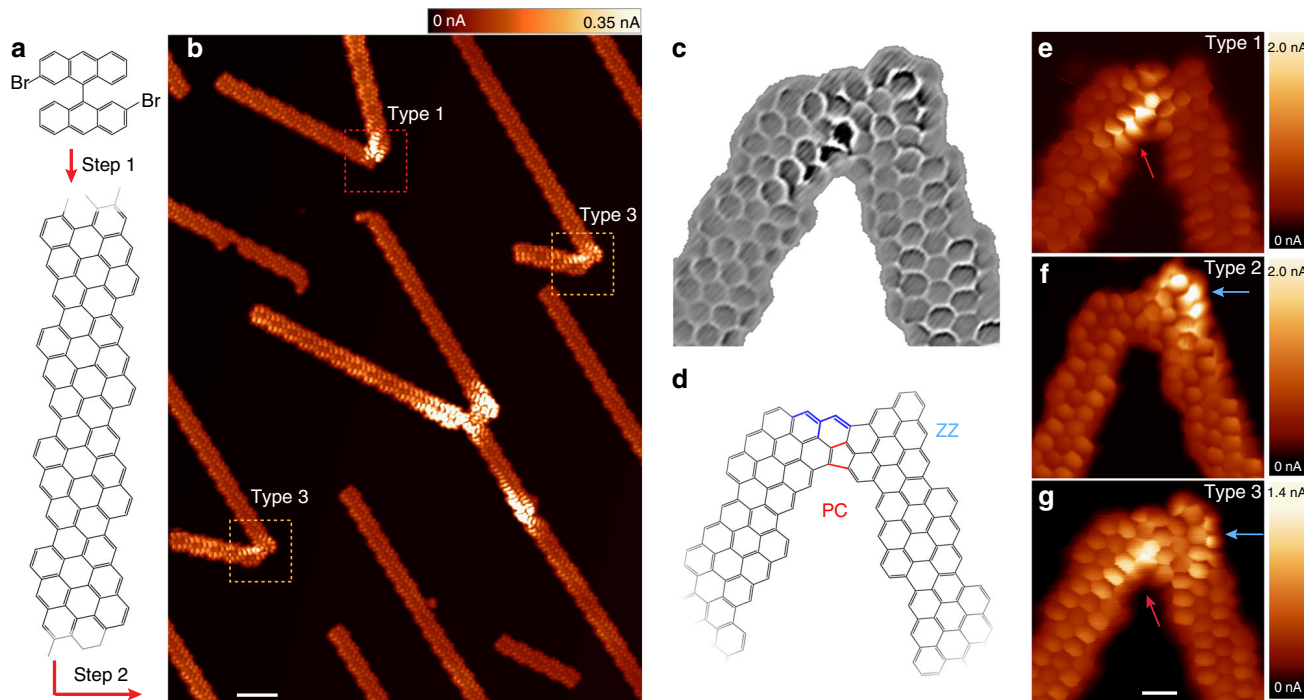


Fig. 1 Formation of GNR junctions. **a** Model structures of the organic precursor 2,2'-dibromo-9,9'-bianthracene and of the on-surface synthesized (3,1) chGNR after Ullmann-like C-C coupling reaction and cyclodehydrogenation on Au(111). **b** Constant-height current images ($V = 2$ mV, scale bar: 2 nm) showing joint chGNR nanostructures, with an angle of -50° , obtained after further annealing the sample. A CO-functionalized tip was used to resolve the chGNR ring structure. Dashed boxes indicate the most characteristic chGNR junctions, whose structure is shown in panels **c**, **d**. **c** Laplace-filtered image of the junction shown in panel **g** to enhance the backbone structure, and **(d)** model structure of the junction. PC labels the pentagonal cove site and the ZZ the zigzag site. **e-g** Constant-height current images ($V = 8$ mV, scale bar 0.5 nm) of the three types of chGNR junctions with same backbone structures but with different LDOS distribution

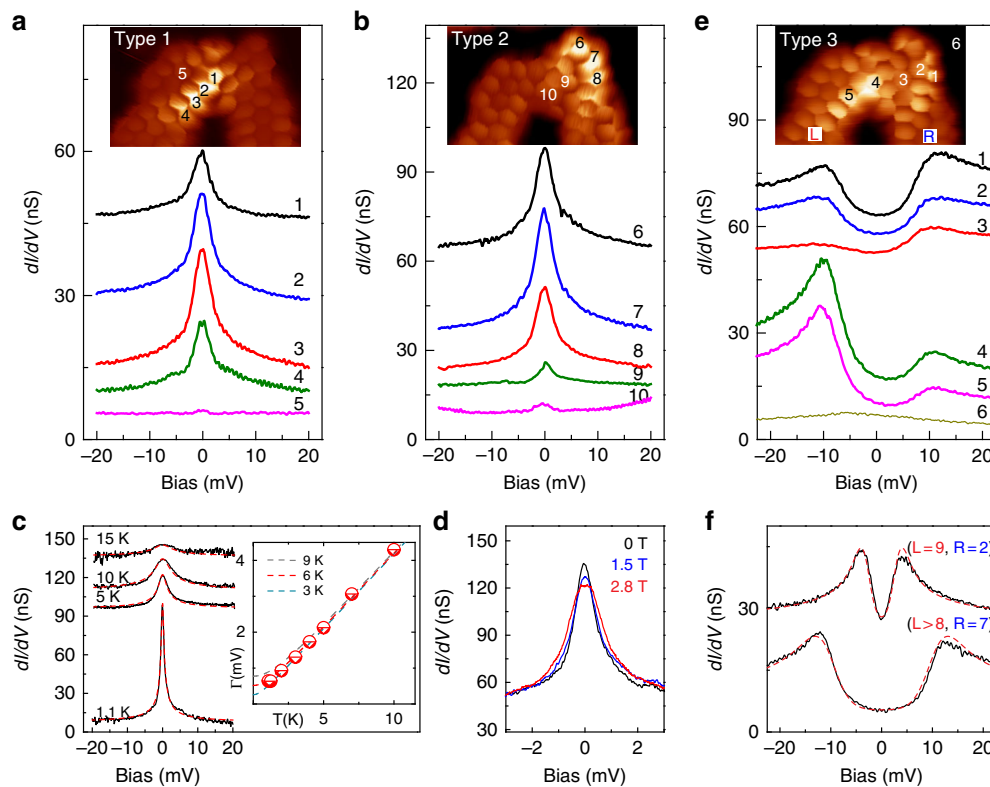


Fig. 2 Zero bias spectral features. **a, b** Kondo resonances over the bright regions of Type 1 and Type 2 junctions, respectively. The zero-bias peaks are mostly detected over four PC rings of Type 1 junctions and over three ZZ rings of Type 2 junctions. **c** Temperature dependence of the Kondo resonance. All spectra were measured over the same PC site. The half width at half maximum (HWHM) at each temperature is extracted by fitting a Frota function (red dashed lines)⁴⁹ and corrected for the thermal broadening of the tip²⁸. The temperature dependence of HWHM was simulated with the empirical expression $\frac{1}{2} \sqrt{(\alpha k_B T)^2 + (2k_B T_K)^2}$ ²⁹, which reproduces the experimental results with a Kondo temperature $T_K \sim 6$ K and $\alpha = 9.5$ (Supplementary Note 3). **d** Magnetic field dependence of a Kondo resonance (over the same PC site) at the field strengths indicated in the figure. **e** Double-peak features around zero bias over Type 3 junctions. **f** Split-peak dI/dV features for nanostructures with different sizes, determined by the number of precursor units in each chGNR, labeled L and R in **e**. The gap width increases with the length of the ribbons (see Supplementary Fig. 16a in Supplementary Note 8). The red dashed lines are fits to our spectra using a model for two coupled spin-1/2 systems³¹. The spectra in **c, d** were acquired with a metal tip, while the others with a CO-terminated tip

2, Fig. 1f), or over both (Type 3, Fig. 1g). Supplementary Note 2 quantifies the probability of finding each type of junction. Despite these different LDOS distributions in the three types of junctions, they all have the same carbon lattice arrangement, shown in Fig. 1d. Such low-energy LDOS enhancements are absent over bare chGNRs segments due to their semiconductor character, and only the bare hexagonal backbone is resolved.

Spectral features around zero-bias. To understand the origin of the enhanced LDOS at the ZZ and PC sites, we recorded differential conductance spectra (dI/dV) on the three types of junctions. Spectra on the bright sites of Type 1 and 2 junctions show very pronounced zero-bias peaks (Fig. 2a, b) localized over the bright sites (spectra 1–4, and 6–8), and vanishing rapidly in neighbor rings (spectra 5, 9, and 10). These are generally ascribed as Abrikosov–Suhl resonances due to the Kondo effect, and named as Kondo resonances^{21,22}. Their observation is a proof of a localized magnetic moment screened by conduction electrons^{27,28} (see Supplementary Note 3). The relationship between the observed peaks and the Kondo effect is proven by measurements of dI/dV spectra at different temperatures (Fig. 2c) and magnetic fields (Fig. 2d). The resonance line width increases with temperature following the characteristic behavior of a Kondo-screened state with a Kondo temperature $T_K \sim 6$ K^{28,29} (Fig. 2c), and broadens with magnetic field as expected for a spin-1/2

2 system (Fig. 2d). Hence, the bright regions are caused by the localization of a single magnetic moment.

Junctions with two bright regions (Type 3) show different low-energy features: two peaked steps in dI/dV spectra at $\sim \pm 10$ meV (Fig. 2e). The steps appear always symmetric with respect to zero bias, and at the same energy over the terminal ZZ segment and over the PC region for a given nanostructure, while vanish quickly away from these sites. Based on the existence of localized spins on bright areas of Type 1 and 2 junctions, we attribute such bias-symmetric peaked steps to the excitation of two exchange coupled spins localized at each junction site by tunneling electrons. The exchange interaction tends to freeze their relative orientation, in this case antiferromagnetically into a singlet ground state. Electrons tunneling into the coupled spin system can inelastically excite a spin reversal in any of them when their energy equals the exchange coupling energy between the spins, i.e., $eV \geq J$. Usually, such singlet–triplet inelastic excitation is revealed in dI/dV spectra as steps at the onset of spin excitations³⁰, from which one can directly determine the strength of the exchange coupling J between the spins. Here, the inelastic spectra additionally show asymmetric peaks on top of the excitation onsets, with a pronounced logarithmic fall off for biases above. Such peaked steps are characteristic of Kondo-like fluctuations of the spin once the anisotropy energy has been overcome by tunneling electrons (i.e. out of equilibrium)^{31–34}. The more pronounced signal for either particle tunneling (over

ZZ) or for hole tunneling (over PC) indicates the spins system lies out of particle-hole symmetry point, with E_F closer to the corresponding singly unoccupied or singly occupied (SO) state, respectively. Hence, the gap between dI/dV peaks in Fig. 2e is a measure of the interaction strength between the two localized spins.

Interestingly, the spectral gap in Type 3 junctions increases with the length of the connecting ribbons. In Fig. 2f we compare low-energy spectra of two junctions with different chGNR lengths. Although the atomic structures of both junctions are identical, the one with shorter ribbons (upper curve; 9 and 2 precursor units) displays a smaller gap than the junction of longer chGNRs (lower curve; >8 and 7 units). Fitting the spectra with a model of two coupled spin-1/2 systems³¹, one obtains the exchange coupling $J = 2.7$ (9.9) meV for the upper (lower) spectrum.

Theory simulations to uncover the origin of spin polarization.

To explain the emergence of localized spins, we simulated the spin-polarized electronic structure of chGNR junctions using both density functional theory (DFT) and mean-field Hubbard (MFH) models (see Supplementary Notes 6 and 7). Figure 3a shows the spin-polarization of a junction of Fig. 1d. The ground state exhibits a net spin localization at the ZZ and PC regions with opposite sign, which is absent in the bare ribbons. The spin distribution along the edge sites reproduces the distribution of dI/dV signal measured in Type 3 junctions. This supports that this signal is an intrinsic effect of junction edge sites, rather than caused by defects or other atomic species.

The origin of the spontaneous magnetization can be rationalized by considering the effect of Coulomb correlations between

π -electrons as described within a tight-binding (TB) model (Fig. 3b). The spin distribution is related to the appearance of two junction states inside the gap of the (3,1)-chGNR electronic bands, localized at the PC and ZZ sites, respectively (Fig. 3c). These are split-off states from the VB of the (3,1)-chGNR, which lies close below E_F ²⁵. In the absence of electron–electron correlations, these two states conform the highest occupied (HO) and lowest unoccupied (LU) molecular states of the nanostructure. Due to the large degree of localization (Supplementary Figs. 10 and 11), the Coulomb repulsion energy U_{HH} between two electrons in the HO state becomes comparable with the energy difference δ between the two localized levels. Hence, in a simplified picture, the two electrons find a lower-energy configuration by occupying each a different, spatially separated in-gap state. These two states become SO, spin-polarized (i.e., they have a net magnetic moment), and exchange coupled as schematically illustrated in Fig. 3b. Similar conclusions regarding the emergence of radical states at PC and ZZ sites can also be reached by applying the empirical Clar’s aromatic π -sextet rule to the close-shell structure of Fig. 1d, as described in the Supplementary Note 4.

According to both DFT (Fig. 3a) and MFH (Supplementary Fig. 14) the magnetic moments are antiferromagnetically aligned into a singlet ground state. Therefore, the inelastic features in dI/dV spectra found over Type 3 junctions (Fig. 2e) are associated to singlet–triplet excitations induced by tunneling electrons. In fact, the smaller excitation energy found for the smaller ribbons in both theory and experiment (Supplementary Note 8) agrees with a weaker exchange interaction due to a larger localization of the spin-polarized states. Alternative scenarios for peaks around E_F , such as single-particle states or Coulomb-split radical states⁶, would show the opposite trend with the system size.

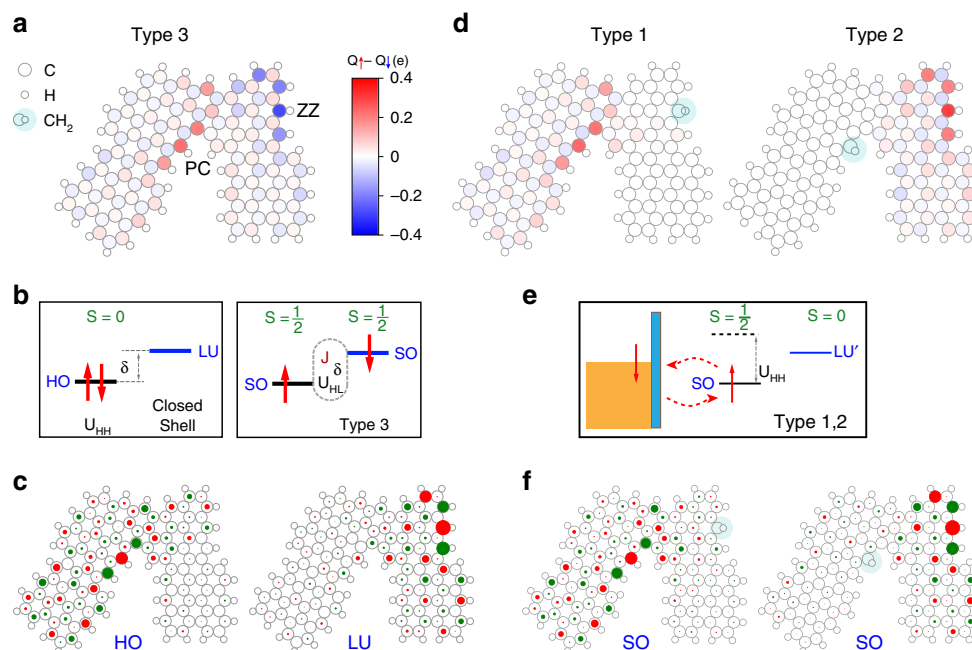


Fig. 3 Calculated electronic states and spin polarization. **a** Spin polarization obtained from DFT simulations in a Mulliken population analysis. The standard junction (all peripheral carbons bonded to H) shows spontaneous spin localization in both PC and ZZ regions, revealing the apparition of radical states. **b** Schema of the spontaneous spin polarization when one of the two electrons in the HO level gets promoted to the LU level to form two separated, exchange coupled spin-1/2 systems (Type 3 junction). This process is energetically favored when the reduction in Coulomb energy $U_{HH} - U_{HL}$ plus exchange energy J exceeds the level separation δ , i.e., $\delta + U_{HL} - J < U_{HH}$. **c** Single-particle TB wave functions (HO/LU) for Type 3 junction. **d** Same as in **a** but now adding a H atom to an external carbon in either the ZZ (Type 1) or PC (Type 2). The passivation with H removes the corresponding radical state and, hence, its spin-polarization. **e** Sketch of the spin-1/2 Kondo state generated with a single radical (Type 1 and 2 junctions). **f** Single-particle TB wave functions (SO) for Type 1 and Type 2 junctions. Red-green colors represent the positive-negative phase

The observation of spin localization in only one of the two radical regions in Type 1 and 2 junctions implies that one of the two edge magnetic moments has vanished. Foreign atoms bonding to a $SO p_z$ orbital remove the local spin and suppress the magnetic signal at this site. Metal atoms can bind to C-sites, but the interaction is too weak to bind to π -radicals over a metal substrate³⁵. Instead, H-passivation of radical sites is a highly probable process occurring on the surface due to the large amount of hydrogen available during the reaction³⁶. DFT simulations show that attaching an extra H atom into an edge carbon in either the ZZ or PC sites leads to its sp^3 hybridization

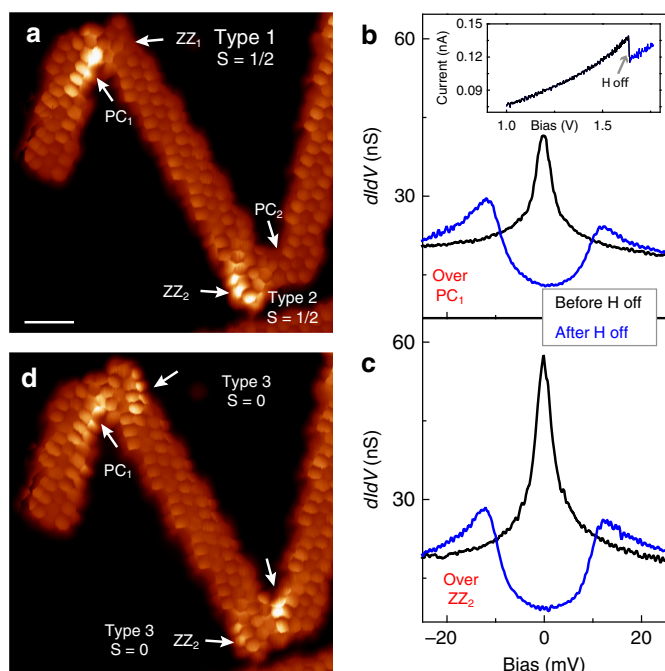


Fig. 4 Spin manipulation by electron-induced removal of extra H-atoms. **a** Constant-height current image of two junctions with extra H atoms ($V = 8$ mV) (scale bar 1 nm). **b, c** dI/dV spectra taken over PC_1 and ZZ_2 regions (indicated in **a**) before (black) and after (blue) the dehydrogenation processes. Inset in **b** shows the current during the process of dehydrogenation. **d** Image with same conditions as in **a** after the electron-induced removal of the extra H-atoms. The dehydrogenation processes were done over the ZZ_1 and PC_2 sites

and the removal of a p_z orbital from the aromatic backbone. This completely quenches the magnetic moment of the passivated region (Fig. 3d), and leaves the junction with a single electron localized at the opposite radical site (Fig. 3e and Supplementary Fig. 7). According to this, a Type 1 junction shows Kondo at the PC site because it has a H atom bonded to the ZZ site that quenches that magnetic moment, and opposite for Type 2. The computed wave function amplitude distributions for the two energetically most favorable adsorption sites (Fig. 3f) are also in excellent agreement with the extension of the Kondo resonance mapped in Fig. 2a, b.

Manipulation of the spin state of the nanostructures. The presence of extra H atoms in Type 1 and 2 junctions was confirmed by electron induced H-atom removal experiments. Figure 4a shows a structure formed by three chGNRs connected via Type 1 and 2 junctions. Accordingly, their dI/dV spectra (black curves in Fig. 4b, c) show a Kondo resonance at the PC_1 and ZZ_2 regions. We placed the STM tip on top of the opposite sites, ZZ_1 and PC_2 , and raised the positive sample bias well above 1 V. A step-wise decrease of the tunneling current indicated the removal of the extra H atom (inset in Fig. 4b). The resulting junction appeared with double bright regions in low-bias images (Fig. 4d), and the PC_1 and ZZ_2 spectra turned into dI/dV steps characteristic of Type 3 junctions (blue curves in Fig. 4b, c). Thus, the removal of H atoms activated the magnetic moment of the initially unpolarized ZZ_1 and PC_2 sites, converting Type 1 and 2 junctions into Type 3, and switching the total spin of the junction from spin to zero.

Contacting the junctions with the STM tip. The magnetic state of the junction was also changed by creating a contact between the STM tip apex and a radical site. π -radicals show some weak reactivity to bond metallic atoms, that allows their manipulation with an STM tip³⁷. In the experiments shown in Fig. 5a, the STM tip was approached to the ZZ sites of a Type 3 junction. A step in the conductance-distance plot (Fig. 5b) indicated the formation of a contact. The created tip-chGNR contact could be stretched up to 3 Å before breaking (retraction step in Fig. 5b), signaling that a chemical bond was formed.

A reference dI/dV spectrum recorded before the bond formation (black point in Fig. 5c) shows the split-peak feature of Type 3 junctions (black spectrum in Fig. 5c). After the bond formation (blue and red points in Fig. 5b), the spectra changed to show Kondo resonances (blue and red spectra in Fig. 5c), persisting during contact retraction until the bond-breaking step,

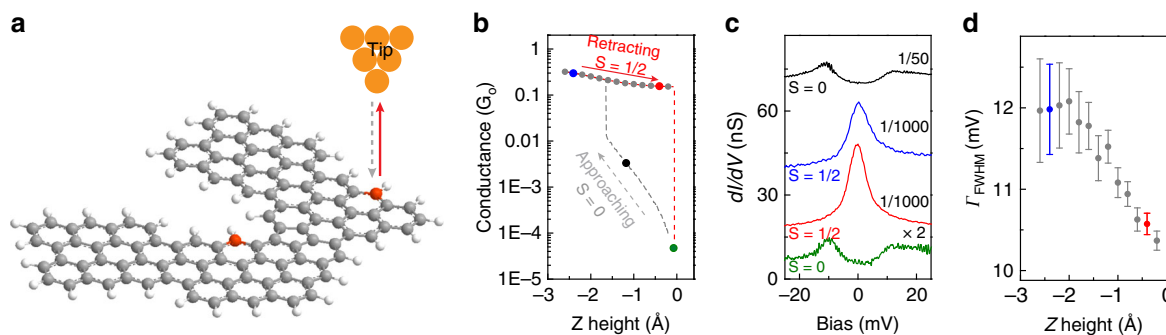


Fig. 5 Kondo effect from the spin embedded in a lifted chGNR junction. **a** Schematics of the process where the tip of the STM is first approached to the ZZ site of a Type 3 junction (gray dashed arrow) and then retracted to lift the junction away from the substrate (red arrow), resulting in a suspended junction between tip and substrate. **b** Simultaneously recorded conductance curve ($V = -50$ mV) during the approach, jump to contact and lift processes. **c** dI/dV spectra recorded at the specific heights indicated with colored points on the curves in **b**. **d** Full widths at half maximum (FWHM) of spectra acquired in the retraction process (points in **c**), extracted from a fit using the Frota function⁴⁹

where double-peak features are recovered (green spectrum in Fig. 5c). The formation of a tip–chGNR bond thus removed the spin of the ZZ site, and the transport spectra reflect the Kondo effect due to the remaining spin embedded in the junction. If the STM tip contacts instead the ZZ radical site of a Type 2 junction (shown in Supplementary Note 5) the initial Kondo resonance disappears from the spectra, signaling the complete demagnetization of the junction. The width of the Kondo resonance in the contacted junctions (blue and red plots in Fig. 5c) is significantly larger than in Type 1 and 2 cases, probably because it incorporates scattering with tip states^{38,39}, and monotonously narrows as the contact is pulled apart (Fig. 5d). The survival of the Kondo effect in the contacted Type 3 junctions is a remarkable outcome of our experiments, which demonstrate the electrical addressability of localized magnetic moments in graphene nanostructure devices.

Discussion

Open shell configurations of extended π systems can be stabilized on-top of insulating layers^{35,40}. The results presented here prove that the intrinsic open-shell character of a graphene nanostructure can survive on the surface of a metal. This is remarkable because it proves that key electron–electron correlations needed for the stabilization of magnetic ground states persist on the metal, in spite of the ubiquitous charge screening by the underlying substrate⁴¹. In addition, the adsorption on the Au(111) substrate has the general trend of hole-doping GNRs^{42,43}, which in some systems caused depopulation of the mid-gap states³⁷. The band structure of the (3,1) chGNR and, in particular, the proximity of the VB to E_{F} , is a crucial aspect to stabilize the electron population of the GNR junction on the surface and hence, for the survival of their magnetic ground state.

Methods

Sample preparation and experimental details. The experiments were performed on two different STMs operating in ultra-high vacuum. A commercial JT STM (from specs) operated at 1.2 K with a magnetic field up to 3 T was used to measure the temperature and magnetic field dependence of the Kondo resonance, while other experiments were done with a home made STM operating at 5 K. Both setups allow in situ sample preparation and transfer into the STM. The Au(111) substrate was cleaned in UHV by repeated cycles of Ne^+ ion sputtering and subsequent annealing to 730 K. The molecular precursor (2,2'-dibromo-9,9'-bianthracene) was sublimated at 170 °C from a Knudsen cell onto the clean Au(111) substrate kept at room temperature. Then the sample was first annealed at 200 °C for 15 min in order to induce the polymerization of the molecular precursors by Ullmann coupling, then the sample was annealed at 250 °C for 5 min to trigger the cyclodehydrogenation to form chiral graphene nanoribbons (chGNRs). A last step annealing at 350 °C for 1 min created nanostructure junctions. A tungsten tip functionalized with a CO molecule was used for high-resolution images. All the images in the manuscript were acquired in constant height mode, at very small voltages, and junction resistances of typically 20 M Ω . The dI/dV signal was recorded using a lock-in amplifier with a bias modulation of $V_{\text{rms}} = 0.1$ mV (Fig. 2d, e) and $V_{\text{rms}} = 0.4$ mV at 760 Hz.

Simulations. We performed calculations with the SIESTA implementation⁴⁴ of DFT. Exchange and correlation (XC) were included within either the local (spin) density approximation (LDA)⁴⁵ or the generalized gradient approximation (GGA)⁴⁶. We used a 400 Ry cutoff for the real-space grid integrations and a double-zeta plus polarization (DZP) basis set generated with an 0.02 Ry energy shift for the cutoff radii. The molecules, represented with periodic unit cells, were separated by a vacuum of at least 10 Å in any direction. The electronic density was converged to a stringent criterion of 10^5 . The force tolerance was set to 0.002 eV/Å. To complement the DFT simulations described above we also performed simulations based on the MFH model, known to provide a good description for carbon π -electron systems^{7,8,15,16,47,48}.

Data availability

The data that support the findings of this study are available from the corresponding author upon reasonable request.

Received: 19 July 2018 Accepted: 11 December 2018

Published online: 14 January 2019

References

- Han, W., Kawakami, R. K., Gmitra, M. & Fabian, J. Graphene spintronics. *Nat. Nanotechnol.* **9**, 794–807 (2014).
- Lieb, E. H. Two theorems on the Hubbard model. *Phys. Rev. Lett.* **62**, 1201 (1989).
- Yazyev, O. V. & Helm, L. Defect-induced magnetism in graphene. *Phys. Rev. B* **75**, 125408 (2007).
- Nair, R. R. et al. Spin-half paramagnetism in graphene induced by point defects. *Nat. Phys.* **8**, 199–202 (2012).
- McCreary, K. M., Swartz, A. G., Han, W., Fabian, J. & Kawakami, R. K. Magnetic moment formation in graphene detected by scattering of pure spin currents. *Phys. Rev. Lett.* **109**, 186604 (2012).
- Gonzalez-Herrero, H. et al. Atomic-scale control of graphene magnetism by using hydrogen atoms. *Science* **352**, 437–441 (2016).
- Fernández-Rossier, J. & Palacios, J. J. Magnetism in graphene nanoislands. *Phys. Rev. Lett.* **99**, 177204 (2007).
- Yazyev, O. V. Emergence of magnetism in graphene materials and nanostructures. *Rep. Prog. Phys.* **73**, 056501 (2010).
- Alexandre, S. S., Lúcio, A. D., Castro Neto, A. H. & Nunes, R. W. Correlated magnetic states in extended one-dimensional defects in graphene. *Nano Lett.* **12**, 5097–5102 (2012).
- Ortiz, R., Lado, J. L., Melle-Franco, M. & Fernández-Rossier, J. Engineering spin exchange in nonbipartite graphene zigzag edges. *Phys. Rev. B* **94**, 094414 (2016).
- Morita, Y., Suzuki, S., Sato, K. & Takui, T. Synthetic organic spin chemistry for structurally well-defined open-shell graphene fragments. *Nat. Chem.* **3**, 197–204 (2011).
- Son, Y.-W., Cohen, M. L. & Louie, S. G. Half-metallic graphene nanoribbons. *Nature* **444**, 347–350 (2006).
- Tao, C. et al. Spatially resolving spin-split edge states of chiral graphene nanoribbons. *Nat. Phys.* **7**, 616–620 (2011).
- Ruffieux, P. et al. On-surface synthesis of graphene nanoribbons with zigzag edge topology. *Nature* **531**, 489–492 (2016).
- Yazyev, O. V., Capaz, R. B. & Louie, S. G. Theory of magnetic edge states in chiral graphene nanoribbons. *Phys. Rev. B* **84**, 115406 (2011).
- Carvalho, A. R., Warnes, J. H. & Lewenkopf, C. H. Edge magnetization and local density of states in chiral graphene nanoribbons. *Phys. Rev. B* **89**, 245444 (2014).
- Sepioni, M. et al. Limits on intrinsic magnetism in graphene. *Phys. Rev. Lett.* **105**, 207205 (2010).
- Nair, R. R. et al. Dual origin of defect magnetism in graphene and its reversible switching by molecular doping. *Nat. Commun.* **4**, 2010 (2013).
- Li, J. et al. Survival of spin state in magnetic porphyrins contacted by graphene nanoribbons. *Sci. Adv.* **4**, eaaq0582 (2018).
- Červenka, J., Katsnelson, M. I. & Flipse, C. F. J. Room-temperature ferromagnetism in graphite driven by two-dimensional networks of pointdefects. *Nat. Phys.* **5**, 840–844 (2009).
- Kondo, J. Resistance minimum in dilute magnetic alloys. *Prog. Theor. Phys.* **32**, 37–49 (1964).
- Ternes, M., Heinrich, A. J. & Schneider, W.-D. Spectroscopic manifestations of the Kondo effect on single adatoms. *J. Phys. Condens. Matter* **21**, 053001 (2009).
- Dienel, T. et al. Resolving atomic connectivity in graphene nanostructure junctions. *Nano Lett.* **15**, 5185–5190 (2015).
- de Oteyza, D. G. et al. Substrate-independent growth of atomically precise chiral graphene nanoribbons. *ACS Nano* **10**, 9000–9008 (2016).
- Merino-Diez, N. et al. Unraveling the electronic structure of narrow atomically precise chiral graphene nanoribbons. *J. Phys. Chem. Lett.* **9**, 25–30 (2018).
- Shiotari, A. et al. Strain-induced skeletal rearrangement of a polycyclic aromatic hydrocarbon on a copper surface. *Nat. Commun.* **8**, 16089 (2017).
- Fernández-Torrente, I., Franke, K. J. & Pascual, J. I. Vibrational Kondo effect in pure organic charge-transfer assemblies. *Phys. Rev. Lett.* **101**, 217203 (2008).
- Zhang, Y.-h et al. Temperature and magnetic field dependence of a kondo system in the weak coupling regime. *Nat. Commun.* **4**, 2110 (2013).
- Nagaoka, K., Jamneala, T., Grobis, M. & Crommie, M. F. Temperature dependence of a single Kondo impurity. *Phys. Rev. Lett.* **88**, 77205 (2002).
- Hirjibehedin, C. F., Lutz, C. P. & Heinrich, A. J. Spin coupling in engineered atomic structures. *Science* **312**, 1021–1024 (2006).
- Ternes, M. Spin excitations and correlations in scanning tunneling spectroscopy. *New J. Phys.* **17**, 63016 (2015).
- Heersche, H. B. et al. Kondo effect in the presence of magnetic impurities. *Phys. Rev. Lett.* **96**, 017205 (2006).

33. Paaske, J. et al. Non-equilibrium singlet-triplet kondo effect in carbon nanotubes. *Nat. Phys.* **2**, 460–464 (2006).
34. Ortiz, R., García-Martínez, N. A., Lado, J. L. & Fernández-Rossier, J. Electrical spin manipulation in graphene nanostructures. *Phys. Rev. B* **97**, 195425 (2018).
35. Pavliček, N. et al. Synthesis and characterization of triangule. *Nat. Nanotechnol.* **12**, 308–311 (2017).
36. Talirz, L. et al. Termini of bottom-up fabricated graphene nanoribbons. *J. Am. Chem. Soc.* **135**, 2060–2063 (2013).
37. Koch, M., Ample, F., Joachim, C. & Grill, L. Voltage-dependent conductance of a single graphene nanoribbon. *Nat. Nanotechnol.* **7**, 713–717 (2012).
38. Jasper-Tönnies, T. et al. Conductance of a freestanding conjugated molecular wire. *Phys. Rev. Lett.* **119**, 066801 (2017).
39. Choi, D.-J., Abufager, P., Limot, L. & Lorente, N. From tunneling to contact in a magnetic atom: the non-equilibrium kondo effect. *J. Chem. Phys.* **146**, 092309 (2017).
40. Wang, S. et al. Giant edge state splitting at atomically precise graphene zigzag edges. *Nat. Commun.* **7**, 11507 (2016).
41. Li, Y., Zhang, W., Morgenstern, M. & Mazzarello, R. Electronic and magnetic properties of zigzag graphene nanoribbons on the (111) surface of Cu, Ag, and Au. *Phys. Rev. Lett.* **110**, 216804 (2013).
42. Ruffieux, P. et al. Electronic structure of atomically precise graphene nanoribbons. *ACS Nano* **6**, 6930–6935 (2012).
43. Merino-Díez, N. et al. Width-dependent band gap in armchair graphene nanoribbons reveals Fermi level pinning on Au(111). *ACS Nano* **11**, 11661–11668 (2017).
44. Soler, J. M. et al. The siesta method for ab initio order-n materials simulation. *J. Phys. Condens. Matter* **14**, 2745–2779 (2002).
45. Ceperley, D. M. & Alder, B. J. Ground state of the electron gas by a stochastic method. *Phys. Rev. Lett.* **45**, 566–569 (1980).
46. Perdew, J. P., Burke, K. & Ernzerhof, M. Generalized gradient approximation made simple. *Phys. Rev. Lett.* **77**, 3865–3868 (1996).
47. Hancock, Y., Uppstu, A., Saloritta, K., Harju, A. & Puska, M. J. Generalized tight-binding transport model for graphene nanoribbon-based systems. *Phys. Rev. B* **81**, 245402 (2010).
48. Papior, N. R. sisl: v0.9. 2. <https://doi.org/10.5281/zenodo.597181> (2018).
49. Frota, H. O. Shape of the Kondo resonance. *Phys. Rev. B* **45**, 1096–1099 (1992).

Acknowledgements

We thank Manuel Vilas-Varela for the synthesis of the chGNR molecular precursor. We are indebted to Carmen Rubio, Dimas G. de Oteyza, Nestor Merino, Nicolás Lorente,

Aran García Lekue, and Daniel Sánchez Portal for fruitful discussions. We acknowledge financial support from Spanish AEI (MAT2016-78293-C6, FIS2017-83780-P, and the Maria de Maeztu Units of Excellence Program MDM-2016-0618), the Basque Government (Department of Education, Grant PI-2015-1-42), the EU project PAMS (610446), the Xunta de Galicia (Centro singular de investigación de Galicia accreditation 2016-2019, ED431G/09), and the European Regional Development Fund (ERDF).

Author contributions

J.L. and J.I.P. devised the experiment. D.P. designed the chGNR molecular precursor. J.L. realized the experiments. M.C. and D.J.C. assisted J.L. in part of the measurements, S.S. and T.F. did the theoretical simulations. All the authors discussed the results. J.L., T.F., and J.I.P. wrote the manuscript.

Additional information

Supplementary Information accompanies this paper at <https://doi.org/10.1038/s41467-018-08060-6>.

Competing interests: The authors declare no competing interests.

Reprints and permission information is available online at <http://npg.nature.com/reprintsandpermissions/>

Publisher's note: Springer Nature remains neutral with regard to jurisdictional claims in published maps and institutional affiliations.



Open Access This article is licensed under a Creative Commons Attribution 4.0 International License, which permits use, sharing, adaptation, distribution and reproduction in any medium or format, as long as you give appropriate credit to the original author(s) and the source, provide a link to the Creative Commons license, and indicate if changes were made. The images or other third party material in this article are included in the article's Creative Commons license, unless indicated otherwise in a credit line to the material. If material is not included in the article's Creative Commons license and your intended use is not permitted by statutory regulation or exceeds the permitted use, you will need to obtain permission directly from the copyright holder. To view a copy of this license, visit <http://creativecommons.org/licenses/by/4.0/>.

© The Author(s) 2019

II

Uncovering the triplet ground state of triangular graphene nanoflakes engineered with atomic precision on a metal surface, *Phys. Rev. Lett.* **124**, 177201 (2020)

Uncovering the Triplet Ground State of Triangular Graphene Nanoflakes Engineered with Atomic Precision on a Metal Surface

Jingcheng Li¹, Sofia Sanz², Jesus Castro-Esteban,³ Manuel Vilas-Varela,³ Niklas Friedrich¹,


Thomas Frederiksen^{2,4,*}, Diego Peña,^{3,†} and Jose Ignacio Pascual^{1,4,‡}

¹*CIC Nanogune BRTA, 20018 Donostia-San Sebastián, Spain*

²*Donostia International Physics Center (DIPC), 20018 Donostia-San Sebastián, Spain*

³*Centro Singular de Investigación en Química Biolóxica e Materiais Moleculares (CiQUS), and Departamento de Química Orgánica, Universidade de Santiago de Compostela, 15705 Santiago de Compostela, Spain*

⁴*Ikerbasque, Basque Foundation for Science, 48013 Bilbao, Spain*

 (Received 16 October 2019; revised manuscript received 17 February 2020; accepted 2 April 2020; published 27 April 2020)

Graphene can develop large magnetic moments in custom-crafted open-shell nanostructures such as triangulene, a triangular piece of graphene with zigzag edges. Current methods of engineering graphene nanosystems on surfaces succeeded in producing atomically precise open-shell structures, but demonstration of their net spin remains elusive to date. Here, we fabricate triangulene-like graphene systems and demonstrate that they possess a spin $S = 1$ ground state. Scanning tunneling spectroscopy identifies the fingerprint of an underscreened $S = 1$ Kondo state on these flakes at low temperatures, signaling the dominant ferromagnetic interactions between two spins. Combined with simulations based on the meanfield Hubbard model, we show that this $S = 1$ π paramagnetism is robust and can be turned into an $S = 1/2$ state by additional H atoms attached to the radical sites. Our results demonstrate that π paramagnetism of high-spin graphene flakes can survive on surfaces, opening the door to study the quantum behavior of interacting π spins in graphene systems.

DOI: 10.1103/PhysRevLett.124.177201

In spite of their apparent simplicity, custom-crafted graphene nanoflakes (GNFs) are predicted to exhibit complex magnetic phenomenology [1] with promising possibilities as active components of a new generation of nanoscale devices [2–4]. As predicted by Lieb’s theorem for bipartite lattices [5], certain shapes of graphene structures may accommodate a spin imbalance in the π electron cloud, resulting in GNFs with a net magnetic moment. Graphene π paramagnetism is more delocalized, mobile, and isotropic than conventional magnetism from d or f states [6] and can be electrically addressed [7,8]. Furthermore, the magnetic moments and their correlations in GNFs can be precisely engineered through their sizes, edge topology, or chemical doping [9–12].

The fabrication of such GNFs has been hindered due to their high reactivity [13]. Because they are open-shell structures, the presence of unpaired electrons (radicals) makes the synthesis difficult. Initially, unsubstituted triangulene was synthesized by dehydrogenating precursor molecules with the tip of a scanning tunneling microscope (STM) [14]. Very recently, triangular GNFs with larger sizes have been synthesized through an on-surface synthetic (OSS) approach [15–17], a strategy for fabricating atomically precise graphene flakes on a metallic surface [18–21]. Despite such progress in fabrication, the magnetic properties of triangular GNFs on a surface have not been demonstrated experimentally.

Here we report the OSS fabrication of triangulene-like GNFs and demonstrate that the GNFs have a triplet ground state. The synthesized GNFs have reduced symmetry compared to triangulene, which increases the localization of the magnetic moments. High-resolution STM images and spectroscopy allow us to identify the two spin centers on the GNFs and map their distribution. Their ferromagnetic correlations are characterized by the spin-1 Kondo effect [22–24], which happens due to the incomplete screening of two coupled spins by conducting electrons of the metal substrate. Our results also show that the strength of correlations between spins depends on the distance between them.

Figure 1(a) shows the chemical structures of the GNF characterized in the experiments, named here extended triangulene (ETRI). This GNF has 19 carbon atoms in one sublattice (highlighted by red circles) and 17 carbon atoms in the other (black circles), which results in a total spin $S = 1$ according to Lieb’s theorem [5]. For comparison, we also produced the GNF in Fig. 1(b) [named as double triangulene (DTRI)], which has 22 carbon atoms in both sublattices and thus a spin $S = 0$ ground state. We synthesized these GNFs by depositing the respective molecular precursors, shown in Figs. 1(c) and 1(d) [details in Supplemental Material (SM) [25]], on a Au(111) surface at 330 °C. The hot surface activates a simultaneous debromination and cyclodehydrogenation step that planarizes them into their final structures.

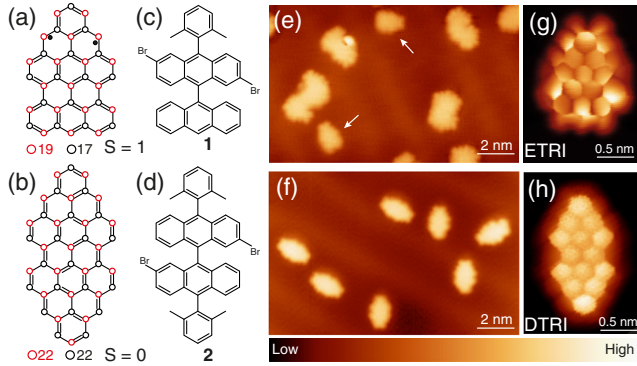


FIG. 1. Chemical structures and synthetic route of extended triangulene and double triangulene. (a), (b) Atomic structures of ETRI and DTRI, which have spin 1 and 0, respectively. Red (black) open circles denote carbon atoms that belong to different sublattices, with the total number of carbon atoms indicated under the structures. (c), (d) Molecular precursors 2,6-dibromo-10-(2,6-dimethylphenyl)-9,9'-bianthracene (precursor 1) and 2,2'-dibromo-10,10'-bis(2,6-dimethylphenyl)-9,9'-bianthracene (precursor 2) used to synthesize ETRI and DTRI, respectively. (e), (f) STM overview images ($V = 0.3$ V, $I = 0.1$ nA) of the formed GNFs from precursors 1 and 2, respectively. The arrows in (e) indicate the ETRI monomers created. (g), (h) Constant height current images ($V = 2$ mV) of ETRI and DTRI with a CO-terminated tip.

Low-temperature STM overview images of the Au (111) surface after deposition of precursors 1 and 2 are shown in Figs. 1(e) and 1(f), respectively. While the reacted precursor 1, ETRI, appears on the surface mostly as monomers and dimers in a ratio of approximately 1:7, nearly all deposited precursors 2, DTRI, remain as monomer species. In every case, the monomers adopt a planar configuration, as expected for the structures in Figs. 1(a) and 1(b). Furthermore, high-resolution STM current images using a CO-terminated tip [34,35] [Figs. 1(g) and 1(h)] reproduce the chemical bond structures of Figs. 1(a) and 1(b), indicating the successful synthesis of ETRI and DTRI. It is worth noting that the current image of DTRI shows merely the backbone structure, as also observed in similar symmetric systems [36], while the current image of ETRI shows additional bright features at the edges. Considering that these images were recorded at 2 mV, the bright features surrounding the backbone structure indicate an enhancement of the local density of states (LDOS) close to Fermi level for the ETRI molecule.

The different shape in the images is better manifested in differential conductance (dI/dV) spectra measured on both types of GNFs [Fig. 2(a)]. The spectrum on ETRI shows a pronounced and narrow (FWHM ~ 1 meV) dI/dV peak centered at zero bias. The zero-bias peak broadens anomalously fast with temperature [as described in Fig. 2(b)] and splits with magnetic fields [Fig. 2(c)], demonstrating that it is a manifestation of the Kondo effect [37]. A (zero-bias) Kondo-derived resonance reflects the screening of a local

spin by conduction electrons [38] and, hence, is a direct proof of the presence of localized magnetic moments on ETRI even when it lies on a metal surface. On the contrary, the spectra taken on DTRI are featureless. Furthermore, both wide-bias range spectra and dI/dV maps reveal their closed-shell ground state (see SM [25]).

The temperature and magnetic field dependence of the Kondo resonances provide further insight on the nature of the spin state of ETRI. Although the Kondo effect is frequently described on $S = 1/2$ systems, it also occurs for higher spin configurations [23,24]. For $S = 1$, a zero-bias resonance reflects a partly screened spin, i.e., with only one interaction channel with the substrate [42]. Similar to the spin-1/2 case, the resonance broadens with temperature [with a Kondo temperature $T_K \sim 6$ K, after Fig. 2(b); see SM [25]] but shows a larger sensitivity to the magnetic field [23,24]. While the Kondo resonance of a $S = 1/2$ system in the strong coupling regime ($T < T_K$) splits linearly with magnetic fields only above a critical field $B_c \geq 0.5k_B T_K / g\mu_b$ [7,43], an underscreened $S = 1$ conserves some magnetic moment, and its zero-bias resonance splits already with $B > 0$ [23,24]. In tunneling spectra, such a peak split should become visible as soon as the Zeeman energy is greater than the thermal broadening ($k_B T$), which, at the 1.2 K of our experimental set up corresponds to fields above 1 Tesla. If the Kondo resonance in Fig. 2(b) were caused by an $S = 1/2$ state, it should appear split in the spectra only for magnetic fields above 3.5 T. However, the peak appears split already at $B = 1.5$ T, proving that the ETRI molecule has an $S = 1$ in an underscreened Kondo state on the gold substrate [25].

The $S = 1$ configuration of the triangular GNFs was further supported by tip-induced manipulation experiments. Because of their biradical character, the zigzag sites show some reactivity and are frequently found passivated by hydrogen atoms produced during the OSS reactions [7,44]. The passivated carbon sites can be identified in high-resolution images by their larger bond length [45] due to the change from sp^2 to sp^3 hybridization. The STM image in Fig. 3(a) shows the bare backbone structure of an ETRI molecule with its characteristic bright features missing due to two additional H atoms passivating the zigzag sites, with its chemical structure shown in Fig. 3(b). The corresponding dI/dV spectrum is featureless around zero bias [black curve in Fig. 3(g)], explaining the absence of bright features in the STM image.

We first cut off one of the passivated H atoms by placing the STM tip on top of site no. 1 in Fig. 3(a) and ramping up the sample bias above 1.5 V [7,44]. The H removal was monitored by a sudden step in the tunneling current [7]. The STM image afterwards appeared with an enhanced LDOS signal around the no. 1 site [Fig. 3(c)], and the dI/dV spectrum on site no. 1 presented a pronounced zero-energy peak [red Fig. 3(g)]. We identify this as $S = 1/2$

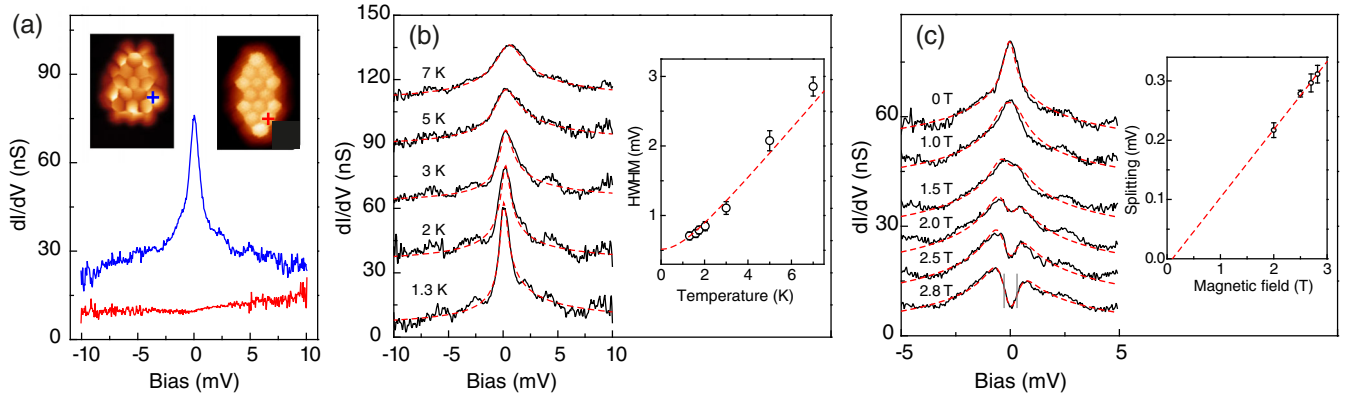


FIG. 2. Kondo resonances in extended triangulene. (a) dI/dV spectra of ETRI (blue curve) and DTRI (red curve) measured at the sites indicated by the colored crosses in the inset. (b) Temperature dependence of the Kondo resonance for an ETRI molecule. The inset plots the half width at half maximum (HWHM) at each temperature, extracted by fitting a Frota function (red dashed lines) [39] and corrected for the thermal broadening of the tip [40]. The plot includes the empirical expression $\sqrt{(\alpha k_B T)^2 + (2k_B T_K)^2}$ [41], fitting the results with $T_K \sim 6$ K and $\alpha = 8.5$. The temperature evolution of the zero-bias conductance, shown as SM [25], agrees with a spin-polarized state in the Kondo regime with energy scale of a few Kelvin. (c) Magnetic field dependence of the Kondo resonance with the field strength indicated in the figure, measured at $T = 1.3$ K. The red dashed lines show the simulated curves using a model for a spin-1 system using the code of Ref. [38]. The inset shows the dependence of Zeeman splitting of the Kondo resonance with magnetic fields, determined from the bias position of steepest slope (indicated on the spectrum at 2.8 T). The dashed line fits the Zeeman splitting with a g factor of 1.98 ± 0.07 . The spectra in (b), (c) are shifted vertically for clarity.

Kondo resonance [7] resulting from the single radical state recovered by the removal of the extra H atom at site no. 1 [Fig. 3(d)]. Following a similar process to cleave the second H-CH bond at site no. 2 recovered bright current features all around the ETRI backbone, resembling the shape of the reference biradical structure of Fig. 1(g). The spectrum

measured again over site no. 1 now shows the Kondo resonance with smaller amplitude and linewidth similar to the one in Fig. 2(a), agreeing with its underscreened $S = 1$ state. As quantified in Fig. 3(h), the Kondo resonance of the doubly dehydrogenated GNFs appeared repetitively with a linewidth of about $\text{HWHM} \sim 0.7$ meV, significantly smaller

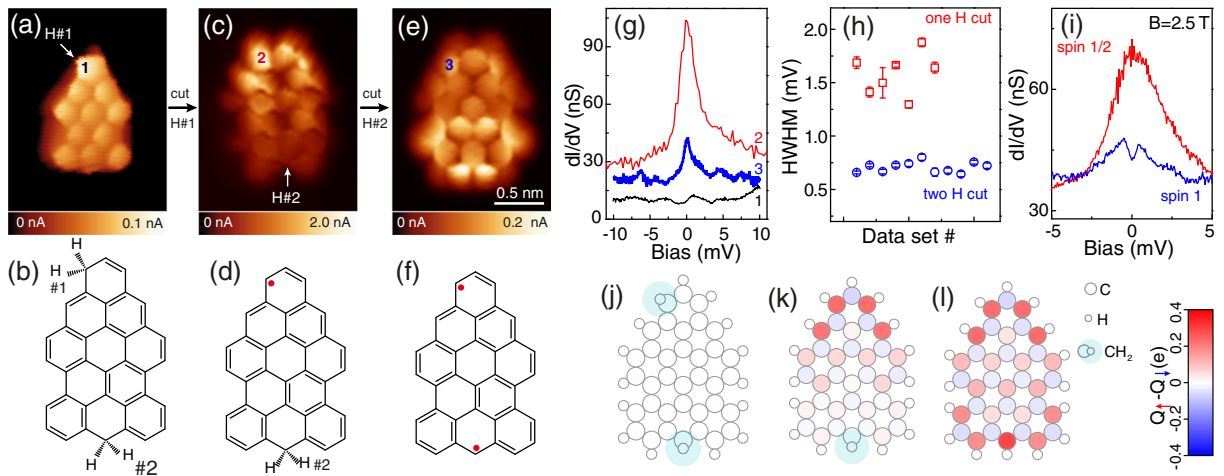


FIG. 3. Spin manipulation by electron-induced removal of extra H atoms. (a) Constant height current image ($V = 2$ mV) of a 2H-ETRI, with its chemical structure shown in (b). (c), (e) Constant height current image ($V = 2$ mV) of the same ETRI of (a) after the electron-induced removal of one and two passivating hydrogen atoms, respectively. The arrows in (a), (c) indicate the STM tip positions during the processes. The corresponding chemical structures are shown in (d), (f). (g) Comparison of dI/dV spectra taken on 1H-ETRI (red data points) and ETRI (blue data points), respectively. (h) Comparison of the HWHM from the Kondo resonance taken on 1H-ETRI (red data points) and ETRI (blue data points), respectively. The value of each data point is extracted by fitting the corresponding Kondo resonances with Frota functions [39]. (i) Comparison of Kondo resonance taken on 1H-passivated ETRI (red curve) and ETRI (blue curve) at a magnetic field of 2.5 T. (j), (k), (l) Spin polarization of 2H-ETRI, 1H-ETRI, and ETRI from meanfield Hubbard simulations.

than in the singly passivated species hinting at their different Kondo states. The spin assignment of each species was further corroborated by comparing their response to a magnetic field of 2.5 T. While the intermediate $S = 1/2$ specie did not present any detectable split of the Kondo resonance, the biradical one exhibited a clear split, as in Fig. 2(c), demonstrating the larger spin polarization of its $S = 1$ underscreened ground state.

The emergence of magnetism in ETRI is reproduced by both meanfield Hubbard (MFH) and density functional theory (DFT) simulations (see SM [25]). Similar to the case of triangulene [1,46], this modified GNF presents two (singly occupied) zero-energy modes, with a triplet ground state clearly preferred over a singlet one by more than 60 meV (see Figs. S9 and S16). The spin polarization [Fig. 3(l)] shows two spin centers localized at opposite sides of the triangular GNF, with a distribution that resembles the experimental current maps [Figs. 1(g) and 3(e)]. We note that their ferromagnetic exchange interaction is much larger than the Kondo energy scale ($k_B T_K < 1$ meV), thus explaining the $S = 1$ underscreened Kondo ground state found in the experiments. MFH simulations also show that hydrogen passivation of the radical states quenches the spins sequentially, turning ETRI into an $S = 1/2$ doublet [Fig. 3(k)] or completely non-magnetic [Fig. 3(j)], as demonstrated by the electron-induced removal of extra H atoms in the experiments.

A paramagnetic ground state was also found on molecular dimers formed during the OSS process [as shown in Fig. 1(e)], but their larger size crucially affects their magnetic properties. Fig. 4(a) shows a high-resolution image of a dimer. Two ETRI moieties are covalently linked together [Fig. 4(b)] following the Ullmann-like C-C coupling of their halogenated sites [47]. During the cyclo-dehydrogenation step, an extra pentagonal ring is created between them, as highlighted by a red bond in Fig. 4(b), reducing the number of radicals of the dimer to only two. The biradical state is experimentally demonstrated in the SM [25].

The STM image of Fig. 4(a) also reproduces bright features around the dimer backbone (indicated with dashed ellipses) corresponding to the localization of the Kondo effect: dI/dV spectra measured on either of the two show pronounced peaks centered at zero bias [Fig. 4(c)], which broaden with temperature [Fig. 4(d)] and magnetic field [Fig. 4(e)]. However, these Kondo resonances broaden faster with T than for the $S = 1$ case of ETRI [both compared in the inset of Fig. 4(d)] and show no split at $B = 2.7$ T, signaling a different magnetic ground state.

Our MFH simulations of ETRI dimers like in Fig. 4(b) confirm their biradical state, but the energy between triplet and singlet solutions are now closer (see SM). On a surface, a magnetic ground state probably behaves as two noninteracting $S = 1/2$ spins. This explains the lack of B -induced split and the faster broadening with T expected

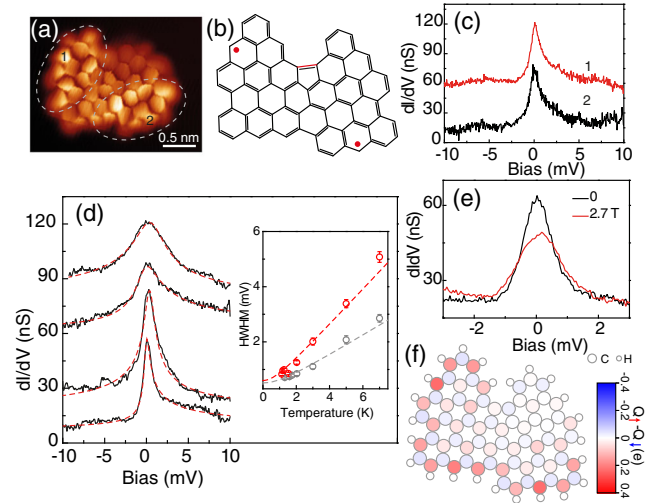


FIG. 4. Magnetic properties of dimers of ETRI. (a) Constant height current image ($V = 2$ mV) of a ETRI dimer with its chemical structure shown in (b). (c) dI/dV spectra taken on the dimer on the sites indicated with corresponding numbers in (a). (d) Temperature dependence of the Kondo resonance taken at site no.2. The spectra are shifted vertically for clarity. The inset plots the HWHM at each temperature, extracted by fitting a Frota function (red dashed lines) [39] and corrected for the thermal broadening of the tip [40]. The inset includes the simulation with the empirical expression $\sqrt{(ak_B T)^2 + (2k_B T_K)^2}$ [41], fitting the results with $T_K \sim 7$ K with $\alpha = 15$. For comparison, the temperature dependence of HWHM from the Kondo resonance taken on a single ETRI monomer (gray data points) is also shown. (e) Kondo resonance taken at location 2 at different magnetic fields at $T = 1.3$ K. (f) Spin polarization of a ETRI dimer from MFH simulations.

for $S = 1/2$ Kondo systems [24]. The spin polarization maps obtained from MFH simulations reproduce the bright current regions on the dimers well [Fig. 4(f)], further corroborating that this signal can be associated to the spin distribution. The origin of such a small magnetic exchange between the two radical states is related to the presence of a pentagon between them and to the larger separation between the two spin centers. In fact, in the absence of this extra C-C bond, MFH simulations find a robust $S = 2$ ground state. Thus, pentagonal rings embedded in certain sites of an open-shell GNF can affect its magnetic state critically by quenching a radical state and modifying the total spin (here by $\Delta S = 1$) [48], just as extra hydrogen atoms do [7], but their placement on a specific site can be designed precisely during the OSS process.

In summary, we have demonstrated the magnetic ground state of graphene flakes fabricated deterministically with a triangularlike shape. The survival of the $S = 1$ state on the metal surface is identified first through the observation of a narrow Kondo resonance, that reacts to magnetic fields as an underscreened spin triplet. The $S = 1$ state was further confirmed through removal of hydrogen atoms by tip

manipulation experiments, which revealed the stepwise emergence of two spins localized at different sides of the flakes. We note that our findings here contrast with the absence of magnetic signals in previous studies of larger triangulene flakes [15,16]. It is therefore an interesting subject for future work to unveil the precise interplay between size and symmetry of GNFs for their magnetic state over a metal surface. Nevertheless, the existence of GNFs with a net spin on a surface opens the door to new investigations of their spin dynamics and coherence over inorganic supports, which are crucial aspects for utilizing graphene nanosystems [49] in quantum spintronic applications.

We are indebted to Carmen Rubio for fruitful discussions. We acknowledge financial support from Spanish AEI (MAT2016-78293-C6, FIS2017-83780-P, and the Maria de Maeztu Units of Excellence Programme MDM-2016-0618), the European Union's Horizon 2020 (FET-Open project SPRING Grant No. 863098), the Basque Departamento de Educación through the Ph.D. Fellowship No. PRE_2019_2_0218 (S. S.), the Xunta de Galicia (Centro singular de investigación de Galicia accreditation, ED431G/09), and the European Regional Development Fund.

*thomas_frederiksen@ehu.eus

†diego.pena@usc.es

‡j.pascual@nanogune.eu

- [1] O. V. Yazyev, *Rep. Prog. Phys.* **73**, 056501 (2010).
- [2] W. L. Wang, O. V. Yazyev, S. Meng, and E. Kaxiras, *Phys. Rev. Lett.* **102**, 157201 (2009).
- [3] W. Han, R. K. Kawakami, M. Gmitra, and J. Fabian, *Nat. Nanotechnol.* **9**, 794 (2014).
- [4] Z. Bullard, E. C. Girão, J. R. Owens, W. A. Shelton, and V. Meunier, *Sci. Rep.* **5**, 7634 (2015).
- [5] E. H. Lieb, *Phys. Rev. Lett.* **62**, 1201 (1989).
- [6] B. Trauzettel, D. V. Bulaev, D. Loss, and G. Burkard, *Nat. Phys.* **3**, 192 (2007).
- [7] J. Li, S. Sanz, M. Corso, D. J. Choi, D. Peña, T. Frederiksen, and J. I. Pascual, *Nat. Commun.* **10**, 200 (2019).
- [8] S. Mishra, D. Beyer, K. Eimre, S. Kezilebieke, R. Berger, O. Gröning, C. A. Pignedoli, K. Müllen, P. Liljeroth, P. Ruffieux, X. Feng, and R. Fasel, *Nat. Nanotechnol.* **15**, 22 (2020).
- [9] J. Fernández-Rossier and J. J. Palacios, *Phys. Rev. Lett.* **99**, 177204 (2007).
- [10] W. L. Wang, S. Meng, and E. Kaxiras, *Nano Lett.* **8**, 241 (2008).
- [11] E. Kan, W. Hu, C. Xiao, R. Lu, K. Deng, J. Yang, and H. Su, *J. Am. Chem. Soc.* **134**, 5718 (2012).
- [12] M. E. Sandoval-Salinas, A. Carreras, and D. Casanova, *Phys. Chem. Chem. Phys.* **21**, 9069 (2019).
- [13] E. Clar and D. G. Stewart, *J. Am. Chem. Soc.* **75**, 2667 (1953).
- [14] N. Pavliček, A. Mistry, Z. Majzik, N. Moll, G. Meyer, D. J. Fox, and L. Gross, *Nat. Nanotechnol.* **12**, 308 (2017).
- [15] S. Mishra, D. Beyer, K. Eimre, J. Liu, R. Berger, O. Gröning, C. A. Pignedoli, K. Müllen, R. Fasel, X. Feng, and P. Ruffieux, *J. Am. Chem. Soc.* **141**, 10621 (2019).
- [16] J. Su, M. Telychko, P. Hu, G. Macam, P. Mutombo, H. Zhang, Y. Bao, F. Cheng, Z.-Q. Huang, Z. Qiu, S. J. R. Tan, H. Lin, P. Jelínek, F.-C. Chuang, J. Wu, and J. Lu, *Sci. Adv.* **5**, eaav7717 (2019).
- [17] S. Mishra, D. Beyer, K. Eimre, R. Ortiz, J. Fernández-Rossier, R. Berger, O. Gröning, C. A. Pignedoli, R. Fasel, X. Feng, and P. Ruffieux, [arXiv:2003.00753](https://arxiv.org/abs/2003.00753).
- [18] J. Cai, P. Ruffieux, R. Jaafar, M. Bieri, T. Braun, S. Blankenburg, M. Muoth, A. P. Seitsonen, M. Saleh, X. Feng, K. Müllen, and R. Fasel, *Nature (London)* **466**, 470 (2010).
- [19] M. Treier, C. A. Pignedoli, T. Laino, R. Rieger, K. Müllen, D. Passerone, and R. Fasel, *Nat. Chem.* **3**, 61 (2011).
- [20] P. Ruffieux, S. Wang, B. Yang, C. Sánchez-Sánchez, J. Liu, T. Dienel, L. Talirz, P. Shinde, C. A. Pignedoli, D. Passerone, T. Dumslaff, X. Feng, K. Müllen, and R. Fasel, *Nature (London)* **531**, 489 (2016).
- [21] S. Clair and D. G. de Oteyza, *Chem. Rev.* **119**, 4717 (2019).
- [22] S. Sasaki, S. De Franceschi, J. M. Elzerman, W. G. van der Wiel, M. Eto, S. Tarucha, and L. P. Kouwenhoven, *Nature (London)* **405**, 764 (2000).
- [23] N. Roch, S. Florens, T. A. Costi, W. Wernsdorfer, and F. Balestro, *Phys. Rev. Lett.* **103**, 197202 (2009).
- [24] J. J. Parks, A. R. Champagne, T. A. Costi, W. W. Shum, A. N. Pasupathy, E. Neuscamman, S. Flores-Torres, P. S. Cornaglia, A. A. Aligia, C. A. Balseiro, G. K. L. Chan, H. D. Abruña, and D. C. Ralph, *Science* **328**, 1370 (2010).
- [25] See Supplemental Material at <http://link.aps.org/supplemental/10.1103/PhysRevLett.124.177201> for synthesis and methods details, and for complementary experimental results and simulations, which includes Refs. [24–31].
- [26] Y. Hancock, A. Uppstu, K. Saloriutta, A. Harju, and M. J. Puska, *Phys. Rev. B* **81**, 245402 (2010).
- [27] N. Papior, *sisl: v0.9.6* (2019).
- [28] Y. Hirshberg and E. Fischer, *J. Chem. Soc.* 629 (1953).
- [29] D. Goldhaber-Gordon, J. Göres, M. A. Kastner, H. Shtrikman, D. Mahalu, and U. Meirav, *Phys. Rev. Lett.* **81**, 5225 (1998).
- [30] D. P. Daroca, P. Roura-Bas, and A. A. Aligia, *Phys. Rev. B* **98**, 245406 (2018).
- [31] R. Ortiz, N. A. García-Martínez, J. L. Lado, and J. Fernández-Rossier, *Phys. Rev. B* **97**, 195425 (2018).
- [32] J. M. Soler, E. Artacho, J. D. Gale, A. García, J. Junquera, P. Ordejón, and D. Sánchez-Portal, *J. Phys. Condens. Matter* **14**, 2745 (2002).
- [33] J. P. Perdew, K. Burke, and M. Ernzerhof, *Phys. Rev. Lett.* **77**, 3865 (1996).
- [34] L. Gross, F. Mohn, N. Moll, P. Liljeroth, and G. Meyer, *Science* **325**, 1110 (2009).
- [35] G. Kichin, C. Weiss, C. Wagner, F. S. Tautz, and R. Temirov, *J. Am. Chem. Soc.* **133**, 16847 (2011).
- [36] D. Beyer, S. Wang, C. A. Pignedoli, J. Melidonie, B. Yuan, C. Li, J. Wilhelm, P. Ruffieux, R. Berger, K. Müllen, R. Fasel, and X. Feng, *J. Am. Chem. Soc.* **141**, 2843 (2019).
- [37] M. Ternes, A. J. Heinrich, and W.-D. Schneider, *J. Phys. Condens. Matter* **21**, 053001 (2009).
- [38] M. Ternes, *New J. Phys.* **17**, 063016 (2015).
- [39] H. O. Frota, *Phys. Rev. B* **45**, 1096 (1992).

- [40] Y.-H. Zhang, S. Kahle, T. Herden, C. Stroh, M. Mayor, U. Schlickum, M. Ternes, P. Wahl, and K. Kern, *Nat. Commun.* **4**, 2110 (2013).
- [41] K. Nagaoka, T. Jamneala, M. Grobis, and M. F. Crommie, *Phys. Rev. Lett.* **88**, 077205 (2002).
- [42] M. Pustilnik and L. I. Glazman, *Phys. Rev. Lett.* **87**, 216601 (2001).
- [43] T. A. Costi, *Phys. Rev. Lett.* **85**, 1504 (2000).
- [44] L. Talirz, H. Söde, J. Cai, P. Ruffieux, S. Blankenburg, R. Jafaar, R. Berger, X. Feng, K. Müllen, D. Passerone, R. Fasel, and C. A. Pignedoli, *J. Am. Chem. Soc.* **135**, 2060 (2013).
- [45] L. Gross, F. Mohn, N. Moll, B. Schuler, A. Criado, E. Guitián, D. Peña, A. Gourdon, and G. Meyer, *Science* **337**, 1326 (2012).
- [46] R. Ortiz, R. Á. Boto, N. García-Martínez, J. C. Sancho-García, M. Melle-Franco, and J. Fernández-Rossier, *Nano Lett.* **19**, 5991 (2019).
- [47] D. G. De Oteyza, A. García-Lekue, M. Vilas-Varela, N. Merino-Díez, E. Carbonell-Sanromà, M. Corso, G. Vasseur, C. Rogero, E. Guitián, J. I. Pascual, J. E. Ortega, Y. Wakayama, and D. Peña, *ACS Nano* **10**, 9000 (2016).
- [48] S. Mishra, D. Beyer, R. Berger, J. Liu, O. Gröning, J. I. Urgel, K. Müllen, P. Ruffieux, X. Feng, and R. Fasel, *J. Am. Chem. Soc.* **142**, 1147 (2020).
- [49] F. Lombardi, A. Lodi, J. Ma, J. Liu, M. Slota, A. Narita, W. K. Myers, K. Müllen, X. Feng, and L. Bogani, *Science* **366**, 1107 (2019).

III

Magnetic interactions between radical pairs in chiral graphene nanoribbons, *Nano Lett.* **22**, 164–171 (2022)

Magnetic Interactions Between Radical Pairs in Chiral Graphene Nanoribbons

Tao Wang,^{*,†} Sofia Sanz,[†] Jesús Castro-Esteban, James Lawrence, Alejandro Berdonces-Layunta, Mohammed S. G. Mohammed, Manuel Vilas-Varela, Martina Corso, Diego Peña,^{*} Thomas Frederiksen,^{*} and Dimas G. de Oteyza^{*}



Cite This: <https://doi.org/10.1021/acs.nanolett.1c03578>



Read Online

ACCESS |



Metrics & More



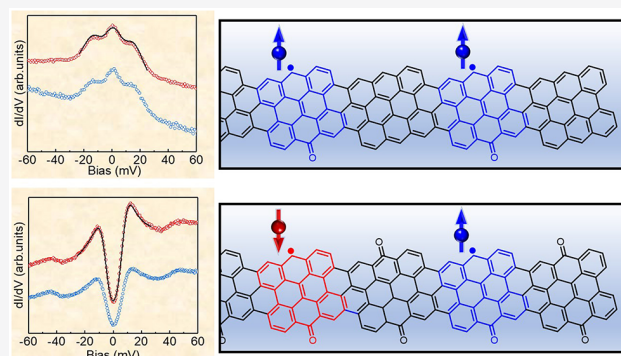
Article Recommendations



Supporting Information

ABSTRACT: Open-shell graphene nanoribbons have become promising candidates for future applications, including quantum technologies. Here, we characterize magnetic states hosted by chiral graphene nanoribbons (chGNRs). The substitution of a hydrogen atom at the chGNR edge by a ketone effectively adds one p_z electron to the π -electron network, producing an unpaired π -radical. A similar scenario occurs for regular ketone-functionalized chGNRs in which one ketone is missing. Two such radical states can interact via exchange coupling, and we study those interactions as a function of their relative position, which includes a remarkable dependence on the chirality, as well as on the nature of the surrounding ribbon, that is, with or without ketone functionalization. Besides, we determine the parameters whereby this type of system with oxygen heteroatoms can be adequately described within the widely used mean-field Hubbard model. Altogether, we provide insight to both theoretically model and devise GNR-based nanostructures with tunable magnetic properties.

KEYWORDS: magnetism, spin interaction, graphene nanoribbon, heteroatom substitution, scanning tunneling microscopy, density functional theory, mean-field Hubbard model



Magnetic carbon nanostructures exhibit attractive properties that differentiate them from the conventional magnetic systems relying on d or f states, like a weaker spin-orbit coupling and a larger spin delocalization.^{1–5} The open-shell character and the corresponding magnetic properties may appear in graphene nanoflakes (GNFs) and nanoribbons (GNRs) with certain topologies for a number of reasons. First, as predicted by Lieb's theorem⁶ sublattice imbalance in a bipartite lattice leads to a net spin inside the nanographene that occurs, for example, in triangulene.⁷ Even with balanced sublattices, topological frustration in GNFs may hinder the pairing of all p_z electrons and result in open-shell structures.⁸ In addition, if the Coulomb repulsion between valence electrons is comparable to the band gap between molecular frontier orbitals, it can prompt the system to host singly occupied orbitals.^{9–13} Finally, a net spin can be introduced to GNFs and GNRs by simply adding/removing an odd number of π -electrons into/from the system.¹⁴ Besides charge transfer scenarios,^{15,16} this can also be achieved by the insertion of odd-membered rings,^{17–20} by an sp^2 to sp^3 rehybridization as driven, for example, by hydrogenation,^{10,21} or by heteroatom substitutions.²² The former two approaches have been increasingly employed^{10,17–20,23} but only few

examples elucidate the latter one²⁴ though with many theoretical predictions.^{22,25,26}

The synthesis and characterization of graphene π -magnetism has seen great advances thanks to the recent development of on-surface synthesis.^{10,14–16,18,19,21,24,27–37} The topologies of GNFs and GNRs can be precisely tuned by the rational design of precursor molecules. Because of their delocalized π -magnetism, magnetic GNFs and GNRs are ideal candidates for the construction of interacting electron spin systems. Most of the reported works are focused on the interactions between radicals on GNFs,^{14,37} whereas the engineering of exchange-coupled spins on extended systems like GNRs, though highly desired, is more scarce.^{24,28,38}

Here, we report the generation of net spins on chiral GNRs (chGNRs) by ketone functionalization as shown in Figure 1a.

Received: September 15, 2021

Revised: December 3, 2021

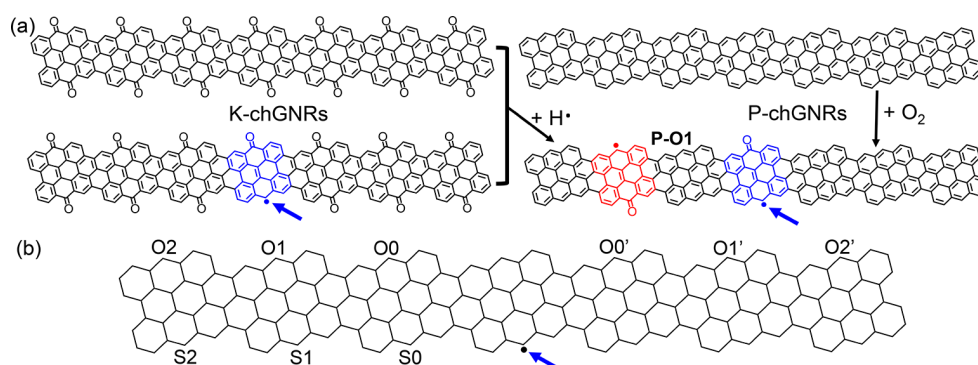


Figure 1. Synthesis and nomenclature of radicals and radical pairs. (a) Schematic drawing for the fabrication of magnetic chGNRs. A π -radical is introduced into chGNRs by the addition/removal of an oxygen into/from P-/K-chGNRs. (b) Labels for the radical pairs in chGNRs. Taking the radical marked with a blue arrow as the reference, each pair is labeled depending on the position of the second π -radical.

Replacing a CH at the pristine chGNR edge by a C=O (carbonyl) adds one π -electron to the system. As a result, the odd number of total electrons causes the appearance of a π -radical. The same is applicable for regularly ketone-functionalized chGNRs³⁹ if a C=O is replaced by a CH. The introduction of a second radical may either maintain the system's open-shell character or result in their hybridization into a closed-shell structure.^{33,37} On the basis of the above, a variety of radical pairs with different geometries were analyzed in our experiments. Combining scanning tunneling microscopy (STM) with theoretical calculations, we reveal how their relative location, the chemical structure of the units surrounding the two radicals and the chirality itself, all influence the spin interactions.

The generation of radical states in chGNRs is schematically displayed in Figure 1a and starts from the readily described synthesis of pristine (P-) and ketone-functionalized (K-) chGNRs on Au(111).^{39,40} In the case of K-chGNRs, a few defective ribbons with one or more missing oxygen atoms normally coexist with intact ribbons.³⁹ The substitution of an oxygen by a hydrogen atom makes the total number of p_z electrons an odd number, thus producing an unpaired π -radical, as indicated by the blue arrow in Figure 1a. In turn, the addition of an oxygen atom to an otherwise P-chGNRs effectively adds one p_z electron and equally brings in a radical. This can be achieved either by exposing P-chGNRs to O₂ and postannealing,⁴¹ or removing most of the ketones of K-chGNRs by exposing them to atomic hydrogen and postannealing.³⁹ Using these procedures, P- and K-chGNRs with single radicals and with radical pairs were produced. Unfortunately, attempts to controllably remove ketone groups by tip manipulation and thereby create radicals at predesigned positions were unsuccessful. We use the following nomenclature to refer to different radical pairs. Taking the radical marked with the blue arrow in Figure 1b as reference, the other labels denote the position of the second radical (Figure 1b). S/O represents the two radicals of a pair located at the same/opposite sides of a chGNR. The following number shows how many precursor units separate a radical pair. A'-mark is used to distinguish the differing configurations resulting from the ribbon's chirality. Finally, P- denotes P-chGNRs in which the radicals are caused by additional ketones and K- denotes K-chGNRs with radicals associated with missing ketones. An example P-O1 radical pair is shown in Figure 1a.

Figure 2a presents the bond-resolving (BR) STM image of a K-chGNR with a single defect using a CO-functionalized

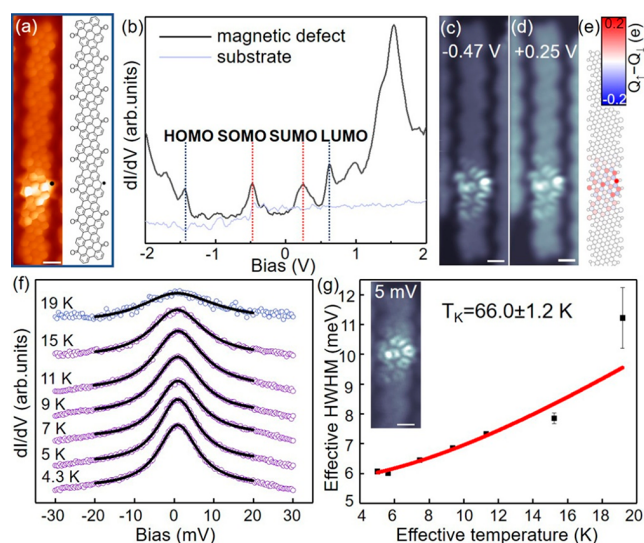


Figure 2. Characterization of single radicals. (a) Constant-height BR-STM image of a K-chGNR with single defect ($V = 5$ mV), together with the corresponding chemical structure. (b) dI/dV spectra at the marked position in (a, black line) and the bare Au(111) substrate (gray line), $V_{rms} = 20$ mV. (c,d) Constant-height dI/dV maps recorded at $V = -0.47$ and 0.25 V, respectively. $V_{rms} = 20$ mV. (e) DFT calculated spin density distribution in K-chGNR with single defect. (f) Temperature dependence of the Kondo resonance. All of the spectra are fitted by a Frota function. (g) Extracted HWHM of the Kondo resonances as a function of temperature, fitted by the Fermi-liquid model. The inset shows a Kondo map measured at 5 mV. Scale bars: 0.5 nm.

probe,⁴² along with the associated chemical structure. At the low bias value used for BR-STM, the unit cell with a missing ketone exhibits brighter contrast, implying the existence of low-energy states. Figure 2b shows the differential conductance spectrum (dI/dV) taken at the marked position in Figure 2a. Apart from the highest occupied and lowest unoccupied molecular orbitals (HOMO and LUMO) of a K-chGNR at -1.45 and 0.65 V, associated with the reported valence and conduction band onsets,³⁹ two in-gap states are clearly visible at -0.47 and 0.25 V. The same local density of states (LDOS) distribution at these two energies in dI/dV maps supports their common origin from the singly occupied/unoccupied molecular orbitals (SOMO/SUMO), separated by a 0.72 eV Coulomb gap.³⁶ In line with the experiments, the spin density calculated for this structure with density functional theory

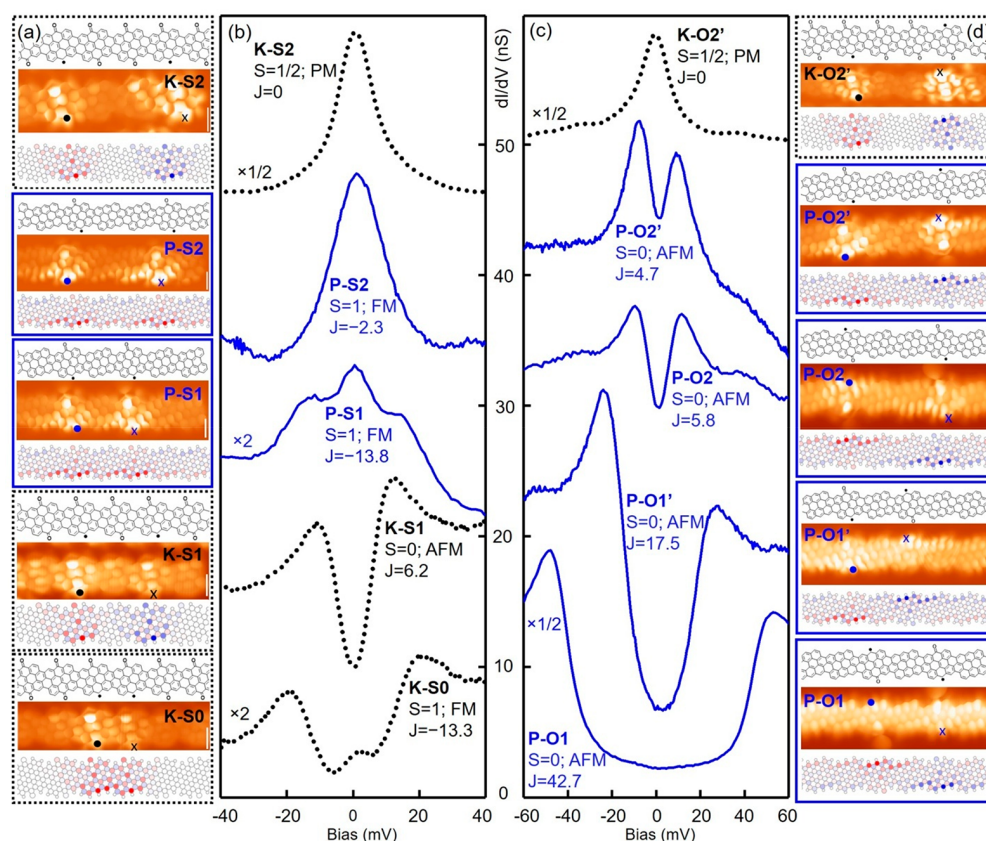


Figure 3. Characterizations of radical pairs. (a,d) BR-STM images ($V = 5$ mV) of experimentally obtained radical pairs at the same (a) and opposite sides (d) on P- and K-chGNRs, together with the chemical structure and DFT calculated spin-polarized LDOS for each case (ground states). (b,c) dI/dV spectra measured at the marked positions in STM images (see comparative spectra at the position of the second radical marked with an x in the Figure S5). The blue solid and black dotted curves refer to radical pairs on P- and K-chGNRs, respectively. P-O1 shows the original signal and other spectra were vertically shifted to match the positions of STM images. Some of the spectra were additionally scaled as marked. Total spin and coupling strength are shown for each case, where PM, FM, and AFM stand for paramagnetic, ferromagnetic and antiferromagnetic coupling, respectively. Lock-in amplitude: 2 mV for P-O1, 1.5 mV for K-S0, 1 mV for other cases. Scale bars: 0.5 nm.

(DFT) with SIESTA^{43,44} (Figure 2e and Figure S1 in Supporting Information) distributes mostly over the “defective” unit cell but extends slightly to the adjacent ones with a clear chirality-driven asymmetry. Evidence of this system’s net spin $S = 1/2$ is detected as a zero-bias peak in the low-energy dI/dV spectra (Figure 2f). It broadens anomalously fast with temperature and can thus be attributed to a Kondo resonance.^{14,45} The half width at half-maximum (HWHM) of the temperature-dependent spectra, as extracted from fits to a Frota function⁴⁶ (Figure 2f), are further fitted to the Fermi-liquid model⁴⁷ (Figure 2g) and result in a Kondo temperature of 66 K. The identical spin distribution of the Kondo map obtained at 5 mV (Figure 2g inset) and of the SOMO/SUMO (Figure 2c,d) further corroborates the origin of the spin density in the SOMO.

An equivalent characterization of a single magnetic defect in P-chGNR is presented in Figure S2. Compared to the K-chGNR case, the SOMO and the associated spin density in P-chGNR show a much more limited contribution on the ketone and mostly distribute over the pristine side of the defective unit cell. The smaller bandgap of P-chGNR as compared to K-chGNR (~ 0.7 vs ~ 2.1 eV),^{39,48} causes a stronger hybridization of the radical states with the frontier molecular orbitals, resulting in a notably more extended distribution into neighboring unit cells (though with a similar chirality-driven

asymmetry) and consequently a lower Coulomb gap of only 0.35 eV.

Next, we focus on chGNRs with radical pairs. Whereas a hybridization of the two radicals may result in a closed-shell ground state with a doubly occupied HOMO, the system can also remain open-shell with the associated SOMOs, if the hybridization energy is lower than the Coulomb repulsion between the corresponding electrons.^{33,37} Our DFT calculations (Figure S1) predict two radicals in closest proximity but opposite GNR sides (i.e., the O0 and O0' cases in both types of chGNRs) to hybridize into a closed-shell ground state, while all of the other radical combinations show open-shell ground states. The experimentally observed P-O0, P-O0', and K-O0' cases confirm their closed-shell character and are displayed in Figure S3 with HOMOs and LUMOs exhibiting distinct LDOS distributions as opposed to the similar appearance expected from SOMO and SUMO.

For the open-shell structures, the exchange interaction between a radical pair can be experimentally accessed from inelastic spin-flip excitations in scanning tunneling spectroscopy.¹⁴ The low-energy dI/dV spectra of radical pairs with a $S = 1$ triplet ground state may exhibit three features: an underscreened Kondo resonance at Fermi level and two side steps symmetrically positioned around the Fermi level. The latter are associated with inelastic triplet-to-singlet spin-flip excitations,^{15,18} and in contrast to their energetic alignment

their intensities may display asymmetries as a result of lacking particle-hole symmetry (that is, the singly occupied orbital is closer to E_F than the singly unoccupied state or vice versa), spin-polarized tips, and so forth.^{10,49} In contrast, the dI/dV spectra of radical pairs with a $S = 0$ singlet ground state exhibit only the two singlet-to-triplet side steps.^{18,19,36,37} As the exchange interaction between the radicals becomes sufficiently weak, equaling singlet and triplet energies, the radicals respond independently from one another and may display only a Kondo resonance. The geometries of the experimentally addressed radical pairs are determined from the BR-STM images displayed in Figure 3a,d, along with their spin densities as calculated with DFT. The associated low-energy dI/dV spectra are shown in Figure 3b,c. In agreement with the above, further confirmed with fits to the spectra (Figure S5) with a perturbative approach up to third order for two coupled $S = 1/2$ systems using the code from Ternes that is explained in detail in ref 49, we conclude the exchange coupling energies and relative alignments for each radical pair as summarized in Table 1. Table 1 also includes the values obtained from

Table 1. Exchange-Interaction Strength J (in meV) Obtained from Experiments and Theoretical Calculations for Multiple Radical Pairs^{a,b}

type	experiment	DFT	MFH-TB(1)	MFH-TB(2)
P-S0		-31.4	-44	-23.2
P-S1	-13.8	-18.4	-15.5	-12.8
P-S2	-2.3	-11	-7.2	-6.4
P-O0	CS	CS	CS	CS
P-O0'	CS	CS	108	CS
P-O1	42.7	35.8	29	28.8
P-O1'	17.5	28	21.4	20.4
P-O2	5.8	11.3	7.8	6.9
P-O2'	4.7	11.8	7.8	7.1
K-S0	-13.3	-24	-50.9	-19
K-S1	6.2	6.4	-6.6	2.1
K-S2	0	0.4	-0.5	0.1
K-O0		CS	CS	CS
K-O0'	CS	CS	109.1	CS
K-O1		29.1	14.4	20.9
K-O1'		-0.5	2.7	0
K-O2		0.1	0.9	0.5
K-O2'	0	0.7	0.3	0

^aPositive (negative) J values indicate preferred antiferromagnetic (ferromagnetic) alignment. ^bCS denotes closed-shell structure.

theoretical calculations. The good match of the DFT results with the experiments underlines the predictive power of the calculations on radical pair geometries not accessed experimentally.

Focusing on the exchange coupling J , it scales inversely with the spatial separation for both P- and K-chGNRs cases. That is, radical pairs separated by less unit cells show larger J values due to the greater overlap of the radical states' wave functions and the associated spin density (Figure 3a,d). Interestingly, J shows a remarkable dependence on the chirality, as observed experimentally with P-O1 and P-O1' and predicted theoretically also for K-O1 and K-O1' (Table 1). The chirality-driven asymmetric extension of the SOMO wave function (and of the associated spin density) into neighboring unit-cells strongly affects their overlap. For example, whereas the spin density of radical states in P-O1 mostly extends toward the central unit

between the radical pairs, it dominantly extends away from each other in P-O1' (Figure 3d). As a consequence, the former shows a much stronger exchange coupling than the latter (42.7 vs 17.5 meV). The exchange coupling strength also varies substantially with the nature of the surrounding GNR, as exemplified here with the presence or absence of the edge functionalization by ketones. Radical states in K-chGNRs extend much less than those in P-chGNRs, promoting in the latter a larger overlap and thus larger J for the same radical pair geometry (Figure 3 and Table 1).

As for the spin's relative alignment, a generally applicable assumption that relies on the preferred antiferromagnetic alignment of electrons in chemical bonds is that, for alternant graphene nanostructures, each of the two sublattices hosts p_z electrons with spin up or down, respectively. Since the ketone group is also sp^2 hybridized, it adds one p_z electron to the system and can to a first approximation be considered as an additional p_z site on its corresponding sublattice. The atoms at same edges of the chGNRs belong to the same sublattice, whereas the atoms at the opposite edge belong to the other sublattice. A radical pair located at the same/opposite side is therefore expected to be ferromagnetically (FM)/antiferromagnetically (AFM) aligned. All experimentally measured radical pairs match this prediction, except K-S1 (AFM ground state; Table 1).

For the conductance spectrum of K-S1, one could argue that the Kondo peak expected from a FM alignment is not visible because its intensity is much lower than that of the spin flip steps (as occurs, e.g., in K-S0, Figure 3b), and its width is comparable to J . In fact, the spectrum can be fitted using Ternes' code⁴⁹ assuming an FM alignment. However, to do so, the tip-sample transmission function represented by the T_0^2 parameter required an anomalously large value. Since we did not change the STM tip during the whole experiment and used comparable tip-sample distances as defined by the STM feedback parameters, it is natural to expect that T_0^2 should be similar for all the spin-coupling scenarios. As shown in Figure S6, whereas all the other fits rendered comparable T_0^2 values, a FM alignment for the K-S1 case required a T_0^2 value an order of magnitude higher and clearly out of the dispersion range, suggesting a preferred AFM alignment of the K-S1 radical pair.

This counterintuitive spin alignment for the K-S1 case is confirmed with DFT calculations, which predict the AFM alignment to be energetically favored. We have additionally performed mean-field Hubbard (MFH) calculations⁵⁰ on this same system, given its greater simplicity and successful application to many open-shell carbon nanostructures.^{14,37} As discussed earlier, the extra p_z electron on the sp^2 hybridized ketone was first considered as an additional p_z site taken to be identical to a carbon p_z orbital. Doing so, MFH calculations with the third nearest-neighbor tight-binding model (3NN-TB) predict a FM ground state for K-S1, in line with the intuitive expectations for radical states on the same ribbon's side but against DFT and experiments (henceforth we call this model MFH-TB(1)). In a counter-experiment, we performed DFT calculations for another system which is more equivalent to a simulation performed with MFH-TB(1), namely a chGNR with methylidene groups (i.e., $C=CH_2$) instead of carbonyl ($C=O$). In this case, the DFT results agree with the intuitive expectations and with the MFH-TB(1), predicting a preferred FM alignment and even a comparable J value (CH_2 -S1 in Figure 4a). It follows that the surprising AFM alignment is unequivocally related to the oxygen atom rather than to the

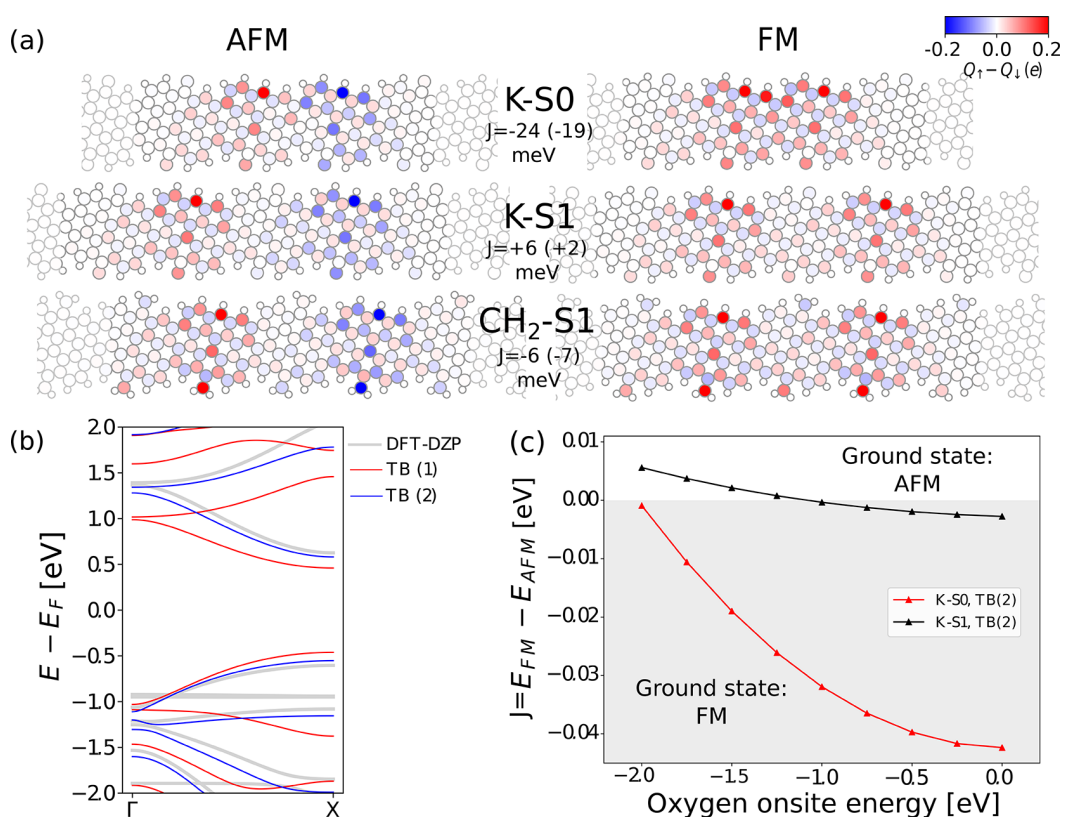


Figure 4. Modeling of radical pairs. (a) Spin-polarized LDOS distribution of radical states as calculated by DFT and J (MFH-TB(2) values are shown in parentheses) in K-S0, K-S1, and CH₂-S1 (all oxygen atoms are replaced by CH₂), respectively. (b) Band structures of intact K-chGNR, acquired from DFT, MFH-TB(1), and MFH-TB(2), respectively. (c) MFH-TB calculated J in K-S0 and K-S1 as a function of oxygen onsite energy in TB(2). The onsite Coulomb repulsion in MFH was set to $U = 3$ eV.

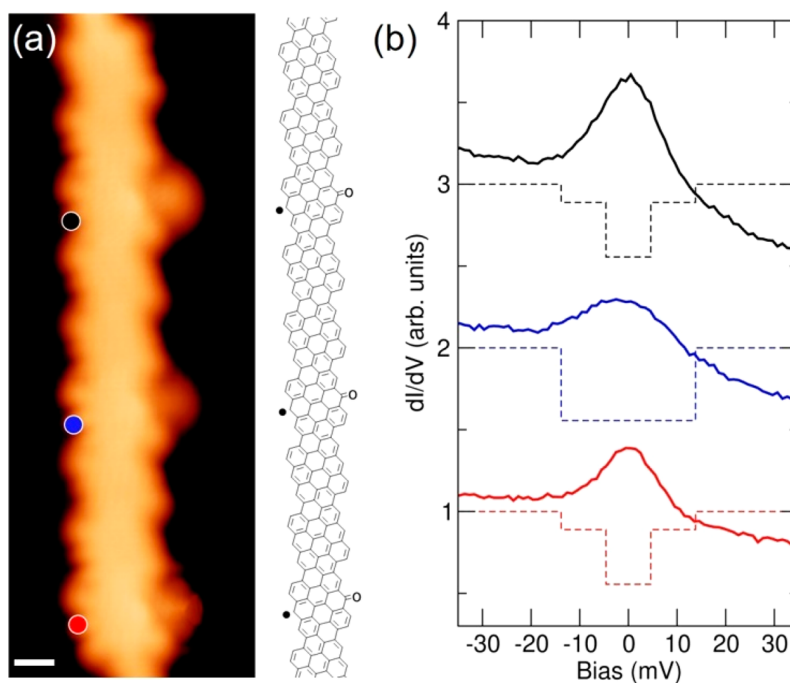


Figure 5. (a) STM image ($U = -100$ mV; $I = -1$ nA) showing a P-chGNR with three P-S2 radicals in a row, together with the corresponding chemical structure. The scale bar is 5 Å. (b) Vertically offset dI/dV spectra (solid lines) obtained at the marked positions in (a), along with the simulated inelastic electron tunneling spectroscopy (dashed lines) for this three-radical spin system. The exchange energy $J = -2.3$ meV, as derived from P-S2 in experiments, is used for the simulation.

mere presence of an extra p_z electron there, exposing insufficient chemical detail in our simple MFH-TB(1) approach.

In an attempt to make the simple MFH calculations also applicable to these more complicated systems including heteroatoms, we have included modified TB parameters (hopping amplitude and on-site energy) for the oxygen heteroatoms in what we call the model MFH-TB(2). To determine the most appropriate parameters, we compare the calculated band structures obtained from DFT for fully ketone-functionalized chGNRs to those obtained with our MFH-TB models (Figure 4b). An improvement of the TB model can be obtained with MFH-TB(2) maintaining for carbon atoms the nearest-neighbor hopping amplitude and on-site energies of 2.7 and 0 eV, respectively, but changing the values to 3.8 and -1.5 eV for oxygen atoms bonded to carbon. Qualitatively the increased hopping amplitude on the C=O bonds can be directly related to its shorter length and the nonzero on-site energy to the increased electronegativity of oxygen. The exchange coupling in radical pairs (both strength and sign) is strongly affected by these two parameters, as depicted for the on-site energy in Figure 4c for K-S0 and K-S1. Applying this optimized model now correctly predicts a preferred AFM alignment for K-S1. Furthermore, MFH-TB(2) also corrects the other wrong predictions of the MFH-TB(1) model, as is the open-shell character of the P-O0' and K-O0' radical pairs and provides for all calculated structures J values very similar to DFT calculations (see Table 1). Altogether, we hereby provide a simple yet accurate parametrization to model these more complex systems beyond pure hydrocarbon structures.

It is worth noting that the insight provided in this work about the pairwise interaction between radicals can be extended also to systems with an increasing number of spins and ultimately even to spin chains. By way of example, three P-S2 radical states in a row (Figure 5a) reveal a clearly broader zero-bias resonance at the central radical (blue data, HWHM = 9 meV, Figure 5b) as compared to the two outer ones (black and red data, HWHM = 7 meV). For this geometry, the three spins are ferromagnetically coupled, leading to a ground state $S = 3/2$ with two distinct spin-flip excitations to the $S = 1/2$ manifold. Theoretical simulations of the corresponding inelastic dI/dV features (Figure 5b, dashed lines) reveal that only the high-energy excitation contributes at the central radical, whereas the outer sites exhibit predominantly the low-energy steps. Although a clear identification of these inelastic transitions in our spectra is hindered by the low energies involved, along with a relatively broad Kondo signal, these calculations are consistent with the experiment and the broader peak at the central spin (Figure 5b). This finding is also in line with the previous work from DiLullo et al.,⁵¹ where the central site on a molecular Kondo chain was found to exhibit a larger resonance width than those at the termini. Although the spins in that case were aligned antiferromagnetically, the same argument actually holds.

In summary, we have characterized the magnetic interactions between radical pairs of diverse geometries hosted by two different types of chGNRs, with and without ketone functionalization at their edges. As confirmed by both experiments and theoretical calculations, the exchange coupling between two radicals shows remarkably large variations depending on their relative location on the same or opposite sides of the GNRs, on the spatial distance between them, on the chiral asymmetry, as well as on the structure of

the GNR surrounding the magnetic state. These results thus provide valuable information on the potential use in the design of graphene-based spin chains and networks with tunable magnetic structures. Furthermore, we demonstrated their modeling by the widely used MFH approximation through a minimal extension to these systems of increased complexity including oxygen heteroatoms, which may greatly expedite the understanding and engineering of GNR-based structures in the future.

■ ASSOCIATED CONTENT

Supporting Information

The Supporting Information is available free of charge at <https://pubs.acs.org/doi/10.1021/acs.nanolett.1c03578>.

Detailed methods of both experiments and calculations; spin density distributions of radical states on magnetic chGNRs by theoretical calculations; characterization of the magnetism of a P-chGNR with a single defect; closed-shell structures; Kondo peak comparison between K-chGNR with single defect and K-S2, K-O2'; simulations of the dI/dV spectra from radical pairs (PDF)

■ AUTHOR INFORMATION

Corresponding Authors

Tao Wang – Donostia International Physics Center, 20018 San Sebastián, Spain; Centro de Física de Materiales CFM/MPC, CSIC-UPV/EHU, 20018 San Sebastián, Spain; orcid.org/0000-0002-6545-5028; Email: taowang@dipc.org

Diego Peña – Centro Singular de Investigación en Química Biológica e Materiais Moleculares (CiQUS) and Departamento de Química Orgánica, Universidade de Santiago de Compostela, 15782 Santiago de Compostela, Spain; orcid.org/0000-0003-3814-589X; Email: diego.pena@usc.es

Thomas Frederiksen – Donostia International Physics Center, 20018 San Sebastián, Spain; Ikerbasque, Basque Foundation for Science, 48013 Bilbao, Spain; orcid.org/0000-0001-7523-7641; Email: thomas_frederiksen@ehu.es

Dimas G. de Oteyza – Donostia International Physics Center, 20018 San Sebastián, Spain; Centro de Física de Materiales CFM/MPC, CSIC-UPV/EHU, 20018 San Sebastián, Spain; Ikerbasque, Basque Foundation for Science, 48013 Bilbao, Spain; orcid.org/0000-0001-8060-6819; Email: d_g_oteyza@ehu.es

Authors

Sofia Sanz – Donostia International Physics Center, 20018 San Sebastián, Spain; orcid.org/0000-0002-2792-2721

Jesús Castro-Esteban – Centro Singular de Investigación en Química Biológica e Materiais Moleculares (CiQUS) and Departamento de Química Orgánica, Universidade de Santiago de Compostela, 15782 Santiago de Compostela, Spain

James Lawrence – Donostia International Physics Center, 20018 San Sebastián, Spain; Centro de Física de Materiales CFM/MPC, CSIC-UPV/EHU, 20018 San Sebastián, Spain; orcid.org/0000-0001-5503-8661

Aljandro Berdonces-Layunta – Donostia International Physics Center, 20018 San Sebastián, Spain; Centro de Física

de Materiales CFM/MPC, CSIC-UPV/EHU, 20018 San Sebastián, Spain

Mohammed S. G. Mohammed – Donostia International Physics Center, 20018 San Sebastián, Spain; Centro de Física de Materiales CFM/MPC, CSIC-UPV/EHU, 20018 San Sebastián, Spain

Manuel Vilas-Varela – Centro Singular de Investigación en Química Biolóxica e Materiais Moleculares (CiQUS) and Departamento de Química Orgánica, Universidade de Santiago de Compostela, 15782 Santiago de Compostela, Spain

Martina Corso – Donostia International Physics Center, 20018 San Sebastián, Spain; Centro de Física de Materiales CFM/MPC, CSIC-UPV/EHU, 20018 San Sebastián, Spain; orcid.org/0000-0002-8592-1284

Complete contact information is available at:
<https://pubs.acs.org/10.1021/acs.nanolett.1c03578>

Author Contributions

[†]T.W. and S.S. contributed equally.

Author Contributions

The manuscript was written through contributions of all authors. All authors have given approval to the final version of the manuscript.

Notes

The authors declare no competing financial interest.

ACKNOWLEDGMENTS

We acknowledge financial support from the MCIN/AEI/10.13039/501100011033 (Grants PID2019-107338RB-C62, PID2019-107338RB-C63, PID2020-115406GB-I00, PCI2019-111933-2 (FLAG-ERA grant LEGOCHIP), and Juan de la Cierva Grant FJC2019-041202-I), the European Union's Horizon 2020 research and innovation program (FET-OPEN project SPRING, Grant No. 863098 and Marie Skłodowska-Curie Actions Individual Fellowship No. 101022150), the Xunta de Galicia (Centro Singular de Investigación de Galicia, 2019-2022, Grant ED431G2019/03), the European Regional Development Fund, the Basque Government (IT-1255-19), the Basque Government (PIBA Grant PI_2020_1_0014), the Basque Departamento de Educación through the Ph.D. scholarship No. PRE_2020_2_0049 (S.S.), the Spanish Research Council (LINKC20002). We thank Dr. Jingcheng Li for fruitful discussions.

REFERENCES

- Han, W.; Kawakami, R. K.; Gmitra, M.; Fabian, J. Graphene Spintronics. *Nat. Nanotechnol.* **2014**, *9* (10), 794–807.
- Yazyev, O. V.; Katsnelson, M. I. Magnetic Correlations at Graphene Edges: Basis for Novel Spintronics Devices. *Phys. Rev. Lett.* **2008**, *100* (4), 047209.
- Pisani, L.; Chan, J. A.; Montanari, B.; Harrison, N. M. Electronic Structure and Magnetic Properties of Graphitic Ribbons. *Phys. Rev. B: Condens. Matter Mater. Phys.* **2007**, *75* (6), 064418.
- Cui, P.; Zhang, Q.; Zhu, H.; Li, X.; Wang, W.; Li, Q.; Zeng, C.; Zhang, Z. Carbon Tetragons as Definitive Spin Switches in Narrow Zigzag Graphene Nanoribbons. *Phys. Rev. Lett.* **2016**, *116* (2), 026802.
- Fernández-Rossier, J.; Palacios, J. J. Magnetism in Graphene Nanoislands. *Phys. Rev. Lett.* **2007**, *99* (17), 177204.
- Lieb, E. H. Two Theorems on the Hubbard Model. *Phys. Rev. Lett.* **1989**, *62* (10), 1201–1204.

(7) Su, J.; Telychko, M.; Song, S.; Lu, J. Triangulenes: From Precursor Design to On-Surface Synthesis and Characterization. *Angew. Chem.* **2020**, *132* (20), 7730–7740.

(8) Wang, W. L.; Yazyev, O. V.; Meng, S.; Kaxiras, E. Topological Frustration in Graphene Nanoflakes: Magnetic Order and Spin Logic Devices. *Phys. Rev. Lett.* **2009**, *102* (15), 157201.

(9) Ezawa, M. Metallic Graphene Nanodisks: Electronic and Magnetic Properties. *Phys. Rev. B: Condens. Matter Mater. Phys.* **2007**, *76* (24), 245415.

(10) Li, J.; Sanz, S.; Corso, M.; Choi, D. J.; Peña, D.; Frederiksen, T.; Pascual, J. I. Single Spin Localization and Manipulation in Graphene Open-Shell Nanostructures. *Nat. Commun.* **2019**, *10* (1), 200.

(11) Konishi, A.; Hirao, Y.; Nakano, M.; Shimizu, A.; Botek, E.; Champagne, B.; Shiomi, D.; Sato, K.; Takui, T.; Matsumoto, K.; Kurata, H.; Kubo, T. Synthesis and Characterization of Teranthene: A Singlet Biradical Polycyclic Aromatic Hydrocarbon Having Kekulé Structures. *J. Am. Chem. Soc.* **2010**, *132* (32), 11021–11023.

(12) Wang, S.; Talirz, L.; Pignedoli, C. A.; Feng, X.; Müllen, K.; Fasel, R.; Ruffieux, P. Giant Edge State Splitting at Atomically Precise Graphene Zigzag Edges. *Nat. Commun.* **2016**, *7* (1), 11507.

(13) Kolmer, M.; Steiner, A.-K.; Izydorczyk, I.; Ko, W.; Englund, M.; Szymonski, M.; Li, A.-P.; Amsharov, K. Rational Synthesis of Atomically Precise Graphene Nanoribbons Directly on Metal Oxide Surfaces. *Science* **2020**, *369* (6503), 571–575.

(14) Song, S.; Su, J.; Telychko, M.; Li, J.; Li, G.; Li, Y.; Su, C.; Wu, J.; Lu, J. On-Surface Synthesis of Graphene Nanostructures with π -Magnetism. *Chem. Soc. Rev.* **2021**, *50* (5), 3238–3262.

(15) Sun, Q.; Mateo, L. M.; Robles, R.; Ruffieux, P.; Lorente, N.; Bottari, G.; Torres, T.; Fasel, R. Inducing Open-Shell Character in Porphyrins through Surface-Assisted Phenalenyl π -Extension. *J. Am. Chem. Soc.* **2020**, *142* (42), 18109–18117.

(16) Zhao, Y.; Jiang, K.; Li, C.; Liu, Y.; Xu, C.; Zheng, W.; Guan, D.; Li, Y.; Zheng, H.; Liu, C.; Luo, W.; Jia, J.; Zhuang, X.; Wang, S. Precise Control of π -Electron Magnetism in Metal-Free Porphyrins. *J. Am. Chem. Soc.* **2020**, *142* (43), 18532–18540.

(17) Jacobse, P. H.; McCurdy, R. D.; Jiang, J.; Rizzo, D. J.; Veber, G.; Butler, P.; Zuzak, R.; Louie, S. G.; Fischer, F. R.; Crommie, M. F. Bottom-up Assembly of Nanoporous Graphene with Emergent Electronic States. *J. Am. Chem. Soc.* **2020**, *142* (31), 13507–13514.

(18) Zheng, Y.; Li, C.; Xu, C.; Beyer, D.; Yue, X.; Zhao, Y.; Wang, G.; Guan, D.; Li, Y.; Zheng, H.; Liu, C.; Liu, J.; Wang, X.; Luo, W.; Feng, X.; Wang, S.; Jia, J. Designer Spin Order in Diradical Nanographenes. *Nat. Commun.* **2020**, *11* (1), 6076.

(19) Zheng, Y.; Li, C.; Zhao, Y.; Beyer, D.; Wang, G.; Xu, C.; Yue, X.; Chen, Y.; Guan, D.-D.; Li, Y.-Y.; Zheng, H.; Liu, C.; Luo, W.; Feng, X.; Wang, S.; Jia, J. Engineering of Magnetic Coupling in Nanographene. *Phys. Rev. Lett.* **2020**, *124* (14), 147206.

(20) Mishra, S.; Beyer, D.; Berger, R.; Liu, J.; Gröning, O.; Urgel, J. I.; Müllen, K.; Ruffieux, P.; Feng, X.; Fasel, R. Topological Defect-Induced Magnetism in a Nanographene. *J. Am. Chem. Soc.* **2020**, *142* (3), 1147–1152.

(21) Li, J.; Sanz, S.; Castro-Esteban, J.; Vilas-Varela, M.; Friedrich, N.; Frederiksen, T.; Peña, D.; Pascual, J. I. Uncovering the Triplet Ground State of Triangular Graphene Nanoflakes Engineered with Atomic Precision on a Metal Surface. *Phys. Rev. Lett.* **2020**, *124* (17), 177201.

(22) Wang, X.; Sun, G.; Routh, P.; Kim, D.-H.; Huang, W.; Chen, P. Heteroatom-Doped Graphene Materials: Syntheses, Properties and Applications. *Chem. Soc. Rev.* **2014**, *43* (20), 7067–7098.

(23) Gonzalez-Herrero, H.; Gomez-Rodriguez, J. M.; Mallet, P.; Moaied, M.; Palacios, J. J.; Salgado, C.; Ugeda, M. M.; Veuillen, J.-Y.; Yndurain, F.; Brihuega, I. Atomic-Scale Control of Graphene Magnetism by Using Hydrogen Atoms. *Science* **2016**, *352* (6284), 437–441.

(24) Friedrich, N.; Brandimarte, P.; Li, J.; Saito, S.; Yamaguchi, S.; Pozo, I.; Peña, D.; Frederiksen, T.; Garcia-Lekue, A.; Sánchez-Portal, D.; Pascual, J. I. Magnetism of Topological Boundary States Induced

by Boron Substitution in Graphene Nanoribbons. *Phys. Rev. Lett.* **2020**, *125* (14), 146801.

(25) Babar, R.; Kabir, M. Ferromagnetism in Nitrogen-Doped Graphene. *Phys. Rev. B: Condens. Matter Mater. Phys.* **2019**, *99* (11), 115442.

(26) Bloński, P.; Tuček, J.; Sofer, Z.; Mazánek, V.; Petr, M.; Pumera, M.; Otyepka, M.; Zbořil, R. Doping with Graphitic Nitrogen Triggers Ferromagnetism in Graphene. *J. Am. Chem. Soc.* **2017**, *139* (8), 3171–3180.

(27) Clair, S.; de Oteyza, D. G. Controlling a Chemical Coupling Reaction on a Surface: Tools and Strategies for On-Surface Synthesis. *Chem. Rev.* **2019**, *119* (7), 4717–4776.

(28) Sun, Q.; Yao, X.; Gröning, O.; Eimre, K.; Pignedoli, C. A.; Müllen, K.; Narita, A.; Fasel, R.; Ruffieux, P. Coupled Spin States in Armchair Graphene Nanoribbons with Asymmetric Zigzag Edge Extensions. *Nano Lett.* **2020**, *20* (9), 6429–6436.

(29) Ruffieux, P.; Wang, S.; Yang, B.; Sánchez-Sánchez, C.; Liu, J.; Dienel, T.; Talirz, L.; Shinde, P.; Pignedoli, C. A.; Passerone, D.; Dumschlaff, T.; Feng, X.; Müllen, K.; Fasel, R. On-Surface Synthesis of Graphene Nanoribbons with Zigzag Edge Topology. *Nature* **2016**, *531* (7595), 489–492.

(30) Liu, J.; Mishra, S.; Pignedoli, C. A.; Passerone, D.; Urgel, J. I.; Fabrizio, A.; Lohr, T. G.; Ma, J.; Komber, H.; Baumgarten, M.; Corminboeuf, C.; Berger, R.; Ruffieux, P.; Müllen, K.; Fasel, R.; Feng, X. Open-Shell Nonbenzenoid Nanographenes Containing Two Pairs of Pentagonal and Heptagonal Rings. *J. Am. Chem. Soc.* **2019**, *141* (30), 12011–12020.

(31) Mateo, L. M.; Sun, Q.; Liu, S.; Bergkamp, J. J.; Eimre, K.; Pignedoli, C. A.; Ruffieux, P.; Decurtins, S.; Bottari, G.; Fasel, R.; Torres, T. On-Surface Synthesis and Characterization of Triply Fused Porphyrin–Graphene Nanoribbon Hybrids. *Angew. Chem., Int. Ed.* **2020**, *59* (3), 1334–1339.

(32) Mishra, S.; Beyer, D.; Eimre, K.; Ortiz, R.; Fernández-Rossier, J.; Berger, R.; Gröning, O.; Pignedoli, C. A.; Fasel, R.; Feng, X.; Ruffieux, P. Collective All-Carbon Magnetism in Triangulene Dimers. *Angew. Chem., Int. Ed.* **2020**, *59* (29), 12041–12047.

(33) Lawrence, J.; Brandimarte, P.; Berdonces-Layunta, A.; Mohammed, M. S. G.; Grewal, A.; Leon, C. C.; Sánchez-Portal, D.; de Oteyza, D. G. Probing the Magnetism of Topological End States in 5-Armchair Graphene Nanoribbons. *ACS Nano* **2020**, *14* (4), 4499–4508.

(34) Sánchez-Grande, A.; Urgel, J. I.; Veis, L.; Edalatmanesh, S.; Santos, J.; Lauwaet, K.; Mutombo, P.; Gallego, J. M.; Brabec, J.; Beran, P.; Nachtigallová, D.; Miranda, R.; Martín, N.; Jelínek, P.; Ěcija, D. Unravelling the Open-Shell Character of Peripentacene on Au(111). *J. Phys. Chem. Lett.* **2021**, *12* (1), 330–336.

(35) Su, X.; Li, C.; Du, Q.; Tao, K.; Wang, S.; Yu, P. Atomically Precise Synthesis and Characterization of Heptaurene with Triplet Ground State. *Nano Lett.* **2020**, *20* (9), 6859–6864.

(36) Mishra, S.; Beyer, D.; Eimre, K.; Kezilebieke, S.; Berger, R.; Gröning, O.; Pignedoli, C. A.; Müllen, K.; Liljeroth, P.; Ruffieux, P.; Feng, X.; Fasel, R. Topological Frustration Induces Unconventional Magnetism in a Nanographene. *Nat. Nanotechnol.* **2020**, *15* (1), 22–28.

(37) Mishra, S.; Yao, X.; Chen, Q.; Eimre, K.; Gröning, O.; Ortiz, R.; Di Giovannantonio, M.; Sancho-García, J. C.; Fernández-Rossier, J.; Pignedoli, C. A.; Müllen, K.; Ruffieux, P.; Narita, A.; Fasel, R. Large Magnetic Exchange Coupling in Rhombus-Shaped Nanographenes with Zigzag Periphery. *Nat. Chem.* **2021**, *13*, 581.

(38) Rizzo, D. J.; Veber, G.; Jiang, J.; McCurdy, R.; Cao, T.; Bronner, C.; Chen, T.; Louie, S. G.; Fischer, F. R.; Crommie, M. F. Inducing Metallicity in Graphene Nanoribbons via Zero-Mode Superlattices. *Science* **2020**, *369* (6511), 1597–1603.

(39) Lawrence, J.; Berdonces-Layunta, A.; Edalatmanesh, S.; Castro-Esteban, J.; Wang, T.; Mohammed, M. S. G.; Vilas-Varela, M.; Jelínek, P.; Peña, D.; de Oteyza, D. G. Circumventing the Stability Problems of Graphene Nanoribbon Zigzag Edges. arXiv. 2021, 2107.12754. <https://arxiv.org/abs/2107.12754> (accessed November 25, 2021).

(40) de Oteyza, D. G.; García-Lekue, A.; Vilas-Varela, M.; Merino-Díez, N.; Carbonell-Sanromà, E.; Corso, M.; Vasseur, G.; Rogero, C.; Guitián, E.; Pascual, J. I.; Ortega, J. E.; Wakayama, Y.; Peña, D. Substrate-Independent Growth of Atomically Precise Chiral Graphene Nanoribbons. *ACS Nano* **2016**, *10* (9), 9000–9008.

(41) Berdonces-Layunta, A.; Lawrence, J.; Edalatmanesh, S.; Castro-Esteban, J.; Wang, T.; Mohammed, M. S. G.; Colazzo, L.; Peña, D.; Jelínek, P.; de Oteyza, D. G. Chemical Stability of (3,1)-Chiral Graphene Nanoribbons. *ACS Nano* **2021**, *15* (3), 5610–5617.

(42) Jelínek, P. High Resolution SPM Imaging of Organic Molecules with Functionalized Tips. *J. Phys.: Condens. Matter* **2017**, *29* (34), 343002.

(43) Soler, J. M.; Artacho, E.; Gale, J. D.; García, A.; Junquera, J.; Ordejon, P.; Sánchez-Portal, D. *Phys. Condens. Matter*. **2002**, *14*, 2745.

(44) Perdew, J. P.; Burke, K.; Ernzerhof, M. *Phys. Rev. Lett.* **1996**, *77*, 3865.

(45) Kondo, J. Resistance Minimum in Dilute Magnetic Alloys. *Prog. Theor. Phys.* **1964**, *32* (1), 37–49.

(46) Frota, H. O. Shape of the Kondo Resonance. *Phys. Rev. B: Condens. Matter Mater. Phys.* **1992**, *45* (3), 1096–1099.

(47) Nagaoka, K.; Jamneala, T.; Grobis, M.; Crommie, M. F. Temperature Dependence of a Single Kondo Impurity. *Phys. Rev. Lett.* **2002**, *88* (7), 077205.

(48) Merino-Díez, N.; Li, J.; Garcia-Lekue, A.; Vasseur, G.; Vilas-Varela, M.; Carbonell-Sanromà, E.; Corso, M.; Ortega, J. E.; Peña, D.; Pascual, J. I.; de Oteyza, D. G. Unraveling the Electronic Structure of Narrow Atomically Precise Chiral Graphene Nanoribbons. *J. Phys. Chem. Lett.* **2018**, *9* (1), 25–30.

(49) Ternes, M. Spin Excitations and Correlations in Scanning Tunneling Spectroscopy. *New J. Phys.* **2015**, *17* (6), 063016.

(50) (<https://github.com/dipc-cc/hubbard>).

(51) DiLullo, A.; Chang, S.-H.; Baadji, N.; Clark, K.; Klöckner, J.-P.; Prosen, M.-H.; Sanvito, S.; Wiesendanger, R.; Hoffmann, G.; Hla, S.-W. Molecular Kondo Chain. *Nano Lett.* **2012**, *12* (6), 3174–3179.

**HAZARD AWARENESS
REDUCES LAB INCIDENTS**

**ACS Essentials of
Lab Safety for
General Chemistry**

A new course from the
American Chemical Society




ACS Institute
Learn. Develop. Excel.

EXPLORE ORGANIZATIONAL SALES
solutions.acs.org/essentialsoflabsafety

REGISTER FOR INDIVIDUAL ACCESS
institute.acs.org/courses/essentials-lab-safety.html

IV

Crossed graphene nanoribbons as beam splitters and mirrors for electron quantum optics, Phys. Rev. B 102, 035436 (2020)

Crossed graphene nanoribbons as beam splitters and mirrors for electron quantum opticsSofia Sanz ^{1,*}, Pedro Brandimarte,¹ Géza Giedke ^{1,2}, Daniel Sánchez-Portal,³ and Thomas Frederiksen ^{1,2,†}¹*Donostia International Physics Center (DIPC), Paseo Manuel de Lardizabal 4, E-20018 Donostia-San Sebastián, Spain*²*IKERBASQUE, Basque Foundation for Science, E-48013 Bilbao, Spain*³*Centro de Física de Materiales (CFM) CSIC-UPV/EHU, Paseo Manuel de Lardizabal 5, E-20018 Donostia-San Sebastián, Spain*

(Received 23 May 2020; accepted 8 July 2020; published 24 July 2020)

We analyze theoretically four-terminal electronic devices composed of two crossed graphene nanoribbons (GNRs) and show that they can function as beam splitters or mirrors. These features are identified for electrons in the low-energy region where a single valence or conduction band is present. Our modeling is based on p_z orbital tight binding with Slater-Koster-type matrix elements fitted to accurately reproduce the low-energy bands from density functional theory calculations. We analyze systematically all devices that can be constructed with either zigzag or armchair GNRs in AA and AB stackings. From Green's function theory the elastic electron transport properties are quantified as a function of the ribbon width. We find that devices composed of relatively narrow zigzag GNRs and AA-stacked armchair GNRs are the most interesting candidates to realize electron beam splitters with a close to 50:50 ratio in the two outgoing terminals. Structures with wider ribbons instead provide electron mirrors, where the electron wave is mostly transferred into the outgoing terminal of the other ribbon, or electron filters where the scattering depends sensitively on the wavelength of the propagating electron. We also test the robustness of these transport properties against variations in the intersection angle, stacking pattern, lattice deformation (uniaxial strain), inter-GNR separation, and electrostatic potential differences between the layers. These generic features show that GNRs are interesting basic components to construct electronic quantum optical setups.

DOI: [10.1103/PhysRevB.102.035436](https://doi.org/10.1103/PhysRevB.102.035436)**I. INTRODUCTION**

The similarities between the wave nature of electrons propagating coherently in ballistic conductors with photon propagation in optical waveguides has spawned the field of electron quantum optics [1,2]. In this way several electronic analogs of optical setups—such as the Mach-Zehnder [3,4] and Fabry-Pérot [5–7] interferometers, as well as the Hanbury Brown–Twiss [8–11] geometry to study the Fermion anti-bunching and the two-particle Aharonov-Bohm [12] effects—have been implemented. Fundamental components for these setups include mirrors (Ms), beam splitters (BSs, i.e., partially transparent mirrors), and wavelength filters. Such control elements for electron beams are important in the fields of quantum information and solid-state quantum computation: By sending a single electron through a BS one can generate a mode-entangled state that can be used to violate a Bell inequality [13] or for quantum teleportation [14,15]. A BS is the central building block of the Hong-Ou-Mandel setup to test the indistinguishability [16] or the entanglement [17] of electrons entering in the two input ports. With two BSs and two oriented Ms the Mach-Zehnder interferometer can be fully implemented, which has been demonstrated to work as a quantum logic processor [18].

A platform with remarkable prospects for electron quantum optics are graphene-based systems, in which several

pioneering experiments on electron beam splitters and related devices have been performed [19,20]. More recently, graphene nanoribbons (GNRs) [21,22] have emerged as attractive candidates for the construction of molecular-scale electronic devices [23] because they inherit some of the exceptional properties from graphene while having tunable electronic properties, such as the opening of a band gap depending on their width and edge topology [24–28]. The electron coherence length in GNRs can be long, with values of the order ~ 100 nm being reported [29–31]. Furthermore, ballistic transport can be rather insensitive to edge defects because of the presence of localized edge states (e.g., in zigzag GNRs) and the dominating Dirac-like physics, that make the current flow maximally through the center of the ribbon [32]. With the advent of bottom-up fabrication techniques, long defect-free samples can be chemically synthesized with both armchair (AGNR) [33] and zigzag (ZGNR) [34] edge topologies via on-surface synthesis. Manipulation of GNRs with scanning tunneling probes has been also demonstrated [35,36], opening the possibility to build two-dimensional multiterminal graphene-based electronic circuits [37–41].

Recently, it has been shown theoretically that two crossed GNRs with a relative angle of 60° can behave as a BS for valence- and conduction-band electrons [42,43], since such four-terminal devices were found to divide the electron beam into two out of the four arms with an equal transmission probability of 50%. In this paper we analyze this possibility more generally and show that all the mentioned beam-control elements (BS, M, filters) can be realized with a suitable choice of two crossed GNRs. More specifically, we compute

*sofia.sanz@dipc.org

†thomas_frederiksen@ehu.eus

the electron transport properties of these devices in terms of the edge topology and width of the GNRs, and the precise alignment and stacking of the ribbons.

The problem is theoretically approached by means of tight-binding (TB) modeling, which is known to reproduce graphitelike systems with sufficient accuracy [44–48] while allowing one to explore a large number of systems of considerable sizes in a fast and transparent way. For instance, the geometry of a crossing between two 50-atom-wide GNRs readily comprises around 10 000 atoms. The main complexity of the modeling lies in the description of the interlayer couplings, for which we use a Slater-Koster parametrization [49] that has proven successful for describing the band structure and velocity renormalization of Dirac electrons in twisted bilayer graphene [50,51]. The employed technique can describe arbitrary device geometries and therefore allows us to also study the robustness of the predicted transport properties against variations in the intersection angle, stacking pattern, lattice deformation (uniaxial strain), inter-GNR separation, and electrostatic potential differences between the layers. With this, we give a complete analysis of the transport properties of crossed GNRs, highlight their tunability, and provide quantitative data that can serve as a guide for design optimization.

This paper is organized as follows: In Sec. II we introduce the general TB Hamiltonian used to describe the kinetics of the electrons traveling through the different devices as well as the scattering formalism used to compute transmission and reflection probabilities of incoming electron waves from the different leads. In Sec. III we present a complete analysis of the transport properties based on the key combinations of stacking pattern, edge topology, and width of the GNRs. Finally, the conclusions and remarks are provided in Sec. IV.

II. METHODOLOGY

The general setup of this study, illustrated in Fig. 1(a), comprises two infinite GNRs crossed with a relative angle $\theta = 60^\circ$ (see Sec. III A for a discussion of this choice of angle). The scattering region (intersection) breaks the translational invariance of the infinite ribbons, for which we will use the Green’s function formalism to solve the Schrödinger equation with open boundary conditions.

The system is divided into the device (scattering) region that contains the intersection between the two ribbons, and the four semi-infinite GNRs (periodic electrodes), represented as red rectangles in Fig. 1(a). The total Hamiltonian is correspondingly split into the different parts

$$H_T = H_d + \sum_{\alpha} (H_{\alpha} + H_{\alpha d}), \quad (1)$$

where H_d is the device Hamiltonian, H_{α} the α -electrode Hamiltonian, and $H_{\alpha d}$ the coupling between these two sub-systems.

A. Tight-binding Hamiltonian

The use of a local basis in combination with Green’s function techniques provides an efficient way for obtaining the transport properties in terms of microscopic parameters.

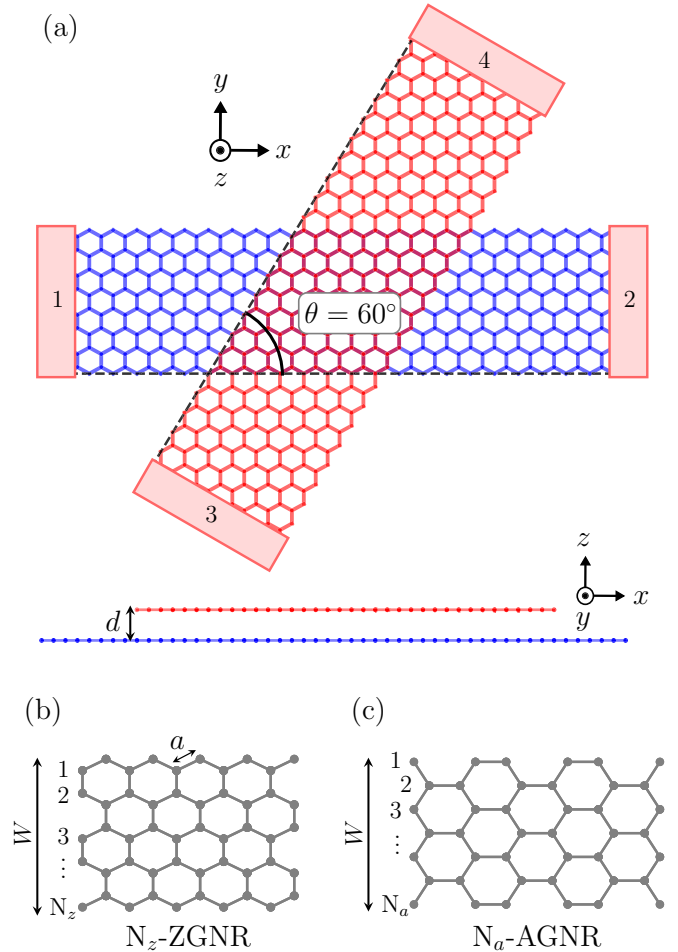


FIG. 1. Illustration of the general setup. (a) A four-terminal device is formed by two crossed 8-ZGNRs with a relative angle $\theta = 60^\circ$. The bottom (top) ribbon is drawn in blue (red) with carbon atoms at each vertex. The four semi-infinite leads, numbered 1–4, are attached in the contact regions represented with red rectangles. The ribbons lie out of plane separated by a distance d along the z axis (see side view). Definition of the width W of (b) ZGNRs and (c) AGNR in terms of the number of carbon atoms N across the ribbon. The interatomic distance is denoted by a .

We write the single-particle TB Hamiltonian in an orthogonal basis as

$$H = \sum_i \epsilon_i c_i^\dagger c_i + \sum_{ij} t_{ij} (c_i^\dagger c_j + \text{H.c.}), \quad (2)$$

where c_i^\dagger (c_i) creates (annihilates) an electron on site i with energy ϵ_i . We further define the Fermi level as $E_F = \epsilon_i$, corresponding to half-filled carbon p_z orbitals. The matrix element t_{ij} between orbitals i and j is described by Slater-Koster-type two-center π and σ bond integrals between two p_z atomic orbitals [49]

$$t_{ij} = V_{pp\pi} (1 - l^2) + V_{pp\sigma} l^2, \quad (3)$$

where l is the cosine of the angle formed between the distance vector \hat{r}_{ij} for the ij atom pair and the unit vector that defines

the z direction [cf. Fig. 1(a)], i.e., $l = \hat{r}_{ij} \cdot \hat{e}_z / |r_{ij}|$. The two-center integrals are expressed as

$$V_{pp\pi} = -t_{\parallel} e^{q_{\pi}(1 - \frac{|r_{ij}|}{a})}, \quad (4)$$

$$V_{pp\sigma} = -t_{\perp} e^{q_{\sigma}(1 - \frac{|r_{ij}|}{d})}, \quad (5)$$

where t_{\parallel} (t_{\perp}) is the *intra*-GNR (*inter*-GNR) hopping parameter between atoms separated by the interatomic (interlayer) distance fixed to $a = 1.42 \text{ \AA}$ ($d = 3.34 \text{ \AA}$) in our model (see Fig. 1). The decay rates of the bond integrals with the atomic separation, q_{σ} and q_{π} , are isotropic and therefore related by $q_{\sigma}/d = q_{\pi}/a$. This model, characterized by t_{\parallel} , t_{\perp} and the decay rate (which can be determined by fixing the second-nearest-neighbor coupling), successfully describes π electrons in twisted bilayer graphene [51]. However, it does not capture many-body effects such as, e.g., the difference in the nearest-neighbor hopping parameter for different lattice sites as in the Slonczewski-Weiss-McClure (SWM) model for graphite [45,52–54].

In this work we use $t_{\parallel} = 2.682 \text{ eV}$ and $t_{\perp} = 0.371 \text{ eV}$. For the third model parameter we refer to the in-plane next-nearest-neighbor matrix element $t' = 0.0027 \text{ eV}$. These parameters were obtained by fitting to the low-energy band structure of AB-stacked bilayer graphene simulated with SIESTA [55] as explained in the Appendix. The satisfactory agreement between TB and density functional theory (DFT) (Fig. 14) further justifies that, at least for our purposes, many-body effects such as in the SWM model can be neglected.

B. Transport calculations

In order to perform transport calculations we use the nonequilibrium Green's function (NEGF) method [56–58]. In particular, to obtain the transmission probabilities ($T_{\alpha\beta}$) between the different pairs of electrodes ($\alpha \neq \beta$), we use the Landauer-Büttiker formula [59],

$$T_{\alpha\beta} = \text{Tr}[\Gamma_{\alpha} G \Gamma_{\beta} G^{\dagger}], \quad \alpha \neq \beta, \quad (6)$$

where $\Gamma_{\alpha} = i(\Sigma_{\alpha} - \Sigma_{\alpha}^{\dagger})$ is the broadening matrix, related to the non-Hermitian part of the retarded electrode self-energy Σ_{α} , due to the coupling of the α th semi-infinite lead to the scattering center and $\alpha, \beta = 1, \dots, 4$ (cf. Fig. 1). Further,

$$G_d = \left(\mathbb{I}E - H_d - \sum_{\alpha} \Sigma_{\alpha} \right)^{-1} \quad (7)$$

is the retarded Green's function of the device region and \mathbb{I} the identity matrix (orthogonal basis). The dependency on the electron energy E of these key quantities is implicit.

The reflection probability ($T_{\alpha\alpha} = R_{\alpha}$) can be conveniently written as a difference between the bulk electrode transmission M_{α} (i.e., the number of open channels/modes in electrode α at a given energy) and the scattered part into the other electrodes ($\sum_{\beta} T_{\alpha\beta}$) as

$$R_{\alpha} = M_{\alpha} - \sum_{\beta \neq \alpha} T_{\alpha\beta}. \quad (8)$$

From Eq. (7) we can also obtain the spectral function A_{α} for states coupled to electrode α ,

$$A_{\alpha} = G \Gamma_{\alpha} G^{\dagger}. \quad (9)$$

The diagonal elements $A_{\alpha}(i, i)/2\pi$ correspond to the local density of states (DOS) at sites i of the scattering states originating from electrode α .

Computationally, we constructed the Hamiltonian matrix with the SISL package [60,61] and computed transmission probabilities and spectral DOS with TBTRANS [61].

III. RESULTS

In this section we present results for the electron transport properties through an extensive set of four-terminal devices formed by two crossed ribbons. We analyze the role of the precise stacking and alignment of the crossing area for both ZGNR- and AGNR-based devices in all their possible configurations.

A. Possible device configurations

The symmetry of the honeycomb lattice yields a perfect matching between the bottom and top GNR lattices for $\theta = 60^{\circ}$. In this situation it is expected that the maximized inter-layer coupling enhances the transfer of electrons between the ribbons, as shown in Refs. [41–43]. In Fig. S1 in the Supplemental Material (SM) [62] we performed transport calculations for crossed 8-ZGNRs both in the AA and AB stackings as a function of the crossing angle between the GNRs, where such behavior is observed for angles approaching 60° . We therefore focus the discussion on devices formed by crossed GNRs with an intersecting angle of $\theta = 60^{\circ}$. However, the inter-GNR transmission is also enhanced for angles within $[50^{\circ}, 70^{\circ}]$, which highlights the tunability of our devices. Note that experiments on twisted bilayer graphene report that the rotation angle between the layers can be precisely controlled down to fractions of a degree (0.01°) [63–65].

For a systematic analysis we begin by considering all the possible devices that can be built with two crossed AA- or AB-stacked GNRs with a relative angle of 60° . These are sketched Fig. 2. In the case of crossed ZGNRs there exist two configurations, the AB stacking [labeled AB, Fig. 2(a)] and the AA stacking [labeled AA, Fig. 2(b)]. These two geometries have different symmetries, indicated by the reflection planes (dashed lines) in Fig. 2. While AB has only one reflection symmetry, AA has two. Here, and in the following, we refer only to symmetries in the xy plane. The additional operation of reflection in the z direction to interchange the top and bottom ribbon is physically not important and therefore implicit.

In the case of AGNRs there are two different AA-stacked configurations [labeled AA-1 and AA-2, Figs. 2(c) and 2(d)], as well as two different AB-stacked configurations [labeled AB-1 and AB-2, Figs. 2(e) and 2(f)]. For instance, starting from AA-1, one can obtain AA-2 by translating the upper (red) ribbon by $-\sqrt{3}a\hat{y}$ with respect to the lower one. Similarly, AB-1 (AB-2) can be obtained from AA-1 by translating the upper (red) ribbon by $+a\hat{x}$ ($-a\hat{x}$) with respect to the lower one. Again, these four generic configurations have different symmetries as indicated in Figs. 2(c)–2(f).

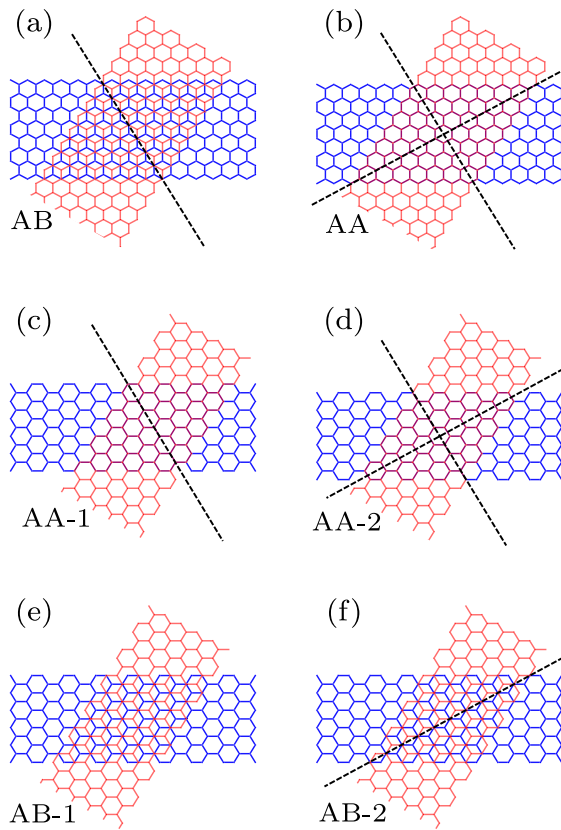


FIG. 2. Geometries of the different stackings that can be constructed from the crossing of two GNRs with a relative angle of 60° . The bottom (top) ribbon is drawn in blue (red) with carbon atoms at each vertex. For ZGNR-based devices there exists only one AA- and one AB-stacked configuration, labeled (a) AB and (b) AA (exemplified here by 8-ZGNR). For AGNR-based devices there exist two AA- and two AB-stacked configurations, labeled (c) AA-1, (d) AA-2, (e) AB-1, and (f) AB-2 (exemplified here by 11-AGNR). The dashed lines show the symmetry (reflection) planes that preserve the Hamiltonian of each crossing when such operation is applied to them.

The reflection planes imply that there are operations which leave the scattering potential (created by the intersection of the two ribbons) unchanged. This is, if we apply one or more reflections across the indicated axes, the Hamiltonian of the new device does not change. Consequently, the Green's function, and all the transport properties derived from it, will also remain unchanged under some particular electrode permutations.

Let us begin by discussing the properties of these six different configurations with particular examples constructed from 8-ZGNRs and 11-AGNRs. In Fig. 3 we show the spectral DOS of scattering electrons that come in from electrode $\alpha = 1$ as obtained from Eq. (9) for each configuration at specific energies. In this real-space representation it is easy to see where the scattered electron wave propagates after being injected into the device. The large DOS that appears in the input electrode region does not correspond to the backscattered electrons, but rather to the DOS of the incoming electrons (as we will show later on). This is also illustrated in Fig. S2 [62],

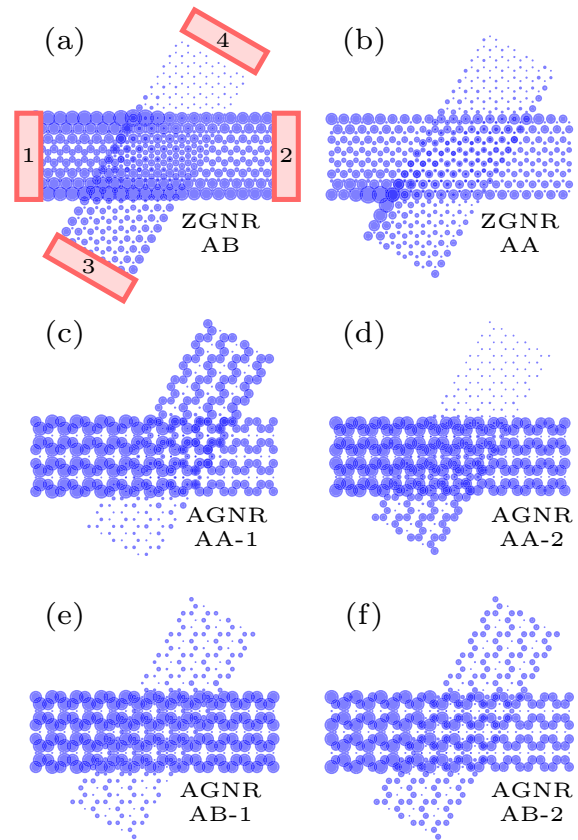


FIG. 3. Spectral DOS of scattering electrons incoming from electrode $\alpha = 1$ obtained from Eq. (9), for the specific geometries defined in Fig. 2: (a) 8-ZGNR AB, (b) 8-ZGNR AA, (c) 11-AGNR AA-1, (d) 11-AGNR AA-2, (e) 11-AGNR AB-1, and (f) 11-AGNR AB-2. The spectral DOS were calculated at $E = 200$ meV for ZGNRs and at $E = 0$ meV for AGNRs.

where we complement the results shown in Fig. 3 by plotting the bond currents between nearest-neighbor atoms, where the arrows indicate the direction of the flowing electrons.

For the ZGNR devices, Figs. 3(a) and 3(b) and Figs. S2(a) and S2(b) show that an electron injected from $\alpha = 1$ in both cases only escapes from the scattering center into electrodes $\beta = 2, 3$, i.e., terminals 1 and 4 are suppressed. This lack of backscattering (and preferential scattering into only one of the two arms of the other ribbon) is a very general and robust feature for ZGNRs which holds for different widths, stackings, and energies, and it is instrumental for the applications we have in mind. An explanation, supported by continuum-model calculations [66,67], is the valley (chirality) preservation in low-energy bands of ZGNRs. For the two AA-stacked AGNR devices, Figs. 3(c) and 3(d) and Figs. S2(c) and S2(d) show that the outgoing terminals $\beta = 1$ and $\beta = 3$ ($\beta = 4$) for AA-1 (AA-2) are suppressed. These two cases are interesting since their relative displacement of only $\sqrt{3}a\hat{y}$ leads to very different electron transport: For AA-1 the split electron turns by 60° , while for AA-2 the bend is 120° . Unlike for ZGNR devices, the suppression of two terminals is not general for all AGNR widths, and rather depends on the AGNR family, as shown in Figs. S5–S16 [62]. In the case of the two AB-stacked

ribbons, Figs. 3(e) and 3(f) show that an electron wave in these devices is scattered qualitatively (yet not quantitatively) similarly and into all outgoing electrodes.

B. Symmetry considerations

Since we deal with four-terminal devices, the matrix of transmission and reflection probabilities, Eqs. (6) and (8), has the general form

$$\mathbf{T} = \begin{pmatrix} R_1 & T_{12} & T_{13} & T_{14} \\ T_{21} & R_2 & T_{23} & T_{24} \\ T_{31} & T_{32} & R_3 & T_{34} \\ T_{41} & T_{42} & T_{43} & R_4 \end{pmatrix}. \quad (10)$$

However, due to symmetries there are not 16 independent quantities in this matrix. First, in the absence of a magnetic field, time reversal symmetry forces $T_{\alpha\beta} = T_{\beta\alpha}$. This reduces the matrix to ten independent elements, e.g., those without the dark gray background ($\alpha > \beta$) in Eq. (10). Second, the symmetries indicated in Fig. 2 reduce the number of independent elements of the matrix further. The reflection plane $y = \sin(-60^\circ)x$ maps the electrode labels (1, 2, 3, 4) \leftrightarrow (4, 3, 2, 1) with unchanged transmissions, e.g., which allows us to consider R_3, R_4, T_{24} , and T_{34} as dependent variables [four of the light gray elements in Eq. (10)]. Similarly, the reflection plane $y = \sin(30^\circ)x$ implies (1, 2, 3, 4) \leftrightarrow (3, 4, 1, 2) and R_3, R_4, T_{23} , and T_{34} as possible dependent variables (four of the light gray elements). The combination of both reflection planes further implies (1, 2, 3, 4) \leftrightarrow (2, 1, 4, 3) and R_2 and T_{23} as further dependent variables (i.e., all gray elements in this case). In summary, depending on the number of symmetries, the transmission probabilities of any given device will be fully characterized by either four, six, or ten independent matrix elements.

Figure 4 shows the full, energy-resolved transmission matrix [Eq. (10)] obtained numerically for devices formed of two crossed ZGNRs in the AB configuration for a range of different ribbon widths W . As ZGNR AB displays only one reflection plane, the transmission probabilities for these systems are, in principle, characterized by six independent quantities. However, qualitatively only four independent ones are readily identified in Fig. 4. Only upon close inspection of the data do all the expected differences emerge. The reason for the seemingly higher symmetry (corresponding to two reflection planes) is the fact that the scattering potential created by the crossings between the GNRs depends exponentially on the atomic distances between the GNRs, and therefore is dominated by the closest atom pairs. These atom pairs, shown in Fig. S3(a) [62], are in fact symmetric with respect to both reflection planes.

More generally, for all the configurations in Fig. 2 we find that the scattering potentials are dominated by terms with at least one reflection plane (Fig. S3). For all practical purposes, the effective symmetry appears higher and it suffices to describe the transmission probabilities with only four or six independent quantities.

In the following we will thus only consider it sufficient to discuss electrons incoming from terminal $\alpha = 1$. However, for

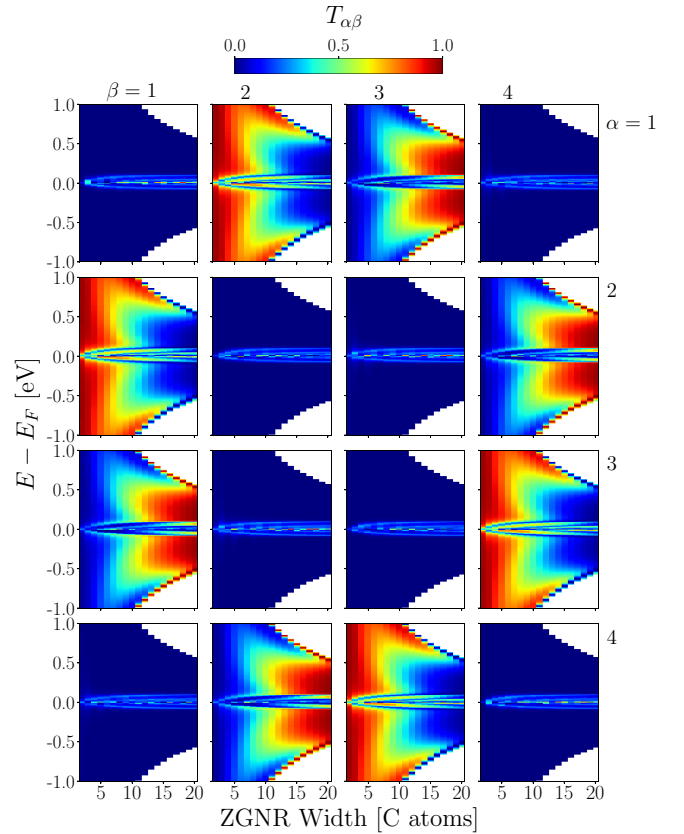


FIG. 4. Full transmission probability matrix $T_{\alpha\beta}$ between all the electrode pairs for ZGNRs crossed in the AB configuration as a function of the ribbon width W and electron energy E . Only data for the first subband are shown (white regions correspond to multiple electronic bands in the ribbons).

completeness we show the full transmission matrices for all the considered systems in Figs. S4–S16 [62].

C. Beam splitters and mirrors

Looking again at Fig. 4 and focusing on the first row (electron beam injected from terminal $\alpha = 1$), we observe distinct regimes where the devices would present particular electron quantum optical characteristics. We are especially interested in geometries for which the transmission matrix allows us to designate two input and two output electrodes in the sense that any electron sent in through one of the input ports is scattered predominantly into the two output ports with very little reflection or transmission into the other input. For instance, the green areas in the plots show where the device behaves as a BS, since they show that the electron beam is scattered only into *two* out of the four possible arms with a transmission probability that lies around $T_{12} \sim T_{13} \sim 0.5$. One can also identify regimes in which the device can work as a M where $T_{13} \sim 1$. This situation corresponds to the red areas in Fig. 4, since the electron would enter from terminal $\alpha = 1$ and turn 120° to go out *exclusively* into terminal $\beta = 3$ with low reflection. The energy dependence of the transmission functions is very symmetric with respect to the Fermi level, reflecting the approximate particle-hole symmetry characteristic

of a half-filled bipartite lattice. Nevertheless, the presence of next-nearest-neighbor couplings in our TB model in principle breaks this symmetry.

On one hand, we note that for energies close to the Fermi level ($|E - E_F| < 0.07$ eV) in Fig. 4, the electron is scattered into all four output ports, which makes this small energy window not very interesting for electron quantum optical purposes. These features probably arise due to the hybridization of states from the flat bands of the individual ribbons in the overlapping area. The band structures for both monolayer and bilayer ZGNRs are shown in Fig. S17 [62]. On the other hand, we note here that outside the low-energy region (where there is more than one electronic band) we find for all systems that reflection and interband scattering play a larger role in the electron transport through these devices, as the number of open channels (modes) grows with energy. In other words, it was not possible to identify conditions for realizing BS or M at energies with multiple subbands in the GNRs. Therefore the following discussion is focused on the energy window corresponding to a single (conduction or valence) band, since the most interesting physics related to the electron quantum optical features were identified here.

D. Quality of the realized mirrors and beam splitters

To obtain a qualitative picture across all the possible systems of the most suitable candidates for BSs or Ms, we construct in the following a figure of merit (FM). On the one hand, we look for candidate systems where a significant part of the scattered electron wave can be transferred to the other ribbon, i.e., that T_{13} or T_{14} is large. We encode this property in the quantity $\tau \equiv \max(T_{13}, T_{14})$. On the other hand, for a suitable BS or M it is important that the reflection *and* transmission to a third electrode should be small. This property is encoded as a “loss” function $\lambda \equiv R_1 + \min(T_{12}, T_{13}, T_{14})$.

Our FM is then defined as

$$FM = e^{-20\lambda} \tanh \left[\frac{1}{20} \left(\frac{1}{|\tau - 1|} - \frac{1}{|\tau - 1/2|} \right) \right]. \quad (11)$$

We use a linear color scale where BSs (FM = -1) appear as black, M’s (FM = 1) as red, and uninteresting systems (FM = 0) as white. We set FM equal to zero whenever there is more than one band per GNR at the energy considered (as it happens, e.g., for large values of $|E - E_F|$). In that case the sum of all transmission probabilities is equal to the number of bands and thus larger than 1. This case is not useful for the devices we have in mind, though a more careful analysis may show how to also use the systems in this energy range. In other words, λ determines the intensity of the plots while τ sets the color. The FM is chosen to be highly selective: It decays to about 1/2 of the maximum value for losses (=transmission probability into the undesired output ports) of about 3%. Similarly, the FM of a loss-free, but unbalanced, BS is reduced to FM = -1/2 at an imbalance of about 57:43. Figures 5 and 6 show the FM for ZGNRs and AGNRs from the metallic $3p + 2$ family, respectively, as a function of electron energy and ribbon width W . Overall, these figures show that the most interesting systems are those composed by ZGNRs or AA-stacked AGNRs. For both types of GNRs one can find devices that behave as BS or as M, respectively. For

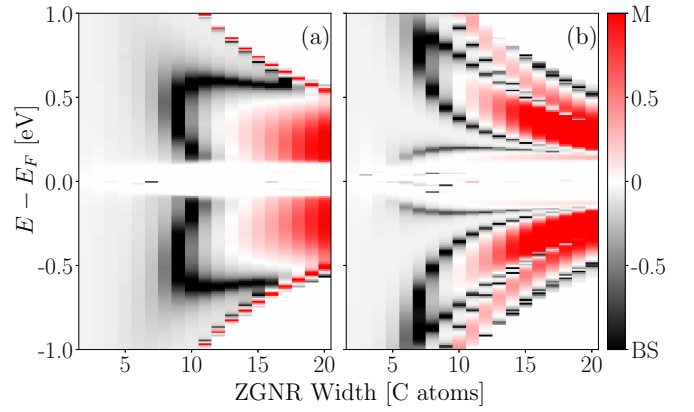


FIG. 5. Figure of merit (FM) for systems composed of ZGNRs in (a) AB or (b) AA configurations. Black and red regions correspond to situations where a given device is suitable as a BS or M, respectively. White regions are unsuitable as BS or M because of large transmission into the other but the desired output ports.

instance, Fig. 5 reflects that the 8-ZGNR devices shown in Figs. 2(a) and 2(b) are good candidates for BS, consistent with the qualitative picture of Figs. 3(a), 3(b) and 4.

For both AA and AB ZGNR devices the transmitted electron wave to the other ribbon is always bent 120° into electrode 3 (see also the full transmission matrices in Figs. 5

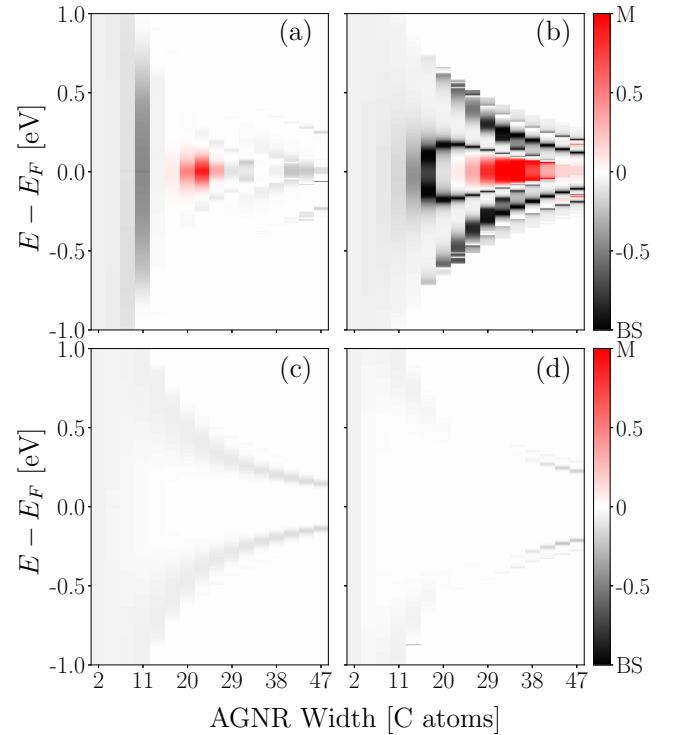


FIG. 6. Figure of merit (FM) for systems composed of AGNRs of the $3p + 2$ family with (a) AA-1, (b) AA-2, (c) AB-1, and (d) AB-2 configurations. Black and red regions correspond to situations where a given device is suitable as a BS or M, respectively. White regions are unsuitable as BS or M because of large transmission into the other but the desired output ports.

and S4 [62]). To obtain a M, where an electron incoming from electrode 1 is almost entirely transferred to electrode 3, one should choose wider ZGNRs.

For the AGNRs the situation is a little more complex. As discussed in Fig. 2, it is possible to form four different stackings (AA-1, AA-2, AB-1, and AB-2). Further, the band gap of AGNRs is determined by the overall ribbon width W , which classifies them into three distinct families $3p$, $3p + 1$, or $3p + 2$ for integer p [24,25,27,28]. This leaves us with 12 different situations, considered in terms of the full transmission matrices in Figs. S5–S16 [62]. We find that the most interesting devices are those built with $(3p + 2)$ -AGNRs in the AA-stacked configurations. However, compared with the ZGNRs, the parameter space for desirable devices is more restricted and the losses are generally larger. Independent of width, the AB-stacked configurations lead to scattering of the electron wave into all terminals.

We also note here that the qualitative difference mentioned in Sec. III A between the 60° turn of the transferred electron wave for AA-1 configuration versus the 120° turn for AA-2 is a robust feature across the different families (Figs. S5–S16 [62]). Additionally, we also find very thin white regions that do not correspond to high losses but to $T_{12} \sim 1$, immersed in red—e.g., seen for $W = 10$ – 15 in Fig. 5(b) and for $W > 20$ in Fig. 6(b). This suggests that crossed GNRs can also work as energy filters. These T_{12} (T_{13}) peaks (dips), also plotted in Fig. S18 for clarification, become narrower as the width of the ribbons grows, which enhances the energy selection.

E. Robustness of the discussed properties

So far we have discussed the different transport properties that can be found in the ideal case, that is commensurate GNRs (AA or AB stacking) with a relative angle of $\theta = 60^\circ$. However, precise control of the device geometry is likely a significant experimental challenge. In this section we therefore proceed to test the robustness of the transport properties against some perturbations of this ideal situation. More specifically, we explore now the exact roles of the intersection angle, deviations from the idealized stacking pattern, lattice deformations via uniaxial strain, variation of the inter-GNR separation, and electrostatic potential differences between the two ribbons.

Since we concluded above that ZGNR devices may be the best candidates for building electron quantum optical setups, we will focus the following discussion around them. We take as the reference device the crossing of two AB-stacked 8-ZGNRs [Fig. 2(a)] and compute the transmission probabilities from terminals $\alpha = 1$ to $\beta = 1, 2, 3, 4$ for each of the above-mentioned perturbations. The AA-stacked 8-ZGNRs were found to display qualitatively similar trends as can be seen from Figs. S19–S23 [62]. We will see that the low-loss property of these devices is thus preserved for the applied variations and in some cases the FM is even significantly enhanced, indicating that almost perfect BS or M could be obtained by tuning the above-mentioned parameters.

1. Intersection angle

We first discuss the effect of small rotations of the on-top ribbon starting from the ideal configuration where $\theta = 60^\circ$. For instance, the twisting angle between the ribbons

introduces separated domains of weakly and strongly coupled atoms in the crossing area that might affect the transport properties of these junctions [68]. To isolate the effect of the intersection angle from that of the precise stacking pattern (translation), we apply the rotation around the center of the scattering region (crossing) indicated with a black dot in Fig. 7(a). This ensures that the center of the junction remains unchanged and the effect of the rotation angle perturbs mostly the edge zones of the crossing.

Figure 8 shows the reflection and transmission probabilities for varying angles $\delta\theta = \pm 2^\circ$. The results for the reference case of $\theta = 60^\circ$ are shown as black lines in all panels. We first note that the reflection probability R_1 does not vary much from its initial value ~ 0 . The same holds for the (unwanted) transmission T_{14} . The main effect is the precise distribution between the transmissions T_{12} and T_{13} .

This shows that the angle can be a physical knob to tune the transmission ratio between the two outgoing terminals of a BS. On the other hand, the approximate particle-hole symmetry found for the ideal AB or AA stacking goes away as the lattice mismatch grows. The reflection plane shown in Fig. 2(a) is also lost for $\delta\theta \neq 0$ (and other geometrical distortions), however, we still identify only four qualitative independent elements in \mathbf{T} for all cases.

2. Lateral translations

To study the precise lattice matching in the crossing area, we performed a series of calculations where the top GNR is translated by Δ_x along the x axis with respect to the bottom GNR [see Fig. 7(b)]. Due to periodicity it is sufficient to consider translation vectors with modulus $\Delta_x \leq 2a \sin(60^\circ) \approx 2.46 \text{ \AA}$.

Figure 9 shows the reflection and transmission probabilities as a function of such translations. Again, the results for the ideal AB stacking are shown as black lines. As for small variations in the intersection angle, even though this geometrical distortion also intensifies the particle-hole asymmetry as the system goes away from the ideal stacking, R_1 and T_{14} remain rather unaffected by translation. In other words, the low-loss situation of these devices is robust with respect to translations. On the other hand, the inter-ribbon transfer process of electrons becomes mostly less effective. We interpret this as due to an overall elongation of interlayer atom distances. For this reason T_{13} slightly decreases with the translating of the on-top ribbon, while T_{12} slightly increases with respect to the reference curves (black lines) for most of the cases.

3. Uniaxial strain

For experimentally grown GNRs it is relevant to consider the strain-induced deformations, e.g., a lattice mismatch with the supporting substrate [69]. But strain can also be applied in a controlled way [70], for example, using a piezoelectric substrate for shrinking or elongating samples by applying a bias voltage [71]. In these directions we study here a simplified scenario of applying the same uniaxial strain ε to both GNRs in the device as defined in Fig. 7(c). As explained in the case of variation of the intersecting angle, to isolate the effect of strain on the transport properties of the device, we apply

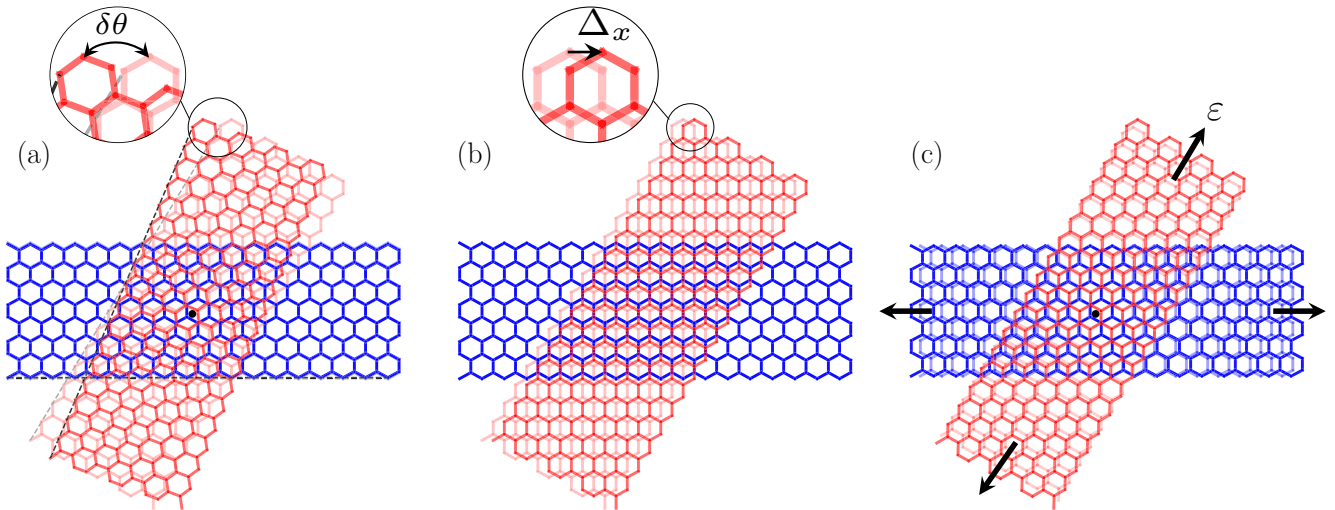


FIG. 7. Sketch of the geometrical distortions applied to the AB-stacked 8-ZGNR device. (a) Rotation by some small angle $\delta\theta$ around the configuration with a relative angle of $\theta = 60^\circ$. The rotation is performed around the center of the scattering region, indicated by a black dot. (b) Translation of the on-top ribbon with respect to the lower one by an amount Δx along the x axis. (c) Strain ϵ is applied along the periodic direction of each ribbon while keeping the center of the scattering (black dot) region unchanged.

the strain with respect to the center of the crossing area [as depicted in Fig. 7(c)]. Otherwise arbitrary lattice mismatches could further modify the transmission curves. The main effect of uniaxial strain is that it induces an anisotropy between the atomic bonds and therefore in the electronic structure of the individual GNRs. Additionally, a strain induces some mismatch of the lattices in the crossing region, and therefore changes the scattering potential. The transport properties of the devices are therefore expected to be sensitive to strain. Figure 10 explores uniaxial strain in the range from -1% (compression) to 1% (stretching). Again, both R_1 and T_{14} are not affected by the lattice deformation, and remain very close to zero in the single-channel energy region.

Looking at the intra- and inter-transmissions T_{12} and T_{13} , the curves vary smoothly around the reference values (black lines). The effects of compression and stretching of the GNRs are quite different: GNR compression causes T_{12} (T_{13}) to increase (decrease), while stretching has the opposite effect. Again, strain can be seen as a physical knob to engineer the device properties. For instance, a strain of $\epsilon \sim 1\%$ brings the system closer to the ideal BS with $T_{12} = T_{13} = 50\%$, while keeping both $R_1 \sim T_{14} \sim 0$. In fact, our FM graph of Fig. 10(e) shows a significant enhancement of the performance of the device as a BS when stretching the device.

4. Interlayer separation

The exponential distance dependence of electron transport in the tunneling regime suggests that the separation between ribbons may considerably affect the transport properties. Figure 11 shows the reflection and transmission probabilities as a function of the GNR separation d within an interval determined by $\pm 0.15 \text{ \AA}$ around a typical van der Waals distance $d = 3.34 \text{ \AA}$ [43,72,73] (black lines in all panels). Apart from the flat-band energy region very close to $E = E_F$, the loss channels characterized by R_1 and T_{14} are largely unaffected.

The main effect of varying d is to control the ratio between the intra- and inter-transmissions T_{12} and T_{13} , which varies smoothly to almost 0:1 as the ribbon separation d is decreased. In the other direction, the ratio goes (unsurprisingly) to 1:0 as the ribbon separation is increased and therefore eventually become decoupled.

The strong variation with the inter-GNR separation suggests that this is a key parameter to tune the transport properties. An ideal 50:50 BS may thus be obtained by applying an external force to the junction for $d \sim 3.30 \text{ \AA}$, while a perfect M is found for $d < 3.20 \text{ \AA}$, as seen in Fig. 11(e), where the plateaus at $FM = 1$ show this behavior. The possibility to use such electromechanical switching has been also proposed to be used for suspended multilayer graphene [74], crossed AGNRs [43], and crossed carbon nanotubes [75].

5. Electrostatic potential differences

Here, we discuss the effect of an electrostatic potential difference between the two ribbons. This could, for instance, correspond to an experimental situation where a bias voltage is applied to the GNR electrodes. We consider a potential difference V that modifies uniformly the on-site energies to $\epsilon_i - E_F = -V/2$ (and consequently the chemical potentials of the electrodes) of the top (red) ribbon and $\epsilon_i - E_F = V/2$ of the bottom (blue) ribbon (see Fig. 1).

Figure 12 shows the reflection and transmission probabilities for the range $|V| \leq 0.5 \text{ V}$. Drastic changes are observed in the energy range between the electrode chemical potentials $[-V/2, V/2]$, where valence bands (VBs) and conduction bands (CBs) of the two GNRs now overlap. In fact, the mixing of VBs and CBs leads to an interchange of the propagation direction: A transferred electron in the bias window turns 60° instead of 120° . In fact, our FM [Fig. 12(e)] shows that the performance of the device is enhanced in the energy window $|E - E_F| \leq V/2$, compared to the unbiased case (black curve). In contrast, the single-channel energy region slightly

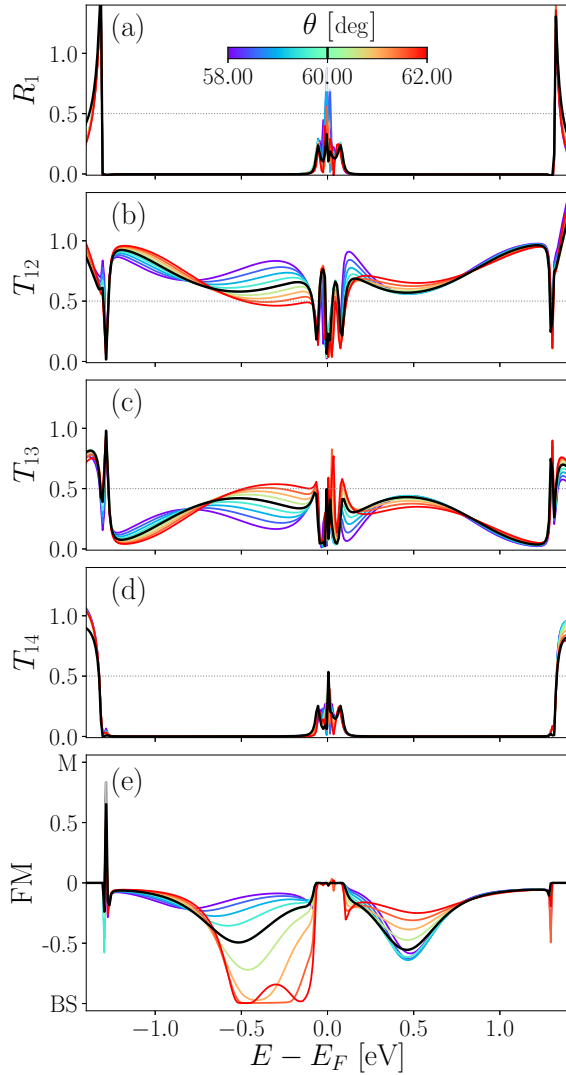


FIG. 8. Variation with respect to the rotation angle between two AB-stacked 8-ZGNRs. Reflection and transmission probabilities, (a) R_1 (b) T_{12} , (c) T_{13} , and (d) T_{14} , and (e) figure of merit as a function of the incoming electron energy $E - E_F$, obtained for different relative angles (θ) between the ribbons (color lines). The reference probabilities ($\theta = 60^\circ$) are plotted in black solid lines.

shrinks, as the chemical potential shifting produces the edge of the single-mode part of the CB (VB) of the bottom (top) ribbon to overlap with more than one mode in the top (bottom) ribbon. The presence of multiple bands in any of the incoming or outgoing electrodes is responsible for the larger reflection and transmission into the other output, e.g., as it happens for energies $|E - E_F| > 1.0$ eV in Figs. 12(a) and 12(d).

Outside the bias window the curves are hardly changed, reflecting a low variability of the transport properties even when the elastically transferred electron wave to the other ribbon is now propagating with a different momentum due to the energy offsets of their band structures.

IV. CONCLUSIONS AND OUTLOOK

In this paper we studied the electronic transport properties of four-terminal devices formed by two intersecting GNRs

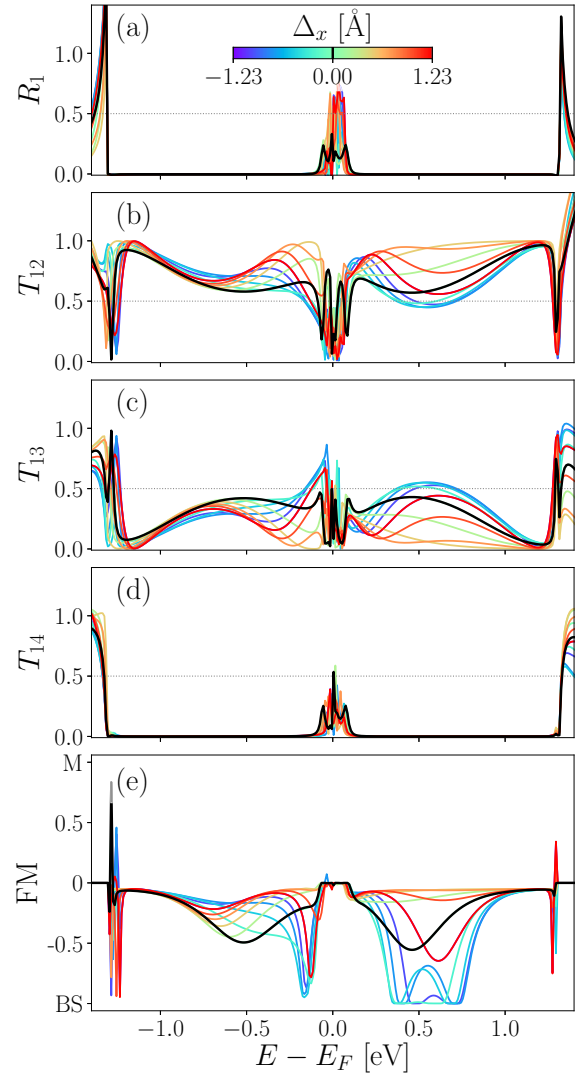


FIG. 9. Variation with respect to the relative lateral displacement between two AB-stacked 8-ZGNRs. Reflection and transmission probabilities, (a) R_1 (b) T_{12} , (c) T_{13} , and (d) T_{14} , and (e) figure of merit as a function of electron energy $E - E_F$, obtained for different translation distances along the x axis (Δ_x) of the on-top ribbon (color lines). The reference probabilities ($\Delta_x = 0$) are plotted in black solid lines.

with a nominal crossing angle of $\theta = 60^\circ$. We presented a complete classification and characterization of the different functionalities that can be found in these type of junctions by varying the edge topology of the GNRs (zigzag or armchair), stacking sequence (AA or AB), width of the ribbons, and energy for the propagating electrons in the valence or conduction bands.

We determined the number of independent transmission probability matrix elements in Eq. (10) that fully characterize their transport behavior: 10, 6, or 4 depending on the degree of symmetry that a given device displays. In practice, however, we found that for low-energy electrons it suffices qualitatively to describe the transmission probabilities with only four independent elements. The reason for this is the fact that the dominant part of the scattering potential contains

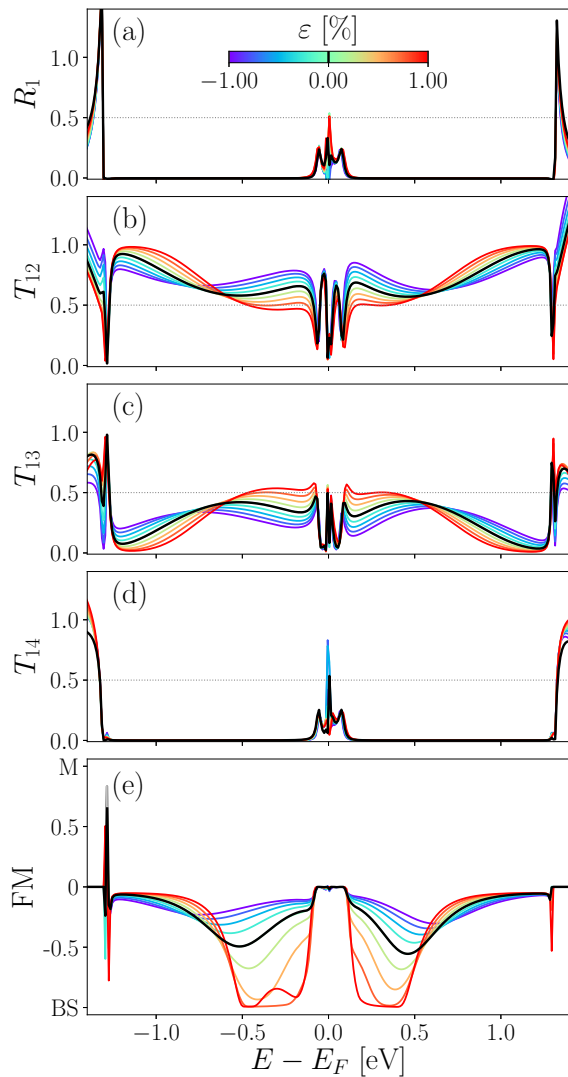


FIG. 10. Variation with respect to the applied uniaxial strain ε along the periodic direction of each GNR for the two AB-stacked 8-ZGNRs. Reflection and transmission probabilities, (a) R_1 (b) T_{12} , (c) T_{13} , and (d) T_{14} , and (e) figure of merit as a function of electron energy $E - E_F$, obtained for different uniaxial strain ε applied to both GNRs along the nonconfined direction (color lines). The reference probabilities ($\varepsilon = 0$) are plotted in black solid lines.

more symmetries than that of the device geometry as a whole. Implicitly, this result also means that the strict geometrical symmetry behind the systems is not critical for the GNR crossings to function as beam splitters.

Besides the BS property, we also identified other interesting electron quantum optical functionalities of these devices. For instance, depending on the GNR width and electron energy the device can also behave as a mirror or an energy filter.

Interestingly, for AA-stacked AGNRs we discovered that there exist two different configurations (AA-1 and AA-2) that show little geometrical difference but behave very differently from each other in terms of the electron transport for low-energy electrons. In the particular case of $3p + 2$ -AGNR crossings, the electron beam is only allowed to turn 60° for

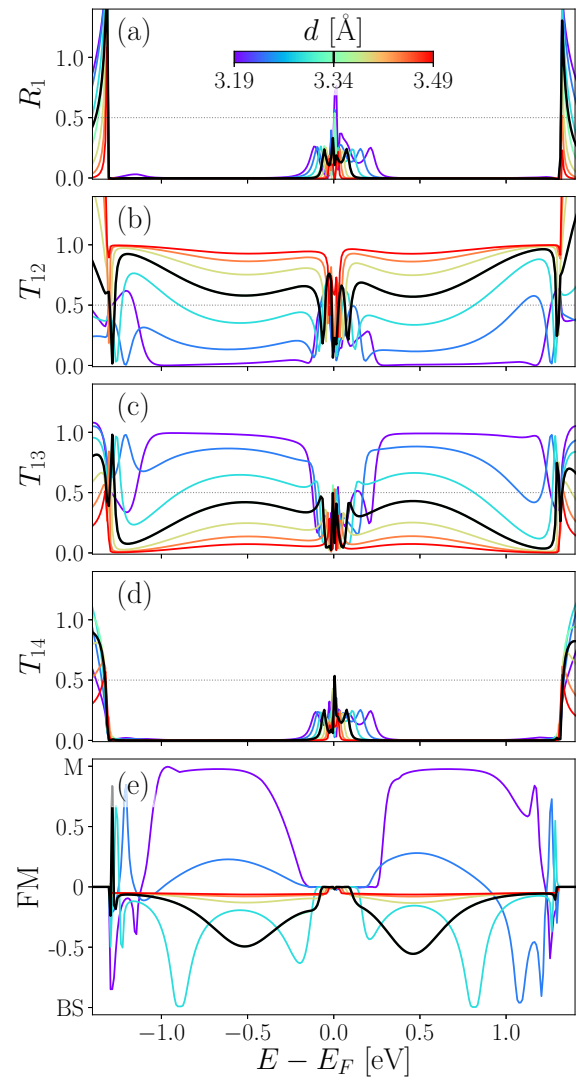


FIG. 11. Variation with respect to the inter-GNR separation of two AB-stacked 8-ZGNRs. Reflection and transmission probabilities, (a) R_1 (b) T_{12} , (c) T_{13} , and (d) T_{14} , and (e) figure of merit as a function of electron energy $E - E_F$ and inter-GNR separation d (color lines). The reference probabilities ($d = 3.34 \text{ \AA}$) are plotted in black solid lines.

the AA-1 configuration, as opposed to 120° for the AA-2 configuration. On the other hand, AB-stacked AGNR devices do not show good electron quantum optical features due to the comparatively larger losses and low inter-GNR transmission. Unfortunately, AA-stacked configurations are probably harder to realize in practice (not the most stable energetically) compared to the AB-stacked one [76]. Combined with a generally larger variability of the AGNR transport behavior, these facts indicate that ZGNRs are more interesting objects for the considered device applications than AGNRs.

We further tested the robustness of the predicted transport properties by studying small variations on the intersecting angle between the ribbons, lattice matching in the crossing area, uniaxial strain, interlayer separation, and finite potential differences for devices composed of 8-ZGNRs. While the overall qualitative behavior was found to be robust under

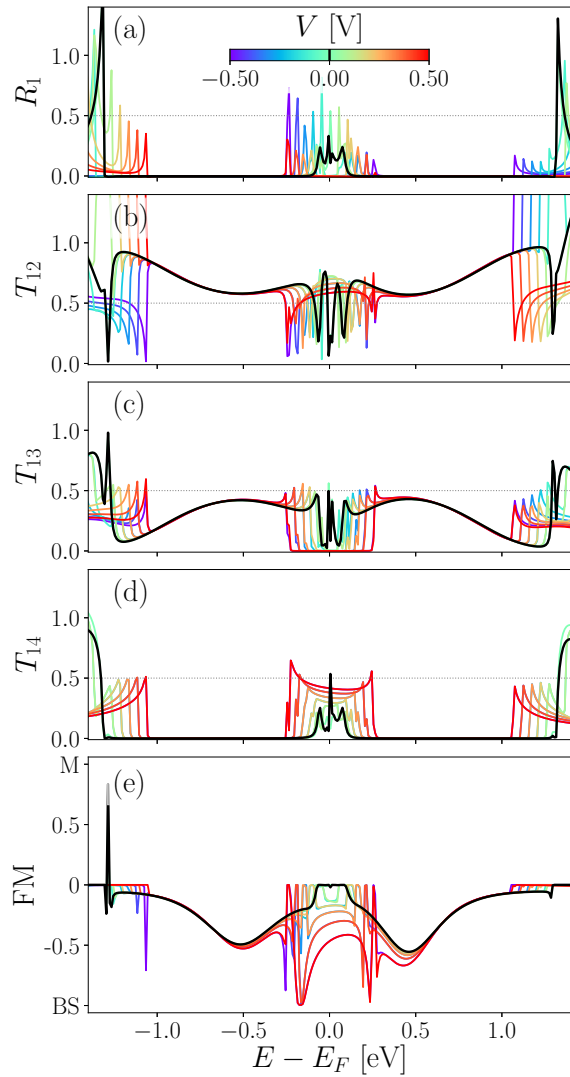


FIG. 12. Variation with respect to potential differences V between the two AB-stacked 8-ZGNRs. Reflection and transmission probabilities, (a) R_1 (b) T_{12} , (c) T_{13} , and (d) T_{14} , and (e) figure of merit as a function of electron energy $E - E_F$, obtained for different values of V (colored lines). The reference probabilities ($V = 0$) are plotted in black solid lines.

these modifications, a strong quantitative response can be obtained—indicating the need to control these effects as well as their potential for *tuning* the crossed-GNR devices. On the other hand, in this work we considered the situation of a spin-degenerate electronic structure. However, ZGNRs have been predicted to develop spin-polarized states localized along the edges of the ribbons close to the Fermi level [24]. This suggests that additional spin-dependent effects could emerge in these devices. The interplay with the physics discussed here could become an interesting topic for future research.

For electron quantum optics applications, the central feature of the considered devices is that they coherently distribute incoming electrons in the intended output ports. In our model, with a precisely given unitary scattering matrix and without considering environmental degrees of freedom, all the considered devices process the input coherently. The analysis of the

operative decoherence processes in GNR-based devices is an important task for future work. In particular, a single pure-state electron injected into one arm of a BS device discussed here is mapped to an (mode-)entangled state of the output ports. Such entanglement could be verified experimentally, for example, by measuring the state’s Bell correlations as discussed in Ref. [13]. A second basic application of the BS device is the Hanbury Brown–Twiss setup [8–11], which can be used to study the indistinguishability of electrons prepared in different input ports by the observation of antibunching in the output ports of the BS. A theoretical analysis of these experiments would include the investigation of the influence of environmental degrees of freedom (phonons, electrons in the substrate, or fluctuating perturbations such as the ones discussed in Sec. III E), and, in the case of the Hanbury Brown–Twiss setup, also the effect of the interaction between electrons in the BS. An important prerequisite for all such experiments are methods to inject single electrons in a well-defined mode and to reliably detect them.

Finally, we envision that the functionalities presented here may be interesting as fundamental building blocks in larger electronic networks based on GNRs. For instance, with four GNRs one could construct the electronic analog of the Mach-Zehnder interferometer, consisting of two beam splitters and two oriented mirrors at the intersection of pairwise parallel ribbons. Such a versatile setup, sensitive to the relative phase shift between two spatially separated pathways, has a wide range of quantum technology applications, e.g., metrology, entanglement, cryptography, and information processing [18].

ACKNOWLEDGMENTS

This work was supported by the project Spanish Ministerio de Economía y Competitividad (MINECO) through the Grants no. FIS2017-83780-P (Graphene Nanostructures “GRANAS”) and no.MAT2016-78293-C6-4R, the Basque Departamento de Educación through the PhD fellowship no. PRE_2019_2_0218 (S.S.), the University of the Basque Country through the Grant no. IT1246-19, and the European Union (EU) through Horizon 2020 (FET-Open project SPRING Grant no. 863098).

APPENDIX: COMPARISON WITH DFT CALCULATIONS

In this Appendix we compare the results presented in the main text with DFT, another popular theoretical approach used in the field of solid state physics. In particular, we choose to compute the electronic structure of AB-stacked bilayer graphene as a model system to establish suitable parameters for the general TB Hamiltonian introduced in Sec. II. We further simulate the electron transport characteristics of the specific device geometries shown in Fig. 2 for detailed benchmarking.

We employ the self-consistent DFT and NEGF methods as implemented in the SIESTA/TRANSIESTA [55,61,77] packages. All calculations of this kind used the van der Waals (vdW) density functional [78] with the modified exchange by Klimeš *et al.* [79]. The core electrons were described with Troullier-Martins pseudopotentials [80] and a double- ζ basis set defined with a 30 meV energy shift was used to

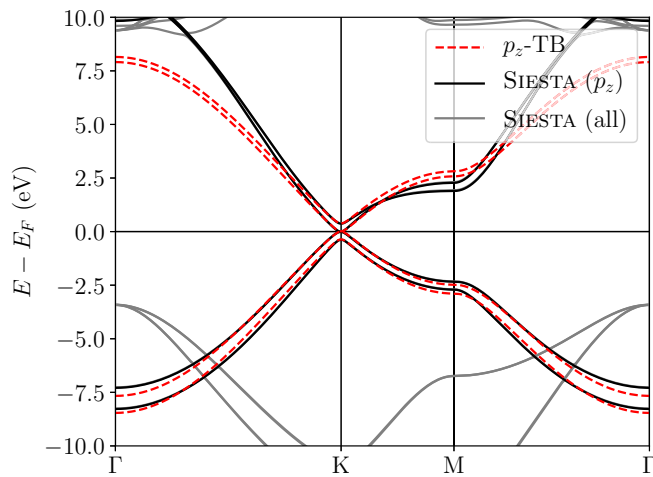


FIG. 13. Band structure of AB-stacked bilayer graphene along the Γ - K - M - Γ path of the Brillouin zone, obtained with DFT (black and gray solid lines) and TB methods (red dashed lines), with the fitted hopping parameters described in the text. The bond length is set to $a = 1.42$ Å and the interlayer separation to $d = 3.34$ Å. Black lines correspond to the graphene π bands (formed by the p_z orbitals) while the gray lines show the graphene σ bands absent in the TB model.

expand the valence-electron wave functions. The fineness of the real-space integration mesh was defined using a 350 Ry energy cutoff. All carbon atoms were saturated at the edges with hydrogen atoms.

Figure 13 shows the calculated electronic bands along the Γ - K - M - Γ path of the Brillouin zone of AB-stacked bilayer graphene obtained with SIESTA [55]. Given the usage of a double- ζ basis set, the orthogonal σ and π bands have simple representations in terms of the $\{s, p_x, p_y\}$ and $\{p_z\}$ basis orbitals, respectively. To map the DFT electronic structure onto the effective TB model in Eqs. (2)–(5), it is thus sufficient to consider only the p_z part of the DFT Hamiltonian. Since we are interested in the low-energy physics, we fitted the TB bands inside an energy window of $|E - E_F| \leq 2$ eV using nonlinear least squares and obtained the following optimal hopping parameters used in the main text: $t_{\parallel} = 2.682$ eV, $t' = 2.7$ meV, and $t_{\perp} = 0.371$ eV. The corresponding TB bands with these parameters are plotted in red dashed lines in Fig. 13, showing a very good agreement in the energy range of relevance in this work. Albeit unnecessary for the purposes here, we note that the significant deviations at the π

band edges can readily be improved with a nonorthogonal TB

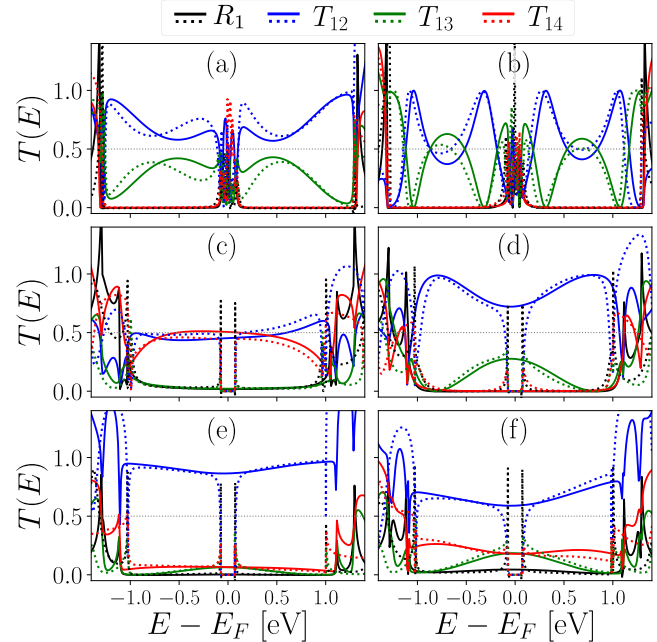


FIG. 14. Reflection and transmission probabilities R_1 (black), T_{12} (blue), T_{13} (green), and T_{14} (red), obtained with both TB (solid lines) and DFT (dotted lines) methods, through the devices of Fig. 2: two crossed 8-ZGNRs in configuration (a) AB and (b) AA, and two crossed 11-AGNRs in configuration (c) AA-1, (d) AA-2, (e) AB-1, and (f) AB-2.

model by introduction of additional parameters for the overlap matrix.

Having fixed the parameters for the TB model, we proceed to compare it against the derived transport properties from DFT-NEGF for the six characteristic devices shown Fig. 2. Figure 14 shows the computed reflection and transmission probabilities from TB (solid lines) and DFT (dotted lines) within an energy window of $|E - E_F| \lesssim 1.5$ eV. Apart from different magnitudes of the AGNR band gap (known to be related to edge effects ignored in this TB modeling [25]), the two models only show minor numerical differences. Overall, the two models provide very similar shapes and quantitative results for the transmission functions. From Figs. 13 and 14 we therefore conclude that the TB method used in the main text provides an accurate description of the essential physics in the energy range we are interested in here.

- [1] J. Splettstoesser and R. J. Haug, Special issue: Single-electron control in solid state devices, *Phys. Status Solidi B* **254**, 1770213 (2017).
- [2] C. Bäuerle, D. C. Glattli, T. Meunier, F. Portier, P. Roche, P. Rouleau, S. Takada, and X. Waintal, Coherent control of single electrons: A review of current progress, *Rep. Prog. Phys.* **81**, 056503 (2018).
- [3] Y. Ji, Y. Chung, D. Sprinzak, M. Heiblum, D. Mahalu, and H. Shtrikman, An electronic Mach-Zehnder interferometer, *Nature (London)* **422**, 415 (2003).

- [4] P. Rouleau, F. Portier, D. C. Glattli, P. Roche, A. Cavanna, G. Faini, U. Gennser, and D. Mailly, Finite bias visibility of the electronic Mach-Zehnder interferometer, *Phys. Rev. B* **76**, 161309(R) (2007).
- [5] Y. Zhang, D. T. McClure, E. M. Levenson-Falk, C. M. Marcus, L. N. Pfeiffer, and K. W. West, Distinct signatures for Coulomb blockade and Aharonov-Bohm interference in electronic Fabry-Pérot interferometers, *Phys. Rev. B* **79**, 241304(R) (2009).
- [6] D. T. McClure, Y. Zhang, B. Rosenow, E. M. Levenson-Falk, C. M. Marcus, L. N. Pfeiffer, and K. W. West, Edge-State

- Velocity and Coherence in a Quantum Hall Fabry-Pérot Interferometer, *Phys. Rev. Lett.* **103**, 206806 (2009).
- [7] E. Carbonell-Sanromà, P. Brandimarte, R. Balog, M. Corso, S. Kawai, A. Garcia-Lekue, S. Saito, S. Yamaguchi, E. Meyer, D. Sánchez-Portal *et al.*, Quantum dots embedded in graphene nanoribbons by chemical substitution, *Nano Lett.* **17**, 50 (2017).
- [8] M. Henny, S. Oberholzer, C. Strunk, T. Heinzel, K. Ensslin, M. Holland, and C. Schönberger, The fermionic Hanbury Brown and Twiss experiment, *Science* **284**, 296 (1999).
- [9] W. D. Oliver, J. Kim, R. C. Liu, and Y. Yamamoto, Hanbury Brown and Twiss-type experiment with electrons, *Science* **284**, 299 (1999).
- [10] P. Samuelsson, E. V. Sukhorukov, and M. Büttiker, Two-Particle Aharonov-Bohm Effect and Entanglement in the Electronic Hanbury Brown-Twiss setup, *Phys. Rev. Lett.* **92**, 026805 (2004).
- [11] I. Neder, N. Ofek, Y. Chung, M. Heiblum, D. Mahalu, and V. Umansky, Interference between two indistinguishable electrons from independent sources, *Nature (London)* **448**, 333 (2007).
- [12] J. Splettstoesser, P. Samuelsson, M. Moskalets, and M. Büttiker, Two-particle Aharonov-Bohm effect in electronic interferometers, *J. Phys. A: Math. Theor.* **43**, 354027 (2010).
- [13] D. Dasenbrook, J. Bowles, J. B. Brask, P. P. Hofer, C. Flindt, and N. Brunner, Single-electron entanglement and nonlocality, *New J. Phys.* **18**, 043036 (2016).
- [14] C. H. Bennett, G. Brassard, C. Crépeau, R. Jozsa, A. Peres, and W. K. Wootters, Teleporting an Unknown Quantum State via Dual Classical and Einstein-Podolsky-Rosen Channels, *Phys. Rev. Lett.* **70**, 1895 (1993).
- [15] T. Debarba, F. Iemini, G. Giedke, and N. Friis, Teleporting quantum information encoded in fermionic modes, *Phys. Rev. A* **101**, 052326 (2020).
- [16] E. Bocquillon, V. Freulon, J.-M. Berroir, P. Degiovanni, B. Plaçaïs, A. Cavanna, Y. Jin, and G. Fève, Coherence and indistinguishability of single electrons emitted by independent sources, *Science* **339**, 1054 (2013).
- [17] V. Giovannetti, D. Frustaglia, F. Taddei, and R. Fazio, Electronic Hong-Ou-Mandel interferometer for multimode entanglement detection, *Phys. Rev. B* **74**, 115315 (2006).
- [18] A. Sarkar, T. K. Bhattacharyya, and A. Patwardhan, Quantum logic processor: Implementation with electronic Mach-Zehnder interferometer, *Appl. Phys. Lett.* **88**, 213113 (2006).
- [19] P. Rickhaus, P. Makk, M.-H. Liu, K. Richter, and C. Schönberger, Gate tuneable beamsplitter in ballistic graphene, *Appl. Phys. Lett.* **107**, 251901 (2015).
- [20] S. Chen, Z. Han, M. M. Elahi, K. M. M. Habib, L. Wang, B. Wen, Y. Gao, T. Taniguchi, K. Watanabe, J. Hone *et al.*, Electron optics with p-n junctions in ballistic graphene, *Science* **353**, 1522 (2016).
- [21] K. Nakada, M. Fujita, G. Dresselhaus, and M. S. Dresselhaus, Edge state in graphene ribbons: Nanometer size effect and edge shape dependence, *Phys. Rev. B* **54**, 17954 (1996).
- [22] M. Fujita, K. Wakabayashi, K. Nakada, and K. Kusakabe, Peculiar localized state at zigzag graphite edge, *J. Phys. Soc. Jpn.* **65**, 1920 (1996).
- [23] F. Schwierz, Graphene transistors, *Nat. Nanotechnol.* **5**, 487 (2010).
- [24] Y.-W. Son, M. L. Cohen, and S. G. Louie, Half-metallic graphene nanoribbons, *Nature (London)* **444**, 347 (2006).
- [25] Y.-W. Son, M. L. Cohen, and S. G. Louie, Energy Gaps in Graphene Nanoribbons, *Phys. Rev. Lett.* **97**, 216803 (2006).
- [26] M. Y. Han, B. Özyilmaz, Y. Zhang, and P. Kim, Energy Band-Gap Engineering of Graphene Nanoribbons, *Phys. Rev. Lett.* **98**, 206805 (2007).
- [27] L. Yang, C.-H. Park, Y.-W. Son, M. L. Cohen, and S. G. Louie, Quasiparticle Energies and Band Gaps in Graphene Nanoribbons, *Phys. Rev. Lett.* **99**, 186801 (2007).
- [28] T. Wassmann, A. P. Seitsonen, A. M. Saitta, M. Lazzeri, and F. Mauri, Structure, Stability, Edge States, and Aromaticity of Graphene Ribbons, *Phys. Rev. Lett.* **101**, 096402 (2008).
- [29] S. Minke, J. Bundesmann, D. Weiss, and J. Eroms, Phase coherent transport in graphene nanoribbons and graphene nanoribbon arrays, *Phys. Rev. B* **86**, 155403 (2012).
- [30] J. Baringhaus, M. Ruan, F. Edler, A. Tejada, M. Sicot, A. Taleb-Ibrahimi, A.-P. Li, Z. Jiang, E. H. Conrad, C. Berger *et al.*, Exceptional ballistic transport in epitaxial graphene nanoribbons, *Nature (London)* **506**, 349 (2014).
- [31] J. Aproz, S. R. Power, P. Bampoulis, S. Roche, A.-P. Jauho, H. J. W. Zandvliet, A. A. Zakharov, and C. Tegenkamp, Ballistic tracks in graphene nanoribbons, *Nat. Commun.* **9**, 4426 (2018).
- [32] L. P. Zârbo and B. K. Nikolić, Spatial distribution of local currents of massless Dirac fermions in quantum transport through graphene nanoribbons, *Europhys. Lett.* **80**, 47001 (2007).
- [33] J. Cai, P. Ruffieux, R. Jaafar, M. Bieri, T. Braun, S. Blankenburg, M. Muoth, A. P. Seitsonen, M. Saleh, X. Feng *et al.*, Atomically precise bottom-up fabrication of graphene nanoribbons, *Nature (London)* **466**, 470 (2010).
- [34] P. Ruffieux, S. Wang, B. Yang, C. Sánchez-Sánchez, J. Liu, T. Dienel, L. Talirz, P. Shinde, C. A. Pignedoli, D. Passerone *et al.*, On-surface synthesis of graphene nanoribbons with zigzag edge topology, *Nature (London)* **531**, 489 (2016).
- [35] M. Koch, F. Ample, C. Joachim, and L. Grill, Voltage-dependent conductance of a single graphene nanoribbon, *Nat. Nanotechnol.* **7**, 713 (2012).
- [36] S. Kawai, A. Benassi, E. Gneco, H. Söde, R. Pawlak, X. Feng, K. Müllen, D. Passerone, C. A. Pignedoli, P. Ruffieux *et al.*, Superlubricity of graphene nanoribbons on gold surfaces, *Science* **351**, 957 (2016).
- [37] D. A. Areshkin and C. T. White, Building blocks for integrated graphene circuits, *Nano Lett.* **7**, 3253 (2007).
- [38] T. Jayasekera and J. W. Mintmire, Transport in multiterminal graphene nanodevices, *Nanotechnology* **18**, 424033 (2007).
- [39] L. Jiao, L. Zhang, L. Ding, J. Liu, and H. Dai, Aligned graphene nanoribbons and crossbars from unzipped carbon nanotubes, *Nano Res.* **3**, 387 (2010).
- [40] B. G. Cook, P. Dignard, and K. Varga, Calculation of electron transport in multiterminal systems using complex absorbing potentials, *Phys. Rev. B* **83**, 205105 (2011).
- [41] A. R. Botello-Méndez, E. Cruz-Silva, J. M. Romo-Herrera, F. López-Urías, M. Terrones, B. G. Sumpter, H. Terrones, J.-C. Charlier, and V. Meunier, Quantum transport in graphene nanonetworks, *Nano Lett.* **11**, 3058 (2011).
- [42] L. R. F. Lima, A. R. Hernández, F. A. Pinheiro, and C. Lewenkopf, A 50/50 electronic beam splitter in graphene nanoribbons as a building block for electron optics, *J. Phys.: Condens. Matter* **28**, 505303 (2016).
- [43] P. Brandimarte, M. Englund, N. Papior, A. Garcia-Lekue, T. Frederiksen, and D. Sánchez-Portal, A tunable electronic beam

- splitter realized with crossed graphene nanoribbons, *J. Chem. Phys.* **146**, 092318 (2017).
- [44] P. R. Wallace, The band theory of graphite, *Phys. Rev.* **71**, 622 (1947).
- [45] M. S. Dresselhaus and G. Dresselhaus, Intercalation compounds of graphite, *Adv. Phys.* **51**, 1 (2002).
- [46] S. Reich, J. Maultzsch, C. Thomsen, and P. Ordejón, Tight-binding description of graphene, *Phys. Rev. B* **66**, 035412 (2002).
- [47] E. McCann and V. I. Fal'ko, Landau-Level Degeneracy and Quantum Hall Effect in a Graphite Bilayer, *Phys. Rev. Lett.* **96**, 086805 (2006).
- [48] L. M. Malard, J. Nilsson, D. C. Elias, J. C. Brant, F. Plentz, E. S. Alves, A. H. Castro Neto, and M. A. Pimenta, Probing the electronic structure of bilayer graphene by Raman scattering, *Phys. Rev. B* **76**, 201401(R) (2007).
- [49] J. C. Slater and G. F. Koster, Simplified LCAO method for the periodic potential problem, *Phys. Rev.* **94**, 1498 (1954).
- [50] J. M. B. Lopes dos Santos, N. M. R. Peres, and A. H. Castro Neto, Graphene Bilayer with a Twist: Electronic Structure, *Phys. Rev. Lett.* **99**, 256802 (2007).
- [51] G. Trambly de Laissardière, D. Mayou, and L. Magaud, Localization of Dirac electrons in rotated graphene bilayers, *Nano Lett.* **10**, 804 (2010).
- [52] L. Malard, M. Pimenta, G. Dresselhaus, and M. Dresselhaus, Raman spectroscopy in graphene, *Phys. Rep.* **473**, 51 (2009).
- [53] A. H. Castro Neto, F. Guinea, N. M. R. Peres, K. S. Novoselov, and A. K. Geim, The electronic properties of graphene, *Rev. Mod. Phys.* **81**, 109 (2009).
- [54] F. Guinea and N. R. Walet, Continuum models for twisted bilayer graphene: Effect of lattice deformation and hopping parameters, *Phys. Rev. B* **99**, 205134 (2019).
- [55] J. M. Soler, E. Artacho, J. D. Gale, A. García, J. Junquera, P. Ordejón, and D. Sánchez-Portal, The SIESTA method for *ab initio* order-*N* materials simulation, *J. Phys.: Condens. Matter* **14**, 2745 (2002).
- [56] L. Kadanoff and G. Baym, *Quantum Statistical Mechanics: Green's Function Methods in Equilibrium and Nonequilibrium Problems*, Frontiers in Physics: A Lecture Note and Reprint Series (W. A. Benjamin, New York, 1962).
- [57] L. V. Keldysh, Diagram technique for nonequilibrium processes, *Sov. Phys. JETP* **20**, 1018 (1965) [*Zh. Eksp. Theor. Fiz.* **47**, 1515 (1964)].
- [58] H. Haug and A.-P. Jauho, *Quantum Kinetics in Transport and Optics of Semiconductors*, 2nd ed. (Springer, Berlin, 2007).
- [59] M. Büttiker, Y. Imry, R. Landauer, and S. Pinhas, Generalized many-channel conductance formula with application to small rings, *Phys. Rev. B* **31**, 6207 (1985).
- [60] N. R. Papior, SISL version 0.9.8 [10.5281/zenodo.3661117](https://zenodo.org/record/3661117) (2020).
- [61] N. Papior, N. Lorente, T. Frederiksen, A. García, and M. Brandbyge, Improvements on non-equilibrium and transport Green function techniques: The next-generation TranSIESTA, *Comput. Phys. Commun.* **212**, 8 (2017).
- [62] See Supplemental Material at <http://link.aps.org/supplemental/10.1103/PhysRevB.102.035436> for the transport properties of the remaining devices (AA-stacked ZGNRs and crossed AGNRs), a detailed version of each crossing's scattering potential, and other complementary simulations.
- [63] G. Li, A. Luican, J. M. B. Lopes dos Santos, A. H. Castro Neto, A. Reina, J. Kong, and E. Y. Andrei, Observation of van Hove singularities in twisted graphene layers, *Nat. Phys.* **6**, 109 (2010).
- [64] Y. Cao, V. Fatemi, A. Demir, S. Fang, S. L. Tomarken, J. Y. Luo, J. D. Sanchez-Yamagishi, K. Watanabe, T. Taniguchi, E. Kaxiras *et al.*, Correlated insulator behaviour at half-filling in magic-angle graphene superlattices, *Nature (London)* **556**, 80 (2018).
- [65] Y. Cao, V. Fatemi, S. Fang, K. Watanabe, T. Taniguchi, E. Kaxiras, and P. Jarillo-Herrero, Unconventional superconductivity in magic-angle graphene superlattices, *Nature (London)* **556**, 43 (2018).
- [66] L. Brey and H. A. Fertig, Electronic states of graphene nanoribbons studied with the Dirac equation, *Phys. Rev. B* **73**, 235411 (2006).
- [67] K. Wakabayashi, Y. Takane, and M. Sgrist, Perfectly Conducting Channel and Universality Crossover in Disordered Graphene Nanoribbons, *Phys. Rev. Lett.* **99**, 036601 (2007).
- [68] H. M. Abdullah, B. V. Duppen, M. Zarenia, H. Bahlouli, and F. M. Peeters, Quantum transport across van der Waals domain walls in bilayer graphene, *J. Phys.: Condens. Matter* **29**, 425303 (2017).
- [69] Z. H. Ni, W. Chen, X. F. Fan, J. L. Kuo, T. Yu, A. T. S. Wee, and Z. X. Shen, Raman spectroscopy of epitaxial graphene on a SiC substrate, *Phys. Rev. B* **77**, 115416 (2008).
- [70] C. Si, Z. Sun, and F. Liu, Strain engineering of graphene: A review, *Nanoscale* **8**, 3207 (2016).
- [71] F. Ding, H. Ji, Y. Chen, A. Herklotz, K. Dörr, Y. Mei, A. Rastelli, and O. G. Schmidt, Stretchable graphene: A close look at fundamental parameters through biaxial straining, *Nano Lett.* **10**, 3453 (2010).
- [72] Y. Baskin and L. Meyer, Lattice constants of graphite at low temperatures, *Phys. Rev.* **100**, 544 (1955).
- [73] Y. X. Zhao and I. L. Spain, X-ray diffraction data for graphite to 20 GPa, *Phys. Rev. B* **40**, 993 (1989).
- [74] Z. Shi, H. Lu, L. Zhang, R. Yang, Y. Wang, D. Liu, H. Guo, D. Shi, H. Gao, E. Wang *et al.*, Studies of graphene-based nanoelectromechanical switches, *Nano Res.* **5**, 82 (2012).
- [75] Y.-G. Yoon, M. S. C. Mazzoni, H. J. Choi, J. Ihm, and S. G. Louie, Structural Deformation and Intertube Conductance of Crossed Carbon Nanotube Junctions, *Phys. Rev. Lett.* **86**, 688 (2001).
- [76] E. Mostaani, N. D. Drummond, and V. I. Fal'ko, Quantum Monte Carlo Calculation of the Binding Energy of Bilayer Graphene, *Phys. Rev. Lett.* **115**, 115501 (2015).
- [77] M. Brandbyge, J.-L. Mozos, P. Ordejón, J. Taylor, and K. Stokbro, Density-functional method for nonequilibrium electron transport, *Phys. Rev. B* **65**, 165401 (2002).
- [78] M. Dion, H. Rydberg, E. Schröder, D. C. Langreth, and B. I. Lundqvist, Van der Waals Density Functional for General Geometries, *Phys. Rev. Lett.* **92**, 246401 (2004).
- [79] J. Klimeš, D. R. Bowler, and A. Michaelides, Chemical accuracy for the van der Waals density functional, *J. Phys.: Condens. Matter* **22**, 022201 (2009).
- [80] N. Troullier and J. L. Martins, Efficient pseudopotentials for plane-wave calculations, *Phys. Rev. B* **43**, 1993 (1991).

V

Spin-polarizing beam splitter realized with crossed zigzag graphene nanoribbons, *Phys. Rev. Lett.* **129**, 037701 (2022)

Spin-Polarizing Electron Beam Splitter from Crossed Graphene Nanoribbons

Sofia Sanz^{1,*}, Nick Papior², Géza Giedke^{1,3}, Daniel Sánchez-Portal⁴,
Mads Brandbyge⁵, and Thomas Frederiksen^{1,3,†}

¹Donostia International Physics Center (DIPC), E-20018 Donostia-San Sebastián, Spain

²DTU Computing Center, Technical University of Denmark, DK-2800 Kongens Lyngby, Denmark

³IKERBASQUE, Basque Foundation for Science, E-48013 Bilbao, Spain

⁴Centro de Física de Materiales (CFM) CSIC-UPV/EHU, E-20018 Donostia-San Sebastián, Spain

⁵Center for Nanostructured Graphene, Department of Physics, Technical University of Denmark, DK-2800 Kongens Lyngby, Denmark



(Received 18 January 2022; accepted 27 May 2022; published 11 July 2022)

Junctions composed of two crossed graphene nanoribbons (GNRs) have been theoretically proposed as electron beam splitters where incoming electron waves in one GNR can be split coherently into propagating waves in *two* outgoing terminals with nearly equal amplitude and zero back-scattering. Here we scrutinize this effect for devices composed of narrow zigzag GNRs taking explicitly into account the role of Coulomb repulsion that leads to spin-polarized edge states within mean-field theory. We show that the beam-splitting effect survives the opening of the well-known correlation gap and, more strikingly, that a *spin-dependent* scattering potential emerges which spin polarizes the transmitted electrons in the two outputs. By studying different ribbons and intersection angles we provide evidence that this is a general feature with edge-polarized nanoribbons. A near-perfect polarization can be achieved by joining several junctions in series. Our findings suggest that GNRs are interesting building blocks in spintronics and quantum technologies with applications for interferometry and entanglement.

DOI: [10.1103/PhysRevLett.129.037701](https://doi.org/10.1103/PhysRevLett.129.037701)

Graphene is an exceptional material with attractive properties to explore fundamental physics and for use in technological applications [1]. While ideal graphene is nonmagnetic, custom-shaped graphene nanostructures can be designed to exhibit complex magnetic phenomenology with promising possibilities for a new generation of nanoscale *spintronics* devices [2,3]. In fact, graphene π magnetism is more delocalized and isotropic than conventional magnetism arising from *d* or *f* orbitals, which makes it electrically accessible [4] and stable even at room temperature [5]. The intrinsically weak spin orbit and hyperfine couplings in graphene lead to long spin coherence and relaxation times [6] as well as a long spin-diffusion length that is expected to reach $\sim 10 \mu\text{m}$ even at room temperature [7]. This makes graphene an interesting platform for designing functionalities such as spin filters [8–11], spin qubits [12,13], and electron quantum optics setups [14].

Graphene nanoribbons (GNRs) have emerged as particularly attractive building blocks for molecular-scale electronic devices because they inherit some of the

exceptional properties from graphene while having tunable electronic properties, such as the band gap dependency on their width and edge topology [8]. With the advent of bottom-up fabrication techniques, long defect-free samples of narrow GNRs can now be chemically produced via on-surface synthesis as demonstrated in the seminal works for armchair [15] and zigzag (ZGNR) [16] ribbons. Furthermore, manipulation of GNRs with scanning tunneling probes [17,18] opens the possibility to build two-dimensional multiterminal graphene-based electronic circuits [19], where their spin properties can be addressed by using spin-polarized tips [20] and probed by shot noise measurements [21].

Indeed, electron transport in GNR networks has been theoretically explored with the Landauer-Büttiker formalism [22] for a rich variety of multiterminal device configurations [23–26]. Most recently, crossed GNR junctions have been proposed as *electron beam splitters* for electron quantum optics [27–29]. In these works it was found that by placing one GNR on top of another with a relative angle of 60° the electron transfer process between the ribbons is strongly enhanced. This enables one to split incoming low-energy electron waves between two outgoing ports with a tunable ratio and negligible reflection probability, an effect with roots in valley (chirality) preservation in the low-energy bands of ZGNRs [30,31]. However, since ZGNRs develop spin-polarized edge states, as theoretically [32] and experimentally [5,33] demonstrated, one may expect that

Published by the American Physical Society under the terms of the [Creative Commons Attribution 4.0 International license](https://creativecommons.org/licenses/by/4.0/). Further distribution of this work must maintain attribution to the author(s) and the published article's title, journal citation, and DOI.

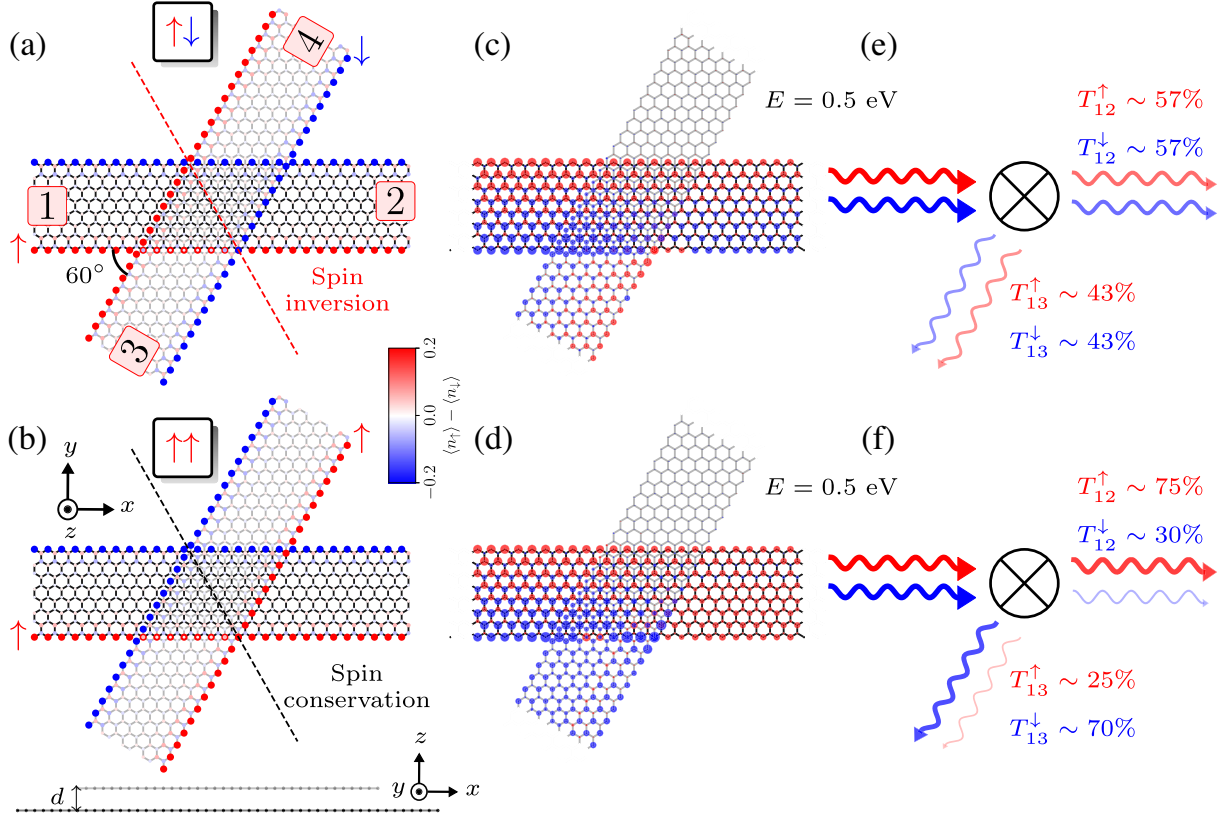


FIG. 1. Transport setup and spin-dependent properties for AB -stacked 8-ZGNR devices. (a),(b) Two different self-consistent solutions for the spin-density distribution in the device region, labeled $\boxed{\uparrow\downarrow}$ and $\boxed{\uparrow\uparrow}$, respectively, defined by the spin orientation of the lower edge of each GNR. The up (down) spin density is shown in red (blue). The lower, horizontal ribbon is plotted in black, while the upper, intersecting at an angle of 60° , is depicted in gray. Electrodes 1–4 are indicated. The ribbons are separated by a distance $d = 3.34 \text{ \AA}$ along the z axis, as displayed in the side view [lower part of (b)]. The dashed lines in each configuration indicate a symmetry axis that maps the device geometry to itself through mirror operations, where the red (black) color of the axis further indicates that the spin index is inverted (conserved) by the symmetry operation. (c),(d) Spin-resolved density of states of scattering states incoming from electrode 1 for the $\boxed{\uparrow\downarrow}$ and $\boxed{\uparrow\uparrow}$ spin configuration, respectively, computed at $E - E_F = 0.5 \text{ eV}$. The dominant spin on each site at this energy is shown in red for up spins and in blue for down spins. (e),(f) Sketch of incoming and outgoing waves through the scattering center (represented by the circled cross) and the corresponding transmission probabilities from calculations.

Coulomb repulsion could give rise to additional interesting features for the charge and spin transport in crossed ZGNRs. For instance, it has been shown that the introduction of *one* rough zigzag edge can be used to boost spin injection [34].

In this Letter, we analyze the electronic structure and quantum transport properties of junctions composed of two infinite ZGNRs crossed with a relative angle of 60° using the mean-field Hubbard (MFH) model in combination with nonequilibrium Green's functions (NEGF) to describe the open quantum systems [35]. We show how the Coulomb repulsion opens a transport band gap and generates a spin-dependent scattering potential in the junction, which enables the devices to be operated as a *spin-polarizing beam splitter*.

For a transparent analysis and efficient numerics we use the Hubbard Hamiltonian [36] within the mean-field approximation, well suited to describe sp^2 carbon systems [2], for both semi-infinite electrodes and device region as shown in Fig. 1, i.e.,

$$H_{\text{MFH}} = \sum_{ij,\sigma} t_{ij} c_{i\sigma}^\dagger c_{j\sigma} + U \sum_{i,\sigma} n_{i\sigma} \langle n_{i\bar{\sigma}} \rangle. \quad (1)$$

Here $c_{i\sigma}$ is the annihilation operator of an electron at site i with spin $\sigma = \{\uparrow, \downarrow\}$ and $n_{i\sigma} = c_{i\sigma}^\dagger c_{i\sigma}$ the corresponding number operator. The matrix element t_{ij} is computed by a two-center integral based on a Slater-Koster parametrization as explained in Ref. [29], and U accounts for the Coulomb interaction between two electrons occupying the same p_z orbital. We fix $U = 3 \text{ eV}$ which is in the typical range that yields a good agreement with *ab initio* calculations [2,9,11,37,38]. The open system described by Eq. (1) is solved self-consistently using the NEGF method [35,39,40] as detailed in the Supplemental Material [41]. The corresponding many-electron state thus takes the form of a single Slater determinant of the occupied single-particle states from the MFH-NEGF equations.

Figure 1(a) shows the device structure for two *AB*-stacked ZGNRs, each with a width of 8 carbon atoms (8-ZGNRs). In principle, away from the crossing (but within the spin correlation length), each of the four electrodes can be imposed one of the two possible symmetry-broken spin configurations at the edges, leading to $2^4/2 = 8$ unique boundary conditions for the device region. The self-consistent solutions to this problem are shown in Figs. S6 and S7 of the Supplemental Material [41] for *AB*- and *AA*-stacked junctions, respectively, along with the electronic energy differences. The spin configurations for the two lowest-energy states with *AB* stacking are shown in Figs. 1(a) and 1(b). In the following we label these as $\uparrow\downarrow$ and $\uparrow\uparrow$, where the first (second) arrow refers to the spin orientation of the lower edge of the horizontal (inclined) GNR. Although the electronic energy of $\uparrow\uparrow$ is found to be 82 meV above that of $\uparrow\downarrow$ with *AB*-stacking, it is interesting to consider both configurations as this (constant) energy penalty may be compensated by a (length-dependent) energy preference for a certain polarization on the extended GNRs through interactions with their environment.

The spin- and energy-resolved transmission probability between any pair of electrodes can be computed from $T_{\alpha\beta}^{\sigma} = \text{Tr}[\mathbf{G}_{\sigma}\mathbf{\Gamma}_{\alpha\sigma}\mathbf{G}_{\sigma}^{\dagger}\mathbf{\Gamma}_{\beta\sigma}]$, where \mathbf{G}_{σ} is the device Green's function and $\mathbf{\Gamma}_{\alpha\sigma} = i(\Sigma_{\alpha\sigma} - \Sigma_{\alpha\sigma}^{\dagger})$ the broadening matrix related to the self-energy $\Sigma_{\alpha\sigma}$ from electrode α and for spin orientation σ [22,39]. Similarly, the site-resolved density of scattering states can be computed as $\mathbf{A}_{\alpha\sigma} = \mathbf{G}_{\sigma}\mathbf{\Gamma}_{\alpha\sigma}\mathbf{G}_{\sigma}^{\dagger}$.

Figures 1(c) and 1(d) show the spatial distribution of the scattering states incoming from electrode 1 in the conduction band. At each lattice site the disk size is proportional to the density of states (summed over spin) while its color indicates the local majority spin. The electron energy is chosen at $E = 0.5$ eV above the Fermi energy $E_F = 0$, i.e., slightly away from the window with edge states. This implies mode propagation involving only a single GNR subband (Supplemental Material, Figs. S3 and S4 [41]), as well as robustness against edge disorder [49]. Figures 1(c) and 1(d) also illustrate how the transmitted wave—for both spin configurations $\uparrow\downarrow$ and $\uparrow\uparrow$ —is split into electrodes 2 and 3 with negligible reflection and amplitude in electrode 4, as expected for the beam splitter. Conceptually, this is expressed with the representation in Figs. 1(e) and 1(f), along with the computed transmission probabilities.

Remarkably, $\uparrow\downarrow$ and $\uparrow\uparrow$ differ substantially when one considers the spin-resolved transmissions. Whereas $\uparrow\downarrow$ does not polarize the current, since the transmission probabilities for both spin channels are equal, the $\uparrow\uparrow$ configuration leads to a ratio of $T_{12}^{\downarrow}/T_{12}^{\uparrow} = 0.4$, i.e., a spin-filtering effect.

For further quantitative analysis, Fig. 2 reports the spin- and energy-resolved transmission and reflection probabilities for an electron injected from terminal 1 into the $\uparrow\downarrow$

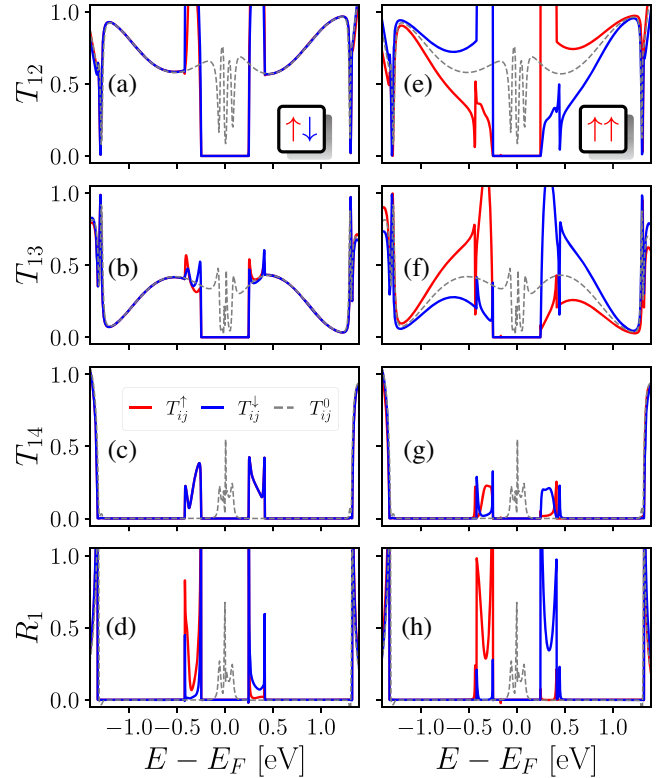


FIG. 2. Spin- and energy-resolved transmission probabilities T_{12} , T_{13} , T_{14} and reflection R_1 for (a)–(d) the $\uparrow\downarrow$ and (e)–(h) $\uparrow\uparrow$ configurations of Fig. 1. Electrons are injected from electrode 1. The red (blue) curves correspond to the up (down) spin components with $U = 3$ eV. For comparison, the corresponding calculations for the unpolarized case ($U = 0$) are indicated by dashed gray lines.

[Figs. 2(a)–2(d)] and $\uparrow\uparrow$ [Figs. 2(e)–2(h)] configurations. For comparison, each panel includes the corresponding results for the unpolarized device ($U = 0$, dashed gray lines) reported previously [29]. The introduction of Coulomb repulsion has two direct consequences: (i) it opens a transport gap near zero energy due to polarization of the edge bands, and (ii) it shifts the states at the Brillouin zone boundary (Figs. S3 and S4 of the Supplemental Material [41]) resulting in the formation of *two* transverse modes at very low energy. While the beam-splitting effect in the two-mode energy range is hampered by substantial scattering and reflection [Figs. 2(d) and 2(h)], it is completely restored in the energy range with only a single mode, i.e., $0.4 \text{ eV} < |E| < 1.3 \text{ eV}$, a condition already identified for unpolarized devices [29]. In fact, the transmission properties for $\uparrow\downarrow$ coincide there with those of the unpolarized device [Figs. 2(a)–2(d)]. On the other hand, for the $\uparrow\uparrow$ configuration the probabilities T_{12} and T_{13} show a strong spin splitting [Figs. 2(e)–2(h)], revealing that the spin-filtering effect emphasized in Figs. 1(d) and 1(f) exists for the whole band.

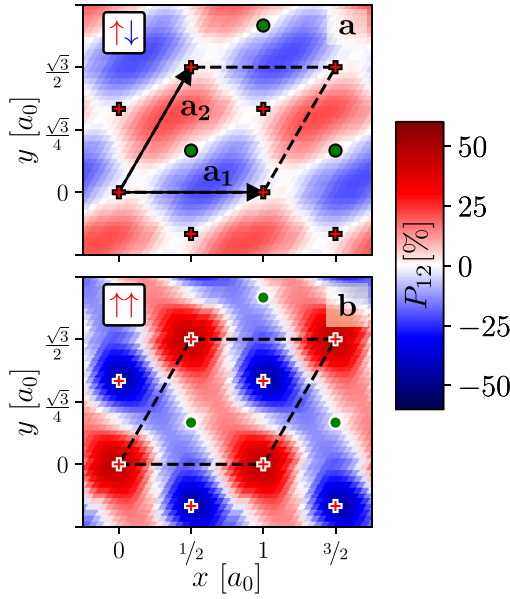


FIG. 3. Spin polarization P_{12} of the current from electrode 1 to 2 as a function of in plane translations of one ribbon with respect to the other for (a) $\uparrow\downarrow$ and (b) $\uparrow\uparrow$ configurations introduced in Fig. 1. The electron energy is in the conduction band at $E = 0.5$ eV. The in plane unit cell (dashed lines) has lattice vectors \mathbf{a}_1 and \mathbf{a}_2 , where $a_0 = 2.46$ Å is the graphene lattice constant. The red crosses (green disks) indicate the high-symmetry configurations with AB (AA) stacking.

This qualitative difference between $\uparrow\downarrow$ and $\uparrow\uparrow$ can be understood by considering the different symmetries that apply to these two configurations. Geometrically, the considered AB-stacked structure possesses one mirror-symmetry plane as shown by the dashed lines in Figs. 1(a) and 1(b) [29]. The difference emerges when one considers symmetry lowering by the spin polarization: For $\uparrow\downarrow$ the spin index maps into the opposite through the mirror operation (red axis) while for $\uparrow\uparrow$ the spin index is conserved. More specifically for $\uparrow\downarrow$, these spatial symmetries impose constraints in the transmission probabilities *between* the spin channels, e.g., that $T_{12}^\sigma = T_{43}^{\bar{\sigma}}$, $T_{13}^\sigma = T_{42}^{\bar{\sigma}}$, etc. Further, considering probability conservation for injection from electrodes 1 or 2, one has the relations $T_{12}^\sigma + T_{13}^\sigma = T_{21}^{\bar{\sigma}} + T_{24}^{\bar{\sigma}} = 1$ (valid when $R_1^\sigma = T_{14}^\sigma = R_2^{\bar{\sigma}} = T_{23}^{\bar{\sigma}} = 0$). Together with time-reversal symmetry ($T_{ij}^\sigma = T_{ji}^{\bar{\sigma}}$) it follows that $T_{12}^\sigma = T_{12}^{\bar{\sigma}}$ in the case of $\uparrow\downarrow$, i.e., that the transmissions are spin *independent*. For $\uparrow\uparrow$ no such condition applies, and the spin channels are decoupled and the transmission probabilities may be very different. Indeed, this is directly seen in our calculations.

If we consider junction imperfections the aforementioned symmetry constraint would be absent and the spin-polarizing effect no longer symmetry forbidden. To examine the relationship between geometry and transport

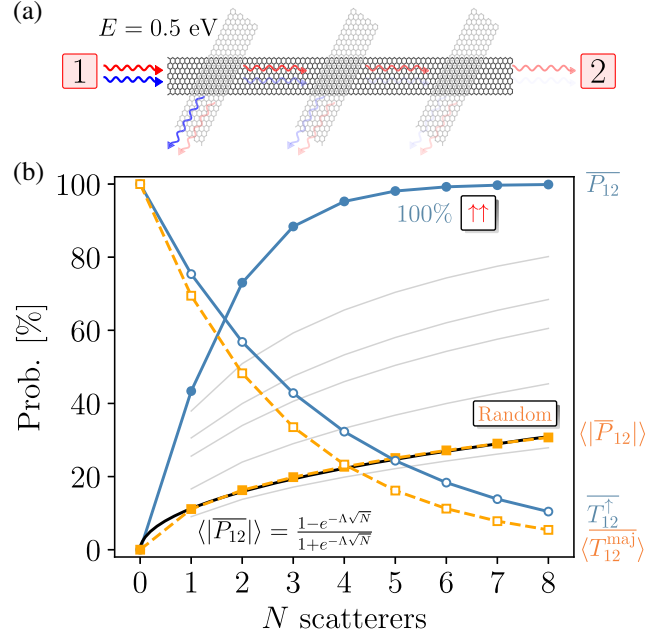


FIG. 4. (a) Sketch of an array of three consecutive AB-stacked 8-ZGNR crossings to enhance the spin-polarized current at the output electrode 2. (b) Spin polarization $\overline{P_{12}}(N)$ (filled symbols) and majority-spin transmission $T_{12}^{\text{maj}}(N)$ (open symbols) as a function of the number of crossings N between terminals 1 and 2 in the conduction band at $E = 0.5$ eV. Two different scenarios are considered: an ideal arrangement of identical $\uparrow\uparrow$ AB crossings (blue circles) as well as a random sampling (orange squares) over 10^7 different spin, intersection angle (within 55 – 65°), and translation configurations drawn from the data in the Supplemental Material, Sec. S11 [41], assuming equal weights. The average polarization $\langle |\overline{P_{12}}(N)| \rangle$ follows an analytic expression (black line, Supplemental Material, Sec. S12 [41]) approaching 1 exponentially in \sqrt{N} . The gray lines indicate the best (1st, 5th, 10th, 25th, 50th) percentiles of the random distribution.

properties we use as a measure the spin polarization in the transmission between a pair of electrodes:

$$P_{\alpha\beta} = \frac{T_{\alpha\beta}^\uparrow - T_{\alpha\beta}^\downarrow}{T_{\alpha\beta}^\uparrow + T_{\alpha\beta}^\downarrow}. \quad (2)$$

Figure 3 shows P_{12} at $E = 0.5$ eV as a function of in plane translations of one ribbon with respect to the other for both $\uparrow\downarrow$ and $\uparrow\uparrow$ configurations. The AB- and AA-stacked geometries are indicated with symbols in the density plots. Evidently, away from these high-symmetry situations the spin-polarizing effect is generally present. The same conclusion holds true also for a range of twist angles (Supplemental Material, Sec. S11 [41]).

At this point it should be noted that it may be difficult to prepare the device in one specific spin configuration, such as the low-energy states $\uparrow\downarrow$ and $\uparrow\uparrow$ discussed up to now. For instance, it is not possible to tune which one is the

energetically lower (and thus at low temperatures thermally stable) state by a homogeneous magnetic field as the Zeeman energy is the same for both solutions. On the other hand, transverse electric fields across the individual electrodes [8] or injection of spin-polarized currents at the edges from the tip of a STM [50] could potentially be strategies to control their magnetization. Nevertheless, our fundamental assumption is that the different collective spin states of the device are sufficiently long lived and robust to be probed by a transient current pulse. This assumption is supported by the fact that our calculations predict that the electronic energy is increased by about 0.20 eV when a magnetic domain wall is inserted into an 8-ZGNR (Supplemental Material, Figs. S6 and S7 [41]), an indication of a very large barrier even compared to room temperature.

The spin-polarizing effect of a single junction discussed above can be enhanced by placing several consecutive crossings to form an array of scatterers as displayed in Fig. 4(a). Because backscattering is negligible in the single-mode energy region, we can approximate the overall transmission probability across an array of N crossings as $\overline{T_{12}^\sigma} \approx \prod_i^N T_{12}^{\sigma(i)}$ where $T_{12}^{\sigma(i)}$ is the transmission of the i th junction. This approximation was tested for the case of $N = 3$ and shows an excellent agreement compared with a calculation of the full device (see the Supplemental Material, Sec. S9 [41]). This idea is exemplified in Fig. 4(b) for two different scenarios: an ideal arrangement of identical $\uparrow\uparrow$ AB-stacked configurations (blue circles) as well as a more realistic situation corresponding to random sampling (orange squares, Supplemental Material, Sec. S12 [41]) over different spin, intersection angle (within 55–65°), and translation configurations. This shows that with four crossings the total current polarization can reach $\overline{P_{12}} \sim 95\%$ with a transmission of $\overline{T_{12}^\uparrow} \sim 32\%$ in the ideal case. Even in the pessimistic case with random junctions, where partial cancellation can occur due to sign changes in the individual P_{12} , the spin polarization $\langle |\overline{P_{12}}| \rangle$ of the array approaches 1 exponentially in \sqrt{N} (black curve, Supplemental Material, Sec. S12 [41]). The best 1st percentile (top gray curve) of the sampled arrays still reaches $\overline{P_{12}} \sim 80\%$ for $N = 8$. Although this statistical analysis is based on the simplifying assumption of equal weights of the configurations, it serves to illustrate that arrays can be interesting even if one does not have precise control over the individual junctions.

In conclusion, we have analyzed the spin-dependent transport properties of crossed ZGNRs using MFH and NEGF theory, and found that the beam-splitting effect reported previously survives in the presence of Coulomb repulsions with two distinct modifications: A transport gap opens at low energies, and a *spin-dependent* scattering potential emerges. Except for specific high-symmetry configurations, this class of electronic devices is generally

predicted to behave as *spin-polarizing beam splitters* with interesting possibilities for electron quantum optics [51]. Such spin-dependent scattering potentials are also obtained with other edge-polarized nanoribbons (Supplemental Material, Sec. S13 [41]). By constructing arrays of junctions the spin-polarizing effect can be enhanced.

Although the proposed devices are ahead of current experiments, a rapid progress in bottom-up fabrication and scanning probe techniques makes it conceivable to assemble nearly defect-free junctions on insulating thin films [52], to drive coherent electron dynamics [53,54], and to characterize electron transport by multiprobe setups [55] or through single-photon emission [56]. Our results add to the vision of using GNR-based devices for spintronics and quantum technologies. For instance, two spin-polarizing beam splitters in combination with a charge detector can be used to deterministically entangle a moving spin qubit [57]. Conversely, a spin-polarizing beam splitter can also be used to determine the entanglement of injected pairs of spins [58]. As an additional application, a high-fidelity spin filter allows “spin-to-charge” conversion and thus a charge-measurement-based spin determination.

This work was supported by the Spanish MCIN/AEI/10.13039/501100011033 (PID2020–115406GB-I00 and PID2019-107338RB-C66), the Basque Department of Education (PRE-2021-2-0190 and PIBA-2020-1-0014), the University of the Basque Country (IT1246-19), and the European Union (EU) through Horizon 2020 (FET-Open project “SPRING” Grant No. 863098).

*sofia.sanz@dipc.org

†thomas_frederiksen@ehu.es

- [1] A. H. Castro Neto, F. Guinea, N. M. R. Peres, K. S. Novoselov, and A. K. Geim, The electronic properties of graphene, *Rev. Mod. Phys.* **81**, 109 (2009).
- [2] O. V. Yazyev, Emergence of magnetism in graphene materials and nanostructures, *Rep. Prog. Phys.* **73**, 056501 (2010).
- [3] W. Han, R. K. Kawakami, M. Gmitra, and J. Fabian, Graphene spintronics, *Nat. Nanotechnol.* **9**, 794 (2014).
- [4] H. González-Herrero, J. M. Gómez-Rodríguez, P. Mallet, M. Moaied, J. J. Palacios, C. Salgado, M. M. Ugeda, J.-Y. Veillen, F. Yndurain, and I. Brihuega, Atomic-scale control of graphene magnetism by using hydrogen atoms, *Science* **352**, 437 (2016).
- [5] G. Z. Magda, X. Jin, I. Hagymási, P. Vancsó, Z. Osváth, P. Nemes-Incze, C. Hwang, L. P. Biró, and L. Tapasztó, Room-temperature magnetic order on zigzag edges of narrow graphene nanoribbons, *Nature (London)* **514**, 608 (2014).
- [6] W. Han and R. K. Kawakami, Spin Relaxation in Single-Layer and Bilayer Graphene, *Phys. Rev. Lett.* **107**, 047207 (2011).
- [7] N. Tombros, C. Jozsa, M. Popinciuc, H. T. Jonkman, and B. J. van Wees, Electronic spin transport and spin precession

- in single graphene layers at room temperature, *Nature (London)* **448**, 571 (2007).
- [8] Y.-W. Son, M. L. Cohen, and S. G. Louie, Half-metallic graphene nanoribbons, *Nature (London)* **444**, 347 (2006).
- [9] Y. Hancock, A. Uppstu, K. Saloritta, A. Harju, and M. J. Puska, Generalized tight-binding transport model for graphene nanoribbon-based systems, *Phys. Rev. B* **81**, 245402 (2010).
- [10] A. Saffarzadeh and R. Farghadan, A spin-filter device based on armchair graphene nanoribbons, *Appl. Phys. Lett.* **98**, 023106 (2011).
- [11] S. S. Gregersen, S. R. Power, and A.-P. Jauho, Nanostructured graphene for spintronics, *Phys. Rev. B* **95**, 121406(R) (2017).
- [12] B. Trauzettel, D. V. Bulaev, D. Loss, and G. Burkard, Spin qubits in graphene quantum dots, *Nat. Phys.* **3**, 192 (2007).
- [13] T. G. Pedersen, C. Flindt, J. Pedersen, N. A. Mortensen, A.-P. Jauho, and K. Pedersen, Graphene Antidot Lattices: Designed Defects and Spin Qubits, *Phys. Rev. Lett.* **100**, 136804 (2008).
- [14] M. Jo, P. Brasseur, A. Assouline, G. Fleury, H.-S. Sim, K. Watanabe, T. Taniguchi, W. Dumnernpanich, P. Roche, D. C. Glattli, N. Kumada, F. D. Parmentier, and P. Roulleau, Quantum Hall Valley Splitters and a Tunable Mach-Zehnder Interferometer in Graphene, *Phys. Rev. Lett.* **126**, 146803 (2021).
- [15] J. Cai, P. Ruffieux, R. Jaafar, M. Bieri, T. Braun, S. Blankenburg, M. Muoth, A. P. Seitsonen, M. Saleh, X. Feng *et al.*, Atomically precise bottom-up fabrication of graphene nanoribbons, *Nature (London)* **466**, 470 (2010).
- [16] P. Ruffieux, S. Wang, B. Yang, C. Sánchez-Sánchez, J. Liu, T. Dienel, L. Talirz, P. Shinde, C. A. Pignedoli, D. Passerone *et al.*, On-surface synthesis of graphene nanoribbons with zigzag edge topology, *Nature (London)* **531**, 489 (2016).
- [17] M. Koch, F. Ample, C. Joachim, and L. Grill, Voltage-dependent conductance of a single graphene nanoribbon, *Nat. Nanotechnol.* **7**, 713 (2012).
- [18] S. Kawai, A. Benassi, E. Gnecco, H. Söde, R. Pawlak, X. Feng, K. Müllen, D. Passerone, C. A. Pignedoli, P. Ruffieux *et al.*, Superlubricity of graphene nanoribbons on gold surfaces, *Science* **351**, 957 (2016).
- [19] L. Jiao, L. Zhang, L. Ding, J. Liu, and H. Dai, Aligned graphene nanoribbons and crossbars from unzipped carbon nanotubes, *Nano Res.* **3**, 387 (2010).
- [20] D. Wortmann, S. Heinze, P. Kurz, G. Bihlmayer, and S. Blügel, Resolving Complex Atomic-Scale Spin Structures by Spin-Polarized Scanning Tunneling Microscopy, *Phys. Rev. Lett.* **86**, 4132 (2001).
- [21] A. Burtzloff, A. Weismann, M. Brandbyge, and R. Berndt, Shot Noise as a Probe of Spin-Polarized Transport through Single Atoms, *Phys. Rev. Lett.* **114**, 016602 (2015).
- [22] M. Büttiker, Y. Imry, R. Landauer, and S. Pinhas, Generalized many-channel conductance formula with application to small rings, *Phys. Rev. B* **31**, 6207 (1985).
- [23] D. A. Areshkin and C. T. White, Building blocks for integrated graphene circuits, *Nano Lett.* **7**, 3253 (2007).
- [24] T. Jayasekera and J. W. Mintmire, Transport in multiterminal graphene nanodevices, *Nanotechnology* **18**, 424033 (2007).
- [25] A. R. Botello-Méndez, E. Cruz-Silva, J. M. Romo-Herrera, F. López-Urías, M. Terrones, B. G. Sumpter, H. Terrones, J.-C. Charlier, and V. Meunier, Quantum transport in graphene nanonetworks, *Nano Lett.* **11**, 3058 (2011).
- [26] T. Cary, E. Costa Girão, and V. Meunier, Electronic properties of three-terminal graphitic nanowiggles, *Phys. Rev. B* **90**, 115409 (2014).
- [27] L. R. F. Lima, A. R. Hernández, F. A. Pinheiro, and C. Lewenkopf, A 50/50 electronic beam splitter in graphene nanoribbons as a building block for electron optics, *J. Phys. Condens. Matter* **28**, 505303 (2016).
- [28] P. Brandimarte, M. Engelund, N. Papior, A. Garcia-Lekue, T. Frederiksen, and D. Sánchez-Portal, A tunable electronic beam splitter realized with crossed graphene nanoribbons, *J. Chem. Phys.* **146**, 092318 (2017).
- [29] S. Sanz, P. Brandimarte, G. Giedke, D. Sánchez-Portal, and T. Frederiksen, Crossed graphene nanoribbons as beam splitters and mirrors for electron quantum optics, *Phys. Rev. B* **102**, 035436 (2020).
- [30] L. Brey and H. A. Fertig, Electronic states of graphene nanoribbons studied with the Dirac equation, *Phys. Rev. B* **73**, 235411 (2006).
- [31] K. Wakabayashi, Y. Takane, and M. Sigrist, Perfectly Conducting Channel and Universality Crossover in Disordered Graphene Nanoribbons, *Phys. Rev. Lett.* **99**, 036601 (2007).
- [32] M. Fujita, K. Wakabayashi, K. Nakada, and K. Kusakabe, Peculiar localized state at zigzag graphite edge, *J. Phys. Soc. Jpn.* **65**, 1920 (1996).
- [33] R. E. Blackwell, F. Zhao, E. Brooks, J. Zhu, I. Piskun, S. Wang, A. Delgado, Y.-L. Lee, S. G. Louie, and F. R. Fischer, Spin splitting of dopant edge state in magnetic zigzag graphene nanoribbons, *Nature (London)* **600**, 647 (2021).
- [34] M. Wimmer, I. Adagideli, S. Berber, D. Tománek, and K. Richter, Spin Currents in Rough Graphene Nanoribbons: Universal Fluctuations and Spin Injection, *Phys. Rev. Lett.* **100**, 177207 (2008).
- [35] S. Sanz, N. Papior, M. Brandbyge, and T. Frederiksen, [10.5281/zenodo.4748765](https://zenodo.org/record/4748765), 2021.
- [36] J. Hubbard, Electron correlations in narrow energy bands, *Proc. R. Soc. A* **276**, 238 (1963).
- [37] J. Fernández-Rossier and J. J. Palacios, Magnetism in Graphene Nanoislands, *Phys. Rev. Lett.* **99**, 177204 (2007).
- [38] J. Li, S. Sanz, M. Corso, D. J. Choi, D. Peña, T. Frederiksen, and J. I. Pascual, Single spin localization and manipulation in graphene open-shell nanostructures, *Nat. Commun.* **10**, 200 (2019).
- [39] N. Papior, N. Lorente, T. Frederiksen, A. García, and M. Brandbyge, Improvements on non-equilibrium and transport Green function techniques: The next-generation TranSiesta, *Comput. Phys. Commun.* **212**, 8 (2017).
- [40] N. Papior, [10.5281/zenodo.6092319](https://zenodo.org/record/6092319).
- [41] See Supplemental Material at <http://link.aps.org/supplemental/10.1103/PhysRevLett.129.037701> for details on methodology and additional calculations, which includes Refs. [42–48].
- [42] H. Feldner, Z. Y. Meng, T. C. Lang, F. F. Assaad, S. Wessel, and A. Honecker, Dynamical Signatures of Edge-State Magnetism on Graphene Nanoribbons, *Phys. Rev. Lett.* **106**, 226401 (2011).

- [43] M. Brandbyge, J.-L. Mozos, P. Ordejón, J. Taylor, and K. Stokbro, Density-functional method for nonequilibrium electron transport, *Phys. Rev. B* **65**, 165401 (2002).
- [44] M. P. L. Sancho, J. M. L. Sancho, J. M. L. Sancho, and J. Rubio, Highly convergent schemes for the calculation of bulk and surface Green functions, *J. Phys. F* **15**, 851 (1985).
- [45] T. Asano and J. Nakamura, Edge-state-induced stacking of zigzag graphene nanoribbons, *ACS Omega* **4**, 22035 (2019).
- [46] E. Mostaani, N. D. Drummond, and V. I. Fal'ko, Quantum Monte Carlo Calculation of the Binding Energy of Bilayer Graphene, *Phys. Rev. Lett.* **115**, 115501 (2015).
- [47] H. Lee, Y.-W. Son, N. Park, S. Han, and J. Yu, Magnetic ordering at the edges of graphitic fragments: Magnetic tail interactions between the edge-localized states, *Phys. Rev. B* **72**, 174431 (2005).
- [48] M. Cahay, M. McLennan, and S. Datta, Conductance of an array of elastic scatterers: A scattering-matrix approach, *Phys. Rev. B* **37**, 10125 (1988).
- [49] L. P. Zârbo and B. K. Nikolić, Spatial distribution of local currents of massless Dirac fermions in quantum transport through graphene nanoribbons, *Europhys. Lett.* **80**, 47001 (2007).
- [50] S. Loth, K. von Bergmann, M. Ternes, A. F. Otte, C. P. Lutz, and A. J. Heinrich, Controlling the state of quantum spins with electric currents, *Nat. Phys.* **6**, 340 (2010).
- [51] E. Bocquillon, V. Freulon, F. D. Parmentier, J.-M. Berroir, B. Plaçais, C. Wahl, J. Rech, T. Jonckheere, T. Martin, C. Grenier *et al.*, Electron quantum optics in ballistic chiral conductors, *Ann. Phys. (Amsterdam)* **526**, 1 (2014).
- [52] P. Jacobse, M. J. J. Mangnus, S. J. M. Zevenhuizen, and I. Swart, Mapping the conductance of electronically decoupled graphene nanoribbons, *ACS Nano* **12**, 7048 (2018).
- [53] S. Baumann, W. Paul, T. Choi, C. P. Lutz, A. Ardavan, and A. J. Heinrich, Electron paramagnetic resonance of individual atoms on a surface, *Science* **350**, 417 (2015).
- [54] S. E. Ammerman, V. Jelic, Y. Wei, V. N. Breslin, M. Hassan, N. Everett, S. Lee, Q. Sun, C. A. Pignedoli, P. Ruffieux *et al.*, Lightwave-driven scanning tunnelling spectroscopy of atomically precise graphene nanoribbons, *Nat. Commun.* **12**, 6794 (2021).
- [55] M. Kolmer, P. Brandimarte, J. Lis, R. Zuzak, S. Godlewski, H. Kawai, A. Garcia-Lekue, N. Lorente, T. Frederiksen, C. Joachim *et al.*, Electronic transport in planar atomic-scale structures measured by two-probe scanning tunneling spectroscopy, *Nat. Commun.* **10**, 1573 (2019).
- [56] M. C. Chong, N. Afshar-Imani, F. Scheurer, C. Cardoso, A. Ferretti, D. Prezzi, and G. Schull, Bright electroluminescence from single graphene nanoribbon junctions, *Nano Lett.* **18**, 175 (2018).
- [57] C. W. J. Beenakker, D. P. DiVincenzo, C. Emary, and M. Kindermann, Charge Detection Enables Free-Electron Quantum Computation, *Phys. Rev. Lett.* **93**, 020501 (2004).
- [58] F. Mazza, B. Braunecker, P. Recher, and A. Levy Yeyati, Spin filtering and entanglement detection due to spin-orbit interaction in carbon nanotube cross-junctions, *Phys. Rev. B* **88**, 195403 (2013).

Supplementary material:
**A spin-polarizing electron beam splitter from crossed graphene
nanoribbons**

Sofia Sanz,^{1,*} Nick Papior,² Géza Giedke,^{1,3} Daniel
Sánchez-Portal,⁴ Mads Brandbyge,^{5,6} and Thomas Frederiksen^{1,3,†}

¹*Donostia International Physics Center (DIPC), E-20018, Donostia-San Sebastián, Spain*

²*DTU Computing Center, Technical University
of Denmark, DK-2800 Kgs. Lyngby, Denmark*

³*IKERBASQUE, Basque Foundation for Science, E-48013, Bilbao, Spain*

⁴*Centro de Física de Materiales (CFM) CSIC-UPV/EHU,
E-20018, Donostia-San Sebastián, Spain*

⁵*Department of Physics, Technical University of Denmark, DK-2800 Kgs. Lyngby, Denmark*

⁶*Center for Nanostructured Graphene (CNG), Denmark*

(Dated: May 21, 2022)

SUMMARY OF CONTENT

In this supplementary material we describe our methodology and present additional calculations that may be interesting for a deeper understanding of the reported effects. In Sec. S1 we explain the details of the calculation with the mean-field Hubbard model (MFH). In Sec. S2 we show the effect of the Coulomb repulsion on the bands of bilayer and monolayer graphene nanoribbons, while in Sec. S3 we show the effect that the size of the scattering region has on the local magnetization of the device. Next in Sec. S4 we plot all the possible spin configurations resulting from the possible combinations of the spin densities of the four electrodes. In Secs. S6 and S7 we show the figure of merit, where we analyze the quality of the device as a spin-beam splitter or mirror, and the spin polarization at a different electronic energy from the one shown in the main text, respectively. In Sec. S8 we compare the transport properties for different ribbon widths. In Sec. S9 we show the quality of the independent scatterers approximation compared to the exact result for a device with three crossings. In Sec. S10 we compare the spin-averaged transmission probabilities with the unpolarized case. In Sec. S11 we explore how possible distortions, such as a small twist angle or a lateral translation of the on-top ribbon with respect to the bottom one, affect the transport properties of individual crossings. In Sec. S12 we describe the used statistical sampling and analytical expression for the averaged spin-polarization shown in Fig. 4(b) of the main text. Finally, in Sec. S13 we analyze the spin-polarizing beam-splitting effect that can be found in junctions formed with other edge-polarized GNRs, such as those built with crossed bearded GNRs.

* sofa.sanz@dipc.org

† thomas_frederiksen@ehu.eus

CONTENTS

Summary of content	2
S1. Solving the MFH with open boundary conditions	4
S2. Effect of U in the band structure of mono- and bilayer ZGNRs	7
S3. Distance from the scattering center to the electrodes	10
S4. All inequivalent spin configurations and transmission curves for AB- and AA-stackings	12
S5. Electronic total energy and magnetization	17
S6. Figure of merit	19
S7. Spin polarization for electrons at other energy values	20
S8. Role of ribbon width	22
S9. Independent-scatterers approximation	23
S10. Averaged transmission probabilities	25
S11. Role of crossing geometry for the spin-polarizing transport effect	27
S12. Statistical analysis of random array devices	29
S13. A spin-polarizing beam splitter with bearded GNRs	34
References	37

S1. SOLVING THE MFH WITH OPEN BOUNDARY CONDITIONS

The Hubbard Hamiltonian in the mean-field approximation model has proven to be in remarkable agreement with quantum Monte Carlo simulations for ZGNR for moderate Coulomb interactions [1]. The complete geometry is divided into the relevant parts here involved: the semi-infinite electrodes and the scattering area (device), where the latter contains the crossing between the two infinite ribbons, $H_T = H_d + \sum_{\alpha} (H_{\alpha} + H_{\alpha d})$, where H_d is the device Hamiltonian and $H_{\alpha}, H_{\alpha d}$ are the α th electrode Hamiltonian and its coupling to the device region. The occupation of the electronic states is defined by Fermi-Dirac statistics with a temperature set to $T = 300$ K. For our system the band gap opening is of the order 500 meV, *i.e.*, $\sim 25 \times kT$ at this temperature (and k the Boltzmann constant), which implies that the distribution function is basically a step function. Therefore, practically there is no difference with the results one would obtain at lower temperatures. We also assume an orthogonal basis of localized atomic orbitals. Further, the qualitative picture presented in the main text is not affected by the numerical choice for the Coulomb repulsion parameter $U = 3$ eV, but only the quantitative results. To show this last statement we have calculated the transmission probabilities for the $\uparrow\uparrow$ device obtained with $U = 1.5$ eV in Fig. S1.

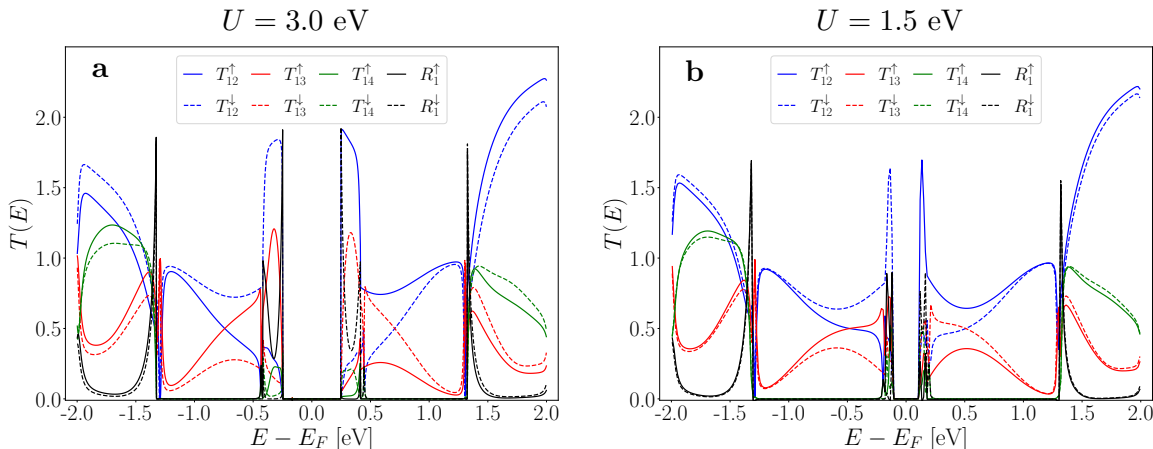


FIG. S1. Transmission probability for an incoming electron from terminal 1 of the $\uparrow\uparrow$ device obtained with (a) $U = 3$ eV and (b) $U = 1.5$ eV.

The computational setup begins by solving the electrodes, where the spin densities $\langle n_{i,\sigma} \rangle$ are found by diagonalization of the infinite ZGNR's unit-cell at each \mathbf{k} -point over the Brillouin zone. The spin-densities will be used to update the Hamiltonian of Eq. (1) in each

iteration, until the convergence criterion is achieved, as implemented in our PYTHON package HUBBARD [2]. To properly account for the effect of the semi-infinite leads in the device Hamiltonian, the spin densities in equilibrium are computed by an integration of the Green's function along a predefined energy contour in the complex plane [3] that we obtained from TRANSIESTA [4],

$$\langle n_{i,\sigma} \rangle = \frac{1}{2\pi} \left[\int_{-\infty}^{\infty} \mathbf{A}_{\sigma}(\varepsilon) n_F(\varepsilon - \mu) d\varepsilon \right]_{ii}, \quad (\text{S1})$$

where $n_F(\varepsilon - \mu)$ is the Fermi distribution with μ the electrochemical potential, $\mathbf{A}_{\sigma} = i(\mathbf{G}_{\sigma} - \mathbf{G}_{\sigma}^{\dagger})$ is the spectral function and $\mathbf{G}_{\sigma}^{-1} = (\varepsilon + i\eta)\mathbf{I} - \mathbf{H}_{C,\sigma} - \sum_{\alpha} \mathbf{\Sigma}_{\alpha,\sigma}$ is the retarded Green's function for each spin component σ . $\mathbf{\Sigma}_{\alpha,\sigma}$ is the self-energy matrix that accounts for the coupling between the α th semi-infinite lead with spin component σ to the scattering region. The self-energy matrices are converged with the Lopez-Sancho recursive method [5] as implemented in the open source, Python-based SISL package [4, 6] using a small broadening of $\eta = 1$ meV. For clarification, the flow diagram of the self-consistent cycle is plotted in Fig. S2.

For equilibrium calculations the electronic contribution to the total energy can be calculated as

$$E_{\text{tot}} = \sum_{\sigma=\uparrow,\downarrow} \frac{1}{2\pi} \int \text{Tr} [\mathbf{A}_{\sigma}(\varepsilon)] n_F(\varepsilon - \mu) \varepsilon d\varepsilon - U \langle n_{\uparrow} \rangle \langle n_{\downarrow} \rangle, \quad (\text{S2})$$

where the left term of Eq. (S2) is the integration of the occupied states while the right term comes from the interaction term of the Hamiltonian. To perform the numerical transport calculations we have used the free and open-source code TBTRANS [4].

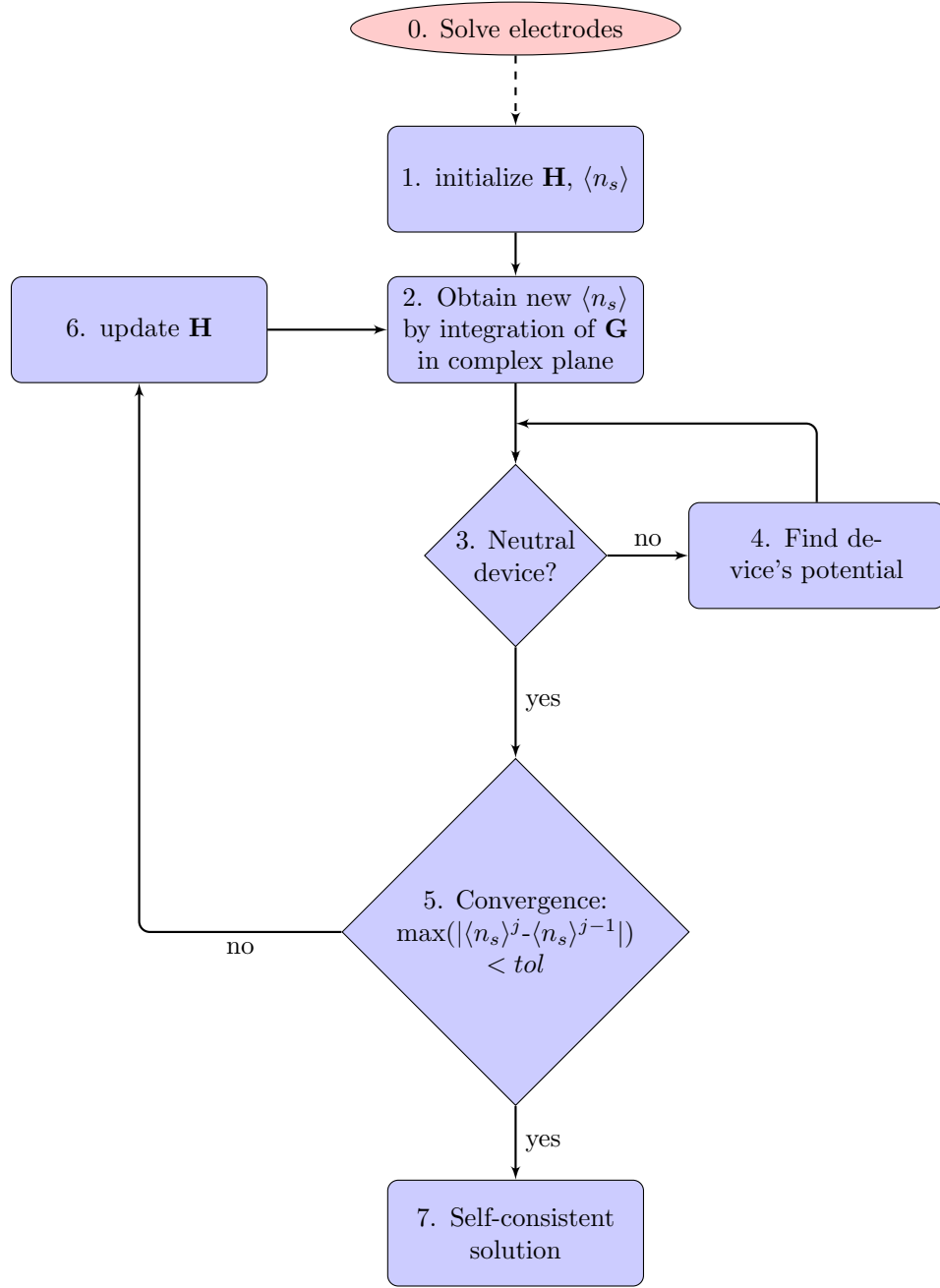


FIG. S2. Convergence process of the MFH model with open boundary conditions.

S2. EFFECT OF U IN THE BAND STRUCTURE OF MONO- AND BILAYER ZGNRS

In this section we show the band structures for periodic mono- and bilayer w -ZGNRs for widths of $w = 8, 16$ carbon atoms across. The geometries of the AA- and AB-stacked ZGNRs are shown in Fig. S3(a,b). In Fig. S3(c-h) we show the band structures for the unpolarized (black dashed lines) and polarized (color lines) Hamiltonians with $U = 3$ eV. The main effect of the interaction term on the electronic structures of these systems is the opening of the correlation gap around E_F . While the larger hybridization in the AA-stacking pushes the edge states further in energy for the unpolarized case (panels (e,f)), which competes with the Coulomb repulsion parameter, in the AB-stacking case the presence of the flat bands (edge states) give rise to the opening of a correlation gap around E_F . The spin distribution of the bilayer ZGNRs (of lowest energy) is composed of two polarized monolayer ZGNRs (antiferromagnetic alignment between the edges of the ribbons) while the atoms that are vertically aligned are also antiferromagnetically aligned. These results are in line with DFT calculations [7].

In Fig. S4 we plot the polarization represented by the center of mass of the wavefunctions $\psi_{n\mathbf{k}}^\uparrow$, calculated as $\int y |\psi_{n\mathbf{k}}^\uparrow|^2 dy$, for the case of the monolayer 8-ZGNR. For an unpolarized wave the center of mass of the wave coincides with the geometrical center of the unit cell, given the inversion symmetry of the ZGNR unit cell. However, for the polarized ZGNR, this is not necessarily the case given the symmetry breaking between the two spin components.

We observe a large polarization of the wave especially in the valence and conduction bands. We also find an interesting behavior of the spin-wave distribution, where the center of mass of the wave transitions from the lower half of the unit cell to the upper half as k goes from Γ to X. This explains the spin majority on the different sublattices depending on the electron energy.

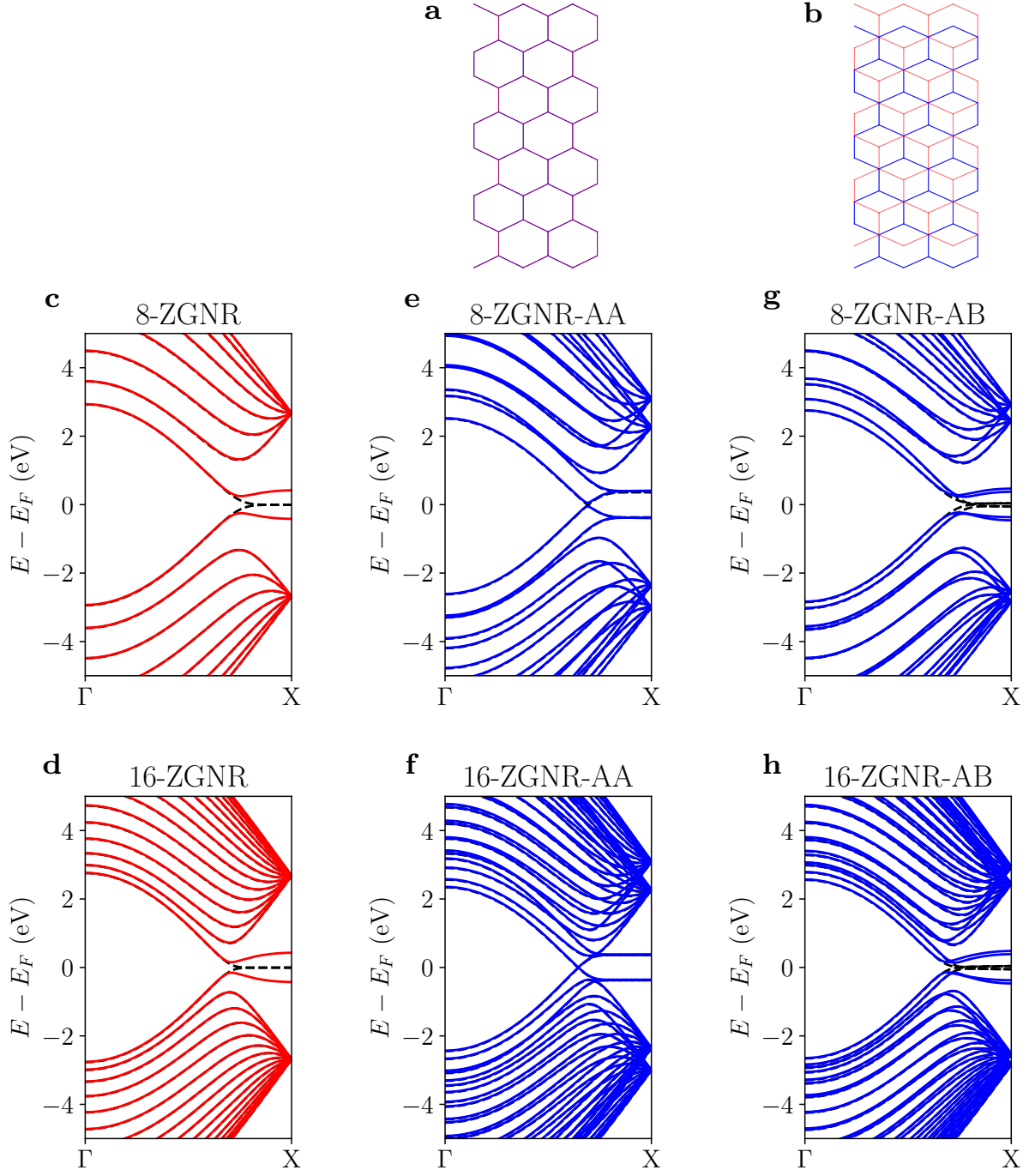


FIG. S3. Band structures of mono- and bilayer w -ZGNRs of different widths. (a,b) Geometry of the AA- and AB-stacked bilayer 8-ZGNRs. Band structure along the Γ -X path for (c,d) monolayer and (e,f) bilayer AA-stacked and (g,h) bilayer AB-stacked 8-ZGNRs. Black dashed lines show the band structures for $U = 0$ and colored lines those obtained after convergence with $U = 3$ eV.

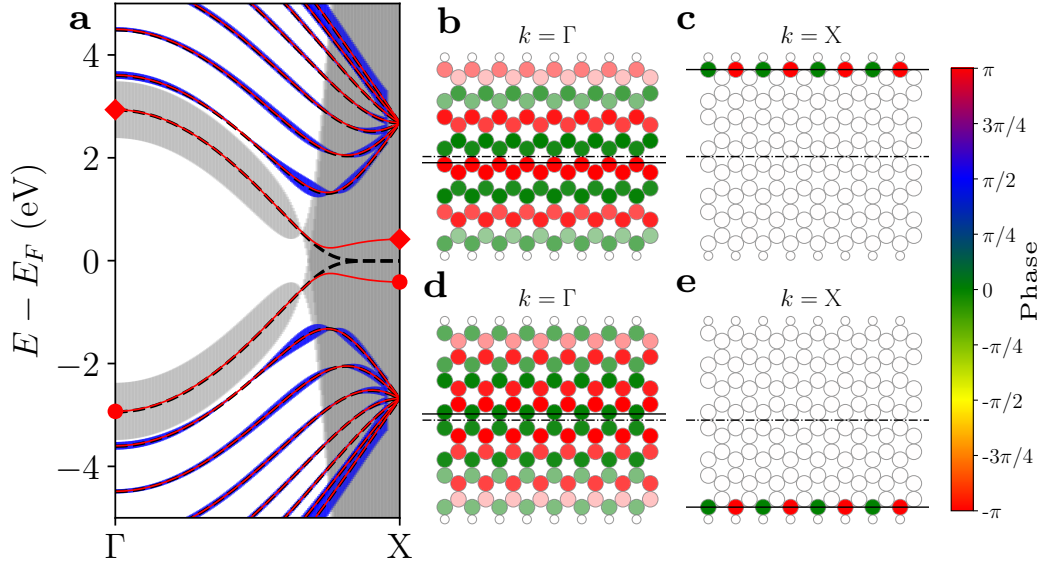


FIG. S4. (a) Band structure for the periodic unpolarized (black dashed lines) and polarized (red solid lines) 8-ZGNR. We also show the position of the center of mass of the wave functions $\psi_{n\mathbf{k}}^\dagger$ plotted as a “fat-band” analysis, where the size of the error bars is computed as $\left| \int y |\psi_{n\mathbf{k}}^\dagger|^2 dy \right|$. We plot the fat-bands in grey for the valence and conduction bands and blue for the remaining bands. (b,c) Spatial distribution of the Bloch wave functions $\psi_{n,\mathbf{k}}^\dagger$ along the conduction (CB) and (d,e) valence bands (VB) computed at $k = \Gamma, X$ respectively. The black solid line indicates the center of mass of the electron wave, while the dashed-dotted line indicates the geometrical center of the unit cell. These \mathbf{k} -points are indicated in red dots (diamonds) along the VB (CB) in panel (a).

S3. DISTANCE FROM THE SCATTERING CENTER TO THE ELECTRODES

Here we show results for the crossed 8-ZGNRs with different GNR lengths, *i.e.*, different distances from the scattering center to the leads. We performed calculations for the same crossing with the same spin configuration ($\boxed{\uparrow\uparrow}$) and compare the spin densities to that corresponding to the perfect (periodic) ribbon solution, *i.e.*, uncoupled ribbons. To do so we plot in real space the difference between the local magnetization, defined as

$$m_i = \langle n_{i\uparrow} \rangle - \langle n_{i\downarrow} \rangle, \quad (\text{S3})$$

for the self-consistent solution of the full device calculation and the local magnetization corresponding to the periodic ribbons, m_i^0 .

In order to preserve the bulk nature for the electrodes, there must be a sufficient distance separating the scattering center from the leads. However, the highly localized Coulomb repulsion term seems to prevent the spin density of the device from being affected by this size effect as Fig. S5 shows that the spin polarization of the coupled ribbons is essentially unaffected by the position of the electrodes. In other words, the inter-GNR coupling induces changes in the electronic structure only in the near vicinity to the crossing.

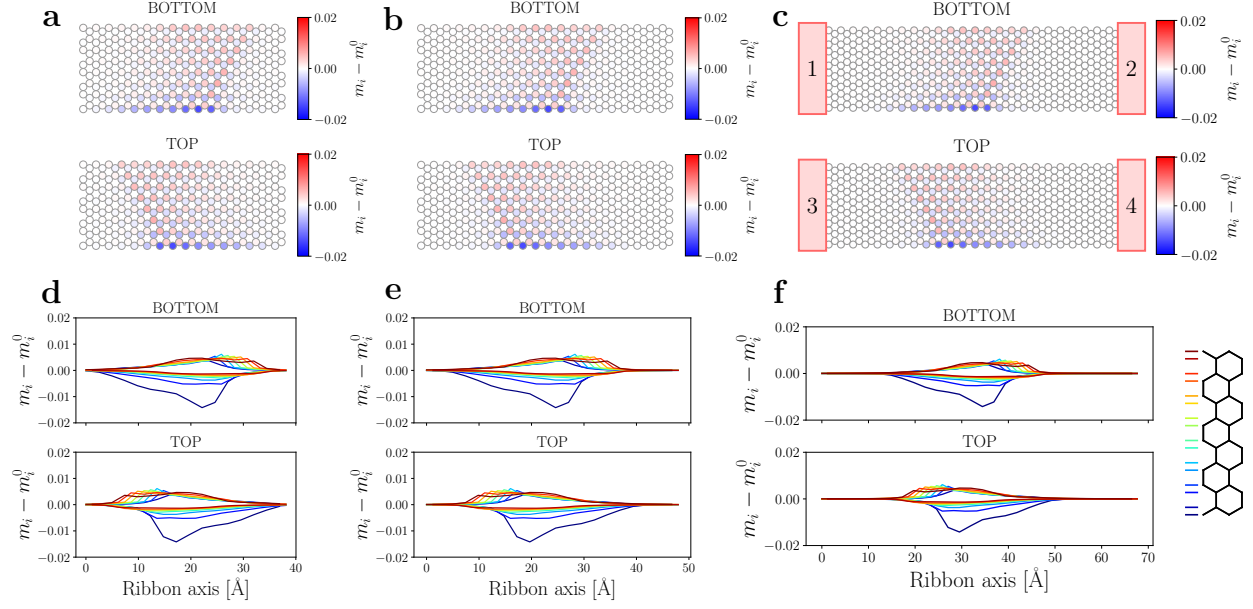


FIG. S5. Convergence study with respect to the size of the device region for AB-stacked 8-ZGNRs in the $\uparrow\uparrow$ configuration. (a-c) Difference between the calculated spin polarization for the 4-terminal device (m_i) and the spin polarization for decoupled ribbons (m_i^0) plotted in real space for different device sizes. We compare three cases, (a) one with a repetition of 16 (~ 38 Å), (b) another with 20 (~ 48 Å) and the last one with (c) 28 (~ 68 Å) ZGNR unit cells. The latter corresponds to the size of the device shown in the main text. (d-f) Profile of $m_i - m_i^0$ along the ribbon axis for different positions across the perpendicular direction (confinement direction). The legend on the left side indicates the transverse position of each profile.

S4. ALL INEQUIVALENT SPIN CONFIGURATIONS AND TRANSMISSION CURVES FOR AB- AND AA-STACKINGS

Here we show all the unique spin configurations for AA- and AB-stacked 8-ZGNRs and the corresponding transmission and reflection probabilities for each spin component. We also list the electronic energy according to Eq. (S2) of each configuration. As mentioned in the main text, each spin configuration for this open quantum system is found by fixing spin density distribution of the 4 electrodes, leading to $2^4/2 = 8$ unique solutions to the imposed boundary conditions (excluding the trivial global inversion of the spin). To show these solutions we plot the difference between the spin densities for the \uparrow and \downarrow spin components, *i.e.*, $\langle n_\uparrow \rangle - \langle n_\downarrow \rangle$, in Figs. S6 and S7 for the AB- and AA-stacking, respectively.

In Tab. S1 we compare the relative electronic energies for the AA- and AB-stacked devices with the 8 unique spin-configurations (a-h) that arise from imposing the spin-densities in the electrodes.

	a $\uparrow\downarrow$	b $\uparrow\uparrow$	c	d	e	f	g	h
AB	0.000	0.082	0.387	0.398	0.202	0.202	0.203	0.203
AA	0.583	0.425	0.847	0.939	0.623	0.623	0.622	0.622

TABLE S1. Electronic energies E_{tot} according to Eq. (S2) for different spin configurations of the AB- (Fig. S6) and AA-stacked (Fig. S7) crossed 8-ZGNRs devices. The energies (in eV) are compared to the configuration of minimum energy corresponding to AB-stacked $\uparrow\downarrow$ in Fig. S6(a).

The first observation is that we find the AA-stacked devices to have larger electronic energy than the AB-stacked ones for all spin configurations (see Tab. S1). This result is in line with other results of this kind [8]. The second observation is that the ground state is the configuration with antiferromagnetic (AFM) alignment between layers, *i.e.*, the atoms that lie one on top of the other have opposite spin index, in line with results published in Ref. [9]. On the other hand, some of the spin configurations involve the presence of domain walls (grain boundaries), if the spin densities of the electrodes belonging to the same ribbon are inverted.

We observe that for configurations that have a single grain boundary, the domain wall moves along the ribbons to leave the scattering area (crossing) with the spin density distri-

bution that corresponds to the ground state configuration [cf. Figs. S6 and S7]. For instance, for the AB-stacked device, the grain boundary in Fig. S6(e-h) moves along the ribbons to leave the crossing with the spin density distribution of Fig. S6(a). Similarly, for the AA-stacked devices, the grain boundary moves along the ribbons to leave the crossing with the spin density distribution of Fig. S7(b). We find that, for the two cases without grain boundaries, the spin configuration of each ribbon deviates very little from that corresponding to the perfect (translationally invariant) 8-ZGNR, showing the weak coupling between them.

On the other hand, Fig. S8 and Fig. S9 shows the transmission and reflection probabilities for the AB- and AA-stacked devices with the different possible spin distributions. As it can be seen in these figures, and following the argument and discussion from the main text, the only systems that have $T_{ij}^\sigma \neq T_{ij}^{\bar{\sigma}}$ are those that only display black symmetry axes (break the symmetry between the spin indices). The transmission probability is computed as mentioned in the main text, while the reflection probability can be computed by subtracting the total outgoing transmission probability to the number of channels/modes existing at a certain energy, M_α ,

$$R_\alpha^\sigma = M_\alpha^\sigma - \sum_{\beta \neq \alpha} T_{\alpha\beta}^\sigma. \quad (\text{S4})$$

We observe that both R_1^s and T_{14}^s are zero for energies lying in the single-band energy region for both stackings and all spin configurations, according to the unpolarized case [10].

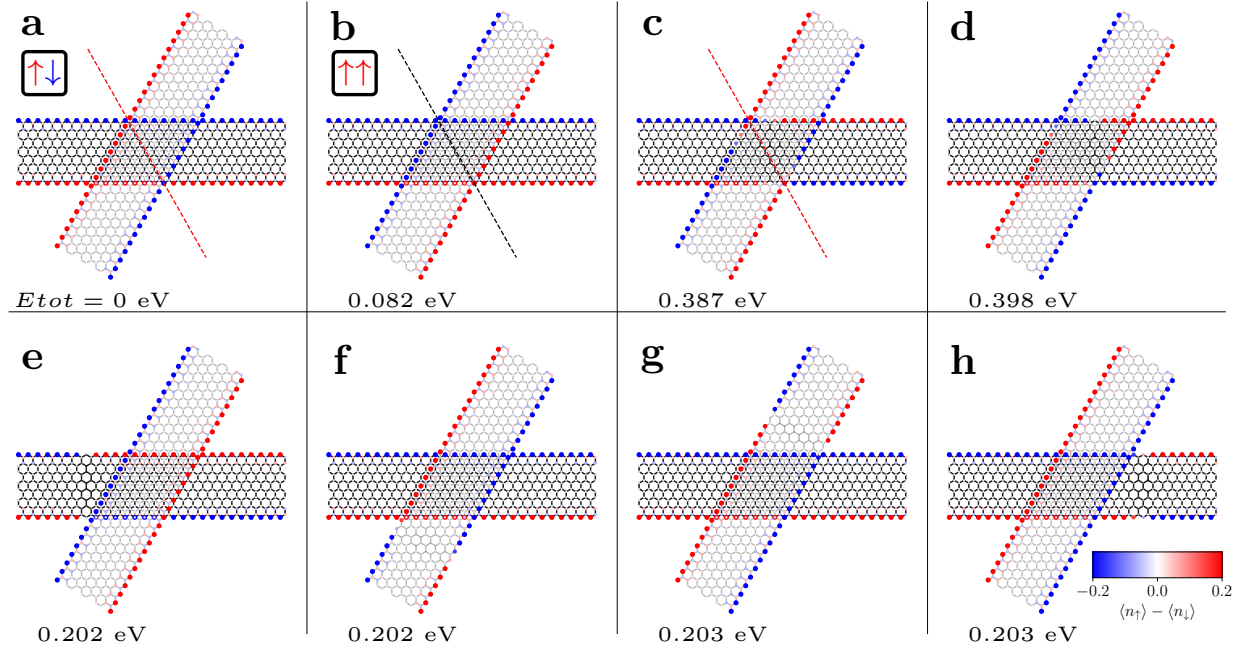


FIG. S6. Spin configurations for the AB-stacked 8-ZGNRs. The electronic energy E_{tot} (in eV) of each configuration (relative to AB-stacked $\uparrow\downarrow$ in panel a) is noted in the bottom left corner in each panel. Red and black dashed lines indicate the symmetry axes.

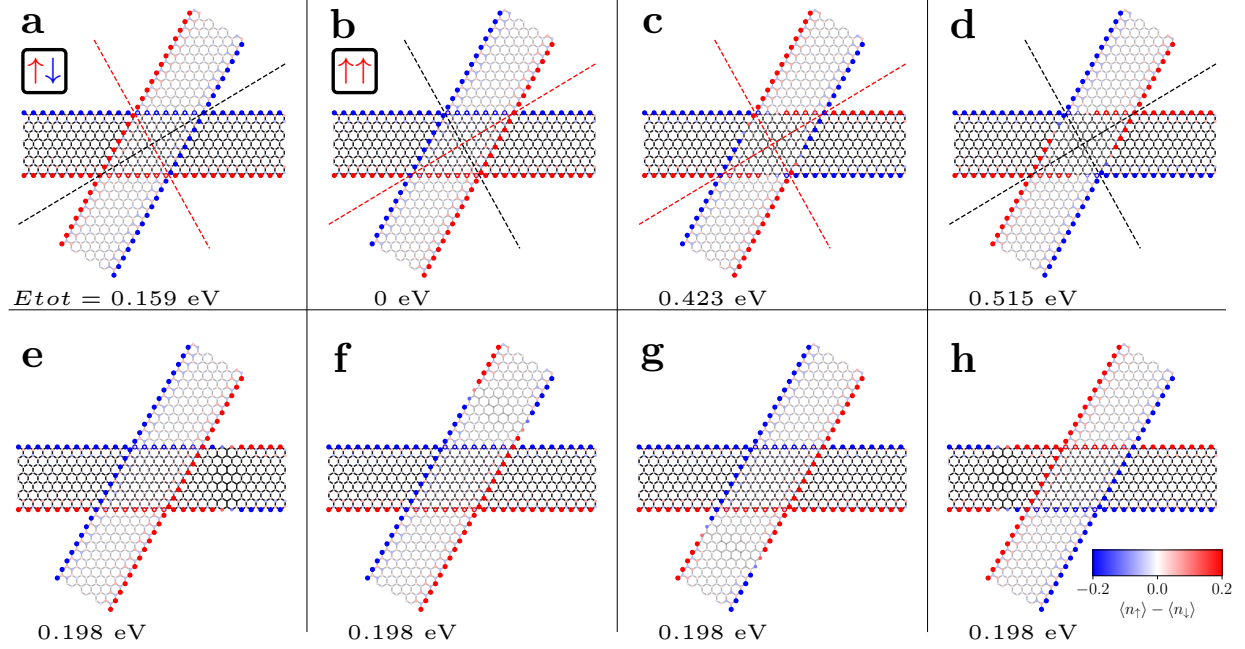


FIG. S7. As Fig. S6 but for the the AA-stacked 8-ZGNRs. The electronic energy E_{tot} (in eV) of each configuration (relative to AA-stacked $\uparrow\uparrow$ in panel b) is noted in the bottom left corner in each panel.

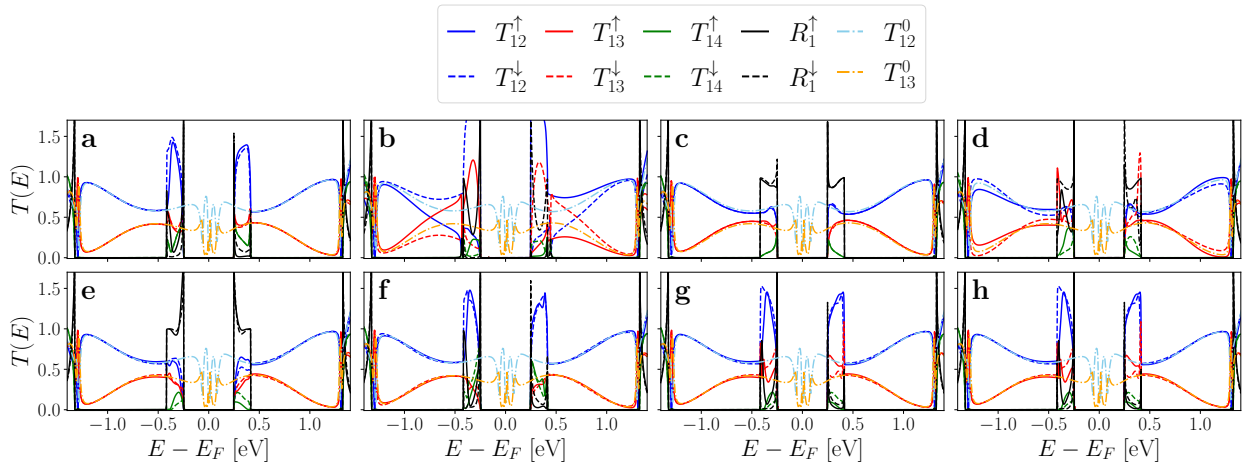


FIG. S8. Transmission and reflection probabilities per spin channel for the AB-stacked 8-ZGNRs shown in Fig. S6. T_{12}^0 and T_{13}^0 are the transmission probabilities between terminals $1 \rightarrow 2$ and $1 \rightarrow 3$ for the unpolarized device.

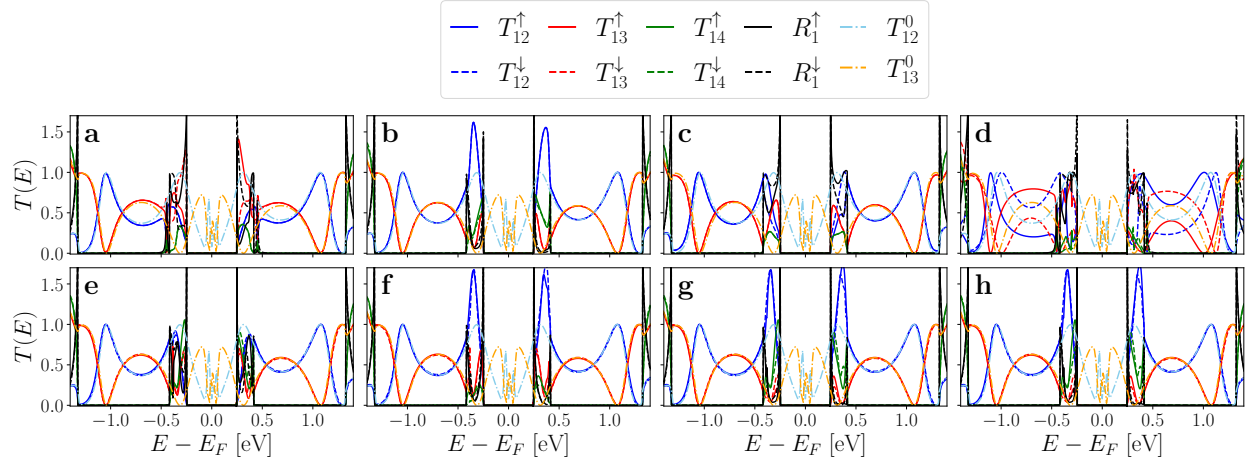


FIG. S9. As Fig. S8 but for the AA-stacked 8-ZGNRs shown in Fig. S7.

S5. ELECTRONIC TOTAL ENERGY AND MAGNETIZATION

Fig. S10 shows the electronic part of the total energy of each device compared to the energy of the uncoupled system, E_0 , as a function of the translation of the on top ribbon with respect to the bottom one starting with the geometry of the AB-stacked device. This energy can be understood as a binding energy between the ribbons. We note that this energy lacks some contributions that are not taken into account in this approximation, *e.g.*, the change in the Van der Waals forces as the two ribbons are translated with respect to each other which determines the precise inter-GNR separation, etc. Here, the geometrical distortion is only encoded through the Slater-Koster parametrization [10].

As mentioned above, the closest stackings to the AB pattern lie in a global minimum. The AA-stacking is a local minimum but more energetic than the AB-stacking. One interesting result is that the plots Fig. S10(a,b) are very similar, showing that the largest contribution to the electronic energy comes from the geometry and that the relative spin density distribution of the ribbons plays a minor role in this physical quantity.

Fig. S10(c,d) show the sum of local *magnetization changes* induced by the inter-GNR interaction, defined as $\sum_i |m_i| - |m_i^0|$. This shows that the magnetization of the device is always lower than that corresponding to the uncoupled ribbons. This last statement makes sense since the effect of the hopping amplitude between the GNRs goes “against” the localization of the electrons, and thus the local magnetization of the system. Therefore the local magnetization of the coupled ribbons will be lower than the magnetization of the uncoupled ribbons, especially in the coupled area. Fig. S10(c,d) also shows that for the configurations with FM inter-layer coupling (AB in Fig. S6b and AA in Fig. S7a, *i.e.*, the atoms that are vertically aligned have equal spin indices), the magnetization decreases more with respect to the perfect 8-ZGNR than configurations with AFM inter-layer coupling (AB in Fig. S6a and AA in Fig. S7b, *i.e.*, the atoms that are vertically aligned have opposite spin indices).

In panels Fig. S10(e,f) we show the maximum backscattering for configurations $\boxed{\uparrow\downarrow}$ and $\boxed{\uparrow\uparrow}$ as a function of the translation of the on-top ribbon with respect to the other one. We hereby see that the low reflection is general for the crossed ZGNRs.

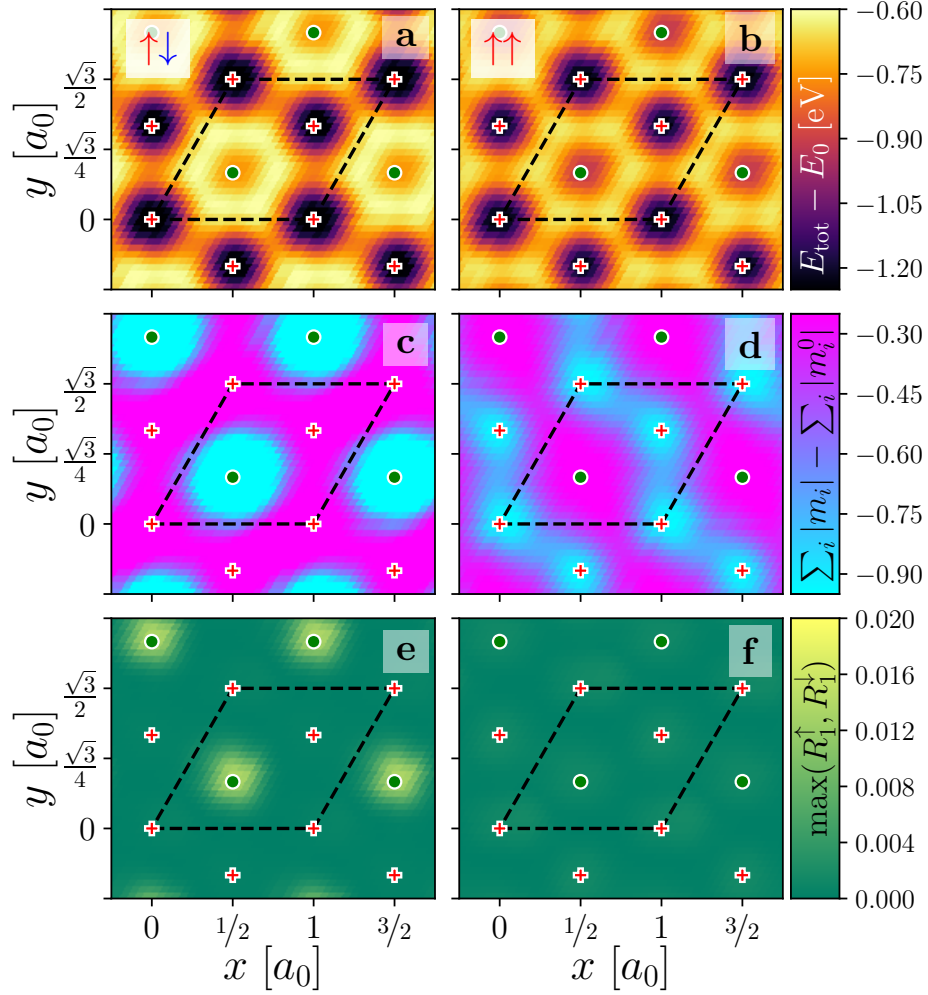


FIG. S10. (a,b) Electronic part of the total energy E_{tot} relative to the energy of the uncoupled system E_0 , (c,d) sum of the absolute value of the magnetization $\sum_i |m_i|$ compared to the uncoupled system $\sum_i |m_i^0|$, and (e,f) maximum backscattering into terminal 1 as function of the translation of the top ribbon with respect to the bottom one for the two possible spin configurations $\boxed{\uparrow\uparrow}$ and $\boxed{\uparrow\downarrow}$, respectively. The dashed parallelogram corresponds to the primitive cell of the problem. Red crosses and green circles indicate the AB- and AA-stacking, respectively.

S6. FIGURE OF MERIT

Fig. S11 shows the quality of the beam splitting or mirror effect per spin channel in the junctions, following the idea of [10], in a figure of merit defined as

$$\text{FM} = e^{-20\lambda} \tanh \left[\frac{1}{20} \left(\frac{1}{|\tau - 1|} - \frac{1}{|\tau - 1/2|} \right) \right], \quad (\text{S5})$$

that was firstly used and defined in the reference from above (the parameters λ, τ and their definition can be found there). Black areas show where the device behaves as a good beam splitter ($T_{12}^s \sim T_{13}^s \sim 0.5$). Red areas would show where the device behaves as a good mirror ($T_{13}^s \sim 1$), however the device is not wide enough to show this behavior (see ref. [10]). White areas indicate devices with almost perfect transmission ($T_{12}^s \sim 1$, since losses ($R^\sigma + T_{14}^s$) are less than 2% for all geometries) that are not of interest for our purposes.

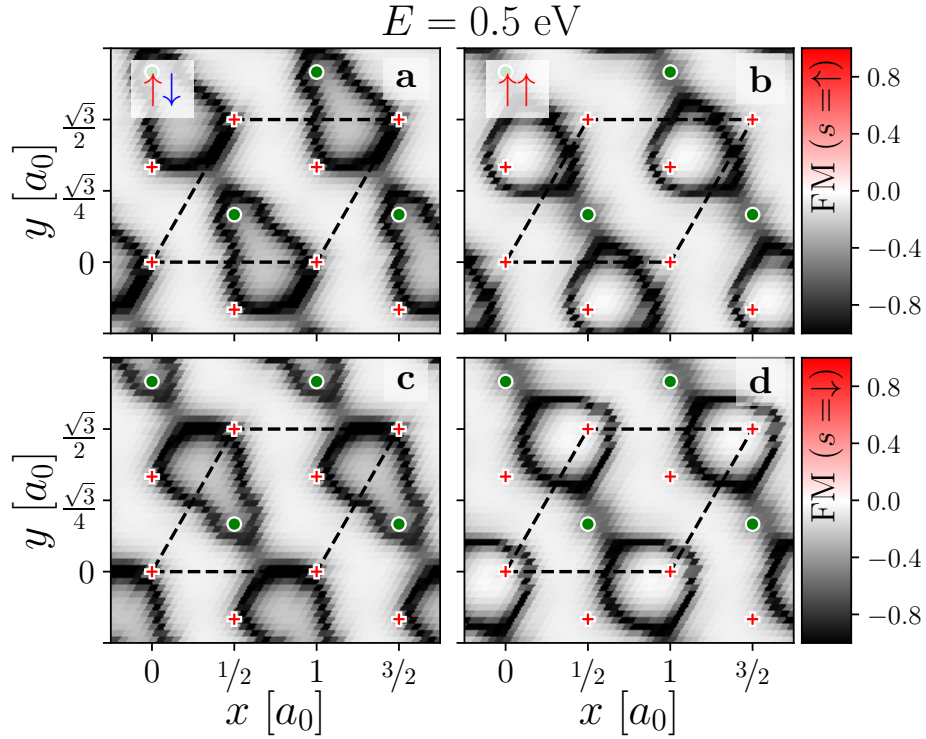


FIG. S11. (a,b) [(c,d)] Figure of merit (FM) for $\sigma = \uparrow$ [$\sigma = \downarrow$] as function of the translation of the top ribbon along the graphene periodicity vectors $\mathbf{a}_1, \mathbf{a}_2$ with respect to the bottom one for the two possible spin configurations ($\uparrow\uparrow$ and $\uparrow\downarrow$, respectively). Red crosses and green circles indicate the AB- and AA-stacking, respectively.

S7. SPIN POLARIZATION FOR ELECTRONS AT OTHER ENERGY VALUES

In the main text we show the scattering states (spectral density of states) for an incoming electron with an energy of $E \sim 0.5$ eV for the AB-stacking four-terminal device. However, the polarization in the transport properties is an energy dependent quantity (as seen for instance in Fig. 2 of the main text). Therefore, for completeness we show in Fig. S12 the spectral density of states for $E \sim 1.0, -0.5, -1.0$ eV. One interesting observation is that panels (b,e) have opposite spin orientation at the edges of the ribbon with respect to panels (c,f). This can be understood from Fig. S4, where the center of mass of the waves changes sign (goes to zero) between $-0.5 (+0.5)$ and $-1.0 (+1.0)$ eV for the VB (CB).

Additionally we also show in Fig. S13 the polarization and the figure of merit for an incoming electron with energy $E \sim 0.5$ eV.

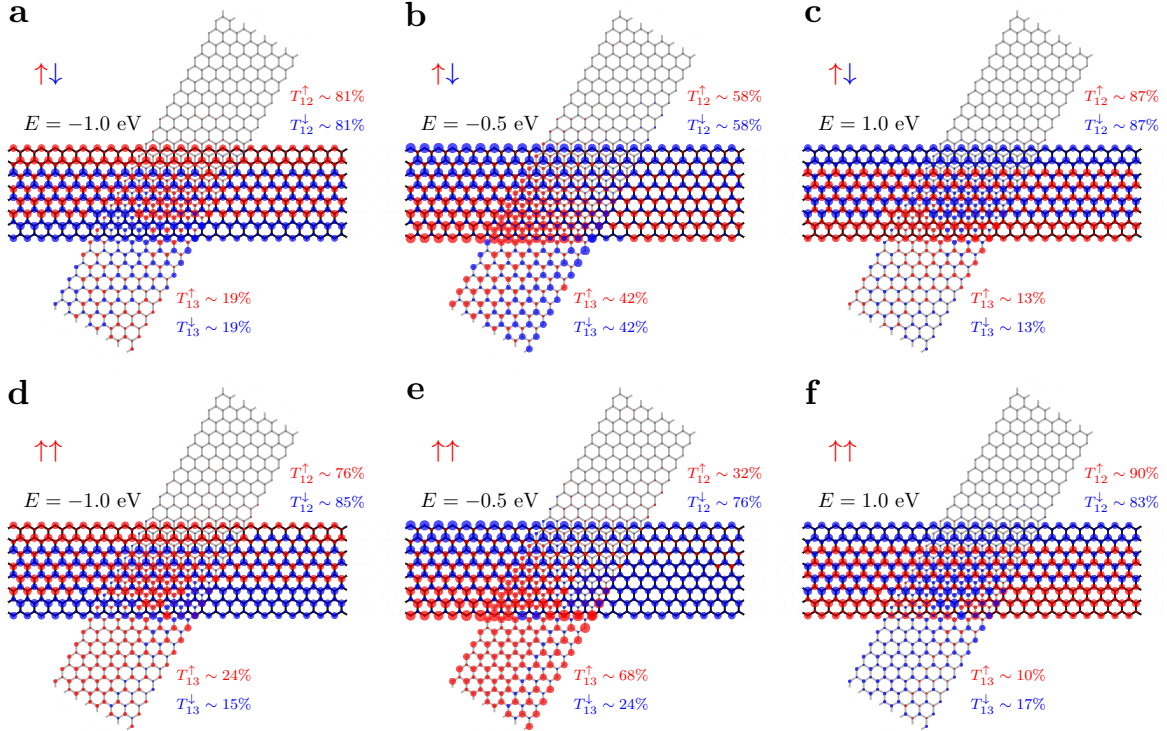


FIG. S12. Scattering states $\mathbf{A} = \mathbf{A}_\uparrow + \mathbf{A}_\downarrow$ for the (a-c) $\uparrow\downarrow$ and (d-f) $\uparrow\uparrow$ spin configuration computed at $E = -1.0, E = -0.5,$ and $E = 1.0$ eV (electrons incoming from the left electrode 1). The dominant spin on each site at this energy is shown in red for up-spins and in blue for down-spins.

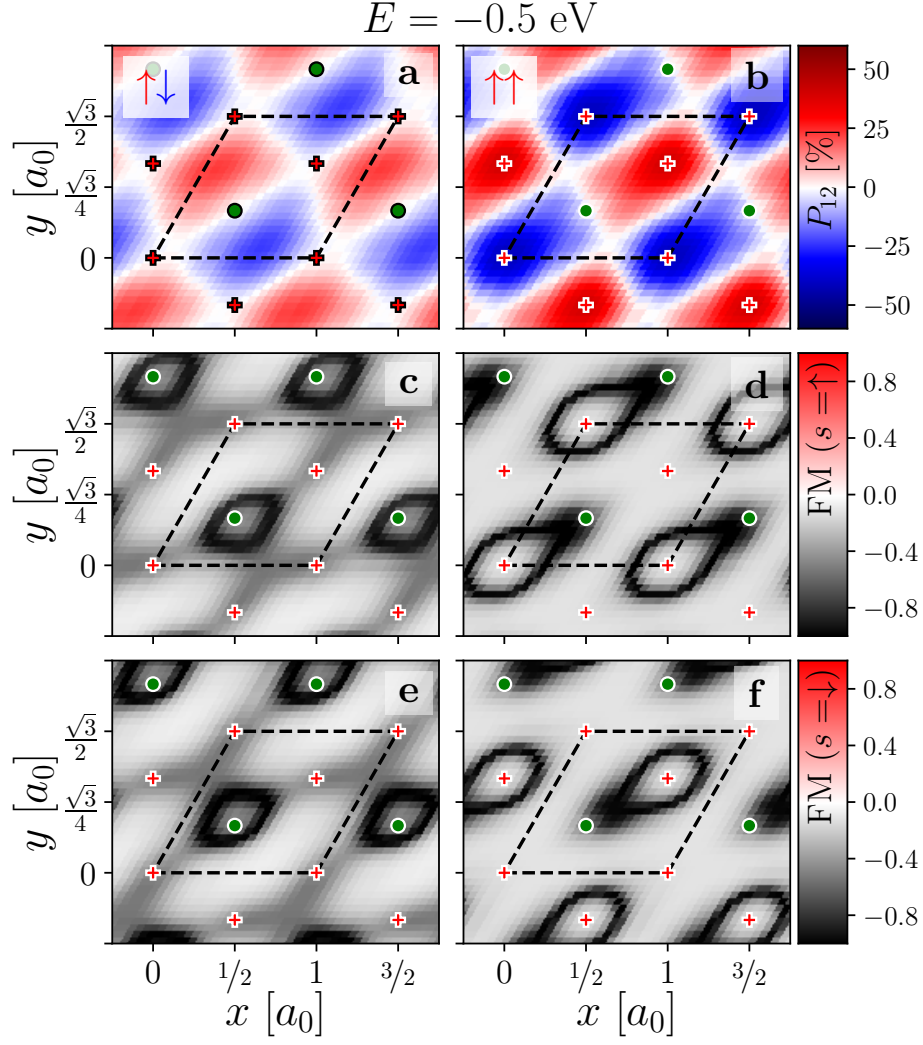


FIG. S13. (a,b) Polarization for an electron incoming from terminal 1 and outgoing in terminal 2 and (c,d) [(e,f)] figure of merit (FM) for $\sigma = \uparrow$ [$\sigma = \downarrow$] as function of the translation of the top ribbon along the graphene periodicity vectors \mathbf{a}_1 , \mathbf{a}_2 with respect to the bottom one for the two possible spin configurations ($\uparrow\uparrow$ and $\uparrow\downarrow$, respectively) obtained at $E = -0.5 \text{ eV}$. Red crosses and green circles indicate the AB- and AA-stacking, respectively.

S8. ROLE OF RIBBON WIDTH

In this section we compute the spin polarization distribution and transmission and reflection probabilities as a function of the electron energy for different ribbon widths for the same crossing and spin configuration (AB- $\uparrow\uparrow$). We see that the different transport behavior for the two different spin channels is general for this crossing. On the other hand, we see that the inter-transmission probability (T_{13}^s) grows with the ribbon width, while the opposite behavior is found for the intra-transmission probability (T_{12}^s). Furthermore, losses ($R_1^s + T_{14}^s$) remain absent independently of the width of the ribbon. These results are in line with the transport properties found for the unpolarized case [cf. Ref [10]].

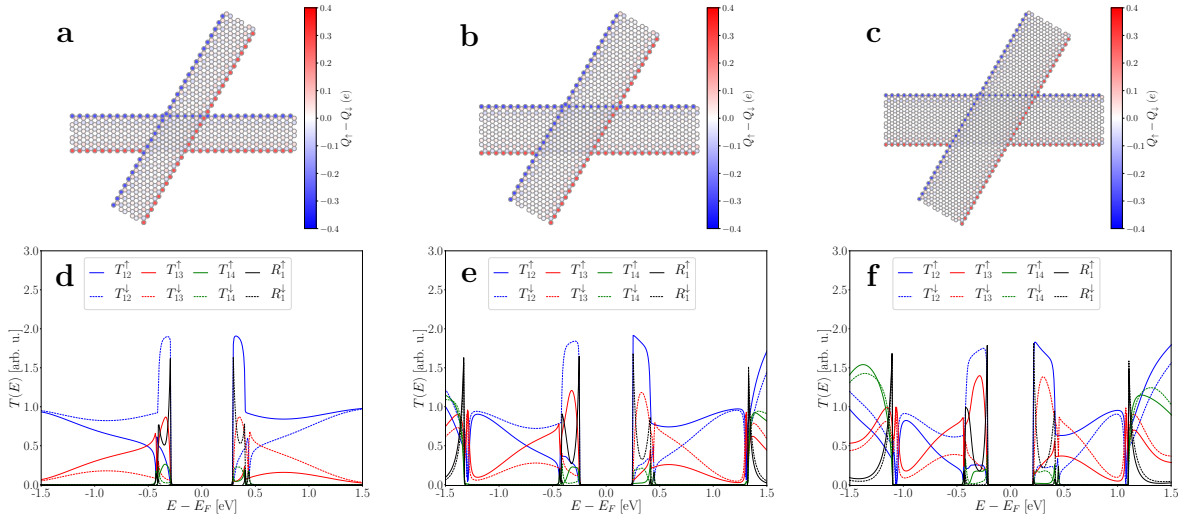


FIG. S14. Transmission coefficients for different ribbon widths. (a-c) Spin polarization for the 4-terminal device formed of two AB-stacked crossed 6-ZGNRs, 8-ZGNRs and 10-ZGNRs, respectively. (d-f) Transmission and reflection probabilities for an incoming electron from terminal 1 for the 6-ZGNRs, 8-ZGNRs and 10-ZGNRs device, respectively.

S9. INDEPENDENT-SCATTERERS APPROXIMATION

To test the independent-scatterers approximation used in the main text (Fig. 4), where we consider each crossing as if it was independent from the others, we chose an array of 3 crossings. For simplicity we consider the unpolarized case although these results can be extrapolated to the polarized device since reflection is absent for this case too. In Fig. S15 we compare the exact transmission probabilities obtained for the full device with TBTRANS [4] with the same transmission probabilities obtained within the independent-scatterers approximation (Eqs. (S6-S12)). This approximation would be exact if one obtained the overall transmission probabilities by coherently combining the scattering matrices of the successive sections using the Feynman paths [11]. Given the fact that there is no reflection for electrons with energies in the single-channel energy region there is no interference between the incoming waves and the reflected ones. Thus, in our approximation we only take the first term of the Feynman path (direct multiplication of the corresponding scattering matrices). Naming the single crossing transmission probabilities with lowercase letters t_{12} , t_{13} and t_{14} , we obtain the transmission probabilities for the full device (named with upper case T_{ij}) as following:

$$T_{12} = t_{12}^3 \tag{S6}$$

$$T_{13} = t_{13} \tag{S7}$$

$$T_{14} = t_{14} \tag{S8}$$

$$T_{15} = t_{12}t_{13} \tag{S9}$$

$$T_{16} = t_{12}t_{14} \tag{S10}$$

$$T_{17} = t_{12}^2t_{13} \tag{S11}$$

$$T_{18} = t_{12}^2t_{14}. \tag{S12}$$

We observe in Fig. S15 that the independent-scatterers approximation is practically exact in the single-channel energy region (where there is only one available mode). The reason for this excellent agreement, as mentioned above, comes from the fact that there is no reflection for these energy values, therefore the interference terms between the backscattered waves disappear. This is not the case outside the single-channel energy region.

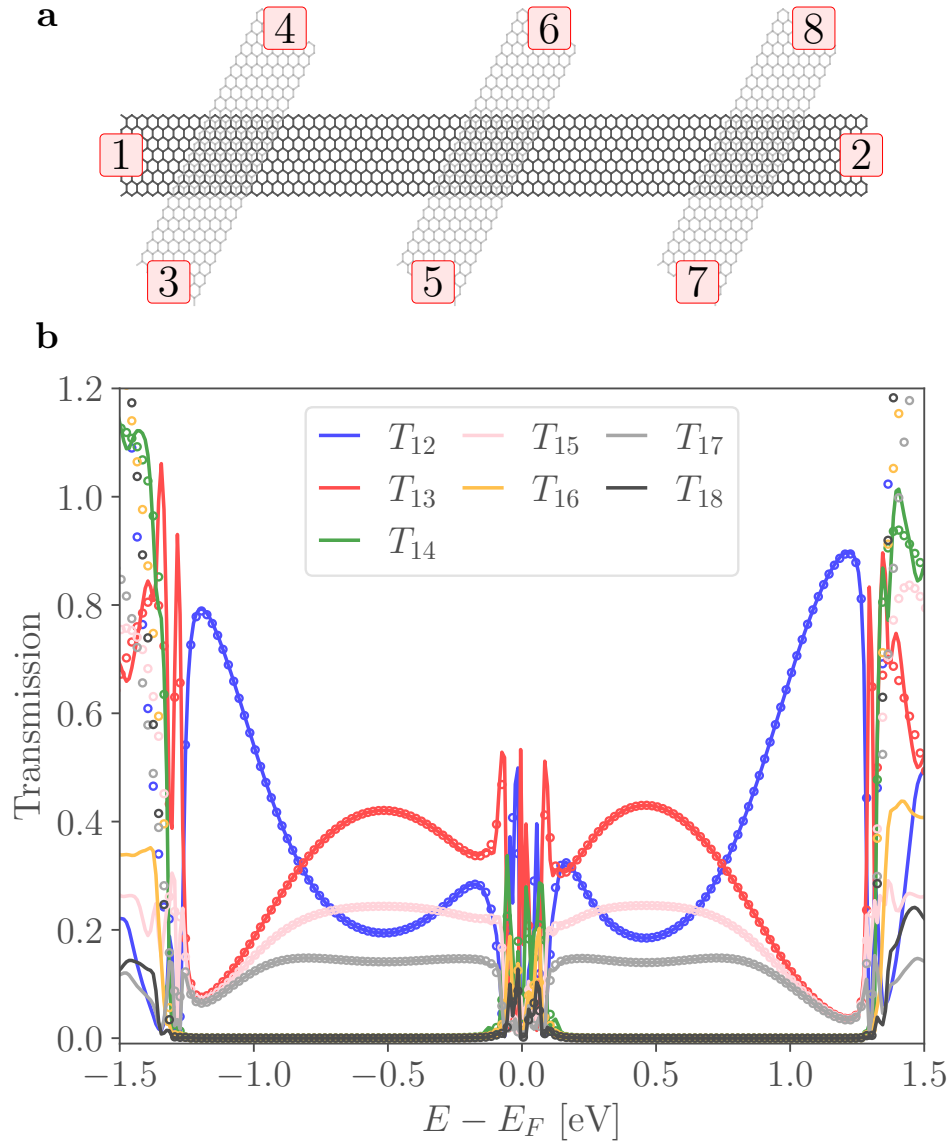


FIG. S15. (a) Geometry of the device with three consecutive crossings. All 8 terminals are indicated in red squares. (b) Transmission probabilities between the different pairs of terminals for an incoming electron in terminal 1 as a function of the electron energy. Solid lines represent the transmission probability for the full device, while open circles represent the obtained transmission probability using the independent-scatterers approximation.

S10. AVERAGED TRANSMISSION PROBABILITIES

In this section we compute the averaged transmission probabilities, calculated as $\bar{T}_{ij} = (T_{ij}^{\uparrow} + T_{ij}^{\downarrow})/2$, for both spin configurations $\boxed{\uparrow\uparrow}$ and $\boxed{\uparrow\downarrow}$ compared to the unpolarized case in Fig. S16. By comparing these results and the ones shown in the main text, it can be seen that while the spin-averaged transmission of the device reproduces our earlier results [10] (*i.e.*, it is affected very little by inclusion of the mean-field Coulomb interaction), we find a strong spin-dependence of the transmission, something that is completely absent in the non-interacting case.

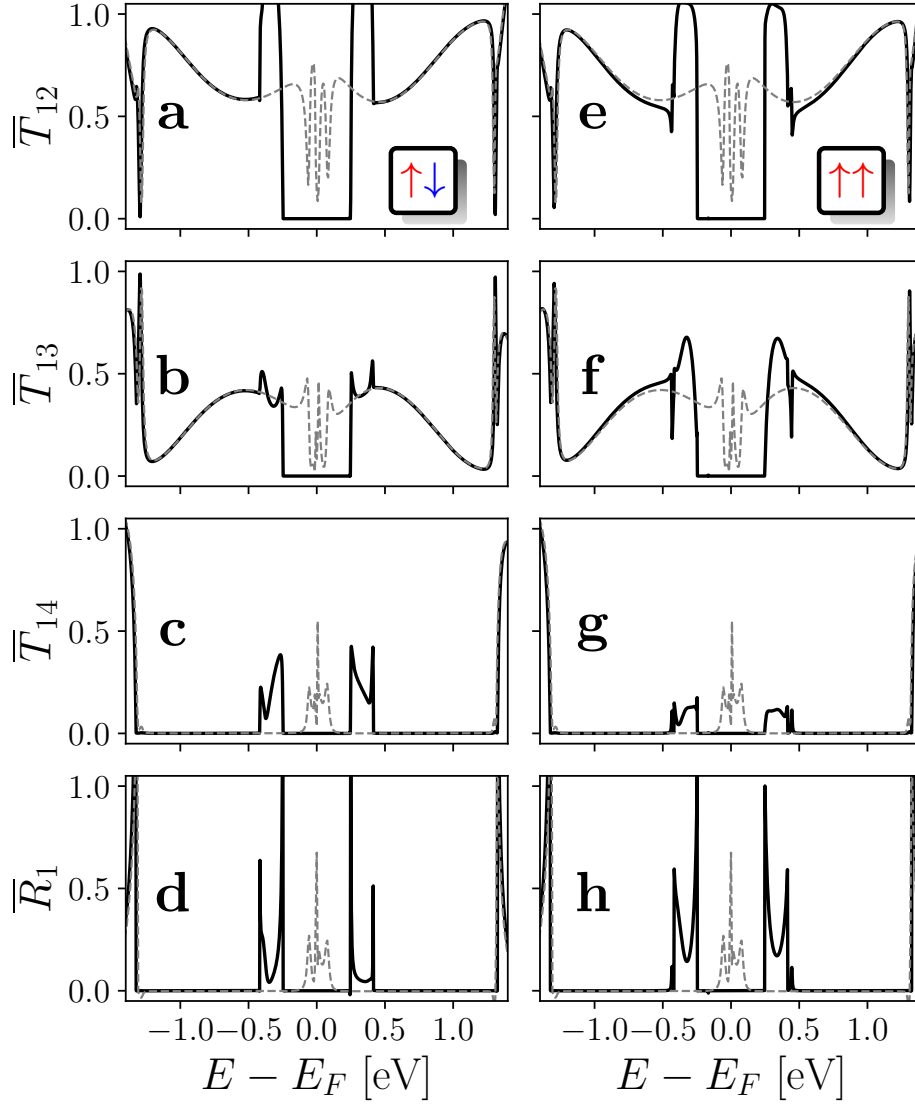


FIG. S16. Black solid lines stand for $\bar{T}_{ij} = (T_{ij}^\uparrow + T_{ij}^\downarrow)/2$ while the gray dashed lines stand for the unpolarized transmission probabilities.

S11. ROLE OF CROSSING GEOMETRY FOR THE SPIN-POLARIZING TRANSPORT EFFECT

We note that there are some experimental challenges to realize the proposed devices, for example to control the stacking registry and the twist angle. These parameters were already assessed in Ref. [10] for unpolarized devices, showing that the beam splitting effect remained largely unaffected by these perturbations, however in that analysis the Coulomb repulsion was not included. For this reason, in this section we study the behavior of the spin transport properties of the crossed ZGNRs for different spin configurations ($\uparrow\uparrow$ and $\uparrow\downarrow$), intersection angles (within $55\text{-}65^\circ$), and stacking registries at the crossing. In Fig. S17 we show both P_{12} and the maximum reflection probability $R_1^>$ as a function of the in-plane translation of the top ribbon with respect to the lower one for different intersection angles and the two spin configurations $\uparrow\downarrow$ and $\uparrow\uparrow$. Here we observe that both $\uparrow\downarrow$ and $\uparrow\uparrow$ configurations still show spin-polarized current generally for different angles and translations. Even in the case of $\uparrow\downarrow$, which diminishes its polarization to $P_{12} \leq 10\%$ for angles $\theta > 64^\circ$, we find that this effect is reverted for $E = -0.5$ eV, where the polarization grows with the angle and only diminishes for $\theta < 56^\circ$ (not shown here). We also observe that backscattering remains rather small for crossed ZGNRs regardless the stacking configuration. This result extends to the whole single-mode energy region (not shown here).

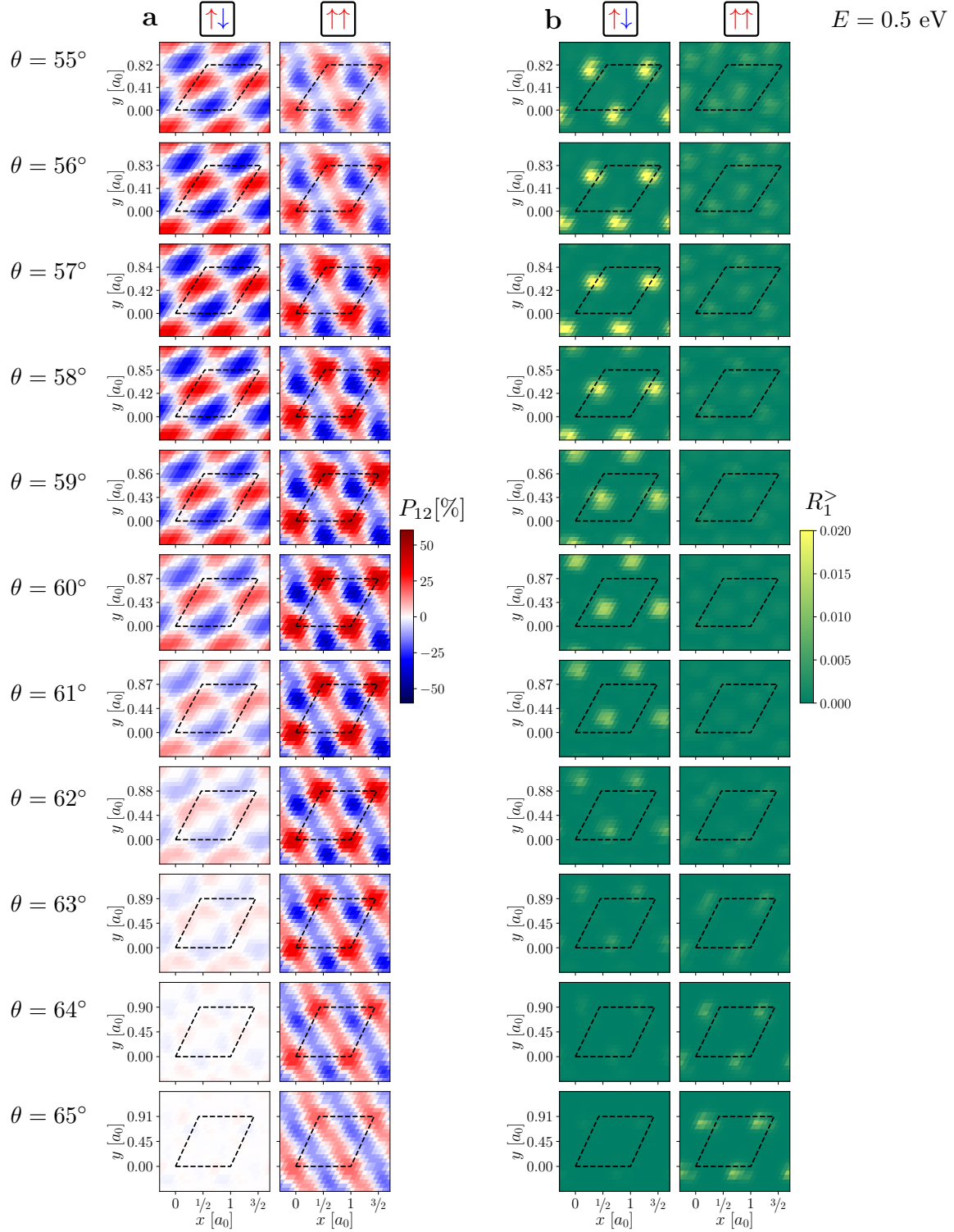


FIG. S17. (a) Spin polarization P_{12} of the current from electrode 1 to 2 and (b) maximum of reflection probability, $R_1^> = \max(R_1^\uparrow, R_1^\downarrow)$ as function of in-plane translations of one ribbon with respect to the other for the $\uparrow\uparrow$ and $\uparrow\downarrow$ spin configurations at different intersection angles. The electron energy is fixed at $E = 0.5$ eV. The unit cell, defined by the lattice vectors of the two ribbons (forming the angle θ), is indicated by the black parallelogram.

S12. STATISTICAL ANALYSIS OF RANDOM ARRAY DEVICES

In this section we provide a description of the statistical analysis behind the results presented in Fig. 4(b) of the main text. We begin with a derivation of the analytic expression of the average absolute spin polarization of arrays $\langle |\overline{P}_{12}| \rangle$.

Starting from Eq. (2) of the main text for the polarization P_{12} of a single junction, we can express the polarization \overline{P}_{12} of an array of N junctions as

$$\overline{P}_{12}(N) = \frac{1 - e^{\overline{\lambda}(N)}}{1 + e^{\overline{\lambda}(N)}}, \quad (\text{S13})$$

where

$$\overline{\lambda}(N) = \sum_{i=1}^N \lambda_i, \quad (\text{S14})$$

$$\lambda_i = \ln \frac{T_{12}^\downarrow(i)}{T_{12}^\uparrow(i)}. \quad (\text{S15})$$

Assuming independent and identical distribution (iid) of the configuration (angle and displacement) of each crossing, it follows from the multiplicative central limit theorem that the ratio $e^{\overline{\lambda}(N)}$ follows a *log-normal* distribution with parameters $\overline{\mu} = \mu N$ and $\overline{w} = w\sqrt{N}$, where μ and w^2 are the mean and variance, respectively, of λ for an individual crossing.

In the unbiased (worst) case, $\mu = 0$, as for the present systems, this allows us to write the *absolute value* averages

$$\langle |\overline{\lambda}(N)| \rangle = \int_{-\infty}^{\infty} ds |s| \mathcal{N}(s, 0, \overline{w}^2) = \overline{w} \sqrt{\frac{2}{\pi}} = w \sqrt{\frac{2N}{\pi}} = \Lambda \sqrt{N}, \quad (\text{S16})$$

$$\begin{aligned} \langle e^{-|\overline{\lambda}(N)|} \rangle &= \int_{-\infty}^{\infty} ds e^{-|s|} \mathcal{N}(s, 0, \overline{w}^2) = e^{\overline{w}^2/2} \operatorname{erfc} \left[\frac{\overline{w}}{\sqrt{2}} \right] = e^{w^2 N/2} \operatorname{erfc} \left[w \sqrt{\frac{N}{2}} \right] \\ &= e^{\pi \Lambda^2 N/4} \operatorname{erfc} \left[\Lambda \frac{\sqrt{\pi N}}{2} \right], \end{aligned} \quad (\text{S17})$$

$$\langle |\overline{P}_{12}(N)| \rangle = \int_{-\infty}^{\infty} ds \left| \frac{1 - e^s}{1 + e^s} \right| \mathcal{N}(s, 0, \overline{w}^2), \quad (\text{S18})$$

where $\langle \dots \rangle$ denotes the statistical average, $\Lambda \equiv \langle |\lambda_1| \rangle$ the average for a single junction, and $\mathcal{N}(s, \overline{\mu}, \overline{w}^2)$ the normal distribution. Note that these expressions are only strictly relevant in our case for $N \rightarrow \infty$, where the use of the normal distribution is fully justified. Fig. S19

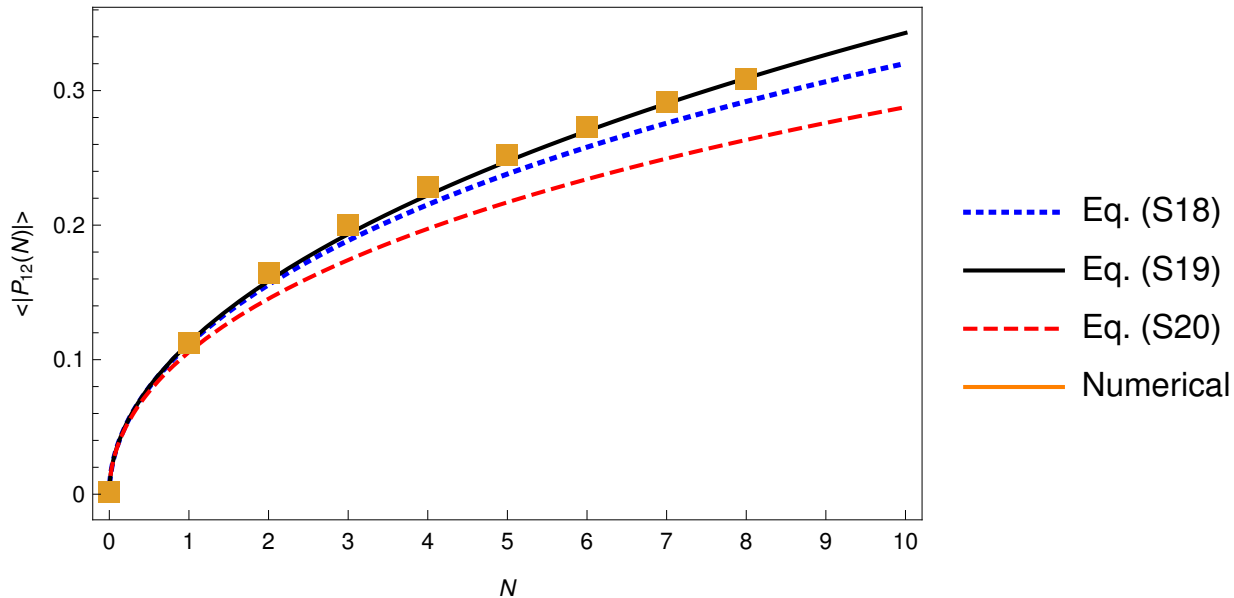


FIG. S18. Comparison of Eqs. (S18)-(S20) (blue, black and red lines, respectively) for the statistical average $\langle |\overline{P}_{12}(N)| \rangle$ against the direct numerical evaluation (orange squares) from the generated random data set, from which one also obtains the parameter $\Lambda \equiv \langle |\lambda_1| \rangle = 0.22602$.

below shows the actual convergence of the distribution for $\bar{\lambda}$ as N increases.

From Eq. (S16) and Eq. (S17) we can write two approximate expressions for the average *absolute polarization*:

$$\langle |\overline{P}_{12}| \rangle \approx \frac{1 - e^{-\langle |\bar{\lambda}(N)| \rangle}}{1 + e^{-\langle |\bar{\lambda}(N)| \rangle}} = \frac{1 - e^{-\Lambda\sqrt{N}}}{1 + e^{-\Lambda\sqrt{N}}}, \quad (\text{S19})$$

$$\langle |\overline{P}_{12}| \rangle \approx \frac{1 - \langle e^{-|\bar{\lambda}(N)|} \rangle}{1 + \langle e^{-|\bar{\lambda}(N)|} \rangle}. \quad (\text{S20})$$

A comparison of the different statistical averages based on the assumption of a normal distribution is shown in Fig. S18 against the direct numerical evaluation of the average for the generated data set. The approach to 1 exponentially in \sqrt{N} according to Eq. (S16) suggests the intuitive interpretation of the spin filtering mechanism in terms of 1D random walk as at each crossing a step λ_i of random length and direction on the real line is added to $\bar{\lambda}$. Note that the approximation Eq. (S16) fits the curve for $\langle |P_{12}| \rangle$ surprisingly well. This is partially accidental and, as seen in Fig. S18, the fit is systematically worse for larger N (as the variance of $\bar{\lambda}(N)$ increases).

Let us next turn to the actual statistical sampling procedure. The data set behind Fig. 4b in of the main text relies on an unbiased sampling of 10^7 different spin-, intersection

angle, and translation configurations for each N drawn from the actual realizations behind Fig. S17. The angle is sampled uniformly within the range $\theta \in [55^\circ, 65^\circ]$ in steps of 1° , while the translations are sampled over the unit cell on a 10×10 uniform grid. In Fig. S19 and Fig. S20 we show the histograms for the quantities $\bar{\lambda}(N)$ and $|\overline{P_{12}}|$. Our assumption of equal probability weight for all configurations is to keep things simple, although in reality the commensurate structures may be energetically favored. The main point of this statistical analysis is to show that a microscopic control over the individual crossings is not necessary to obtain a spin-polarizing array.

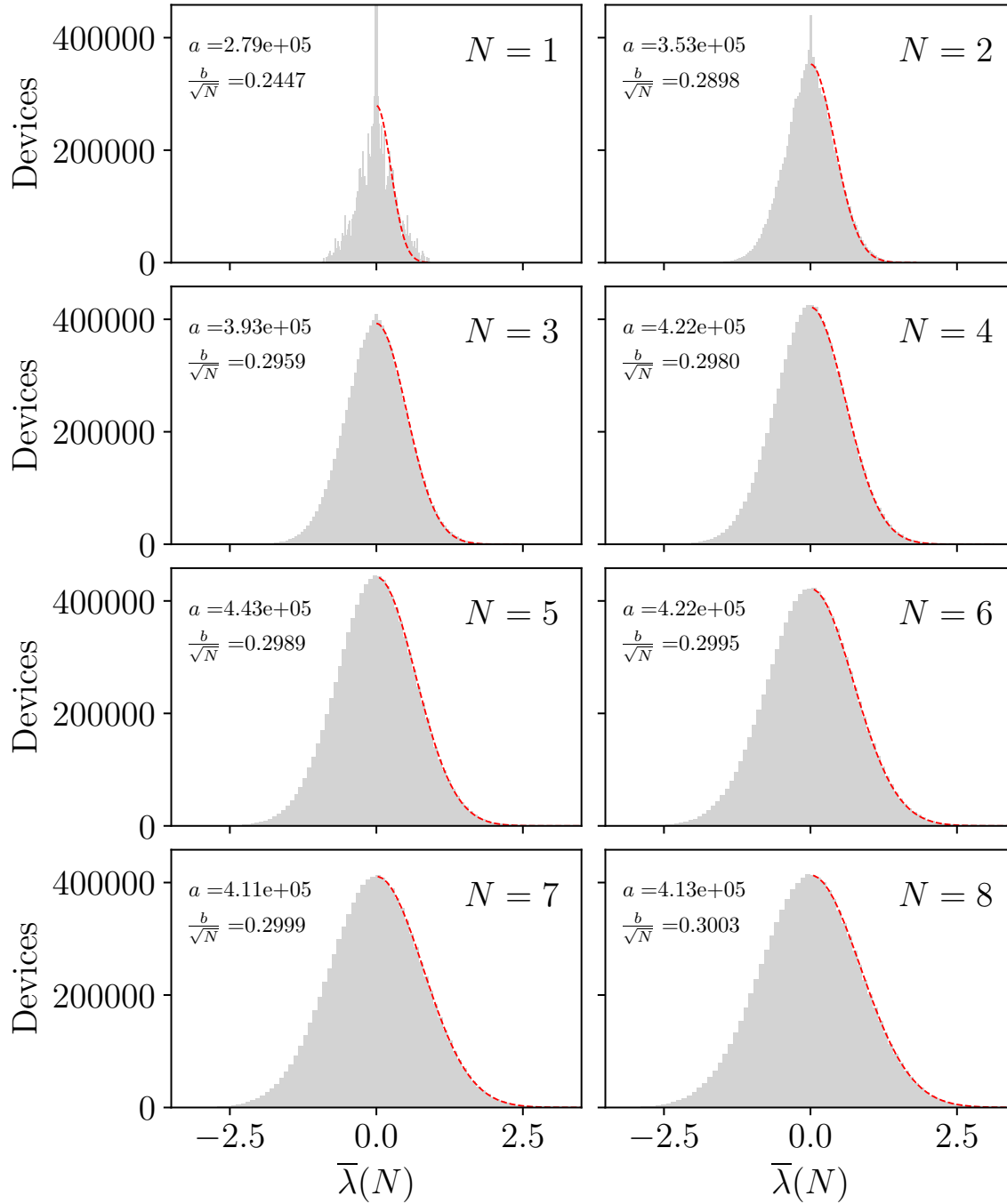


FIG. S19. Histogram of the distribution (100 bins) of $\bar{\lambda}(N)$ from 10^7 random devices. The red dashed lines correspond to a Gaussian fitting $f(\bar{\lambda}) = a \exp\left(-\bar{\lambda}^2/2b^2\right)$, where the resulting fitting parameters a, b are indicated in each panel.

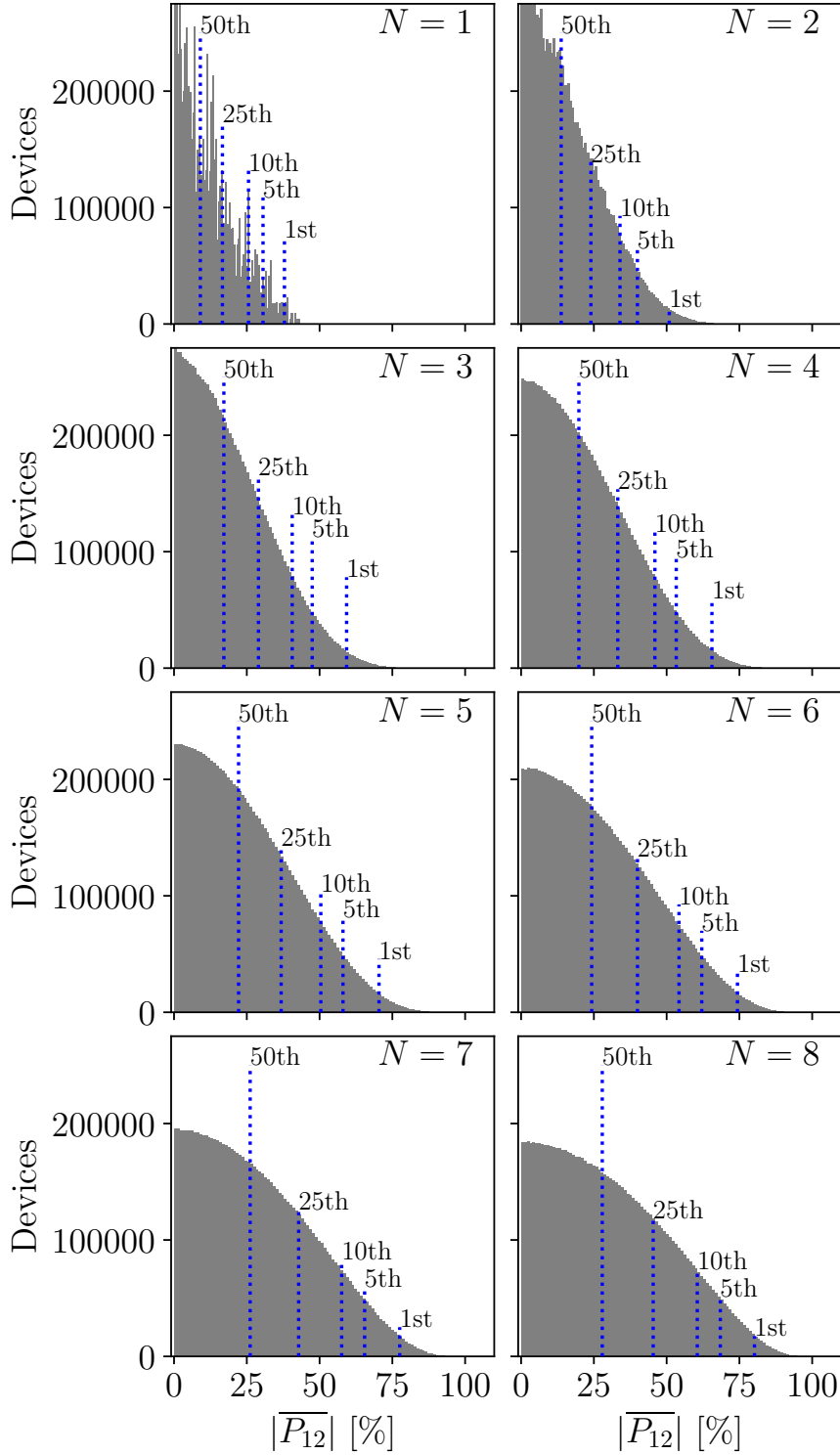


FIG. S20. Histogram of the distribution (100 bins) of $|\overline{P}_{12}|$ from 10^7 random devices. The best (1, 5, 10, 25, 50)th percentiles are indicated with blue dotted lines in each panel.

S13. A SPIN-POLARIZING BEAM SPLITTER WITH BEARDED GNRs

In this section we analyze the transport properties of intersecting bearded GNRs. The band structure and geometry of this structure is shown in Fig. S21. Although, to our knowledge, these systems have not yet been synthesized, we discuss these devices to complete our analysis on spin polarizing beam splitters formed by two crossed general GNRs. This type of GNRs are oriented along the zigzag direction but display different physical edges than ZGNRs. However, they present similar spin-polarized edge states as seen in Fig. S21. In Fig. S22 we plot both the self-consistent solutions $\boxed{\uparrow\uparrow}$ and $\boxed{\uparrow\downarrow}$ and the scattering states for this device, while in Fig. S23 we show the more detailed transmission probabilities for an incoming electron into terminal 1 as a function of the electronic energy. Figures S22 and S23 supports that both the beam splitting effect and the spin-polarizing scattering potential are general features of junctions with *edge-polarized GNRs*.

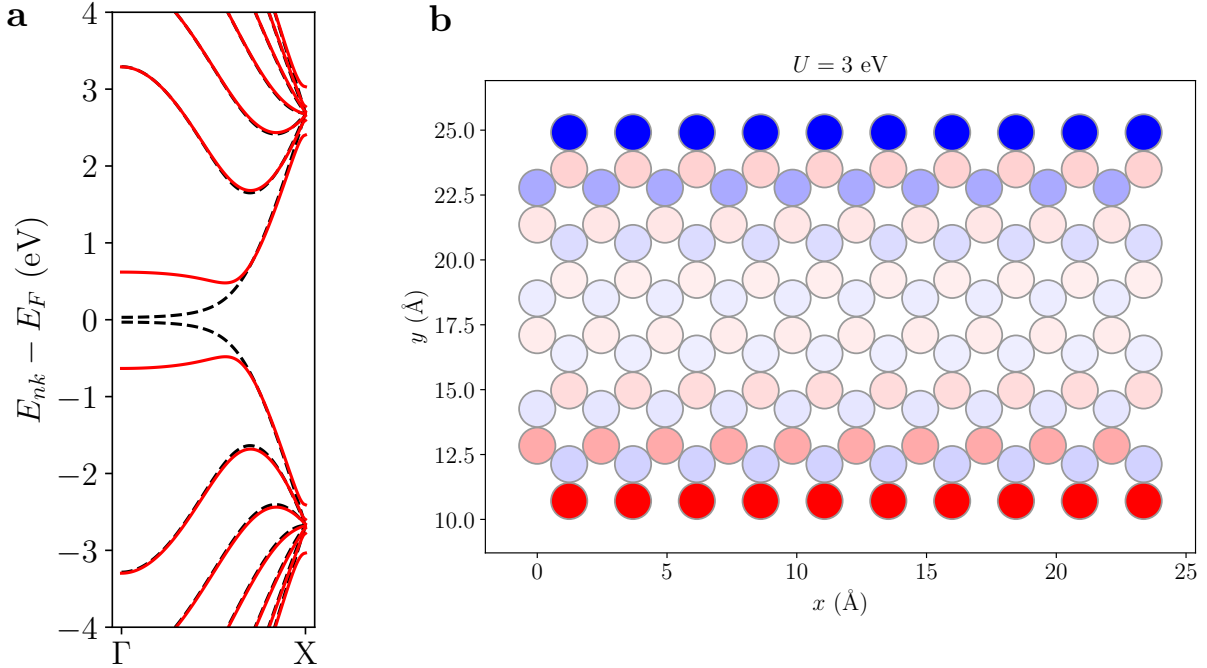


FIG. S21. (a) Band structure for the bearded GNR calculated with $U = 0$ (dashed black lines) and $U = 3$ eV (solid red lines). (b) Spin density for the periodic structure ($U = 3$ eV).

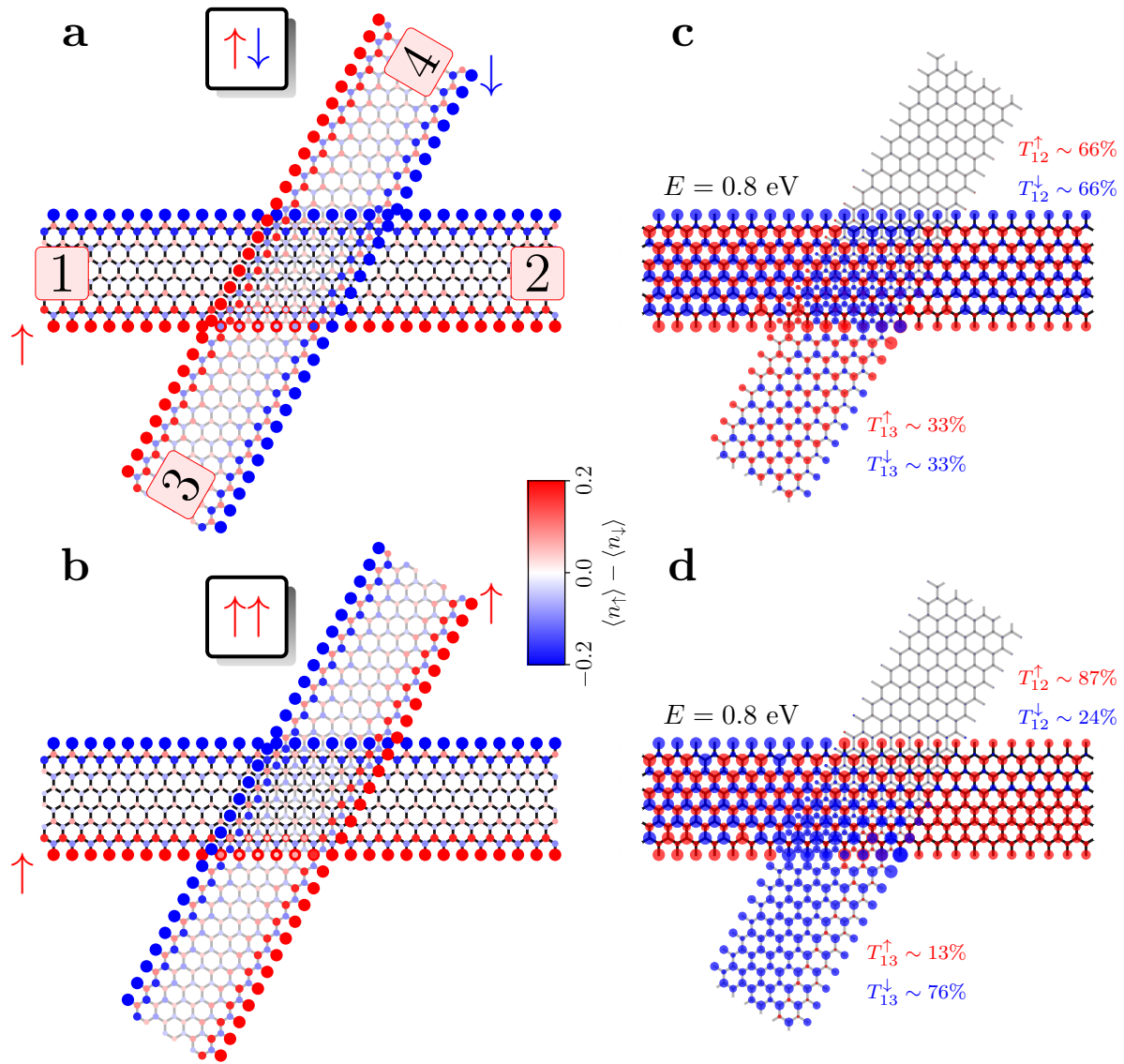


FIG. S22. (a,b) Spin density distribution for the crossed bearded-GNRs with an intersection angle of $\theta = 60^\circ$. (c,d) Spin-resolved scattering states for an incoming electron from terminal 1 calculated at $E = 0.8$ eV. The dominant spin on each site at this energy is shown in red for up-spins and in blue for down-spins. The transmission probabilities T_{12}^σ and T_{13}^σ are annotated.

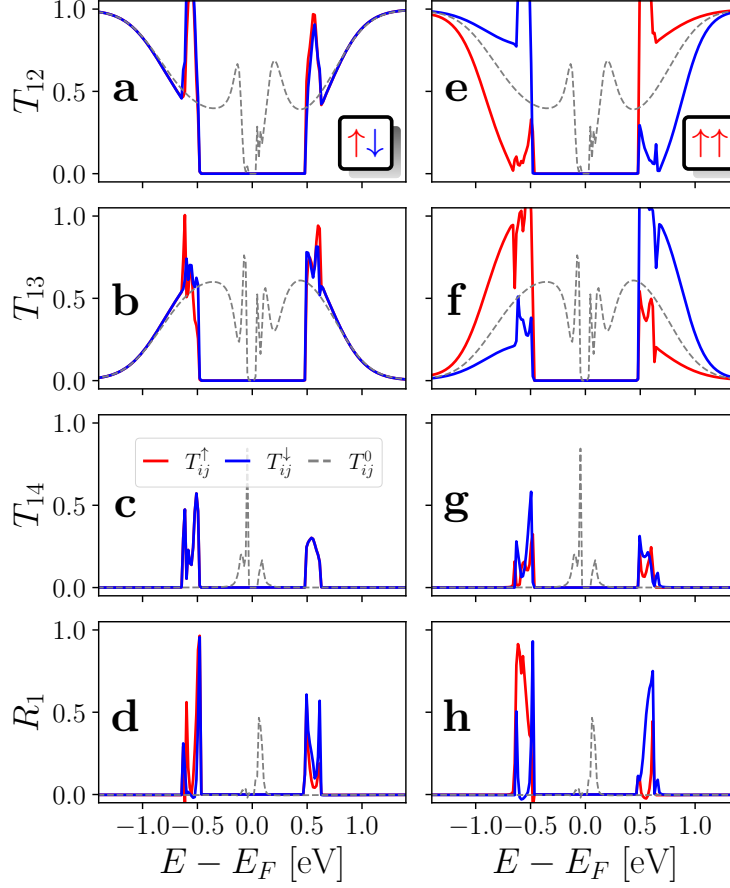


FIG. S23. Spin- and energy-resolved transmission probabilities T_{12} , T_{13} , T_{14} , and reflection R_1 for (a-d) the $\uparrow\downarrow$ and (e-h) $\uparrow\uparrow$ configurations. Electrons are injected from electrode 1. The red (blue) curves correspond to the up (down) spin components with $U = 3$ eV. For comparison, the corresponding calculations for the unpolarized case is indicated by dashed gray lines.

-
- [1] H. Feldner, Z. Y. Meng, T. C. Lang, F. F. Assaad, S. Wessel, and A. Honecker, *Phys. Rev. Lett.* **106**, 226401 (2011).
- [2] S. Sanz, N. Papior, M. Brandbyge, and T. Frederiksen, *hubbard: v0.1.0* (2021).
- [3] M. Brandbyge, J.-L. Mozos, P. Ordejón, J. Taylor, and K. Stokbro, *Phys. Rev. B* **65**, 165401 (2002).
- [4] N. Papior, N. Lorente, T. Frederiksen, A. García, and M. Brandbyge, *Comp. Phys. Commun.* **212**, 8 (2017).
- [5] M. P. L. Sancho, J. M. L. Sancho, J. M. L. Sancho, and J. Rubio, *J. Phys. F: Met. Phys.* **15**, 851 (1985).
- [6] N. Papior, *sisl: v0.11.0* (2021).
- [7] T. Asano and J. Nakamura, *ACS Omega* **4**, 22035 (2019).
- [8] E. Mostaani, N. D. Drummond, and V. I. Fal'ko, *Phys. Rev. Lett.* **115**, 115501 (2015).
- [9] H. Lee, Y.-W. Son, N. Park, S. Han, and J. Yu, *Phys. Rev. B* **72**, 174431 (2005).
- [10] S. Sanz, P. Brandimarte, G. Giedke, D. Sánchez-Portal, and T. Frederiksen, *Phys. Rev. B* **102**, 035436 (2020).
- [11] M. Cahay, M. McLennan, and S. Datta, *Phys. Rev. B* **37**, 10125 (1988).

Bibliography

- [1] G. E. Moore, “*Progress in digital integrated electronics [Technical literature, Copyright 1975 IEEE. Reprinted, with permission. Technical Digest. International Electron Devices Meeting, IEEE, 1975, pp. 11-13.]*”, [IEEE J. Solid-State Circuits](#) **11**, 36–37 (2006).
- [2] G. E. Moore, “*Cramming more components onto integrated circuits, Reprinted from Electronics, volume 38, number 8, April 19, 1965, pp.114 ff.*”, [IEEE J. Solid-State Circuits](#) **11**, 33–35 (2006).
- [3] M. Bohr, “*14 nm process technology: Opening new horizons*”, <https://www.intel.co.uk/content/www/uk/en/architecture-and-technology/bohr-14nm-idf-2014-brief.html> (2014).
- [4] M. Bohr, “*Technology leadership*”, <https://newsroom.intel.com/newsroom/wp-content/uploads/sites/11/2017/09/mark-bohr-on-intels-technology-leadership.pdf> (2017).
- [5] K. S. Novoselov, A. K. Geim, S. V. Morozov, D. Jiang, Y. Zhang, S. V. Dubonos, I. V. Grigorieva, and A. A. Firsov, “*Electric field effect in atomically thin carbon films*”, [Science](#) **306**, 666–669 (2004).
- [6] K. S. Novoselov, A. K. Geim, S. V. Morozov, D. Jiang, M. I. Katsnelson, I. V. Grigorieva, S. V. Dubonos, and A. A. Firsov, “*Two-dimensional gas of massless Dirac fermions in graphene*”, [Nature](#) **438**, 197–200 (2005).
- [7] A. K. Geim and K. S. Novoselov, “*The rise of graphene*”, [Nature Materials](#) **6**, 183–191 (2007).
- [8] G. Iannaccone, F. Bonaccorso, L. Colombo, and G. Fiori, “*Quantum engineering of transistors based on 2D materials heterostructures*”, [Nat. Nanotechnol.](#) **13**, 183–191 (2018).

- [9] F. Schwierz, “*Graphene transistors*”, *Nat. Nanotechnol.* **5**, 487–496 (2010).
- [10] W. Mehr, J. Dabrowski, J. C. Scheytt, G. Lippert, Y.-H. Xie, M. C. Lemme, M. Ostling, and G. Lupina, “*Vertical graphene base transistor*”, *IEEE Electron Device Lett.* **33**, 691–693 (2012).
- [11] S. Vaziri, G. Lupina, C. Henkel, A. D. Smith, M. Östling, J. Dabrowski, G. Lippert, W. Mehr, and M. C. Lemme, “*A graphene-based hot electron transistor*”, *Nano Lett.* **13**, 1435–1439 (2013).
- [12] T. Ohta, A. Bostwick, T. Seyller, K. Horn, and E. Rotenberg, “*Controlling the electronic structure of bilayer graphene*”, *Science* **313**, 951–954 (2006).
- [13] E. V. Castro, K. S. Novoselov, S. V. Morozov, N. M. R. Peres, J. M. B. L. dos Santos, J. Nilsson, F. Guinea, A. K. Geim, and A. H. C. Neto, “*Biased bilayer graphene: semiconductor with a gap tunable by the electric field effect*”, *Phys. Rev. Lett.* **99**, 216802 (2007).
- [14] P. Gava, M. Lazzeri, A. M. Saitta, and F. Mauri, “*Ab initio study of gap opening and screening effects in gated bilayer graphene*”, *Phys. Rev. B* **79**, 165431 (2009).
- [15] Y. Zhang, T.-T. Tang, C. Girit, Z. Hao, M. C. Martin, A. Zettl, M. F. Crommie, Y. R. Shen, and F. Wang, “*Direct observation of a widely tunable bandgap in bilayer graphene*”, *Nature* **459**, 820–823 (2009).
- [16] A. Rycerz, J. Tworzydło, and C. W. J. Beenakker, “*Valley filter and valley valve in graphene*”, *Nat. Phys.* **3**, 172–175 (2007).
- [17] M. Settnes, S. R. Power, M. Brandbyge, and A.-P. Jauho, “*Graphene nanobubbles as valley filters and beam splitters*”, *Phys. Rev. Lett.* **117**, 276801 (2016).
- [18] J. Cai, P. Ruffieux, R. Jaafar, M. Bieri, T. Braun, S. Blankenburg, M. Muoth, A. P. Seitsonen, M. Saleh, X. Feng, K. Müllen, and R. Fasel, “*Atomically precise bottom-up fabrication of graphene nanoribbons*”, *Nature* **466**, 470 (2010).
- [19] L. Grill, M. Dyer, L. Lafferentz, M. Persson, M. V. Peters, and S. Hecht, “*Nano-architectures by covalent assembly of molecular building blocks*”, *Nat. Nanotechnol.* **2**, 687–691 (2007).
- [20] S. Clair and D. G. de Oteyza, “*Controlling a chemical coupling reaction on a surface: tools and strategies for on-surface synthesis*”, *Chem. Rev.* **119**, 4717–4776 (2019).

- [21] O. V. Yazyev and L. Helm, “*Defect-induced magnetism in graphene*”, *Phys. Rev. B* **75**, 125408 (2007).
- [22] Y.-W. Son, M. L. Cohen, and S. G. Louie, “*Energy gaps in graphene nanoribbons*”, *Phys. Rev. Lett.* **97**, 216803 (2006).
- [23] H. González-Herrero, J. M. Gómez-Rodríguez, P. Mallet, M. Moaied, J. J. Palacios, C. Salgado, M. M. Ugeda, J.-Y. Veullen, F. Yndurain, and I. Brihuega, “*Atomic-scale control of graphene magnetism by using hydrogen atoms*”, *Science* **352**, 437–441 (2016).
- [24] R. Fasel, “*How to induce magnetism in graphene*”, <https://sciglow.com/how-to-induce-magnetism-in-graphene/> (2019).
- [25] S. Mishra, D. Beyer, K. Eimre, S. Kezilebieke, R. Berger, O. Gröning, C. A. Pignedoli, K. Müllen, P. Liljeroth, P. Ruffieux, X. Feng, and R. Fasel, “*Topological frustration induces unconventional magnetism in a nanographene*”, *Nat. Nanotechnol.* **15**, 22–28 (2020).
- [26] Y. Kopelevich, P. Esquinazi, J. H. S. Torres, and S. Moehlecke, “*Ferromagnetic- and superconducting-like behavior of graphite*”, *J. Low Temp. Phys.* **119**, 691–702 (2000).
- [27] P. Esquinazi, A. Setzer, R. Höhne, C. Semmelhack, Y. Kopelevich, D. Spemann, T. Butz, B. Kohlstrunk, and M. Lösche, “*Ferromagnetism in oriented graphite samples*”, *Phys. Rev. B* **66**, 024429 (2002).
- [28] B. Trauzettel, D. V. Bulaev, D. Loss, and G. Burkard, “*Spin qubits in graphene quantum dots*”, *Nat. Phys.* **3**, 192–196 (2007).
- [29] A. R. Rocha, V. M. García-suárez, S. W. Bailey, C. J. Lambert, J. Ferrer, and S. Sanvito, “*Towards molecular spintronics*”, *Nature Materials* **4**, 335–339 (2005).
- [30] D. G. de Oteyza and T. Frederiksen, “*Carbon-based nanostructures as a versatile platform for tunable π -magnetism*”, *J. Phys.: Condens. Matter* (2022).
- [31] O. V. Yazyev, “*Emergence of magnetism in graphene materials and nanostructures*”, *Rep. Prog. Phys.* **73**, 056501 (2010).
- [32] W. L. Wang, S. Meng, and E. Kaxiras, “*Graphene nanoflakes with large spin*”, *Nano Lett.* **8**, 241–245 (2008).

- [33] J. Fernández-Rossier and J. J. Palacios, “Magnetism in graphene nanoislands”, *Phys. Rev. Lett.* **99**, 177204 (2007).
- [34] E. Kan, W. Hu, C. Xiao, R. Lu, K. Deng, J. Yang, and H. Su, “Half-metallicity in organic single porous sheets”, *J. Am. Chem. Soc.* **134**, 5718–5721 (2012).
- [35] T. Stuyver, B. Chen, T. Zeng, P. Geerlings, F. De Proft, and R. Hoffmann, “Do diradicals behave like radicals?”, *Chem. Rev.* **119**, 11 291–11 351 (2019).
- [36] J. Li, S. Sanz, M. Corso, D. J. Choi, D. Peña, T. Frederiksen, and J. I. Pascual, “Single spin localization and manipulation in graphene open-shell nanostructures”, *Nat. Commun.* **10**, 200 (2019).
- [37] J. Li, N. Friedrich, N. Merino, D. G. de Oteyza, D. Peña, D. Jacob, and J. I. Pascual, “Electrically addressing the spin of a magnetic porphyrin through covalently connected graphene electrodes”, *Nano Lett.* **19**, 3288–3294 (2019).
- [38] J. Li, S. Sanz, J. Castro-Esteban, M. Vilas-Varela, N. Friedrich, T. Frederiksen, D. Peña, and J. I. Pascual, “Uncovering the triplet ground state of triangular graphene nanoflakes engineered with atomic precision on a metal surface”, *Phys. Rev. Lett.* **124**, 177201 (2020).
- [39] N. Friedrich, P. Brandimarte, J. Li, S. Saito, S. Yamaguchi, I. Pozo, D. Peña, T. Frederiksen, A. Garcia-Lekue, D. Sánchez-Portal, and J. I. Pascual, “Magnetism of topological boundary states induced by boron substitution in graphene nanoribbons”, *Phys. Rev. Lett.* **125**, 146801 (2020).
- [40] S. Mishra, D. Beyer, K. Eimre, R. Ortiz, J. Fernández-Rossier, R. Berger, O. Gröning, C. A. Pignedoli, R. Fasel, X. Feng, and P. Ruffieux, “Collective all-carbon magnetism in triangulene dimers”, *Angew. Chem. Int. Ed.* **59**, 12 041–12 047 (2020).
- [41] S. Mishra, G. Catarina, F. Wu, R. Ortiz, D. Jacob, K. Eimre, J. Ma, C. A. Pignedoli, X. Feng, P. Ruffieux, J. Fernández-Rossier, and R. Fasel, “Observation of fractional edge excitations in nanographene spin chains”, *Nature* **598**, 287–292 (2021).
- [42] S. Mishra, X. Yao, Q. Chen, K. Eimre, O. Gröning, R. Ortiz, M. Di Giovannantonio, J. C. Sancho-García, J. Fernández-Rossier, C. A. Pignedoli, K. Müllen, P. Ruffieux, A. Narita, and R. Fasel, “Large magnetic exchange coupling in rhombus-shaped nanographenes with zigzag periphery”, *Nat. Chem.* **13**, 581–586 (2021).

- [43] J. Hieulle, S. Castro, N. Friedrich, A. Vegliante, F. R. Lara, S. Sanz, D. Rey, M. Corso, T. Frederiksen, J. I. Pascual, and D. Peña, “*On-surface synthesis and collective spin excitations of a triangulene-based nanostar*”, *Angew. Chem. Int. Ed.* **60**, 25 224–25 229 (2021).
- [44] A. A. Ovchinnikov, “*Multiplicity of the ground state of large alternant organic molecules with conjugated bonds*”, *Theor. Chim. Acta* **47**, 297–304 (1978).
- [45] E. H. Lieb, “*Two theorems on the Hubbard model*”, *Phys. Rev. Lett.* **62**, 1201–1204 (1989).
- [46] R. Ortiz, R. A. Boto, N. García-Martínez, J. C. Sancho-García, M. Melle-Franco, and J. Fernández-Rossier, “*Exchange rules for diradical π -conjugated hydrocarbons*”, *Nano Lett.* **19**, 5991–5997 (2019).
- [47] R. R. Nair, M. Sepioni, I.-L. Tsai, O. Lehtinen, J. Keinonen, A. V. Krasheninnikov, T. Thomson, A. K. Geim, and I. V. Grigorieva, “*Spin-half paramagnetism in graphene induced by point defects*”, *Nat. Phys.* **8**, 199–202 (2012).
- [48] K. M. McCreary, A. G. Swartz, W. Han, J. Fabian, and R. K. Kawakami, “*Magnetic moment formation in graphene detected by scattering of pure spin currents*”, *Phys. Rev. Lett.* **109**, 186604 (2012).
- [49] A. Berdonces-Layunta, J. Lawrence, S. Edalatmanesh, J. Castro-Esteban, T. Wang, M. S. G. Mohammed, L. Colazzo, D. Peña, P. Jelínek, and D. G. de Oteyza, “*Chemical stability of (3,1)-chiral graphene nanoribbons*”, *ACS Nano* **15**, 5610–5617 (2021).
- [50] M. Solà, “*Forty years of Clar’s aromatic π -sextet rule*”, *Front. Chem.* **1**, 1–8 (2013).
- [51] S. Chen, Z. Han, M. M. Elahi, K. M. M. Habib, L. Wang, B. Wen, Y. Gao, T. Taniguchi, K. Watanabe, J. Hone, A. W. Ghosh, and C. R. Dean, “*Electron optics with p - n junctions in ballistic graphene*”, *Science* **353**, 1522–1525 (2016).
- [52] J. Splettstoesser, P. Samuelsson, M. Moskalets, and M. Büttiker, “*Two-particle Aharonov-Bohm effect in electronic interferometers*”, *J. Phys. A* **43**, 354027 (2010).
- [53] C. Bäuerle, D. C. Glattli, T. Meunier, F. Portier, P. Roche, P. Roulleau, S. Takada, and X. Waintal, “*Coherent control of single electrons: a review of current progress*”, *Rep. Prog. Phys.* **81**, 056503 (2018).

- [54] U. Sivan, M. Heiblum, C. P. Umbach, and H. Shtrikman, “*Electrostatic electron lens in the ballistic regime*”, *Phys. Rev. B* **41**, 7937–7940 (1990).
- [55] J. Spector, H. L. Stormer, K. W. Baldwin, L. N. Pfeiffer, and K. W. West, “*Electron focusing in two-dimensional systems by means of an electrostatic lens*”, *Appl. Phys. Lett.* **56**, 1290–1292 (1990).
- [56] P. Rickhaus, P. Makk, M.-H. Liu, K. Richter, and C. Schönenberger, “*Gate tuneable beamsplitter in ballistic graphene*”, *Appl. Phys. Lett.* **107**, 251901 (2015).
- [57] P. Avouris, Z. Chen, and V. Perebeinos, “*Carbon-based electronics*”, *Nat. Nanotechnol.* **2**, 605–615 (2007).
- [58] Z. Chen, Y.-M. Lin, M. J. Rooks, and P. Avouris, “*Graphene nano-ribbon electronics*”, *Phys. E: Low-Dimens. Syst. Nanostructures* **40**, 228–232 (2007).
- [59] Y.-W. Son, M. L. Cohen, and S. G. Louie, “*Half-metallic graphene nanoribbons*”, *Nature* **444**, 347–349 (2006).
- [60] K. Nakada, M. Fujita, G. Dresselhaus, and M. S. Dresselhaus, “*Edge state in graphene ribbons: Nanometer size effect and edge shape dependence*”, *Phys. Rev. B* **54**, 17954–17961 (1996).
- [61] K. Wakabayashi, M. Fujita, H. Ajiki, and M. Sigrist, “*Electronic and magnetic properties of nanographite ribbons*”, *Phys. Rev. B* **59**, 8271–8282 (1999).
- [62] N. M. R. Peres, A. H. Castro Neto, and F. Guinea, “*Conductance quantization in mesoscopic graphene*”, *Phys. Rev. B* **73**, 195411 (2006).
- [63] M. I. Katsnelson, “*Conductance quantization in graphene nanoribbons: adiabatic approximation*”, *Eur. Phys. J. B* **57**, 225–228 (2007).
- [64] A. H. Castro Neto, F. Guinea, N. M. R. Peres, K. S. Novoselov, and A. K. Geim, “*The electronic properties of graphene*”, *Rev. Mod. Phys.* **81**, 109–162 (2009).
- [65] S. Minke, J. Bundesmann, D. Weiss, and J. Eroms, “*Phase coherent transport in graphene nanoribbons and graphene nanoribbon arrays*”, *Phys. Rev. B* **86**, 155403 (2012).
- [66] J. Baringhaus, M. Ruan, F. Edler, A. Tejada, M. Sicot, A. Taleb-Ibrahimi, A.-P. Li, Z. Jiang, E. H. Conrad, C. Berger, C. Tegenkamp, and W. A. de Heer, “*Exceptional ballistic transport in epitaxial graphene nanoribbons*”, *Nature* **506**, 349 (2014).

- [67] J. Aprozanz, S. R. Power, P. Bampoulis, S. Roche, A.-P. Jauho, H. J. W. Zandvliet, A. A. Zakharov, and C. Tegenkamp, “Ballistic tracks in graphene nanoribbons”, *Nat. Commun.* **9**, 4426 (2018).
- [68] L. P. Zârbo and B. K. Nikolić, “Spatial distribution of local currents of massless Dirac fermions in quantum transport through graphene nanoribbons”, *EPL* **80**, 47001 (2007).
- [69] P. Ruffieux, S. Wang, B. Yang, C. Sánchez-Sánchez, J. Liu, T. Dienel, L. Talirz, P. Shinde, C. A. Pignedoli, D. Passerone, T. Dumslaff, X. Feng, K. Müllen, and R. Fasel, “On-surface synthesis of graphene nanoribbons with zigzag edge topology”, *Nature* **531**, 489 (2016).
- [70] M. Koch, F. Ample, C. Joachim, and L. Grill, “Voltage-dependent conductance of a single graphene nanoribbon”, *Nat. Nanotechnol.* **7**, 713–717 (2012).
- [71] S. Kawai, A. Benassi, E. Gnecco, H. Söde, R. Pawlak, X. Feng, K. Müllen, D. Passerone, C. A. Pignedoli, P. Ruffieux, R. Fasel, and E. Meyer, “Superlubricity of graphene nanoribbons on gold surfaces”, *Science* **351**, 957–961 (2016).
- [72] M. S. Fuhrer, J. Nygård, L. Shih, M. Forero, Y.-G. Yoon, M. S. C. Mazzoni, H. J. Choi, J. Ihm, S. G. Louie, A. Zettl, and P. L. McEuen, “Crossed nanotube junctions”, *Science* **288**, 494–497 (2000).
- [73] D. A. Areshkin and C. T. White, “Building blocks for integrated graphene circuits”, *Nano Lett.* **7**, 3253–3259 (2007).
- [74] T. Jayasekera and J. W. Mintmire, “Transport in multiterminal graphene nanodevices”, *Nanotechnology* **18**, 424033 (2007).
- [75] A. R. Botello-Méndez, E. Cruz-Silva, J. M. Romo-Herrera, F. López-Urías, M. Terrones, B. G. Sumpter, H. Terrones, J.-C. Charlier, and V. Meunier, “Quantum transport in graphene nanonetworks”, *Nano Lett.* **11**, 3058–3064 (2011).
- [76] L. R. F. Lima, A. R. Hernández, F. A. Pinheiro, and C. Lewenkopf, “A 50/50 electronic beam splitter in graphene nanoribbons as a building block for electron optics”, *J. Phys.: Condens. Matter* **28**, 505303 (2016).
- [77] P. Brandimarte, M. Engelund, N. Papior, A. Garcia-Lekue, T. Frederiksen, and D. Sánchez-Portal, “A tunable electronic beam splitter realized with crossed graphene nanoribbons”, *J. Chem. Phys.* **146**, 092318 (2017).

- [78] W. Han, R. K. Kawakami, M. Gmitra, and J. Fabian, “*Graphene spintronics*”, *Nat. Nanotechnol.* **9**, 794–807 (2014).
- [79] H. Min, J. E. Hill, N. A. Sinitsyn, B. R. Sahu, L. Kleinman, and A. H. MacDonald, “*Intrinsic and Rashba spin-orbit interactions in graphene sheets*”, *Phys. Rev. B* **74**, 165310 (2006).
- [80] O. V. Yazyev, “*Hyperfine interactions in graphene and related carbon nanostructures*”, *Nano Lett.* **8**, 1011–1015 (2008).
- [81] M. Slota, A. Keerthi, W. K. Myers, E. Tretyakov, M. Baumgarten, A. Ardavan, H. Sadeghi, C. J. Lambert, A. Narita, K. Müllen, and L. Bogani, “*Magnetic edge states and coherent manipulation of graphene nanoribbons*”, *Nature* **557**, 691–695 (2018).
- [82] O. V. Yazyev and M. I. Katsnelson, “*Magnetic correlations at graphene edges: Basis for novel spintronics devices*”, *Phys. Rev. Lett.* **100**, 047209 (2008).
- [83] W. Han and R. K. Kawakami, “*Spin relaxation in single-layer and bilayer graphene*”, *Phys. Rev. Lett.* **107**, 047207 (2011).
- [84] N. Tombros, C. Jozsa, M. Popinciuc, H. T. Jonkman, and B. J. van Wees, “*Electronic spin transport and spin precession in single graphene layers at room temperature*”, *Nature* **448**, 571–574 (2007).
- [85] M. Fujita, K. Wakabayashi, K. Nakada, and K. Kusakabe, “*Peculiar localized state at zigzag graphite edge*”, *J. Phys. Soc. Jpn.* **65**, 1920–1923 (1996).
- [86] G. Z. Magda, X. Jin, I. Hagymási, P. Vancsó, Z. Osváth, P. Nemes-Incze, C. Hwang, L. P. Biró, and L. Tapasztó, “*Room-temperature magnetic order on zigzag edges of narrow graphene nanoribbons*”, *Nature* **514**, 608–611 (2014).
- [87] R. E. Blackwell, F. Zhao, E. Brooks, J. Zhu, I. Piskun, S. Wang, A. Delgado, Y.-L. Lee, S. G. Louie, and F. R. Fischer, “*Spin splitting of dopant edge state in magnetic zigzag graphene nanoribbons*”, *Nature* **600**, 647–652 (2021).
- [88] S. S. Gregersen, S. R. Power, and A.-P. Jauho, “*Nanostructured graphene for spintronics*”, *Phys. Rev. B* **95**, 121406 (2017).
- [89] M. Wimmer, I. Adagideli, S. Berber, D. Tománek, and K. Richter, “*Spin currents in rough graphene nanoribbons: Universal fluctuations and spin Injection*”, *Phys. Rev. Lett.* **100**, 177207 (2008).

- [90] S. Sanz Wuhl, N. Papior, M. Brandbyge, and T. Frederiksen, “*hubbard: v0.2.0*”. <https://doi.org/10.5281/zenodo.4748765>
- [91] J. M. Soler, E. Artacho, J. D. Gale, A. García, J. Junquera, P. Ordejón, and D. Sánchez-Portal, “*The SIESTA method for ab initio order- N materials simulation*”, *J. Phys.: Condens. Matter* **14**, 2745 (2002).
- [92] M. Brandbyge, J.-L. Mozos, P. Ordejón, J. Taylor, and K. Stokbro, “*Density-functional method for nonequilibrium electron transport*”, *Phys. Rev. B* **65**, 165401 (2002).
- [93] N. R. Papior, “*sisl: v0.11.0*”. <https://doi.org/10.5281/zenodo.597181>
- [94] N. Papior, N. Lorente, T. Frederiksen, A. García, and M. Brandbyge, “*Improvements on non-equilibrium and transport Green function techniques: The next-generation transiesta*”, *Comput. Phys. Commun.* **212**, 8 – 24 (2017).
- [95] T. Wang, S. Sanz, J. Castro-Esteban, J. Lawrence, A. Berdonces-Layunta, M. S. G. Mohammed, M. Vilas-Varela, M. Corso, D. Peña, T. Frederiksen, and D. G. de Oteyza, “*Magnetic interactions between radical pairs in chiral graphene nanoribbons*”, *Nano Lett.* **22**, 164–171 (2022).
- [96] S. Sanz, P. Brandimarte, G. Giedke, D. Sánchez-Portal, and T. Frederiksen, “*Crossed graphene nanoribbons as beam splitters and mirrors for electron quantum optics*”, *Phys. Rev. B* **102**, 035436 (2020).
- [97] S. Sanz, N. Papior, G. Giedke, D. Sánchez-Portal, M. Brandbyge, and T. Frederiksen, “*Spin-polarizing electron beam splitter from crossed graphene nanoribbons*”, *Phys. Rev. Lett.* **129**, 037701 (2022).
- [98] M. Paulsson, “*Non equilibrium Green’s functions for dummies: Introduction to the one particle NEGF equations*”, *arXiv e-prints*, [arXiv:/0210519](https://arxiv.org/abs/0210519) (2006).
- [99] S. Datta, *Electronic transport in mesoscopic systems*. Cambridge: Cambridge University Press, 1995.
- [100] M. Paulsson, F. Zahid, and S. Datta, “*Resistance of a molecule*”, <https://nanohub.org/resources/123> (2003).
- [101] S. Datta, *Quantum transport: Atom to transistor*. Cambridge University Press, 2005.

- [102] M. P. L. Sancho, J. M. L. Sancho, and J. Rubio, “*Quick iterative scheme for the calculation of transfer matrices: application to Mo (100)*”, *J. Phys. F* **14**, 1205–1215 (1984).
- [103] M. P. L. Sancho, J. M. L. Sancho, J. M. L. Sancho, and J. Rubio, “*Highly convergent schemes for the calculation of bulk and surface Green functions*”, *J. Phys. F* **15**, 851–858 (1985).
- [104] A.-P. Jauho, N. S. Wingreen, and Y. Meir, “*Time-dependent transport in interacting and noninteracting resonant-tunneling systems*”, *Phys. Rev. B* **50**, 5528–5544 (1994).
- [105] H. Haug and A.-P. Jauho, *Quantum kinetics in transport and optics of semiconductors*, 2nd ed. Springer, Berlin, Heidelberg, 2008.
- [106] C. J. O. Verzijl, J. S. Seldenthuis, and J. M. Thijssen, “*Applicability of the wide-band limit in DFT-based molecular transport calculations*”, *J. Chem. Phys.* **138**, 094102 (2013).
- [107] F. Covito, F. G. Eich, R. Tuovinen, M. A. Sentef, and A. Rubio, “*Transient charge and energy flow in the wide-band limit*”, *J. Chem. Theory Comput.* **14**, 2495–2504 (2018).
- [108] P. H. Jacobse, A. Kimouche, T. Gebraad, M. M. Ervasti, J. M. Thijssen, P. Liljeroth, and I. Swart, “*Electronic components embedded in a single graphene nanoribbon*”, *Nat. Commun.* **8**, 119 (2017).
- [109] P. Jacobse, M. J. J. Mangnus, S. J. M. Zevenhuizen, and I. Swart, “*Mapping the conductance of electronically decoupled graphene nanoribbons*”, *ACS Nano* **12**, 7048–7056 (2018).
- [110] D. S. Fisher and P. A. Lee, “*Relation between conductivity and transmission matrix*”, *Phys. Rev. B* **23**, 6851–6854 (1981).
- [111] F. Evers, R. Korytár, S. Tewari, and J. M. van Ruitenbeek, “*Advances and challenges in single-molecule electron transport*”, *Rev. Mod. Phys.* **92**, 035001 (2020).
- [112] R. Landauer, “*Spatial variation of currents and fields due to localized scatterers in metallic conduction*”, *IBM J. Res. Dev.* **1**, 223–231 (1957).

- [113] M. Büttiker, Y. Imry, R. Landauer, and S. Pinhas, “Generalized many-channel conductance formula with application to small rings”, *Phys. Rev. B* **31**, 6207–6215 (1985).
- [114] M. Buttiker, “Coherent and sequential tunneling in series barriers”, *IBM J. Res. Dev.* **32**, 63–75 (1988).
- [115] N. Kobayashi, M. Brandbyge, and M. Tsukada, “First-principles study of electron transport through monatomic Al and Na wires”, *Phys. Rev. B* **62**, 8430–8437 (2000).
- [116] J. Taylor, M. Brandbyge, and K. Stokbro, “Conductance switching in a molecular device: The role of side groups and intermolecular interactions”, *Phys. Rev. B* **68**, 121101 (2003).
- [117] M. Paulsson and M. Brandbyge, “Transmission eigenchannels from nonequilibrium Green’s functions”, *Phys. Rev. B* **76**, 115117 (2007).
- [118] E. Scheer, N. Agrait, J. C. Cuevas, A. L. Yeyati, B. Ludoph, A. Martín-Rodero, G. R. Bollinger, J. M. van Ruitenbeek, and C. Urbina, “The signature of chemical valence in the electrical conduction through a single-atom contact”, *Nature* **394**, 154–157 (1998).
- [119] N. Agrait, A. L. Yeyati, and J. M. van Ruitenbeek, “Quantum properties of atomic-sized conductors”, *Phys. Rep.* **377**, 81–279 (2003).
- [120] M. Büttiker, “Four-terminal phase-coherent conductance”, *Phys. Rev. Lett.* **57**, 1761–1764 (1986).
- [121] M. Cahay, M. McLennan, and S. Datta, “Conductance of an array of elastic scatterers: A scattering-matrix approach”, *Phys. Rev. B* **37**, 10 125–10 136 (1988).
- [122] L. Pauling, “The nature of the chemical bond. Application of results obtained from the quantum mechanics and from a theory of paramagnetic susceptibility to the structure of molecules”, *J. Am. Chem. Soc.* **53**, 1367–1400 (1931).
- [123] A. Szabo, A. Szabó, and N. Ostlund, *Modern quantum chemistry: Introduction to advanced electronic structure theory*. Macmillan, 1982.
- [124] R. M. Martin, *Electronic structure: Basic theory and practical methods*. Cambridge University Press, 2004.

- [125] P. R. Wallace, “*The band theory of graphite*”, *Phys. Rev.* **71**, 622–634 (1947).
- [126] P. Vogl, H. P. Hjalmarson, and J. D. Dow, “*A Semi-empirical tight-binding theory of the electronic structure of semiconductors*”, *J. Phys. Chem. Solids* **44**, 365–378 (1983).
- [127] J.-M. Jancu, R. Scholz, F. Beltram, and F. Bassani, “*Empirical spds* tight-binding calculation for cubic semiconductors: General method and material parameters*”, *Phys. Rev. B* **57**, 6493–6507 (1998).
- [128] B. O. Roos, P. R. Taylor, and P. E. Sigbahn, “*A complete active space SCF method (CASSCF) using a density matrix formulated super-CI approach*”, *Chem. Phys.* **48**, 157 – 173 (1980).
- [129] N. Ashcroft and N. Mermin, *Solid state physics*. Cengage Learning, 2011.
- [130] C. Kittel, *Introduction to solid state physics*, 6th ed. New York: John Wiley & Sons, Inc., 1986.
- [131] J. Singleton, *Band theory and electronic properties of solids*. New York: Oxford University Press, 2001.
- [132] J. M. Arrieta, *Modelling of plasmonic and graphene nanodevices*, ser. Springer Theses. Springer International Publishing, 2014.
- [133] C. M. Goringe, D. R. Bowler, and E. Hernández, “*Tight-binding modelling of materials*”, *Rep. Prog. Phys.* **60**, 1447–1512 (1997).
- [134] P. Ordejón, “*Order-N tight-binding methods for electronic-structure and molecular dynamics*”, *Comput. Mater. Sci.* **12**, 157–191 (1998).
- [135] E. Hückel, “*Quantentheoretische Beiträge zum Benzolproblem*”, *Z. Phys.* **70**, 204–286 (1931).
- [136] E. Hückel, “*Quantentheoretische Beiträge zum Benzolproblem*”, *Z. Phys.* **72**, 310–337 (1931).
- [137] E. Hückel, “*Quantentheoretische Beiträge zum Problem der aromatischen und ungesättigten Verbindungen. III*”, *Z. Phys.* **76**, 628–648 (1932).
- [138] F. Bloch, “*Über die Quantenmechanik der Elektronen in Kristallgittern*”, *Z. Phys.* **52**, 555–600 (1929).

- [139] J. C. Slater and G. F. Koster, “*Simplified LCAO method for the periodic potential problem*”, *Phys. Rev.* **94**, 1498–1524 (1954).
- [140] E. Dobardžić, M. Dimitrijević, and M. V. Milovanović, “*Generalized Bloch theorem and topological characterization*”, *Phys. Rev. B* **91**, 125424 (2015).
- [141] J. Zak, “*Berry’s phase for energy bands in solids*”, *Phys. Rev. Lett.* **62**, 2747–2750 (1989).
- [142] Y. Hancock, A. Uppstu, K. Saloriutta, A. Harju, and M. J. Puska, “*Generalized tight-binding transport model for graphene nanoribbon-based systems*”, *Phys. Rev. B* **81**, 245402 (2010).
- [143] K. Sugawara, T. Sato, S. Souma, T. Takahashi, and H. Suematsu, “*Fermi surface and edge-localized states in graphite studied by high-resolution angle-resolved photoemission spectroscopy*”, *Phys. Rev. B* **73**, 045124 (2006).
- [144] D. Huertas-Hernando, F. Guinea, and A. Brataas, “*Spin-orbit coupling in curved graphene, fullerenes, nanotubes, and nanotube caps*”, *Phys. Rev. B* **74**, 155426 (2006).
- [145] Y. Yao, F. Ye, X.-L. Qi, S.-C. Zhang, and Z. Fang, “*Spin-orbit gap of graphene: First-principles calculations*”, *Phys. Rev. B* **75**, 041401 (2007).
- [146] S. Konschuh, M. Gmitra, and J. Fabian, “*Tight-binding theory of the spin-orbit coupling in graphene*”, *Phys. Rev. B* **82**, 245412 (2010).
- [147] I. Nikiforov, E. Dontsova, R. D. James, and T. Dumitrică, “*Tight-binding theory of graphene bending*”, *Phys. Rev. B* **89**, 155437 (2014).
- [148] A. J. Pearce, E. Mariani, and G. Burkard, “*Tight-binding approach to strain and curvature in monolayer transition-metal dichalcogenides*”, *Phys. Rev. B* **94**, 155416 (2016).
- [149] S. Reich, J. Maultzsch, C. Thomsen, and P. Ordejón, “*Tight-binding description of graphene*”, *Phys. Rev. B* **66**, 035412 (2002).
- [150] Y. Kobayashi, K.-i. Fukui, T. Enoki, K. Kusakabe, and Y. Kaburagi, “*Observation of zigzag and armchair edges of graphite using scanning tunneling microscopy and spectroscopy*”, *Phys. Rev. B* **71**, 193406 (2005).

- [151] Y. Niimi, T. Matsui, H. Kambara, K. Tagami, M. Tsukada, and H. Fukuyama, “*Scanning tunneling microscopy and spectroscopy of the electronic local density of states of graphite surfaces near monoatomic step edges*”, [Phys. Rev. B](#) **73**, 085421 (2006).
- [152] Y. Zhang, Y.-W. Tan, H. L. Stormer, and P. Kim, “*Experimental observation of the quantum Hall effect and Berry’s phase in graphene*”, [Nature](#) **438**, 201–204 (2005).
- [153] L. Brey and H. A. Fertig, “*Electronic states of graphene nanoribbons studied with the Dirac equation*”, [Phys. Rev. B](#) **73**, 235411 (2006).
- [154] L. Brey and H. A. Fertig, “*Edge states and the quantized Hall effect in graphene*”, [Phys. Rev. B](#) **73**, 195408 (2006).
- [155] L. Yang, C.-H. Park, Y.-W. Son, M. L. Cohen, and S. G. Louie, “*Quasiparticle energies and band gaps in graphene nanoribbons*”, [Phys. Rev. Lett.](#) **99**, 186801 (2007).
- [156] L. Sun, P. Wei, J. Wei, S. Sanvito, and S. Hou, “*From zigzag to armchair: The energetic stability, electronic and magnetic properties of chiral graphene nanoribbons with hydrogen-terminated edges*”, [J. Phys.: Condens. Matter](#) **23**, 425301 (2011).
- [157] W. Jaskólski, A. Ayuela, M. Pelc, H. Santos, and L. Chico, “*Edge states and flat bands in graphene nanoribbons with arbitrary geometries*”, [Phys. Rev. B](#) **83**, 235424 (2011).
- [158] O. V. Yazyev, R. B. Capaz, and S. G. Louie, “*Theory of magnetic edge states in chiral graphene nanoribbons*”, [Phys. Rev. B](#) **84**, 115406 (2011).
- [159] Z. Jiang and Y. Song, “*Band gap oscillation and novel transport property in ultrathin chiral graphene nanoribbons*”, [Phys. B: Condens. Matter](#) **464**, 61–67 (2015).
- [160] N. Merino-Díez, J. Li, A. Garcia-Lekue, G. Vasseur, M. Vilas-Varela, E. Carbonell-Sanromà, M. Corso, J. E. Ortega, D. Peña, J. I. Pascual, and D. G. de Oteyza, “*Unraveling the electronic structure of narrow atomically precise chiral graphene nanoribbons*”, [J. Phys. Chem. Lett.](#) **9**, 25–30 (2018).

- [161] J. Li, S. Sanz, N. Merino-Díez, M. Vilas-Varela, A. Garcia-Lekue, M. Corso, D. G. de Oteyza, T. Frederiksen, D. Peña, and J. I. Pascual, “*Topological phase transition in chiral graphene nanoribbons: from edge bands to end states*”, *Nat. Commun.* **12**, 5538 (2021).
- [162] J. Hubbard, “*Electron correlations in narrow energy bands*”, *Proc. Math. Phys. Eng. Sci.* **276**, 238–257 (1963).
- [163] J. Hubbard and B. H. Flowers, “*Electron correlations in narrow energy bands III. An improved solution*”, *Proc. Math. Phys. Eng. Sci.* **281**, 401–419 (1964).
- [164] J. Kanamori, “*Electron correlation and ferromagnetism of transition metals*”, *Prog. Theor. Phys.* **30**, 275–289 (1963).
- [165] M. C. Gutzwiller, “*Effect of correlation on the ferromagnetism of transition metals*”, *Phys. Rev. Lett.* **10**, 159–162 (1963).
- [166] F. H. L. Essler, H. Frahm, F. Göhmann, A. Klümper, and V. E. Korepin, *The one-dimensional Hubbard model*. Cambridge University Press, 2005.
- [167] T. O. Wehling, E. Şaşıoğlu, C. Friedrich, A. I. Lichtenstein, M. I. Katsnelson, and S. Blügel, “*Strength of effective Coulomb interactions in graphene and graphite*”, *Phys. Rev. Lett.* **106**, 236805 (2011).
- [168] A. R. Carvalho, J. H. Warnes, and C. H. Lewenkopf, “*Edge magnetization and local density of states in chiral graphene nanoribbons*”, *Phys. Rev. B* **89**, 245444 (2014).
- [169] H. Feldner, Z. Y. Meng, T. C. Lang, F. F. Assaad, S. Wessel, and A. Honecker, “*Dynamical signatures of edge-state magnetism on graphene nanoribbons*”, *Phys. Rev. Lett.* **106**, 226401 (2011).
- [170] S. Mishra, D. Beyer, K. Eimre, J. Liu, R. Berger, O. Gröning, C. A. Pignedoli, K. Müllen, R. Fasel, X. Feng, and P. Ruffieux, “*Synthesis and characterization of π -extended triangulene*”, *J. Am. Chem. Soc.* **141**, 10621–10625 (2019).
- [171] J. E. Hirsch, “*Two-dimensional Hubbard model: Numerical simulation study*”, *Phys. Rev. B* **31**, 4403–4419 (1985).
- [172] J. S. Andrews, D. Jayatilaka, R. G. Bone, N. C. Handy, and R. D. Amos, “*Spin contamination in single-determinant wavefunctions*”, *Chem. Phys. Lett.* **183**, 423–431 (1991).

- [173] D. Sanchez-Portal, E. Artacho, and J. M. Soler, “*Projection of plane-wave calculations into atomic orbitals*”, *Solid State Commun.* **95**, 685 – 690 (1995).
- [174] R. S. Mulliken, “*Electronic population analysis on LCAO–MO molecular wave functions. I*”, *J. Chem. Phys.* **23**, 1833–1840 (1955).
- [175] H. J. Monkhorst and J. D. Pack, “*Special points for Brillouin-zone integrations*”, *Phys. Rev. B* **13**, 5188–5192 (1976).
- [176] L. F. Shampine, “*Numerical recipes, the art of scientific computing. By W. H. Press, B. P. Flannery, S. A. Teukolsky, and W. T. Vetterling*”, *Am. Math. Mon.* **94**, 889–893 (1987).
- [177] P. Pulay, “*Convergence acceleration of iterative sequences. The case of scf iteration*”, *Chem. Phys. Lett.* **73**, 393–398 (1980).
- [178] P. Pulay, “*Improved SCF convergence acceleration*”, *J. Comput. Chem.* **3**, 556–560 (1982).
- [179] P. Hohenberg and W. Kohn, “*Inhomogeneous electron gas*”, *Phys. Rev.* **136**, B864–B871 (1964).
- [180] W. Kohn and L. J. Sham, “*Self-consistent equations including exchange and correlation effects*”, *Phys. Rev.* **140**, A1133–A1138 (1965).
- [181] O. F. Sankey and D. J. Niklewski, “*Ab initio multicenter tight-binding model for molecular-dynamics simulations and other applications in covalent systems*”, *Phys. Rev. B* **40**, 3979–3995 (1989).
- [182] J. P. Perdew and A. Zunger, “*Self-interaction correction to density-functional approximations for many-electron systems*”, *Phys. Rev. B* **23**, 5048–5079 (1981).
- [183] J. P. Perdew, K. Burke, and M. Ernzerhof, “*Generalized gradient approximation made simple*”, *Phys. Rev. Lett.* **77**, 3865–3868 (1996).
- [184] A. García, N. Papior, A. Akhtar, E. Artacho, V. Blum, E. Bosoni, P. Brandimarte, M. Brandbyge, J. I. Cerdá, F. Corsetti, R. Cuadrado, V. Dikan, J. Ferrer, J. Gale, P. García-Fernández, V. M. García-Suárez, S. García, G. Huhs, S. Illera, R. Korytár, P. Koval, I. Lebedeva, L. Lin, P. López-Tarifa, S. G. Mayo, S. Mohr, P. Ordejón, A. Postnikov, Y. Pouillon, M. Pruneda, R. Robles, D. Sánchez-Portal, J. M. Soler, R. Ullah, V. W.-z. Yu, and J. Junquera, “*Siesta: Recent developments and applications*”, *J. Chem. Phys.* **152**, 204108 (2020).

- [185] M. Dion, H. Rydberg, E. Schröder, D. C. Langreth, and B. I. Lundqvist, “*Van der Waals density functional for general geometries*”, *Phys. Rev. Lett.* **92**, 246401 (2004).
- [186] K. Berland and P. Hyldgaard, “*Exchange functional that tests the robustness of the plasmon description of the van der Waals density functional*”, *Phys. Rev. B* **89**, 035412 (2014).
- [187] D. R. Hamann, M. Schlüter, and C. Chiang, “*Norm-conserving pseudopotentials*”, *Phys. Rev. Lett.* **43**, 1494–1497 (1979).
- [188] G. B. Bachelet, D. R. Hamann, and M. Schlüter, “*Pseudopotentials that work: From H to Pu*”, *Phys. Rev. B* **26**, 4199–4228 (1982).
- [189] L. Kleinman and D. M. Bylander, “*Efficacious Form for Model Pseudopotentials*”, *Phys. Rev. Lett.* **48**, 1425–1428 (1982).
- [190] S. G. Louie, S. Froyen, and M. L. Cohen, “*Nonlinear ionic pseudopotentials in spin-density-functional calculations*”, *Phys. Rev. B* **26**, 1738–1742 (1982).
- [191] E. Clar and D. G. Stewart, “*Aromatic hydrocarbons. LXV. Triangulene derivatives¹*”, *J. Am. Chem. Soc.* **75**, 2667–2672 (1953).
- [192] S. Sasaki, S. De Franceschi, J. M. Elzerman, W. G. van der Wiel, M. Eto, S. Tarucha, and L. P. Kouwenhoven, “*Kondo effect in an integer-spin quantum dot*”, *Nature* **405**, 764–767 (2000).
- [193] N. Roch, S. Florens, T. A. Costi, W. Wernsdorfer, and F. Balestro, “*Observation of the underscreened Kondo effect in a molecular transistor*”, *Phys. Rev. Lett.* **103**, 197202 (2009).
- [194] J. J. Parks, A. R. Champagne, T. A. Costi, W. W. Shum, A. N. Pasupathy, E. Neuscamman, S. Flores-Torres, P. S. Cornaglia, A. A. Aligia, C. A. Balseiro, G. K.-L. Chan, H. D. Abruña, and D. C. Ralph, “*Mechanical control of spin states in spin-1 molecules and the underscreened Kondo effect*”, *Science* **328**, 1370–1373 (2010).
- [195] X. Wang, G. Sun, P. Routh, D.-H. Kim, W. Huang, and P. Chen, “*Heteroatom-doped graphene materials: syntheses, properties and applications*”, *Chem. Soc. Rev.* **43**, 7067–7098 (2014).

- [196] G. Trambly de Laissardière, D. Mayou, and L. Magaud, “*Localization of Dirac electrons in rotated graphene bilayers*”, *Nano Lett.* **10**, 804–808 (2010).
- [197] E. Mostaani, N. D. Drummond, and V. I. Fal’ko, “*Quantum Monte Carlo calculation of the binding energy of bilayer graphene*”, *Phys. Rev. Lett.* **115**, 115501 (2015).
- [198] H. Lee, Y.-W. Son, N. Park, S. Han, and J. Yu, “*Magnetic ordering at the edges of graphitic fragments: Magnetic tail interactions between the edge-localized states*”, *Phys. Rev. B* **72**, 174431 (2005).
- [199] K. V. Raman, A. M. Kamerbeek, A. Mukherjee, N. Atodiresi, T. K. Sen, P. Lazić, V. Caciuc, R. Michel, D. Stalke, S. K. Mandal, S. Blügel, M. Münzenberg, and J. S. Moodera, “*Interface-engineered templates for molecular spin memory devices*”, *Nature* **493**, 509–513 (2013).
- [200] Z. Bullard, E. C. Girão, J. R. Owens, W. A. Shelton, and V. Meunier, “*Improved all-carbon spintronic device design*”, *Sci. Rep.* **5**, 7634 (2015).
- [201] F. Lombardi, A. Lodi, J. Ma, J. Liu, M. Slota, A. Narita, W. K. Myers, K. Müllen, X. Feng, and L. Bogani, “*Quantum units from the topological engineering of molecular graphenoids*”, *Science* **366**, 1107–1110 (2019).
- [202] A. A. Khajetoorians, J. Wiebe, B. Chilian, and R. Wiesendanger, “*Realizing all-spin-based logic operations atom by atom*”, *Science* **332**, 1062–1064 (2011).
- [203] S. Dutta, S. Lakshmi, and S. K. Pati, “*Electron-electron interactions on the edge states of graphene: A many-body configuration interaction study*”, *Phys. Rev. B* **77**, 073412 (2008).
- [204] R. Ortiz, N. A. García-Martínez, J. L. Lado, and J. Fernández-Rossier, “*Electrical spin manipulation in graphene nanostructures*”, *Phys. Rev. B* **97**, 195425 (2018).
- [205] A. Sarkar, T. K. Bhattacharyya, and A. Patwardhan, “*Quantum logic processor: Implementation with electronic Mach-Zehnder interferometer*”, *Appl. Phys. Lett.* **88**, 213113 (2006).
- [206] M. Yamamoto, S. Takada, C. Bäuerle, K. Watanabe, A. D. Wieck, and S. Tarucha, “*Electrical control of a solid-state flying qubit*”, *Nat. Nanotechnol.* **7**, 247–251 (2012).

- [207] Y. Aharonov and D. Bohm, “*Significance of electromagnetic potentials in the quantum theory*”, *Phys. Rev.* **115**, 485–491 (1959).